MAPPING THE PROBABILITY AND UNCERTAINTY OF LIQUEFACTION-INDUCED GROUND FAILURE

by

Daniel T. Gillins

A dissertation submitted to the faculty of
The University of Utah
in partial fulfillment of the requirements for the degree of

Doctor of Philosophy

Department of Civil and Environmental Engineering

The University of Utah

December 2012

The University of Utah Graduate School

STATEMENT OF DISSERTATION APPROVAL

The dissertation of **Daniel T. Gillins**

has been approved by the following supervisory committee members:

Steven F. Bartlett	, Chair	09/10/2012 Date Approved
Evert C. Lawton	, Member	09/10/2012 Date Approved
Lawrence D. Reaveley	, Member	09/10/2012 Date Approved
Glenn W. Johnson	, Member	09/10/2012 Date Approved
Kathleen Nicoll	, Member	09/10/2012 Date Approved

and by Chris P. Pantelides , Chair of

the Department of **Civil and Environmental Engineering**

and by Charles A. Wight, Dean of The Graduate School.

ABSTRACT

This paper proposes a probabilistic-based method to produce liquefaction-induced ground failure maps so that hazard levels can be assessed for a large area, such as a county, township, or quadrangle. The method focuses on using probabilistic approaches to map estimates of liquefaction-induced lateral spread displacement, and defining the uncertainty associated with the displacement estimates. The proposed mapping method uses a newly developed empirical model for estimating quantities of lateral spread displacement, current probabilistic liquefaction triggering analyses, probabilistic strong ground motion estimates, surficial geologic maps, digital elevation models, and geotechnical data compiled into a spatial database. The proposed method accounts for variations in soil conditions, age, topography, spatial distribution, and major sources of uncertainty. Such major uncertainties include variability over space, lack of or poor quality data, and limitations of the empirical models to estimate liquefaction phenomena. The proposed mapping method accounts for these uncertainties by Monte Carlo random sampling.

Soil type and thickness are important factors in estimating horizontal displacement from lateral spread. Thus, this paper presents a new empirical model for estimating the amount of lateral spread displacement based on these factors, along with other factors such as earthquake magnitude, distance to the seismic source, and

topography. In addition, the paper discusses how cone penetration test (CPT) data can be used in conjunction with the proposed empirical model to estimate the amount of lateral spread displacement.

To test its suitability and provide an example, the proposed mapping method is implemented to produce probabilistic liquefaction triggering and lateral spread displacement maps for a study area in Weber County, Utah. The new maps indicate substantial risk for liquefaction-induced ground failure in the study area during large-magnitude seismic events. This is because the study area is filled with potentially liquefiable sediments, nearly all subsurface explorations encountered shallow groundwater, and the study area is near the seismically active Wasatch fault zone. Large uncertainties in the mapped estimates leads to producing maps for 16^{th}, 50^{th}, and 84^{th} percentile probabilities—enabling estimation of a distribution of probabilities.

TABLE OF CONTENTS

LIST OF TABLES

LIST OF FIGURES

ACKNOWLEDGEMENTS

The Weber Basin Water Conservancy District, and the U.S. Geological Survey (USGS), Department of the Interior, under USGS award number G12AP20074, supported portions of this research. I am grateful to these agencies for their funding and technical interest.

This liquefaction hazard mapping project is based on available geotechnical data. I would like to thank those government agencies, engineering firms, and engineers who were willing to provide vital data. For instance, thanks to the Weber Basin Water Conservancy District, Utah Department of Transportation (UDOT), Weber County Recorder's office, the City of Ogden, and many others.

I would also like to express my appreciation to my dissertation committee. Thank you for your time, advice, lessons, assistance, and review of this research. I especially want to acknowledge Dr. Steven F. Bartlett, chair of this committee. This research would not have been accomplished without his expertise, willingness to work, thoughtful ideas, and much needed guidance.

Finally, I am grateful for the patience of my wife and the encouragement from my family. Thank you!

CHAPTER 1

INTRODUCTION

Research Project Background

Liquefaction-induced ground failure can cause significant damage to infrastructure and other facilities during major earthquakes. Ground displacements ranging from a few tenths of a meter to several meters are common in liquefaction prone areas (Bartlett and Youd 1992). Ground failures from most-recent earthquakes in Japan and New Zealand raise questions about our ability to assess, delineate and quantify the hazard in vulnerable locations. The best defense against such damage is to first, identify areas prone to liquefaction-induced ground failure; then, establish planning, development, and engineering strategies to mitigate the hazard. The purpose of this research is to develop a method to produce liquefaction-induced ground failure maps so that hazard levels can be assessed for a large area (i.e., county, township, quadrangle, etc.). The research focuses on: (1) using probabilistic methods to map estimates of lateral spread displacement potential for a large study area; and, (2) estimate the uncertainty associated with the displacement estimates. The intent is to develop a mapping method that is applicable to all areas in the United States with significant risk of damage from liquefaction.

To test its suitability and provide an example, the mapping method is implemented to produce new probabilistic liquefaction hazard maps for the urban area (i.e., Wasatch Front) of Weber County, Utah. Unfortunately, many locales along the Wasatch Front have considerable liquefaction hazard due to the common presence of loose, saturated, cohesionless soils and the proximity to sources of significant seismic shaking, such as the Wasatch fault zone. Harty and Lowe (2003) identified numerous prehistoric liquefaction-induced flow failures and lateral spreads along the Wasatch Front. Because of the relatively high potential of liquefaction damage, previous researchers have mapped areas susceptible to liquefaction in the urban areas of Utah.

Mapping of liquefaction hazards for urban areas located along the Wasatch Front began in the 1980s when Utah State University received a National Earthquake Hazards Reduction Program (NEHRP) grant to assess Davis County (Anderson and Keaton 1982; Anderson et al. 1994). Their mapping techniques were further developed and extended to map liquefaction hazards in eleven additional counties in northern and central Utah, including Weber County (e.g., Anderson et al. 1994b).

However, since the production of the Anderson et al. maps, there have been several advancements that warrant the development of new maps. Such advancements include: (1) progress in probabilistic liquefaction triggering and lateral spread analyses (e.g., Cetin et al. 2004, Moss et al. 2006, Bartlett et al. 2005, Bartlett et al. 2010b); (2) updated probabilistic strong ground motion estimates via the USGS National Seismic Hazard Mapping Project (Peterson et al. 2008); (3) larger amounts of quality geotechnical data due to recent development; (4) support over the past two decades by the National Cooperative Geologic Mapping Program to federal, state, and university partners to

produce digital surficial geologic maps; and, (5) widespread adoption and use of Geographic Information Systems (GIS) to store and analyze spatial databases.

In 2003, members from government, academia, and industry with expertise in liquefaction mapping formed the Utah Liquefaction Advisory Group (ULAG). This group seeks to guide future mapping efforts, establish a consensus on technical approaches and needs, and form partnerships with private and government entities to accomplish goals. Since its inception, this group has developed mapping methods and produced new liquefaction hazard maps for Salt Lake County (Bartlett et al. 2005; 2010a,b). Their mapping method for Salt Lake County is based on a relatively extensive database of compiled geotechnical investigations, including: Standard Penetration Tests (SPT), Cone Penetrometer Tests (CPT), Shear Wave Velocity (V_S) measurements, and other measures of soil properties (i.e., soil classification, fines content, mean grain size, etc.). From this subsurface database, members of ULAG employed the Youd et al. (2002) empirical model to estimate lateral spread displacement at each borehole location. Using mapped surficial geology as constraints, they then generalized these point estimates to produce liquefaction hazard maps for Salt Lake County.

However, there are less developments and geotechnical data in other areas in Utah vulnerable to liquefaction damage (i.e., Weber, Utah, Davis, and Box Elder County). To extend the mapping program to these areas, the method must be modified significantly. The primary issues to address are: (1) how to estimate liquefaction-induced ground failure hazards for geologic units that lack or have little geotechnical data; and, (2) how to quantify the uncertainty in the estimates given varying levels of data quality and

statistical support within the mapped domain. These issues must be successfully resolved in order to develop a defensible and reliable mapping methodology.

Organization of the Dissertation

This dissertation consists of three journal quality papers that I intend to submit for publication within scholarly engineering journals. Each of these papers represents a separate chapter within this dissertation; specifically, Chapters 3, 4, and 5. Additional information that did not fit in these papers is in the appendices.

Chapter 2 contains a literature review and evaluation of several existing approaches to predict liquefaction-induced ground failures. The chapter also includes a brief review of previous efforts to map liquefaction hazards in urban areas of Utah.

Chapter 3 discusses significant revisions to the Youd et al. (2002) empirical model for predicting liquefaction-induced lateral spread displacements. These revisions make the empirical model more parsimonious and implementable for regional hazard analysis while preserving much of its original predictive power. The chapter also provides guidance on how to use data from the Cone Penetration Test (CPT) to predict lateral spread displacements.

Chapter 4 proposes a reliability-based method to map estimates of the probability of liquefaction triggering and lateral spread displacement exceeding specified thresholds for a scenario earthquake. The method uses the revised empirical model discussed in Chapter 3, and accounts for major sources of uncertainty in the mapped estimates using Monte Carlo random sampling.

After implementing the mapping method proposed in Chapter 4, Chapter 5 presents probabilistic liquefaction-induced ground failure maps for the Wasatch Front of Weber County, Utah. Chapter 5 also describes how to define the uncertainties in the mapped probabilities.

Chapter 6 contains a discussion of the conclusions and major findings of this research.

Finally, the appendices contain an explanation of the structure of the geotechnical database for the mapping project, histograms of geotechnical data for several geologic units in the study area, additional probabilistic liquefaction-induced ground failure maps for Weber County, and Matlab® computer programming code for reducing raw data and performing numerous calculations.

References

Anderson, L. R., and Keaton, J. R., 1982. Development of a soil liquefaction potential map, in *Proc., Int. Conf on Soil Dynamics and Earthquake Engineering*, Southampton, England, July 13-15.

Anderson, L. R., Keaton, J. R., Aubry, K., and Ellis, S. J., 1994. *Liquefaction Potential Map for Davis County, Utah, Complete Technical Report, Utah Geological Survey Contract Report 94-7*, Salt Lake City, UT.

Anderson, L. R., Keaton, J. R., and Bay, J. A., 1994b. *Liquefaction Potential Map for the Northern Wasatch Front, Utah, Complete Technical Report, Utah Geological Survey Contract Report 94-6*, Salt Lake City, UT.

Bartlett, S. F., and Youd, T. L., 1992. *Empirical Analysis of Horizontal Ground Displacement Generated by Liquefaction-Induced Lateral Spreads, Technical Report NCEER-92-0021*, National Center for Earthquake Engineering Research, Buffalo, NY.

Bartlett, S. F., Erickson, G., Leeflang, B., Solomon, B. J., 2010a. *Probabilistic Liquefaction Potential and Liquefaction-Induced Ground Failure Maps for the Urban Wasatch Front: Phase III, Fiscal Year 2006, U.S.G.S. Research Award No. 06HQGR0015*, Denver, CO.

Bartlett, S. F., Gerber, T. M., Hinckley, D., 2010b. *Probabilistic Liquefaction Potential and Liquefaction-Induced Ground Failure Maps for the Urban Wasatch Front: Phase IV, Fiscal Year 2007: Collaborative Research with University of Utah and Brigham Young University, U.S.G.S. Research Award Nos. 07HQGR0021 and 07HQGR0024*, Denver, CO.

Bartlett S. F., Olsen, M. J., and Solomon, B. J., 2005. *Probabilistic Liquefaction Potential and Liquefaction-Induced Ground Failure Maps for the Urban Wasatch Front: Collaborative Research with the University of Utah, Utah State University and the Utah Geological Survey, Phase I, FY2004, U.S.G.S. Research Award No. 04HQGR0026*, Reston, VA.

Cetin, K. O., Seed, R. B., Kiureghian, A. D., Tokimatsu, K., Harder, L. F., Jr., Kayen, R. E., and Moss, R. E., 2004. Standard Penetration Test-based probabilistic and deterministic assessment of seismic soil liquefaction potential, *J. Geotech. Geoenviron. Eng.* **130**(12), 1314 – 1340.

Harty, K. M., and Lowe, M., 2003. *Geologic Evaluation and Hazard Potential of Liquefaction-Induced Landslides along the Wasatch Front, Utah, Utah Geological Survey Special Study 104*, Salt Lake City, UT, 40 pp., 16 pl.

Moss, R. E. S., Seed, R. B., Kayen, R. E., Stewart, J. P., Kiureghian, A. D., and Cetin, K. O., 2006. CPT-based probabilistic and deterministic assessment of in situ seismic soil liquefaction potential, *J. Geotech. Geoenviron. Eng.* **132**(8), 1032 – 1051.

National Research Council (NRC), 1985. *Liquefaction of Soils During Earthquakes*, National Academy Press, Washington D. C., 240 pp.

Petersen, M. D., Frankel, A. D., Harmsen, S. C., Mueller, C. S., Haller, K. M., Wheeler, R. L., Wesson, R. L., Zeng, Y., Boyd, O. S., Perkins, D. M., Luco, N., Field, E. H., Wills, C. J., and Rukstales, K. S., 2008. *Documentation for the 2008 Update of the United States National Seismic Hazard Maps, U.S. Geological Survey Open-File Report 2008–1128*, Reston, VA, 61 pp.

Youd, T. L., Hansen, C. M., and Bartlett S. F., 2002. Revised multilinear regression equations for prediction of lateral spread displacement, *J. Geotech. Geoenviron. Eng.* **128**(12), 1007-1017.

CHAPTER 2

REVIEW OF EXISTING METHODS TO PREDICT LIQUEFACTION-INDUCED GROUND FAILURES

Abstract

Liquefaction-induced ground failures can cause severe and costly damage to the built-up environment. Hence, numerous researchers have developed techniques to predict and map the potential severity of ground failures induced by liquefaction during earthquakes. Such techniques are based on geologic setting, topographic conditions, seismic hazards, the thickness of potentially liquefiable soils, and/or geotechnical data. Because the mechanisms that produce liquefaction-induced ground failures are complex, approaches to predict ground failures are often based on empirical or semiempirical approaches. This paper reviews and evaluates many of the popular approaches used by researchers. In addition, this paper discusses previous efforts in Utah to map potential liquefaction-induced ground failure hazards during large seismic events. Based on this literature review, there is a need to develop a new method to map predictions of liquefaction-induced lateral spread displacements during earthquakes, and estimate the uncertainty of these predictions.

Introduction

Soil liquefaction occurs when saturated soil loses significant shear resistance due to cyclic loads generated usually by major earthquakes. The phenomenon is most commonly observed in saturated, loosely deposited, poorly-cemented, and young, sandy soils. Such loose, sandy soils tend to compress or densify under loading. If the soil is saturated with water, increased pore water pressures are generated as the soil attempts to reach a denser state. When large loads are rapidly applied or repeated many times, the excess pore water pressure in the soil does not have sufficient time to dissipate. Such undrained conditions result in a decrease in the effective stresses of the soil, causing the soil to lose shear resistance and behave more like a liquid.

Upon liquefaction, sediments undergo various types of ground deformation that can be very damaging. On relatively flat ground, structures atop the liquefied layer may tip or settle due to loss of bearing strength. In addition, blocks of mostly intact, surficial soil above the liquefied layer of sediment may collide and jostle during ground oscillations (NRC 1985). On gentle slopes (typically ground slopes between 0.3 to 5%), these blocks of soil may displace down slope or towards a free-face (i.e., channel or abrupt depression), along a shear zone formed by liquefaction (Bartlett and Youd 1992). Such displacements are called lateral spreads, which may tear or compress foundations, and shear utility lines. On steeper slopes, catastrophic flow failures may occur where tens of kilometers of blocks of surficial sediment can travel tens of meters (Youd 1984). The eruption of sand and water onto the ground surface (sand boils or blows) may accompany all of these ground failures during liquefaction.

Because of the potential for severe and costly damage to infrastructure and other facilities due to liquefaction, numerous researchers have developed approaches to predict liquefaction-induced ground failures. Such predictions are most commonly mapped in regions prone to major earthquakes. This paper reviews and evaluates many of the popular approaches to predict liquefaction-induced ground failure hazards.

Many of the urban areas in Utah (i.e., the Wasatch Front) are filled with potentially liquefiable sediments and are prone to large-magnitude seismic hazards. Hence, researchers have produced liquefaction hazard maps in several urban areas in Utah (e.g., Anderson et al. 1994, Anderson et al. 1994b, Solomon et al. 2004, Bartlett et al. 2005; 2010a,b). This paper also briefly reviews these mapping efforts.

Predictions from Seismicity and Geology

Youd and Perkins (1978) were some of the first authors to develop a procedure that uses geologic and seismological information to produce liquefaction-induced ground failure potential maps. The procedure required combination of two constituent maps: (1) a ground failure opportunity map, and (2) a ground failure susceptibility map. The ground failure opportunity map is based on estimates of regional seismicity and a correlation between earthquake magnitude and distance from a seismic energy source. Ground failure opportunity occurs when the intensity of seismic shaking is strong enough to cause liquefaction in susceptible materials.

The ground failure susceptibility map is based on data of Quaternary geology and correlations between geologic setting and susceptibility to liquefaction-induced ground failure. Youd and Perkins (1978) compiled a table of criteria necessary for evaluating

ground failure susceptibility of various depositional environments, as shown in Table 2.1. In that table, they noted that liquefaction resistance of soils increases with age. Combination of the ground failure opportunity maps and the ground failure susceptibility maps generate a map showing the potential for liquefaction-induced ground failure, or a ground failure potential map. These maps are useful for identifying areas where further site-specific investigations are needed. However, these maps lack the geotechnical data required for a more comprehensive analysis.

Predictions from Liquefaction Potential

From case studies of liquefaction in Japan, Iwasaki et al. (1979) introduced a parameter that describes the potential severity of liquefaction called the liquefaction potential index (LPI). The LPI assumes the severity of liquefaction is proportional to: (1) the thickness of the liquefiable deposit; (2) the proximity of the liquefiable deposit to the surface; and, (3) the amount that the factor of safety (FS) against liquefaction is less than one. In this case, FS is the ratio of soil capacity to resist liquefaction to seismic demand imposed upon the soil by the earthquake. Iwasaki et al. (1979) defined the LPI by eqn. (2.1).

$$LPI = \int_0^{20m} Fw(z)dz \tag{2.1}$$

where F is defined by eqn. (2.2) and $w(z)$ is defined by eqn. (2.3).

Table 2.1. Estimated susceptibility of sedimentary deposits to liquefaction during strong seismic shaking (after Youd and Perkins 1978)

Type of Deposit (1)	General Distribution of Cohesionless sediments in deposits (2)	Likelihood that Cohesionless Sediments, When Saturated, Would be Susceptible to Liquefaction (by Age of Deposit)			
		<500 yr (3)	Holocene (4)	Pleistocene (5)	Pre-Pleistocene (6)
(a) Continental Deposits					
River Channel	Locally Variable	Very High	High	Low	Very Low
Floodplain	Locally Variable	High	Moderate	Low	Very Low
Alluvial Fan and Plain	Widespread	Moderate	Low	Low	Very Low
MarineTerraces/ Plains	Widespread	-----	Low	Very Low	Very Low
Delta and Fan-delta	Widespread	High	Moderate	Low	Very Low
Lacustrine and Playa	Variable	High	Moderate	Low	Very Low
Colluvium	Variable	High	Moderate	Low	Very Low
Talus	Widespread	Low	Low	Very Low	Very Low
Dunes	Widespread	High	Moderate	Low	Very Low
Loess	Variable	High	High	High	Unknown
Glacial Till	Variable	Low	Low	Very Low	Very Low
Tuft	Rare	Low	Low	Very Low	Very Low
Tephra	Widespread	High	High	?	?
Residual Soils	Rare	Low	Low	Very Low	Very Low
Sebkha	Locally Variable	High	Moderate	Low	Very Low
(b) Coastal Zone					
Delta	Widespread	Very High	High	Low	Very Low
Esturine	Locally Variable	High	Moderate	Low	Very Low
Beach					
High Wave Energy	Widespread	Moderate	Low	Very Low	Very Low
Low Wave Energy	Widespread	High	Moderate	Low	Very Low
Lagoonal	Locally Variable	High	Moderate	Low	Very Low
Fore Shore	Locally Variable	High	Moderate	Low	Very Low
(c) Artificial					
Uncompacted Fill	Variable	Very High	-----	-----	-----
Compacted Fill	Variable	Low	-----	-----	-----

$$F = \begin{cases} 1 - FS & \text{for } FS \leq 1 \\ 0 & \text{for } FS > 1 \end{cases} \tag{2.2}$$

$$w(z) = 10 - 0.5 \cdot z \tag{2.3}$$

Because surface effects from liquefaction at depths greater than 20 meters are rarely reported, the summing of the LPI is limited to a depth (z) of 20 meters.

Based on case history data of ground failures, Iwasaki et al. (1982) and Toprak and Holzer (2003) correlated the significance of LPI values to surface manifestations of liquefaction. Iwasaki et al. (1982) concluded that severe liquefaction is likely to occur at sites with LPI > 15, and is not likely at sites with LPI < 5. Toprak and Holzer (2003) concluded that sand boils typically occur where LPI $\geq$ 5, and lateral spreads typically occur where LPI $\geq$ 12.

Numerous researchers have mapped the LPI to describe the spatial variability of the severity of liquefaction hazards in a study area. For instance, Holzer et al. (2006) combined a surficial geology base map and over 200 CPT soundings to determine values of FS for each geological unit in the Oakland, California area. They found values of FS using the simplified procedure (introduced by Seed and Idriss 1971; updated by Youd et al. 2001). Utilizing an LPI threshold value of 5 for the surface manifestations of liquefaction, Holzer et al. (2006) calculated cumulative frequency distributions of LPI for each geological unit in the study area; and, set the resulting distributions equal to the percent of area for each unit predicted to liquefy for a scenario seismic event. This approach offers some advantages to a purely deterministic analysis of whether or not

liquefaction triggers. However, the drawback with this approach is that these maps do not quantify the expected amount of ground displacement. This makes them less attractive from an engineering standpoint, where damage is strongly related to the quantity of ground displacement. In addition, the Holzer et al. (2006) mapping method assumes that each mapped geological unit is spatially homogeneous, and does not consider variations in topography.

Analyzing CPT data in three different regions in the United States, Lenz and Baise (2007) concluded there is significant variability of LPI within a given geological unit, and significant overlap of LPI values between geological units. They further concluded that to fully characterize this variability, regional liquefaction classification schemes should provide a distribution of liquefaction potential. As an alternative to using distributions, Lenz and Baise (2007) suggested geostatistical methods (such as kriging) to interpolate between data points to provide spatial information about liquefaction potential. However, often during regional hazard mapping projects, there are insufficient amounts of spatial data to develop a kriging model.

Predictions from the Thickness of the Liquefiable Layer

The thickness of loosely deposited, saturated, cohesionless deposits is one of the most significant factors affecting the severity of liquefaction. Based on field data from two large earthquakes in Japan, Ishihara (1985) found a relationship between the thicknesses of a soil layer susceptible to liquefaction and the occurrence of surface effects due to liquefaction. Using liquefaction triggering criteria in the Japanese bridge code, Ishihara calculated the thickness of the liquefiable layers and the thickness of the

overlying non-liquefiable layers. Thickness data are shown in Figure 2.1 for numerous sites. From these data, Ishihara (1985) developed curves for predicting the occurrence of surface effects due to liquefaction, as shown in Figure 2.2. Many engineers have used these thickness relationships to assess the potential for liquefaction-induced ground failures in their study areas.

Youd and Garris (1995) evaluated Ishihara's criteria by testing it against a wider range of site and earthquake conditions. They divided liquefaction-induced surface effects (or lack of effects) into four categories: (1) no observed surface effects; (2) sand boils and small ground fissures, but without noticeable lateral ground displacement; (3) sand boils and fissures plus the effects of ground oscillation; (4) surface effects generated by lateral spreads, including a consistent pattern of lateral ground displacement. Their study found that Ishihara's criteria for predicting surface effects is insufficient at numerous sites where ground oscillations or lateral spreads occurred.

O'Rourke and Pease (1997) reached the same conclusion that Ishihara's criteria for predicting surface effects are not valid at several sites in San Francisco where lateral spreads or ground oscillations occurred during major earthquakes in 1906 and 1989. Based on numerous borehole investigations in the San Francisco area, they used geographic information systems (GIS) and kriging models to develop contours of the thickness of the liquefiable deposits in the area. O'Rourke and Pease (1997) found the measurements of lateral spread displacement are approximately equal to 30 percent of the thickness of liquefiable deposits, with a coefficient of determination, R^2, equal to 0.50. O'Rourke and Pease (1997) also found that areas with liquefiable deposits thicker than two meters are generally highly susceptible to liquefaction.

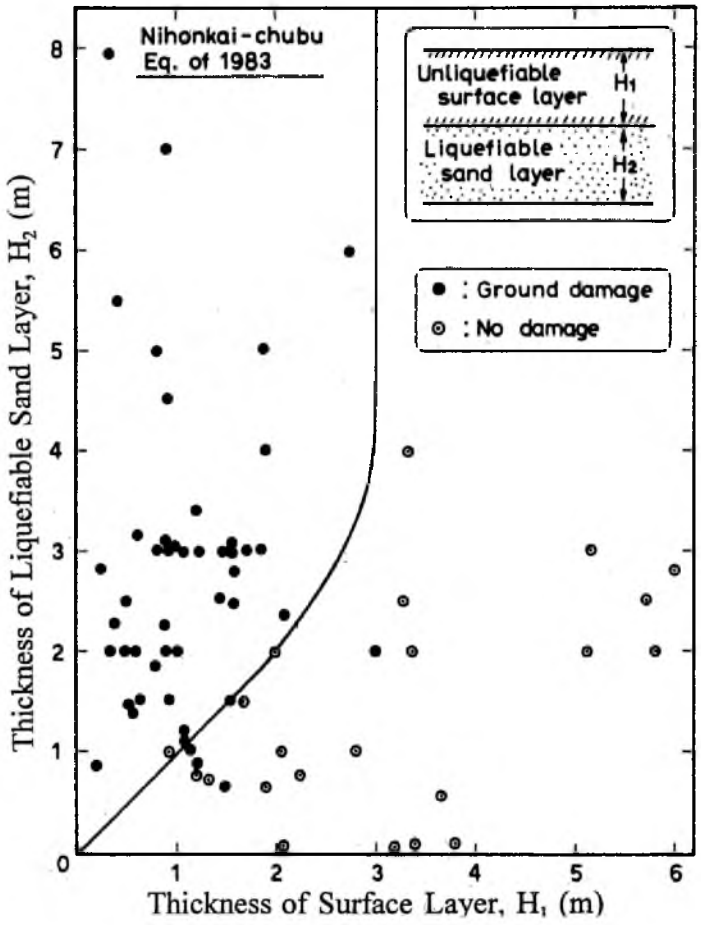

Figure 2.1. Thickness of liquefied and overlying non-liquefied layers compiled by Ishihara (1985) for determining occurrence and nonoccurrence of surface effects of liquefaction (Youd and Garris 1995)

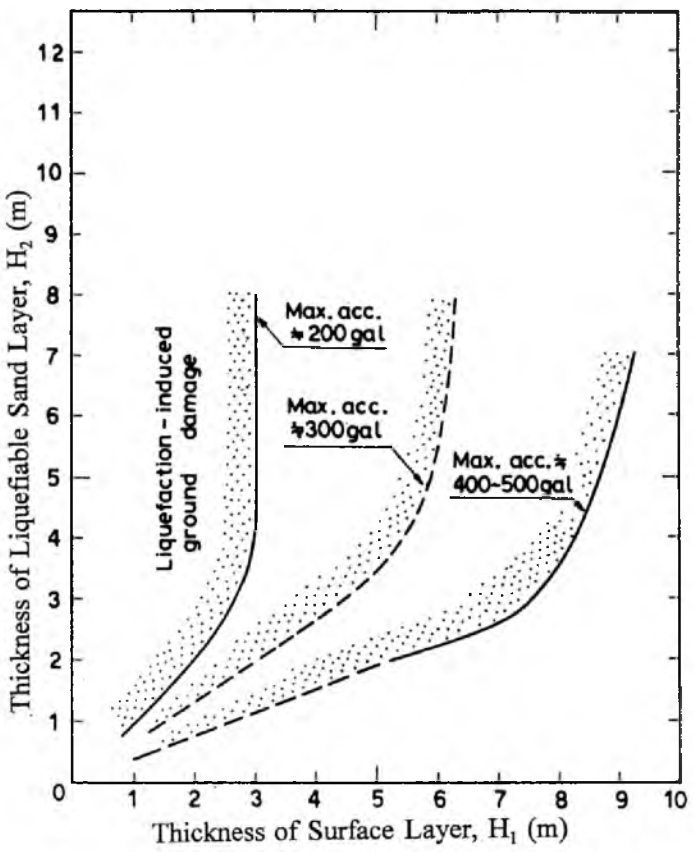

Figure 2.2 Boundary curves proposed by Ishihara (1985) for determining the occurrence and nonoccurrence of surface effects of liquefaction (Youd and Garris 1995)

The O'Rourke and Pease (1997) method for mapping the thickness of the liquefiable deposits in a given area provides a means of locating areas susceptible to severe liquefaction-induced ground failures. The method also predicts the amount of expected lateral spread displacement. However, because the linear correlation between the thickness of a liquefiable deposit with the amount of lateral spread has a relatively low coefficient of determination, other parameters are needed in the predictive model to more accurately estimate lateral spread displacement.

Predictions from Empirical Models

Lateral spread displacement on gently sloping ground is generally the most pervasive type of liquefaction-induced ground failure generated by earthquakes (NRC 1985). Accordingly, when analyzing areas susceptible to liquefaction, it is paramount to assess lateral spread hazards. Because the mechanisms that produce lateral spreads are complex, procedures for predicting lateral spread displacements are often empirical or semiempirical. This section discusses some of the numerous empirical models for predicting lateral spread displacements; specifically, those introduced by: Hamada et al. (1986), Youd and Perkins (1987), Bartlett and Youd (1992, 1995), Rauch and Martin (2000), Bardet et al. (2002), and Youd et al. (2002). The next section discusses semiempirical models for predicting lateral spread displacements.

Hamada et al. (1986) observed lateral spread displacements induced by liquefaction in the cities of Niigata and Noshiro, Japan, during the 1964 Niigata and 1983 Nihonkai-Chubu earthquakes, respectively. Hamada et al. noticed both the thickness of the liquefied layer, and the slope along the longitudinal axis of each displaced block influences the magnitude of the lateral spread displacement. They proposed the regression model shown in eqn. (2.4).

$$D = 0.75 \cdot H^{0.50} \cdot \theta^{0.33} \tag{2.4}$$

where D is the estimated amount of lateral spread displacement (m), θ is the larger of the ground surface slope or the slope of the lower boundary of the liquefied zone (%), and H is the thickness of the liquefied layer of soil (m). This thickness-slope model does not

consider the importance of varying earthquake factors. For instance, it only appears to produce reasonable estimates for earthquakes with magnitude, Mw ≈ 7.5, and for highly liquefiable sediments that are located approximately 20 to 30 km from the seismic source (Bartlett and Youd 1990). In addition, the liquefied deposits in the Niigata and Noshiro cities consist of relatively uniform, medium to fine-grained, clean sands. Extrapolation of the regression equation to coarser or finer sediments yields poorer predictions (Bartlett and Youd 1990).

Youd and Perkins (1987) introduced the Liquefaction Severity Index (LSI) model to characterize the severity of liquefaction effects at a locality by a single number. They evaluated cases of liquefaction-induced lateral spreads that occurred on gentle slopes or into river channels with widths greater than 10 meters. Their study was restricted to Holocene floodplains, deltas, or other fluvial deposits. Based on these specific geologic deposits and site conditions, Youd and Perkins developed the regression model shown in eqn. (2.5).

$$Log(LSI) = -3.49 - 1.86 \cdot LogR + 0.98 \cdot M \tag{2.5}$$

where LSI is the estimated maximum amount of lateral spread displacement (inches), M is the moment magnitude of the earthquake (M_w), and R is the horizontal distance from the seismic energy source (km). As defined, the LSI represents an estimate of the maximum ground displacement normalized to the above site conditions; therefore, failures with smaller displacements could be expected in areas with older deposits, and failures with larger displacements could be expected in areas with steep slopes or

unusually loose deposits. Thus, the LSI model is insufficient for mapping predicted values of ground displacement in areas not specific to the above conditions. Bardet et al. (2002) found the LSI model is inaccurate for a wider range of site conditions.

Bartlett and Youd (1992, 1995) developed a more comprehensive empirical model using multilinear regression (MLR) analyses of factors that most strongly influenced lateral spreads from a large database of case histories. Their empirical model relates lateral spread displacements to topographical, seismic, and soil factors. Youd et al. (2002) further updated the coefficients of the MLR model based on inclusion of data from more recent lateral spread case studies and corrections to the original dataset. The Youd et al. (2002) empirical model is shown in 2 equations, according to the controlling topographic conditions at the point of interest. Eqn. (2.6) is for free-face conditions (e.g., presence of a river channel or steep topographical depression), and eqn. (2.7) is for gently sloping ground conditions.

$$Log(D_H) = \begin{pmatrix} -16.713 + 1.532 \cdot M - 1.406 \cdot Log(R^*) - 0.012 \cdot R + 0.592 \cdot Log(W) + \\ +0.540 \cdot Log(T_{15}) + 3.413 \cdot Log(100 - F_{15}) - 0.795 \cdot Log(D50_{15} + 0.1 \text{ mm}) \end{pmatrix} \quad (2.6)$$

$$Log(D_H) = \begin{pmatrix} -16.213 + 1.532 \cdot M - 1.406 \cdot Log(R^*) - 0.012 \cdot R + 0.338 \cdot Log(S) + \\ +0.540 \cdot Log(T_{15}) + 3.413 \cdot Log(100 - F_{15}) - 0.795 \cdot Log(D50_{15} + 0.1 \text{ mm}) \end{pmatrix} \quad (2.7)$$

where D_H is the estimated lateral spread displacement (m); M is the moment magnitude of the earthquake (M_w); R is the nearest horizontal or mapped distance from the site to the seismic energy source (km); and, R^* is a nonlinear magnitude-distance function calculated by eqn. (2.8).

$$R^* = R + 10^{0.89M - 5.64} \tag{2.8}$$

W is the ratio of the height of the free-face to the horizontal distance between the base of the free-face and the point of interest (%); S is the ground slope (%); T_{15} is the cumulative thickness (m) of saturated, cohesionless deposits in the upper 15 meters of the soil profile with corrected Standard Penetration Test (SPT) blows counts, $N_{1,60} \leq 15$; F_{15} is the average fines content (percentage of sediment passing a No. 200 sieve) of the materials comprising T_{15} (%); and, $D50_{15}$ is the average mean grain size of the materials comprising T_{15} (mm).

Implementation of the Youd et al. (2002) empirical model requires sufficient site-specific geotechnical information such as thickness, fines content, and mean grain size of layers susceptible to lateral spread. Often during regional hazard mapping, such information is not readily available. Hence, some researchers have used estimates, or averages, of these factors in applying the empirical model to map predictions of lateral spread displacement for a particular seismic event (e.g., Olsen et al. 2007). However, averaging or estimating factors results in predictions of lateral spread displacement with indeterminate confidence.

To avoid the issue of insufficient data, Rauch and Martin (2000) grouped case histories of individual lateral spreads displacement vectors into "slide areas", and proposed the Empirical Prediction of Liquefaction-Induced Lateral Spreading (EPOLLS). In EPOLLS, the modeler selects one of three MLR equations for predicting the average lateral spread displacement based on the amount of data in the study area.

Figure 2.3 shows the MLR equations and a flow chart of the EPOLLS method. The first MLR equation is regional-EPOLLS, which predicts average lateral spread displacement solely from the following seismic factors: earthquake moment magnitude, distance to fault rupture, peak ground acceleration, and duration of strong shaking. If topographic and geometric factors are also known in the study area, the modeler should select the second MLR equation, site-EPOLLS. Site-EPOLLS predicts average lateral spread displacement by including the following factors with the seismic factors: ground surface slope, height of the free-face, and the length of the sliding area. Finally, if soil factors are also known from sufficient geotechnical investigations, the modeler should select the most comprehensive and third MLR equation: geotechnical-EPOLLS. Geotechnical-EPOLLS predicts average lateral spread displacement by including the following factors to the fore mention factors: depth to the point in the site profile with the lowest resistance to liquefaction, and depth to the top of the layer with the lowest resistance to liquefaction. The EPOLLS method provides empirical means to predict lateral spread displacement at a study area with varying levels of known factors. Unlike the Youd et al. (2002) empirical model, the regional and site-EPOLLS methods can be used to predict the average lateral spread displacement without knowing specific geotechnical information. However, the EPOLLS method only predicts the average overall magnitude of all measurable lateral spread displacements at a slide area, instead of predicting lateral spread displacements at specific points in the study area. In addition, EPOLLS offers no guidance on how to assess the spatial extent of potential slide areas.

Bardet et al. (2002) suggested removing the geotechnical variables F_{15} and $D50_{15}$ from the Bartlett and Youd empirical model because these variables are the least likely to

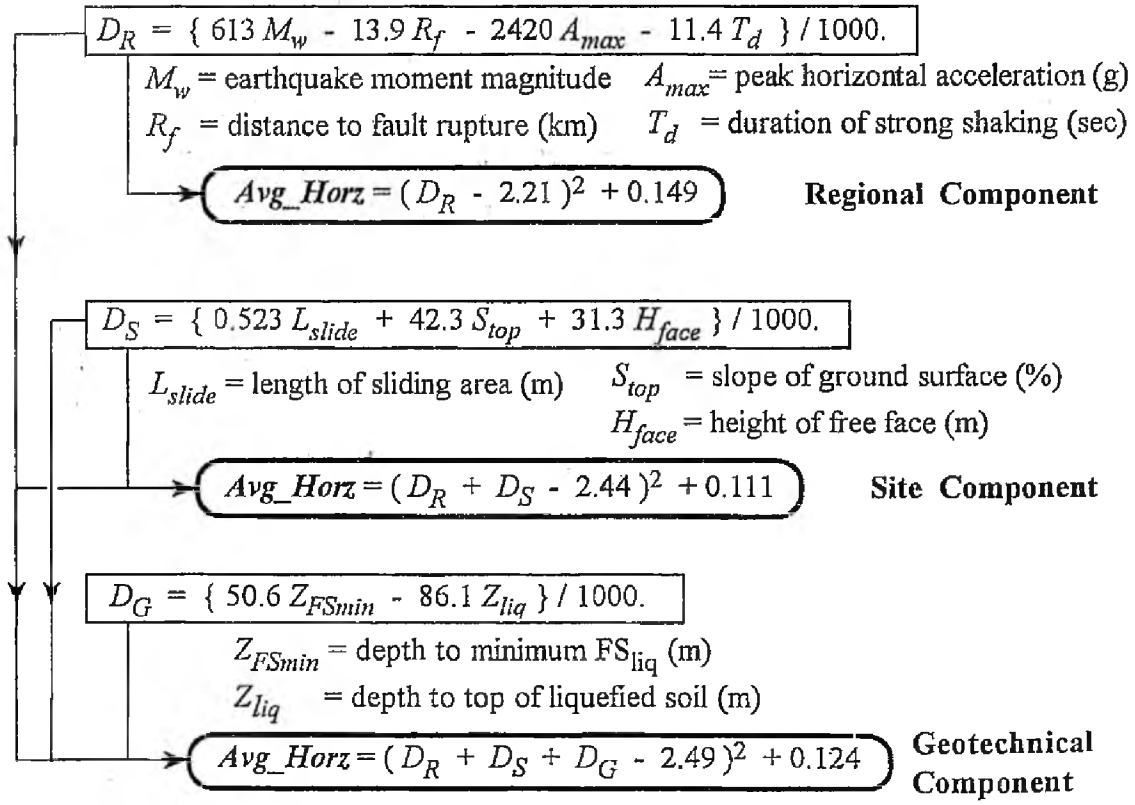

Figure 2.3. The EPOLLS method for predicting average lateral spread displacement of an overall slide area in meters (Rauch and Martin 2000)

be available for regional mapping of lateral spread displacements. Therefore, Bardet et al. (2002) proposed new MLR equations based on the same case history data compiled by Bartlett and Youd (1992, 1995). They divided these data into two sets: (A) complete data for all ranges of displacement amplitude, and (B) data limited to displacement amplitudes smaller than 2 meters. Their empirical model has the general form shown in eqn. (2.9).

$$Log(D_H + 0.01\text{ m}) = b_o + b_{off} + b_1 M + b_2 LogR + b_3 R + b_4 LogW + b_5 LogS + b_6 LogT_{15} \quad (2.9)$$

where the variables D_H, M, R, W, S, and T_{15} are as defined for eqns. (2.6) and (2.7). The partial regression coefficients for this model are shown in Table 2.2 for datasets A and B.

For free-face cases, b_5 is set to zero, and the value of b_{off} is used as specified in Table 2.2. For ground-slope cases, b_4 and b_{off} are both set to zero. Overall, the Bardet et al. (2002) empirical model enables estimation of lateral spread displacements for cases where there is little information on the soil grain distribution. However, removing the geotechnical variables from the Youd et al. (2002) empirical model introduces more uncertainty in the estimate of the lateral spread displacement. The predictive performance of the empirical model is often judged by the coefficient of determination, R^2. For the Youd et al. (2002) empirical model, the adjusted value of R^2 equals 83.3%. For the Bardet et al. (2002) empirical model, the adjusted value of R^2 is significantly smaller: 64.3% for both datasets A and B (see Table 2.2). This means that only 64.3% of the variability in the dependent variable is explained by the independent variables.

Table 2.2. Values of MLR coefficients and adjusted R^2 for the Bardet et al. (2002) empirical model

	Dataset	
Coefficients	A	B
b_o	-6.815	-6.747
b_{off}	-0.465	-0.162
b_1	1.017	1.001
b_2	-0.278	-0.289
b_3	-0.026	-0.021
b_4	0.497	0.090
b_5	0.454	0.203
b_6	0.558	0.289
R^2 adjusted	64.25%	64.27%

Predictions from Semiempirical Models

Semiempirical methods for characterizing liquefaction are based on a growing set of laboratory studies calibrated to a growing database of case studies. This section discusses predicting liquefaction-induced lateral spread displacements based on strain potential models of Zhang et al. (2004), and Faris (2004). This section also briefly describes using laboratory results to map potential volumetric strain and shear strain induced by liquefaction (see Rosinski et al. 2004).

Zhang et al. (2004) proposed a semiempirical approach for predicting liquefaction-induced lateral spread displacements using SPT and CPT data, liquefaction case histories, and laboratory tests. Their approach is based on laboratory test results (from Ishihara and Yoshimine 1992, and Seed 1979) of the maximum cyclic shear strain (γ_{max}) induced during undrained cyclic loading of saturated sandy soils. Zhang et al. found a relationship (see Figure 2.4) between three properties of the saturated sandy soil: γ_{max}, the factor of safety against liquefaction (FS), and the relative density (D_r). From this relationship, Zhang et al. (2004) define the lateral displacement index (LDI), per eqn. (2.10).

$$LDI = \int_0^{z_{max}} \gamma_{max} dz \tag{2.10}$$

where z_{max} is the maximum depth below all of the layers with a calculated $FS < 2$ (up to 23 meters).

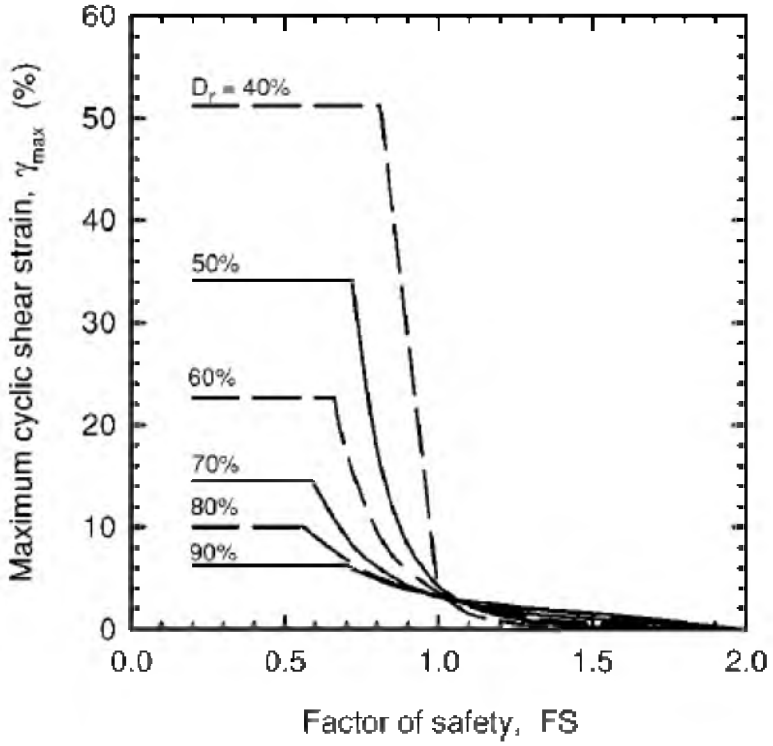

Figure 2.4. Relationship between the maximum cyclic shear strain and factor of safety against liquefaction for different relative densities of clean sands (Zhang et al. 2004)

There are numerous correlations for estimating relative densities from either SPT or CPT data. For SPT data, Zhang et al. (2004) suggests using a modified version of a correlation introduced by Meyerhof (1957), per eqn. (2.11). For CPT data, Zhang et al. (2004) suggests using a modified version of a correlation introduced by Tatsuoka et al. (1990), per eqn. (2.12). Unfortunately, neither of these equations defines the uncertainty in the predicted variable.

$$D_r = 14\sqrt{N_{1,60}} \tag{2.11}$$

$$D_r = -85 + 76 \cdot Log(q_{c1N}) \tag{2.12}$$

where D_r is the relative density of clean sand (%), $N_{1,60}$ is limited to 42 blows, and q_{c1N} is the normalized CPT tip resistance corrected for effective overburden stresses (see Robertson and Wride 1998).

Zhang et al. (2004) developed an empirical model by regression analyses of LDI and topographic factors at several lateral spread case histories. Their model is divided into two equations, according to the controlling topographic conditions at the point of interest. Eqn. (2.13) is for gently sloping ground without a free-face. Eqn. (2.14) is for level ground with a free-face.

$$LD = (S + 0.2) \cdot LDI \quad \text{for } 0.2\% < S < 3.5\% \tag{2.13}$$

$$LD = 6(L/H)^{-0.8} \cdot LDI \quad \text{for } 4 < L/H < 40 \tag{2.14}$$

where LD is the estimated lateral spread displacement (m), S is the ground slope (%), L is the horizontal distance between the base of the free-face and the point of interest (m), and H is the height of the free-face (m).

The Zhang et al. (2004) semiempirical approach enables use of CPT data to predict lateral spread displacements. However, they developed their approach using only five available case histories with CPT data. Additional case history data, especially with CPT data, are needed to further evaluate their proposed approach.

Faris (2004) proposed a similar semiempirical approach for predicting liquefaction-induced lateral spread displacements using SPT data, liquefaction case histories, and laboratory research from Wu (2002). Wu (2002) compiled a database of high-quality laboratory tests and developed a laboratory testing program to investigate the influence of relative density and confining stress on the development of post-liquefaction shear and volumetric strain. Wu performed unidirectional, undrained, cyclic simple shear tests on fully saturated samples of sand. From these tests, Wu determined the maximum shear strain attainable in the sand and called this the limiting shear strain. Faris (2004) renamed the limiting shear strain the strain potential index (SPI). Laboratory test results of SPI as a function of the normalized cyclic shear stress ratio (CSR^*) and equivalent clean-sand corrected SPT blow counts ($N_{1,60,cs}$) are shown as solid curves in Figure 2.5. Refer to Seed et al. (2001) for full definitions of CSR^* and $N_{1,60,cs}$. By extrapolating the laboratory results, Faris (2004) added the dashed curve in Figure 2.5, which represents 75% shear strain potential.

Next, Faris (2004) introduced the displacement potential index (DPI), which is the summation of values of SPI for each potentially liquefiable layer of a site profile multiplied by the thickness of the layer (see eqn. (2.15)).

$$DPI = \sum SPI \times \Delta z \tag{2.15}$$

where DPI is in meters, SPI is in percent, and the summation occurs over all potentially liquefiable layers of thickness Δz, in meters.

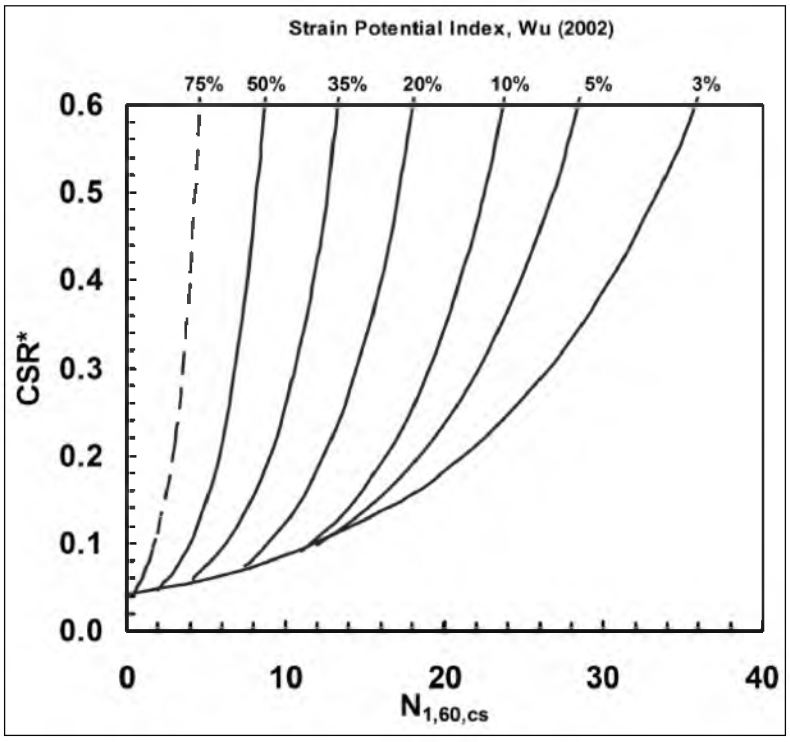

Figure 2.5. Strain potential index curves based on Wu (2002) laboratory tests (Faris 2004)

Faris (2004) developed empirical models by Bayesian updating analyses of DPI and topographic factors at several lateral spreading case histories. Faris included the moment magnitude of the earthquake (M) as a model parameter to capture the additional influence of duration on the resulting lateral spread displacement. Eqn (2.16) predicts the maximum displacement on a particular lateral spread, D_{max}. Eqn. (2.17) predicts the average displacement on a particular lateral spread, D_{avg}.

$$D_{\max} = \exp\left[1.0443 \cdot \ln DPI_{\max} + 0.0046 \cdot \ln \alpha + 0.0029 \cdot M\right] \qquad (2.16)$$

$$D_{avg} = \exp\left[0.6911 \cdot \ln DPI_{avg} + 0.0036 \cdot \ln \alpha + 0.0011 \cdot M\right] \qquad (2.17)$$

where D_{max} and D_{avg} are in meters; DPI_{max} is the maximum value of DPI determined from an SPT borehole in a slide area (m); DPI_{avg} is the average value of DPI determined from all SPT boreholes in a slide area (m); and, α accounts for topographic conditions at a slide area as defined in eqn (2.18).

$$\alpha = \begin{cases} \dfrac{H}{0.25 \cdot L} & \text{for free-face cases} \\ S & \text{for sloping ground cases} \\ \dfrac{H + 0.01 \cdot S \cdot 0.25 \cdot L}{0.25 \cdot L} & \text{for free-face and sloping ground cases} \end{cases} \tag{2.18}$$

where S is the average ground slope (%) of the slide area, L is the length of the slide area (m), and H is the height of the free-face (m).

Like the EPOLLS method, the semiempirical approach introduced by Faris (2004) predicts either average or maximum lateral spread displacements for an entire site or slide area. The method does not predict lateral spread displacements at specific points in the study area.

Both semiempirical approaches by Zhang et al. (2004) and Faris (2004) are based on the assumption that each layer of liquefied soil will reach its theoretical shear strain potential or maximum cyclic shear strain when exposed to a particular level of strong ground motion. Such theoretical shear strain potential is based on laboratory measurements of certain saturated, clean sand. It is unclear if shear strains measured in

the laboratory will conform to permanent shear strains developed in situ during liquefaction.

With surficial geologic maps and 650 geotechnical boreholes, Rosinski et al. (2004) also used the laboratory tests of Wu (2002) to predict volumetric strain and shear strain of potentially liquefiable layers of soil in each borehole (i.e., layers with $FS < 1$). By spatial interpolation of data between each borehole, they predicted average strains for each geological unit given a seismic event in the Santa Clara Valley, California, and mapped these average strains into regional liquefaction hazard maps. These maps not only yield the potential of deposits for liquefaction, but also estimate the amount of surface disruptions due to liquefaction. Rosinski et al. (2004) found by geostatistical methods that borehole investigations must be within 800 meters of one another in order to interpolate the thickness of potentially liquefiable sediments. This requires a dense database of subsurface explorations. They concluded that late Holocene deposits have the highest susceptibility of liquefaction, while early Holocene and late Pleistocene deposits have much lower liquefaction susceptibility.

Mapping Efforts in Utah

Because many urban areas of Utah are filled with loosely deposited, saturated sediments that are susceptible to liquefaction during major earthquakes, various liquefaction hazard maps have been created in Utah. This began in the 1980s when Utah State University collected available SPT borehole data, performed additional CPT soundings, and assessed the potential of liquefaction triggering at each geotechnical investigation during major earthquakes (e.g., Anderson et al. 1994, Anderson et al.

1994b). They determined critical acceleration values needed to trigger liquefaction in layers of potentially liquefiable soil based on the simplified method introduced by Seed (1979) (Anderson and Keaton 1982). They then compared these acceleration values to probabilistic predictions of strong ground motion studies. By using surficial geologic maps and geological data as constraints, they developed liquefaction potential maps delineating land areas into zones of low, moderate, and high liquefaction potential. In their time, these maps were useful to government agencies and consultants. Their mapping method did not attempt to predict the amount of liquefaction-induced ground displacement.

Other liquefaction hazard maps have been created along the Wasatch Front predicting liquefaction, lateral spreading, and liquefaction-induced ground settlement (Solomon et al. 2004). Solomon et al. produced these maps using HAZUS®, which is a computer program developed by the Federal Emergency Management Agency (FEMA). HAZUS® bases its analysis of liquefaction-induced ground failure on the LSI for various geologic regions, and ground motion attenuation relationships. These maps were not created using any site-specific geotechnical data. Solomon et al. (2004) stated that using geotechnical data in their mapping efforts would improve accuracy.

More recently, members of the Utah Liquefaction Advisory Group (ULAG) compiled a relatively extensive geotechnical database of SPT, CPT, and V_s investigations. Based on these subsurface data, they produced new liquefaction hazard maps in Salt Lake County, including: probabilistic liquefaction triggering maps (Bartlett et al. 2010a), scenario lateral spread hazard maps (Bartlett et al. 2005, Olsen et al. 2007), and probabilistic liquefaction-induced ground displacement maps (Bartlett et al. 2010b).

These researchers estimated lateral spread displacements at each SPT borehole based on the Youd et al. (2002) empirical model. As discussed, the Youd et al. (2002) empirical model requires sufficient site-specific geotechnical information such as fines content and mean grain size of layers susceptible to lateral spread. If a borehole lacked this specific geotechnical information, they used average values in the corresponding geologic unit. By using surficial geologic maps as constraints, they generalized the resulting point estimates to produce the hazard maps. This mapping method does not define the uncertainty in the mapped estimates of liquefaction-induced ground failures. The method is reasonable in areas with extensive geotechnical sampling and sufficient data; however, in areas that lack or have little geotechnical data, there is a need for a new mapping method.

Conclusions

Certain criteria must be clearly defined, in order to produce the desired liquefaction-induced ground failure maps. From the above literature survey, it is desirable to develop maps based upon the following criteria: (1) recent seismic studies, such as those completed by the National Seismic Hazard Mapping Project (NSHMP), under the direction of the USGS (see Petersen et al. 2008); (2) current surficial geologic maps; (3) degree of ground slope and/or size of an influential free-face; and, (4) geotechnical data. Using criteria 1 through 4, the maps should: (5) predict the quantity of liquefaction-induced lateral spread displacement and (6) estimate the uncertainty of these predictions. It is important to assess lateral spread hazards because they are generally the most pervasive type of liquefaction-induced ground failure generated by earthquakes

(NRC 1985). The amount of liquefaction-induced damage is strongly correlated with the amount of horizontal displacement resulting from lateral spread.

There are numerous methods for predicting liquefaction-induced ground failures. However, in order to meet all six of the above criteria, only four methods previously discussed apply. These methods are: (1) the Youd et al. (2002) empirical model; (2) the geotechnical-EPOLLS method (Rauch and Martin 2000); (3) the Zhang et al. (2004) semiempirical approach utilizing the LDI; and, (4) the Faris (2004) semiempirical approach utilizing the DPI. The other discussed methods do not meet the above criteria. For instance, liquefaction potential maps based solely on seismicity and geology (Youd and Perkins 1978) do not include geotechnical data. The Hamada et al. (1986) empirical model does not include seismic factors; and, the LSI model introduced by Youd and Perkins (1987) lacks geotechnical factors and is limited to very specific geologic settings. Maps based on the LPI, such as from Holzer et al. (2006) delineate areas of high liquefaction potential, but do not predict the quantity of lateral spread displacement. Predictions of the severity of liquefaction-induced surface effects based upon the thickness of the liquefiable layers (as introduced by Ishihara 1985) also do not predict the quantity of lateral spread displacement; furthermore, these predictions are inaccurate when tested against a wider range of site and earthquake conditions (Youd and Garris 1995). Finally, the models introduced by Bardet et al. (2002) and O'Rourke and Pease (1997) have relatively low coefficients of determination; thus, other parameters are needed in their predictive models to more accurately estimate lateral spread displacements.

Previous mapping efforts in Utah also do not meet the above criteria. Maps by Anderson et al. predict liquefaction susceptibility and potential, but do not predict amounts of lateral spread displacement. Maps by Solomon et al. (2004) are based upon the LSI and lack geotechnical data. There are many advantages to the recent mapping projects in Utah (e.g., Bartlett et al. 2005; 2010a,b). For instance, the recent Utah mapping projects are based upon a substantial quantity of geotechnical data coupled with mapped geologic units. They are also based on strong ground motion estimates from current national seismic hazard maps and predictions of lateral spread displacements from the Youd et al. (2002) empirical model. However, implementation of the Youd et al. (2002) empirical model requires sufficient geotechnical data; such as the fines content and mean grain size of each layer in a SPT borehole that is susceptible to lateral spread. Often during regional mapping of liquefaction hazards, such data are not readily available. Hence, at locations lacking these site-specific data, recent Utah mapping methods used the average geotechnical values from the corresponding geologic unit. Due to this averaging, it is difficult to define the uncertainty in the mapped estimates of lateral spread displacement.

Although the Youd et al. (2002) empirical model is somewhat difficult to apply in regions lacking sufficient geotechnical data, the other approaches that meet the above criteria have some limitations. The geotechnical-EPOLLS method (Rauch and Martin 2000), and the DPI semiempirical approach (Faris 2004) yield average or maximum predictions of lateral spread displacements for an entire slide area, instead of predicting displacements at specific points in the area. Neither approach gives guidance on how to adequately assess the spatial extent of potential slide areas. The LDI semiempirical

approach (Zhang et al. 2004) is attractive because it enables predictions of liquefaction-induced lateral spread displacements from CPT data. This approach is based on the relationship of relative densities and laboratory measurements of maximum cyclic shear strain of clean sands. However, site-specific measurements of relative densities are rarely available; hence, Zhang et al. suggested using correlations to predict relative densities of clean sands from SPT and CPT penetration resistance data. The uncertainty in the predictions of relative densities from these correlations is undefined. Additionally, the semiempirical approaches by Zhang et al. (2004) and Faris (2004) are based on the assumption that each layer of potentially liquefiable soil will reach its theoretical maximum shear strain potential during a specific level of strong ground motion. It is unclear if shear strains measured in the laboratory on samples of clean sand will conform to permanent shear strains developed in cohesionless layers in situ during liquefaction.

In conclusion, there is a need to develop or modify a method in order to predict lateral spread displacements and produce liquefaction-induced ground failure maps that meet the above criteria. The method should predict lateral spread displacements at desired points in the study area. Often, when producing regional hazard maps (especially from available data), there are geologic units with poorly defined geotechnical properties and large variations in the quality of geotechnical data. Therefore, it is desirable to develop a method that also defines the uncertainty associated with the predictions of liquefaction-induced lateral spread displacement.

References

Anderson, L. R., and Keaton, J. R., 1982. Development of a soil liquefaction potential map, in *Proc., Int. Conf on Soil Dynamics and Earthquake Engineering*, Southampton, England, July 13-15.

Anderson, L. R., Keaton, J. R., Aubry, K., and Ellis, S. J., 1994. *Liquefaction Potential Map for Davis County, Utah, Complete Technical Report, Utah Geological Survey Contract Report 94-7*, Salt Lake City, UT.

Anderson, L. R., Keaton, J. R., and Bay, J. A., 1994b. *Liquefaction Potential Map for the Northern Wasatch Front, Utah, Complete Technical Report, Utah Geological Survey Contract Report 94-6*, Salt Lake City, UT.

Bardet, J. P., Tobita, T., Mace, N., and Hu, J., 2002. Regional modeling of liquefaction-induced ground deformation, *Earthquake Spectra* **18**(1), 19-46.

Bartlet, S. F., and Youd, T. L., 1990. *Evaluation of Ground Failure Displacement Associated with Soil Liquefaction: Compilation of Case Histories, Misc. Paper S-73-1*, Dept. of the Army, U.S. Army Corps of Engineers, Washington D.C., 84 pp.

Bartlett, S. F., and Youd, T. L., 1992. *Empirical Analysis of Horizontal Ground Displacement Generated by Liquefaction-Induced Lateral Spreads, Technical Report NCEER-92-0021*, National Center for Earthquake Engineering Research, Buffalo, NY.

Bartlett, S. F., and Youd, T. L., 1995. Empirical prediction of liquefaction-induced lateral spread, *J. Geotech. Eng.* **121**(4), 316-328.

Bartlett, S. F., Erickson, G., Leeflang, B., Solomon, B. J., 2010a. *Probabilistic Liquefaction Potential and Liquefaction-Induced Ground Failure Maps for the Urban Wasatch Front: Phase III, Fiscal Year 2006, U.S.G.S. Research Award No. 06HQGR0015*, Denver, CO.

Bartlett, S. F., Gerber, T. M., Hinckley, D., 2010b. *Probabilistic Liquefaction Potential and Liquefaction-Induced Ground Failure Maps for the Urban Wasatch Front: Phase IV, Fiscal Year 2007: Collaborative Research with University of Utah and Brigham Young University, U.S.G.S. Research Award Nos. 07HQGR0021 and 07HQGR0024*, Denver, CO.

Bartlett S. F., Olsen, M. J., and Solomon, B. J., 2005. *Probabilistic Liquefaction Potential and Liquefaction-Induced Ground Failure Maps for the Urban Wasatch Front: Collaborative Research with the University of Utah, Utah State University and the Utah Geological Survey, Phase I, FY2004, U.S.G.S. Research Award No. 04HQGR0026*, Reston, VA.

Faris, A. T., 2004. *Probabilistic Models for Engineering Assessment of Liquefaction-Induced Lateral Spreading Displacements, PhD. Dissertation*, Department of Civil and Environmental Engineering, University of California, Berkeley, CA.

Hamada, M., Yasuda, S., Isoyama, R., and Emoto, K., 1986. Study on liquefaction induced permanent ground displacements, in *Report for the Association for the Development of Earthquake Prediction in Japan,* Tokyo, Japan, 87 pp.

Holzer, T. L., Bennett, M. J., Noce, T. E., Padovani, A. C., and Tinsley, J .C., 2006. Liquefaction hazard mapping with LPI in the Greater Oakland, California, area, *Earthquake Spectra* **22**(3), 693-708.

Ishihara, K., 1985. Stability of Natural Deposits during Earthquakes, in *Proc., 11th Int. Conf on Soil Mechanics and Found. Eng.,* Rotterdam, The Netherlands, pp. 321-376.

Ishihara, K., and Yoshimine, M., 1992. Evaluation of settlements in sand deposits following liquefaction during earthquakes, *Soils Found.* **32**(1), 173-188.

Iwasaki, T., Tatsuoka, F., Tokida, K., and Yasuda, S., 1978. A practical method for assessing soil liquefaction potential based on case studies at various sites in Japan, in *Proc. 2nd Int. Conf on Microzonation,* San Francisco, CA, pp. 885-896.

Iwasaki, T., Tokida, K., Tatsuoka, F., Watanabe, S., Yasuda, S., and Sato, H., 1982. Microzonation for soil liquefaction potential using simplified methods, in *Proc. 3rd Int. Conf on Microzonation*, Seattle, WA, pp. 1319-1330.

Lenz, J., and Baise, L. G., 2007. Variability of LPI across geologic units for regional liquefaction mapping, in *Geo-Denver 2007: New Peaks in Geotechnics, Dynamic Response and Soil Properties (GSP 160)*, M. M. Dewoolkar and J. P. Koester (editors), ASCE, Denver, CO, 10 pp.

Meyerhof, G. G., 1957. Discussion on research on determining the density of sands, in *Proc., 4th Int. Conf of Soil Mechanics and Foundation Eng.,* vol. 3, London, England, 110 pp.

National Research Council (NRC), 1985. *Liquefaction of Soils During Earthquakes*, National Academy Press, Washington D. C., 240 pp.

Olsen, M. J., Bartlett, S. F., and Solomon, B. J., 2007. Lateral spread hazard mapping of the Northern Salt Lake Valley, Utah for a M7.0 scenario earthquake, *Earthquake Spectra* **23**(1), 95-113.

O'Rourke, T. D., and Pease, J. W., 1997. Mapping liquefiable layer thickness for seismic hazard assessment, *J. Geotech. Eng*, **123**(1), 46-56.

Petersen, M. D., Frankel, A. D., Harmsen, S. C., Mueller, C. S., Haller, K. M., Wheeler, R. L., Wesson, R. L., Zeng, Y., Boyd, O. S., Perkins, D. M., Luco, N., Field, E. H., Wills, C. J., and Rukstales, K. S., 2008. *Documentation for the 2008 Update of the United States National Seismic Hazard Maps, U.S. Geological Survey Open-File Report 2008–1128*, Reston, VA, 61 pp.

Rauch, A. F., and Martin, J. R., 2000. EPOLLS model for predicting average displacements on lateral spreads, *J. Geotech. Geoenviron. Eng.* **126**(4), 360-371.

Robertson, P. K., and Wride, C. E., 1998. Evaluating cyclic liquefaction potential using the cone penetration test, *Canadian Geotechnical Journal* **35**(3), 442–459.

Rosinski, A., Knudsen, K. L., Wu, J., Seed, R. B., and Real, C. R., 2004. Development of regional liquefaction-induced deformation hazard maps, in *GeoTrans 2004, Geotechnical Engineering for Transportation Projects (GSP No. 126)*, M. K. Yegian and E. Kavazanjian (editors), ASCE, Los Angeles, CA, pp. 797-806.

Seed, H. B., 1979. Soil liquefaction and cyclic mobility evaluation for level ground during earthquakes, *Journal of Geotechnical Engineering Div.* **105**(2), 201-255.

Seed, H. B., and Idriss, I. M., 1971. Simplified Procedure for Evaluating Soil Liquefaction Potential, *Journal of Soil Mechanics and Found. Div.* **97**(9), 1249-1273.

Seed, R. B., Cetin, K. O., Moss, R. E. S., Kammerer, A. M., Wu, J., Pestana, J. M., and Riemer, M. F., 2001. Recent advances in soil liquefaction engineering and seismic site response evaluation, in *Proc., 4th Int. Conf on Recent Advances in Geotechnical Earthquake Engineering and Soil Dynamics*, S. Prakash (editor), Paper No. SPL-2, San Diego, CA, 45 pp.

Solomon, B. J., Storey, N. S., Wong, I., Silva, W., Gregor, N., Wright, D., and McDonald, G., 2004. *Earthquake-Hazards Scenario for a M7 Earthquake on the Salt Lake City Segment of the Wasatch Fault Zone, Utah Geological Survey Special Study 111DM*, Salt Lake City, UT.

Tatsuoka, F., Zhou, S., Sato, T., and Shibuya, S., 1990. Method of evaluating liquefaction potential and its application, in *Rep. on Seismic Hazards in the Soil Deposits in Urban Areas*, Ministry of Education of Japan, pp. 75-109.

Toprak, S., and Holzer, T. L., 2003. Liquefaction potential index: field assessment, *J. Geotech. Geoenviron. Eng.* **129**(4), 315-322.

Wu, J., 2002. *Liquefaction Triggering and Post Liquefaction Deformations of Monterey 0/30 Sand under Uni-Directional Cyclic Simple Shear Loading, PhD. Dissertation*, Department of Civil and Environmental Engineering, University of California, Berkeley, CA.

Youd, T. L., 1984. Geologic effects—liquefaction and associated ground failure, in *Proc. of the Geologic and Hydrologic Hazards Training Program*, *U.S. Geological Survey Open-File Report 84-760*, C. Kitzmiller (compiler), Reston, VA, pp. 210-232.

Youd, T. L., and Garris, C. T., 1995. Liquefaction-induced ground-surface disruption, *J. Geotech. Eng.* **121**(11), 805-809.

Youd, T. L., Hansen, C. M., and Bartlett S. F., 2002. Revised multilinear regression equations for prediction of lateral spread displacement, *J. Geotech. Geoenviron. Eng.* **128**(12), 1007-1017.

Youd, T. L., Idriss, I. M., Andrus, R. D., Arango, I., Castro, G., Christian, J. T., Dobry, R., Finn, W. D. L., Harder, L. F., Jr., Hynes, M. E., Ishihara, K., Koester, J. P., Liao, S. S. C., Marcuson, W. F., III, Martin, G. R., Mitchell, J. K., Moriwaki, Y., Power, M. S., Robertson, P. K., Seed, R. B., Stokoe, K. H., II, 2001. Liquefaction resistance of soils: summary report from the 1996 NCEER and 1998 NCEER/NSF workshops on evaluation of liquefaction resistance of soils, *J. Geotech. Geoenviron. Eng.* **127**(10), 817-833.

Youd, T.L., and Perkins, D.M., 1978. Mapping liquefaction-induced ground failure potential, *Journal of the Geotechnical Engineering Division* **104**, No. GT4, 433-446.

Youd, T. L., and Perkins, D. M., 1987. Mapping of liquefaction severity index, *J. Geotech. Eng.* **113**(11), 1374-1392.

Zhang, G., Robertson, P. K., and Brachman, R. W., 2004. Estimating liquefaction-induced lateral displacements using the standard penetration test or cone penetration test, *J. Geotech. Eng.* **130**(8), 861-871.

CHAPTER 3

MULTILINEAR REGRESSION EQUATIONS FOR PREDICTING LATERAL SPREAD DISPLACEMENTS FROM SOIL TYPE AND CPT DATA

Abstract

This paper presents a new empirical model for estimating the amount of horizontal displacement resulting from liquefaction-induced lateral spread. The proposed approach modifies the Youd et al. (2002) multilinear regression model so that it is applicable to a wider range of geotechnical data and is easier to apply to site-specific engineering evaluations and to regional hazard mapping. This paper shows that earthquake magnitude, distance to the seismic source, topography, layer thickness, and soil type are important factors in estimating horizontal displacement resulting from lateral spread. It also discusses how cone penetration test (CPT) data can be used in conjunction with the proposed model to estimate the amount of lateral spread displacement. The CPT approach is validated using geotechnical data obtained from a liquefaction hazard mapping project in Utah.

Introduction

Hamada et al. (1986), Youd and Perkins (1987), Bartlett and Youd (1992, 1995), Rauch and Martin (2000), Youd et al. (2002), Bardet et al. (2002), Baska (2002), Zhang et al. (2004), and Faris et al. (2006) have introduced empirical and semiempirical methods for predicting the amount of lateral spread displacement at potentially liquefiable sites. For the most part, these researchers derived their models from statistical regression techniques of compiled case histories of liquefaction-induced lateral spread.

The widely used multilinear regression (MLR) model of Youd et al. (2002) is based on earthquake source, topographical, and soil factors that have been shown to be statistically significant in estimating the amount of liquefaction-induced lateral spread displacement at liquefied sites (Bartlett and Youd 1992). That research has shown that moment magnitude, horizontal distance to the fault or seismic source, presence of a free face (e.g., river channel or steep topographical depression), and the degree of ground slope in the vicinity of the site have a significant influence on the magnitude and nature of the displacement pattern. In addition, soil factors such as the thickness of loose, saturated, cohesionless sediments, and their corresponding fines content and mean grain size strongly influence the amount of lateral spread displacement. Other factors may play a role, but their contributing influence is less significant than the fore mention factors (Bartlett and Youd 1992).

However, implementation of the Youd et al. (2002) model requires sufficient site-specific geotechnical information such as thickness, fines content, and mean grain size of layers susceptible to lateral spread. In some cases, such information is not readily available (e.g., regional hazard mapping) and estimates, or averages, of these factors are

sometimes used in applying the MLR model (Olsen et al. 2007). To avoid this insufficiency issue, some researchers have removed site-specific factors from the empirical model to make them more adaptable to regional analyses (e.g., Bardet et al. 2002). Although removal of the certain factors from the MLR model simplifies the data requirements for the analysis, it also introduces more uncertainty into the estimate of the lateral spread displacement and reduces the predictive power of the model.

In general, the preferred MLR model is one that includes all factors statistically correlated with the dependent variable. The predictive performance of the model is often judged by the coefficient of determination, R^2. The coefficient generally increases with the number of independent variables added to the model, if the independent variables are not overly cross-correlated. Thus, a "full" model, which uses as many variables as possible, is the most reliable model from a predictive standpoint and has the highest R^2 value. However, in a statistical sense, a "full" model may not be the most parsimonious model because some independent variables only incrementally improve the performance of the model and their inclusion may not be justified by the effort and expense required to obtain such information. For example, in regional mapping studies, where preexisting data are used, not all sites have the required information to implement a "full" model, often resulting in compromises and the use of a "reduced" model.

This paper discusses significant revisions to the Youd et al. (2002) empirical model to make it more parsimonious and implementable for regional hazard analysis while preserving much of its original predictive power. It also provides guidance on how to incorporate CPT soundings into the lateral spread predictions.

The "Full" MLR Model

Eqn. (3.1) lists the general form of the "full" Youd et al. (2002) MLR model.

$$LogD_H = \begin{matrix} b_o + b_{off}\alpha + b_1 M + b_2 LogR^* + b_3 R + b_4 LogW + b_5 LogS + b_6 LogT_{15} + \\ + b_7 Log(100 - F_{15}) + b_8 Log(D50_{15} + 0.1\ \text{mm}) \end{matrix} \quad (3.1)$$

where D_H is the estimated horizontal spread displacement (m); M is the moment magnitude of the earthquake (M_w); R is the nearest horizontal or mapped distance from the site to the seismic energy source (km); and, R^* is a nonlinear magnitude-distance function calculated by eqn. (3.2).

$$R^* = R + 10^{0.89M - 5.64} \quad (3.2)$$

W is the ratio of the height of the free face to the horizontal distance between the base of the free face and the point of interest (%); S is the ground slope (%); T_{15} is the cumulative thickness (m) of saturated, cohesionless deposits in the upper 15 meters of the soil profile with corrected Standard Penetration Test (SPT) blows counts, $N_{1,60} \leq 15$; F_{15} is the average fines content (percentage of sediment passing a No. 200 sieve) of the materials comprising T_{15} (%); $D50_{15}$ is the average mean grain size of the materials comprising T_{15} (mm); and, α is a dummy variable defining the controlling topographic conditions at the point of interest. For sloping-ground conditions, α is set to zero, W is set to 1, and site-specific estimates of *S (%)* are entered. For free-face conditions, α and S are set to 1, and site-specific values of *W (%)* are entered. Youd et al. (2002) computed the following

partial regression coefficients for eqn. (3.1): b_o = -16.213, b_{off} = -0.500, b_1 = 1.532, b_2 = -1.406, b_3 = -0.012, b_4 = 0.592, b_5 = 0.338, b_6 = 0.540, b_7 = 3.413, and b_8 = -0.795.

The importance of each variable in the regression model is tested by an analysis of variance (ANOVA) table, which comprises an F-test. The F-statistic is computed to verify that a linear relationship exists between the dependent variable and at least one of the independent variables. Table 3.1 summarizes the ANOVA results for eqn. (3.1). Since the F-statistic is much larger than the critical value for the null distribution at the 5% significance level, then the probability that none of the independent variables are correlated to the dependent variable is essentially zero (P-value $\approx$ 0). Therefore, for this case, the full model is statistically significant for predicting the dependent variable, $Log\ D_H$. The coefficient of determination for the full model, R^2, is 83.6%; and, the standard deviation of the predicted variable, σ_{logDH}, is 0.1970.

Removing the F_{15} and $D50_{15}$ Variables from the MLR Model

Bardet et al. (2002) have suggested removing the F_{15} and $D50_{15}$ variables from the full MLR model because these factors are the least likely to be available, especially for regional studies. Upon removal of the F_{15} and $D50_{15}$ variables, the "reduced" model has the general form shown in eqn. (3.3).

Table 3.1. ANOVA results of eqn. (3.1), the full MLR model

Source of Variation	Sum of Squares	Deg. of Freedom	Mean Squares	F-statistic	P-value
Regression	93.53	9	10.3923	267.9	0.000
Error	18.39	474	0.0388		
Total	111.92	483			

$$LogD_H = b_o + b_{off}\alpha + b_1 M + b_2 LogR^* + b_3 R + b_4 LogW + b_5 LogS + b_6 LogT_{15} \quad (3.3)$$

Upon regression of the case history database compiled by Youd et al. (2002), eqn. (3.3) has the following partial regression coefficients: b_o = -9.087, b_{off} = -0.353, b_1 = 1.428, b_2 = -0.902, b_3 = -0.020, b_4 = 0.401, b_5 = 0.293, and b_6 = 0.560. Table 3.2 summarizes the ANOVA results for eqn. (3.3). Although the F-statistic remains much larger than the critical value for the null distribution at the 5% significance level, R^2 for the reduced model has decreased to 66.6%; which means only 66.6% of the variability in the dependent variable, *Log* D_H, is explained by the independent variables. Also, the variance of the regression equation (i.e., *MSE*) has more than doubled that of the full model; and, the standard deviation of the predicted variable, σ_{logDH}, has significantly increased to 0.2802.

Figure 3.1a depicts predicted values of D_H from eqn. (3.3) versus measured values of D_H from the case history database of Youd et al. (2002). The solid line on the plot (that is at 45 degrees from the origin) represents a perfect prediction line or a mean-estimate line. Points plotting near this line represent displacements that are closely predicted by the model. The dashed lines, plotted at 2:1 and 1:2 slopes, represent a 100% over-prediction boundary and a 50% under-prediction boundary, respectively.

Table 3.2. ANOVA results of eqn. (3.3), the reduced MLR model

Source of Variation	Sum of Squares	Deg. of Freedom	Mean Squares	F-statistic	P-value
Regression	74.56	7	10.6520	135.7	0.000
Error	37.35	476	0.0785		
Total	111.92	483			

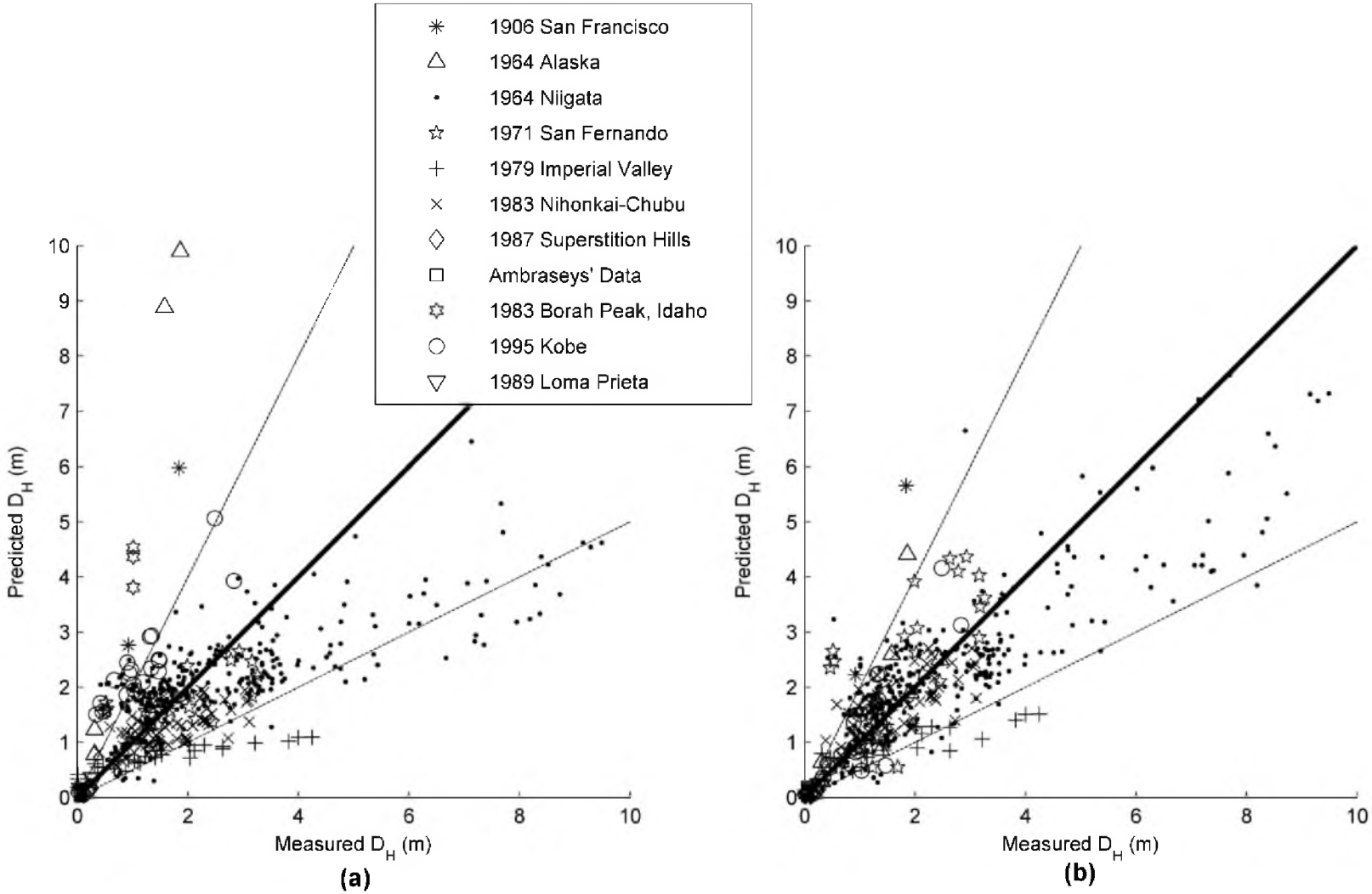

Figure 3.1. Predicted lateral spread displacement using (a) eqn. (3.3), or (b) eqn. (3.4), versus measured lateral spread displacement from the case history database of Youd et al. (2002)

Points plotting above or below these bounds represent displacements that are being over or under-predicted by a factor of 2 or greater. Figure 3.1a shows that 18.6 % (90 out of 484) of the displacements predicted by eqn. (3.3) fall outside these bounds—of which many fall well outside the bounds.

Other points in Figure 3.1a, as grouped and symbolized by earthquake, also trend in one direction, either consistently above or below the 1:1 line. For instance, eqn. (3.3) heavily over-predicts all of the displacements recorded for the 1964 Alaska earthquake. Instead of following the 1:1 line, these points plot along a line approximately 80 degrees left of the horizontal axis. It is important to note that in the Alaska earthquake, high amounts of fines and small mean grain sizes were found in many of the boreholes. Therefore, because the predictive power of the model (eqn. (3.3)) has been reduced, and because of its overall lack of fit, it is desirable to seek other variables to replace F_{15} and $D50_{15}$ in the model without compromising its predictive power.

Adding the Soil Description Variables to the MLR Model

We found that the soil classification obtained from the borehole logs could supplant F_{15} and $D50_{15}$. Often there is a description or classification of the soil recorded on a borehole log with the corresponding SPT N values, and we wanted to test if these descriptions might be used in the regression analyses to replace F_{15} and $D50_{15}$. Figure 3.2 is a plot of borehole data at a site in Alaska from the lateral spread database compiled by Bartlett and Youd (1992). This figure shows SPT $N_{1,60}$ values and corresponding soil descriptions at a site with groundwater located near the surface. The five shaded layers indicate zones that are cohesionless, saturated and have values of $N_{1,60} \leq 15$. The sum of

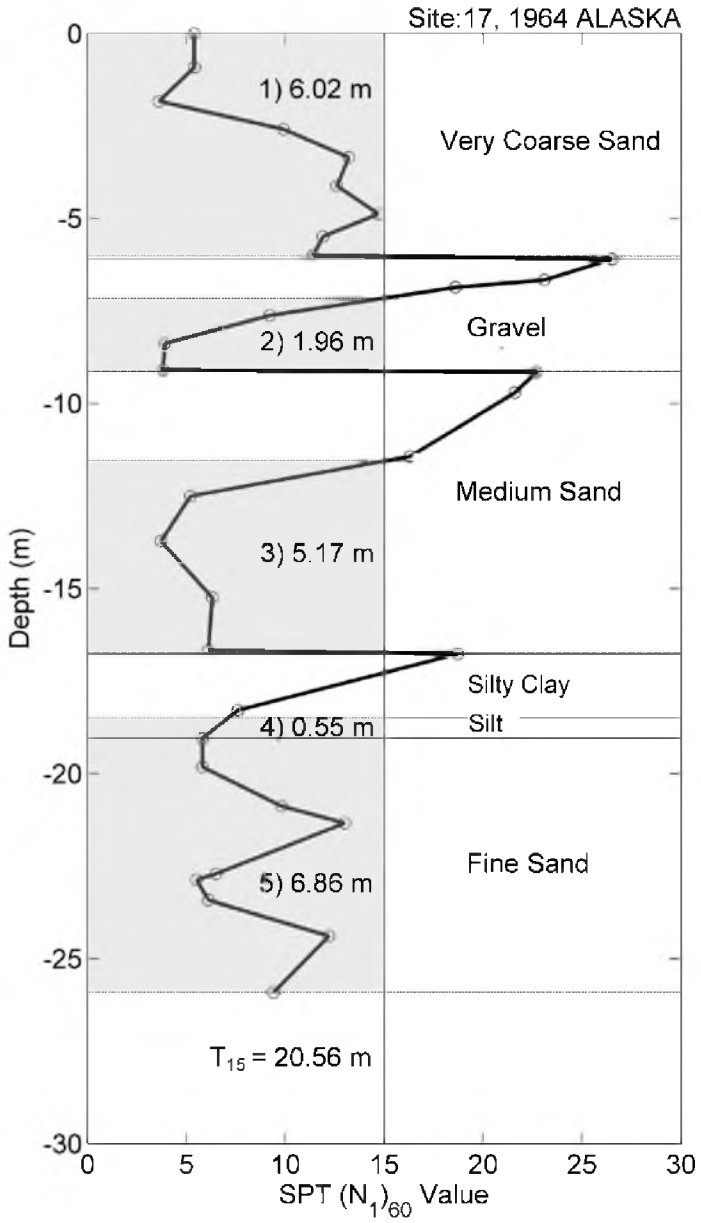

Figure 3.2. Boring log at Railroad Bridge Milepost 147.4, Matanuska River, Alaska. The five shaded layers comprise T_{15} at this site

the thickness of these 5 layers, T_{15}, is equal to 20.6 meters. Layers like those shown in Figure 3.2 can be found for every T_{15} value in the Youd et al. (2002) lateral spread database.

To implement our approach, we assigned a soil index, *SI*, to each T_{15} layer according to the most general soil description or Unified Soil Classification System (USCS) symbol. Table 3.3 summarizes the mean and standard deviation of the mean grain size ($\overline{D50}$ and $\sigma_{D50,}$ respectively), and the mean and standard deviation of the fines content ($\overline{FC}$ and $\sigma_{FC,}$ respectively) for all of these T_{15} layers in the database, grouped according to soil description from the boring logs. In order to complete the definition of *SI* for each soil type, Table 3.3 also includes an index for cohesive soil that is not susceptible to liquefaction (i.e., *SI = 6)*.

By including soil classification variables in the MLR model in lieu of the F_{15} and $D50_{15}$ variables, the modified model has the general form shown in eqn. (3.4).

$$LogD_H = \begin{array}{c} b_o + b_{off}\alpha + b_1 M + b_2 LogR^* + b_3 R + b_4 LogW + b_5 LogS + \\ + b_6 LogT_1 + a_1 x_1 + a_2 x_2 + a_3 x_3 + a_4 x_4 + a_5 x_5 \end{array} \quad (3.4)$$

where x_i is the ratio of T_{15} in a borehole that has an *SI* value (defined in Table 3.3) equal to *i*. For example, the borehole plotted in Figure 3.2 has x_1 = 1.96 / 20.6 = 0.10; x_2 = 6.02 / 20.6 = 0.29; x_3 = 0.25; x_4 = 0.33; and, x_5 = 0.03. Of course, the sum of all values of *x* in the borehole equals 1.

Following the same technique as Bartlett and Youd (1992), we used an inverse-weighted averaging scheme to assign computed values of *x* to every displacement vector.

Table 3.3. Descriptions and distributions of T_{15} layers in Youd et al. (2002) database

Typical Soil Descriptions in Database	Count n	$\overline{D50}$ (mm)	σ_{D50} (mm)	$\overline{FC}$ (%)	σ_{FC} (%)	General USCS Symbol	Soil Index SI
Silty gravel with sand, silty gravel, fine gravel	6	5.69	4.26	18.3	6.4	GM	1
Very coarse sand, sand and gravel, gravelly sand	7	2.15	0.83	7.5	6.4	GM-SP	2
Coarse sand, sand with some gravel	32	0.62	0.18	7.0	4.2	SP	2
Sand, medium to fine sand, sand with some silt	76	0.35	0.02	4.6	2.3	SP-SM	3
Fine sand, sand with silt	50	0.17	0.05	14.3	11.0	SM	4
Very fine sand, silty sand, dirty sand, silty/clayey sand	39	0.11	0.12	36.6	12.4	SM-ML	4
Sandy silt, silt with sand	38	0.07	0.08	57.9	12.2	ML	5
Silty clay, lean clay (not part of T_{15})	--	--	--	--	--	CL	6

This averaging scheme assigns the largest weight to the borehole located closest to the displacement location, and decreasingly smaller weights to boreholes located at greater distances.

Eqn. (3.4) has the following partial regression coefficients based on regression of the lateral spread database of Youd et al. (2002): b_o = -8.453, b_{off} = -0.342, b_1 = 1.348, b_2 = -1.068, b_3 = -0.017, b_4 = 0.453, b_5 = 0.334, b_6 = 0.588, a_1 = -0.647, a_2 = -0.176, a_3 = 0.278, a_4 = 0.032, and a_5 = -0.571. Table 3.4 summarizes the ANOVA results for eqn. (3.4). As can be seen, the F-statistic increased to 156.5 and remains much larger than the critical value for the null distribution at the 5% significance level. This indicates that eqn. (3.4) is statistically significant for predicting the dependent variable, $Log\ D_H$. Moreover, the R^2 for this model is 80.0%, and the standard deviation of the predicted variable, σ_{logDh}, is 0.2182. These values are similar to those found for the full MLR model (eqn. (3.1)). For comparison, R^2 is only 3.6% less, and σ_{logDH} is only 0.0212 more than the value found for eqn. (3.1). In addition, Figure 3.1b shows predicted values of D_H from eqn. (3.4) versus measured values of D_H from the case history database. Comparing this plot with Figure 3.1a, more points fall between the bounds of the 1:2 and 2:1 sloped lines (88.8% of the points compared to 81.4% in Figure 3.1a). These comparisons demonstrate that SI is a reasonable surrogate of F_{15} and $D50_{15}$ for predicting lateral spread displacement.

Table 3.4. ANOVA results of eqn. (3.4), the modified MLR model

Source of Variation	Sum of Squares	Deg. of Freedom	Mean Squares	F-statistic	P-value
Regression	89.48	12	7.4567	156.5	0.000
Error	22.44	471	0.0476		
Total	111.92	483			

The values of the partial regression coefficients for the soil description variables indicate their relative influence on displacement. For example, the maximum of these coefficients is a_3, indicating that fine to medium-grained sands with low fines content are associated with larger lateral spread displacement than other soil types. Coarse grained material, especially gravels with sufficient fines content to impede drainage, have smaller coefficient values. Very fine-grained materials, such as sandy silts, have a negative partial regression coefficient, which means they produce smaller displacements on average when compared with the mean estimate from the regression model.

To further show how soil type and thickness affect the amount of lateral spread displacement, the variable T_{15} can be adjusted to an equivalent "clean sand" value, $T_{15,cs}$. We define $T_{15,cs}$ as a T_{15} value for fine to medium-grained clean sand only, which occurs when $x_3 = 1$ and all other x's $= 0$. This new variable is calculated by using the final 6 terms in eqn. (3.4), as listed in eqn. (3.5).

$$b_6 LogT_1 + [\mathbf{a}][\mathbf{x}] = b_6 LogT_1 + a_1 x_1 + a_2 x_2 + a_3 x_3 + a_4 x_4 + a_5 x_5 \tag{3.5}$$

where $[\mathbf{a}]$ is a vector for a_1 through a_5, and $[\mathbf{x}]$ is a vector for x_1 through x_5. Inserting $T_{15} = T_{15,cs}$, $x_1 = x_2 = x_4 = x_5 = 0$, and $x_3 = 1$, into the right-hand side of eqn. (3.5) results in eqn. (3.6).

$$b_6 LogT_{15} + [\mathbf{a}][\mathbf{x}] = b_6 LogT_{15,cs} + a_3 \tag{3.6}$$

We solve for $T_{15,cs}$, as shown in eqn. (3.7).

$$T_{15,cs} = T_{15} \cdot 10 \wedge \left(\frac{[\mathbf{a}][\mathbf{x}] - a_3}{b_6} \right) \tag{3.7}$$

Values of $T_{15,cs}$ for a given borehole provide a single geotechnical variable that can be substituted into eqn. (3.4) for T_{15} (with $x_3 = 1$ and all other x 's = 0). Most of the ax terms in eqn. (3.4) are thereby removed, because their values of $x = 0$. Using a single regression variable also shows how soil type and thickness jointly affect lateral spreading. For example, Figure 3.3 shows values of $T_{15,cs}$ plotted versus T_{15} for various soil types. This figure demonstrates that 1 meter of saturated, clean, fine to medium-grained sand with $N_{1,60} \leq 15$ has about the same displacement potential as15 meters of saturated soil that is either gravel or silt with $N_{1,60} \leq 15$.

Estimating Soil Description Variables, x_i, with CPT Data

The Cone Penetration Test (CPT) has undergone rapid development and is widely used in liquefaction evaluations. It would be useful to develop an approach to apply eqn. (3.4) to such data. Numerous researchers have developed relationships between CPT data and soil type, typically by the use of charts (e.g., Schmertmann 1978, Douglas and Olsen 1981, Olsen and Malone 1988, Robertson et al. 1986, Robertson 1990, Jefferies and Davies 1991).

Robertson (1990) introduced one of the most popular CPT-based charts to define soil behavior type. This chart links normalized CPT tip resistance, Q_{tn}, and normalized friction ratio, F_r, to the in situ mechanical soil behavior, named the "normalized soil behavior type" (SBTn).

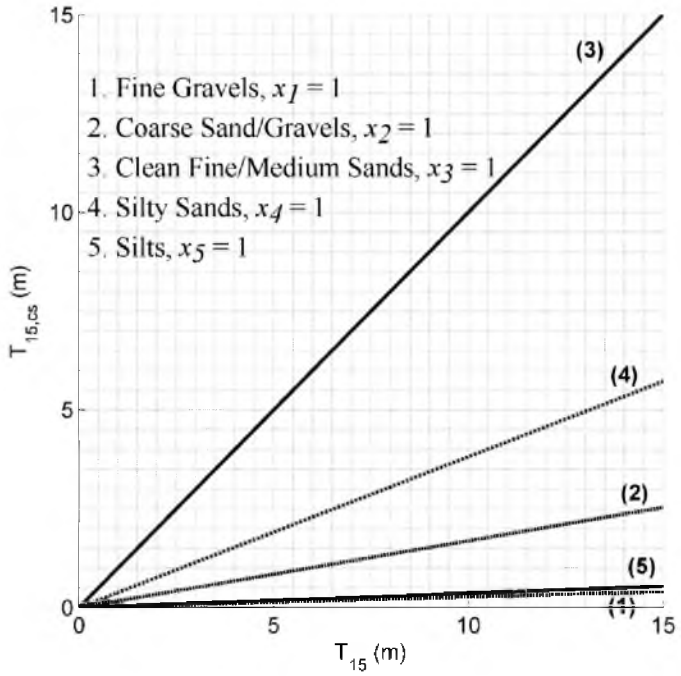

Figure 3.3. T_{15} vs. $T_{15,cs}$ according to soil index

Often, soil classification such as the USCS which is based on grain-size distribution and plasticity of disturbed samples, relate well with CPT-based SBTn (e.g., Molle 2005).

Jefferies and Davies (1993) introduced an index to define the soil behavior type, named the Soil Behavior Type Index, I_c. This index is simply the radius of concentric circles which plot on Jefferies and Davies (1991) SBTn chart. Robertson and Wride (1998) modified the definition of I_c such that certain values of I_c will approximate the boundaries of SBTn zones 2-7 on the Robertson (1990) Q_t - F_r SBTn chart (see base layer of Figure 3.4). Zhang et al. (2002) most recently updated the definition of I_c, which is shown in eqn. (3.8). Jefferies and Davies (1993) suggested that I_c could be used to develop empirical correlations of CPT-based data that vary with soil type.

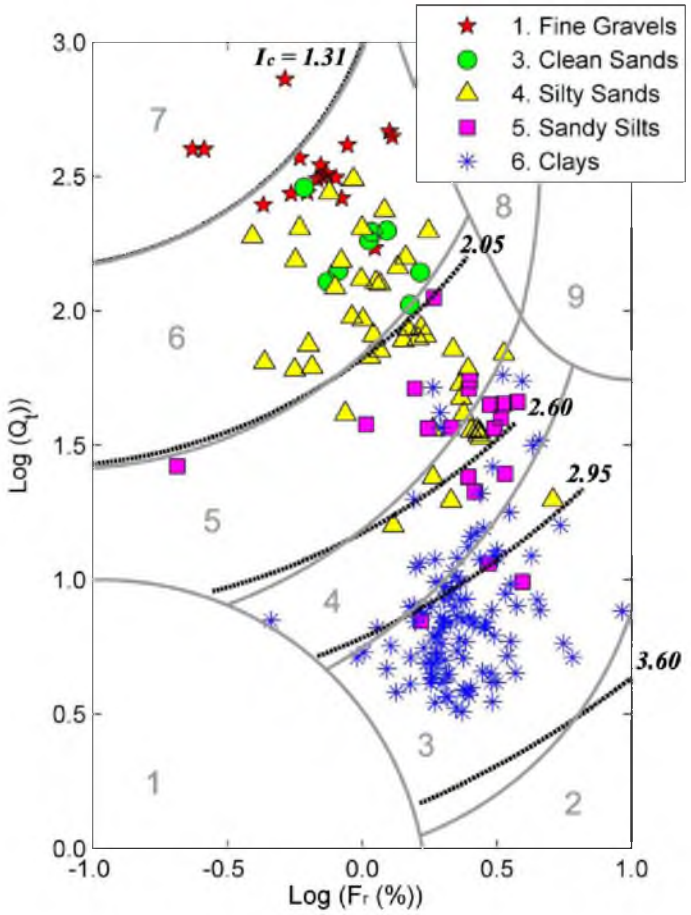

Figure 3.4. Data from Weber County, Utah, plotted on Robertson (1990) Q_t - F_r SBTn chart with contours of I_c

$$I_c = [(3.47 - LogQ_{tn})^2 + (LogF_r + 1.22)^2]^{0.5} \tag{3.8}$$

With this in mind, we compiled available "pairs" of side-by-side SPT borings and CPT soundings in Weber County, Utah into a database. From this, there are 205 samples that were classified according to the USCS from laboratory measurements. Based on these evaluations, we assigned the samples values of *SI*, as defined in Table 3.3. In addition, at the depth intervals where these samples were taken, we found the median

values of Q_{tn}, F_r, and I_c from the adjacent CPT soundings. Figure 3.4 plots these CPT data, symbolized by *SI*, on the Robertson (1990) Q_t - F_r SBTn chart. As can be seen, data with the same *SI* group together in reasonably distinct areas of the SBTn chart; thus, I_c appears to be a good discriminator of soil type, although silty sands (*SI* = 4) have somewhat high scatter. (We note that the Weber County database lacks samples with *SI* = 2, but the method presented below could be extended to include this soil type, if the database was expanded. Almost all of the samples in the lateral spread database of Youd et al. (2002) with *SI* = 2 are from Japanese case studies).

Figure 3.5 shows histograms of I_c, grouped by *SI*, from the Weber County database. A normal probability density function is fitted to each dataset. Table 3.5 lists the mean and standard deviation ($\overline{I_c}$ and s_{Ic}, respectively) of I_c for each *SI* along with results of a Lilliefors' goodness-of-fit test for normality. A Lilliefors' test is a special type of the Kolmogorov-Smirnov (K-S) statistical test used to test the null hypothesis that data come from a normally distributed population where the mean and standard deviation parameters are estimated rather than fully known (such as due to a small sample size). Since the computed *k*-statistic values are less than the critical values at the 5% significance level, then the null hypothesis that the data are normally distributed cannot be rejected.

With confidence that the groups are normally distributed, we next verified that I_c statistically discriminates between each group of *SI*. A one-way ANOVA test rejects the global null hypothesis that the means, $\overline{I_c}$, are the same across the groups of *SI* at the 5% significance level. We then used multiple comparison procedures to determine if the means differ between groups.

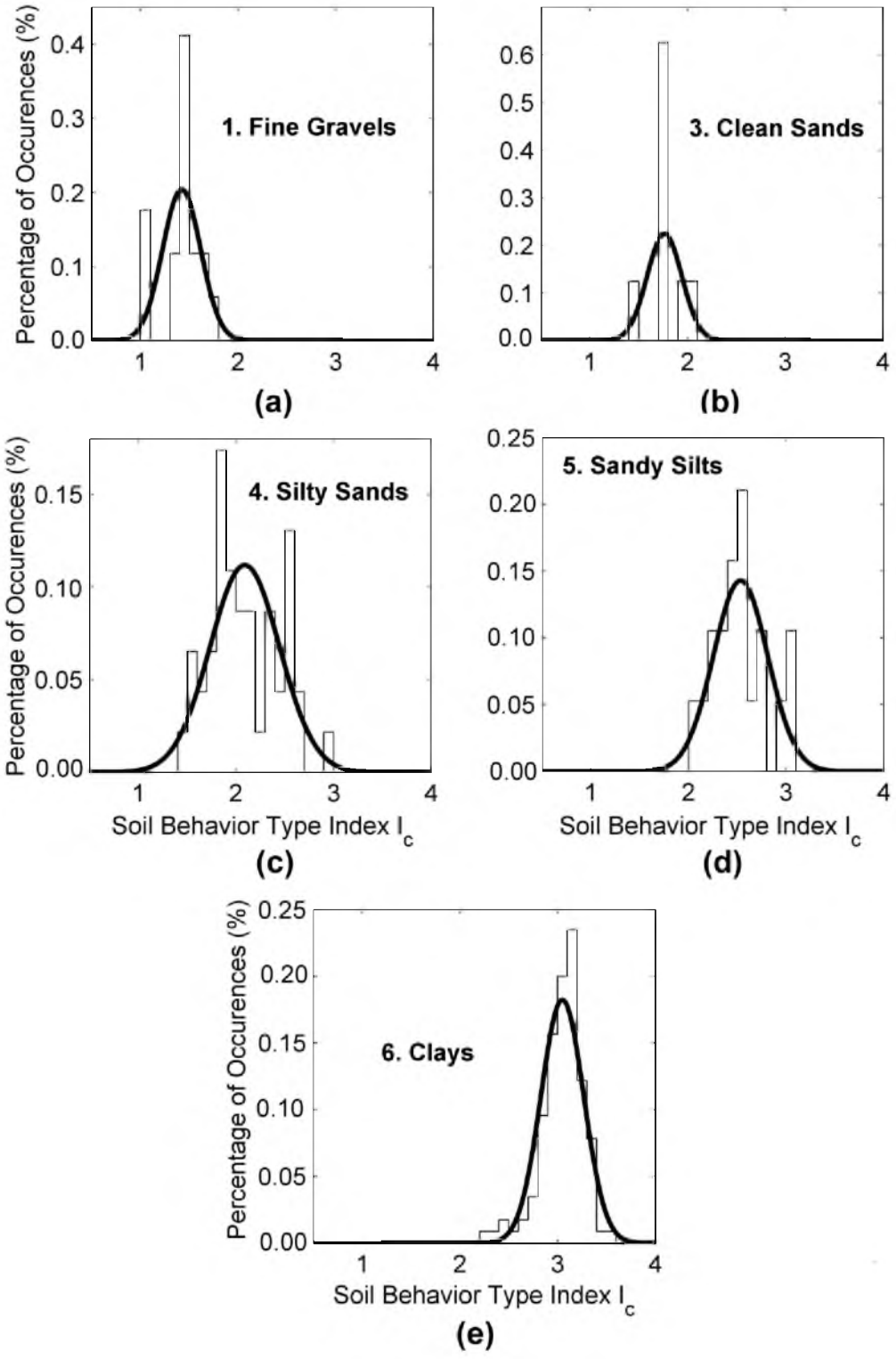

Figure 3.5. Histograms of I_c and fitted normal probability density functions for (a) $SI = 1$, (b) $SI = 3$, (c) $SI = 4$, (d) $SI = 5$, (e) $SI = 6$; data from Weber County, Utah

Table 3.5. Lilliefors' goodness-of-fitness test results for normality

Soil Index	Count n	$\overline{I_c}$	s_{Ic}	P-Value	k Stat.	critical value
1	17	1.42	0.195	0.084	0.197	0.208
3	8	1.76	0.178	0.056	0.283	0.286
4	46	2.09	0.357	0.546	0.085	0.129
5	19	2.53	0.279	0.422	0.141	0.199
6	115	3.05	0.219	0.143	0.075	0.084

Figure 3.6 graphically displays the results of the comparison using the Tukey—Kramer single-step method at the 5% significance level. Because none of the horizontal lines of each group overlap, the means of each group are statistically different.

Due to small sample sizes and similar variances of I_c for SI =1 and SI =3, we performed a two-sample F-test of the hypothesis that these two groups come from normal distributions with the same variance. The test finds that the F-statistic = 1.208, and the P-value = 0.841. Therefore, the null hypothesis cannot be rejected at the 5% significance level. The pooled variance of I_c for SI =1 and SI =3 is 0.036; and, the pooled standard deviation, s_{Ic}, is 0.190.

If it is assumed that each of the five soil types listed in Table 3.5 have the same probability of being encountered randomly in situ, then eqn. (3.9) is true for determining the probability of a particular soil index, $P(SI = i)$, given a value of I_c.

$$P(SI = i \mid I_c) = \frac{N(\overline{I_{ci}}, s_{Ici}^2)}{\sum_{i=1}^{M} N(\overline{I_{ci}}, s_{Ici}^2)} \tag{3.9}$$

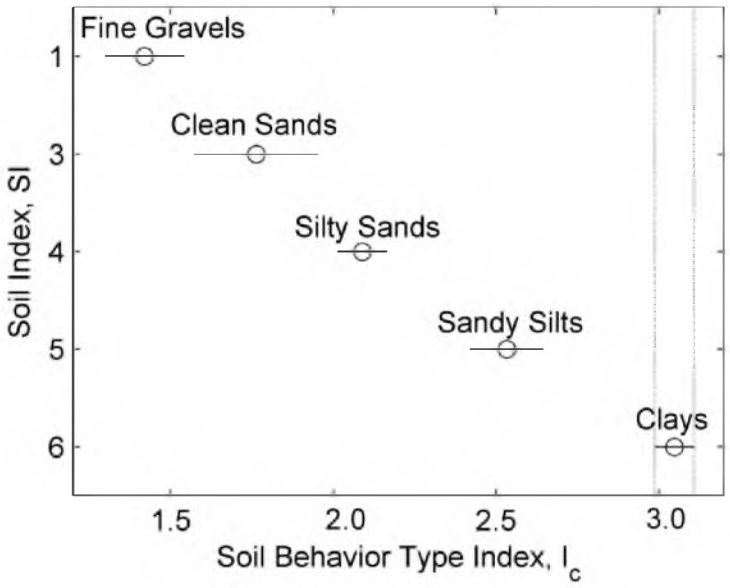

Figure 3.6. Multiple comparisons of the means of I_c, grouped by *SI*; data from Weber County, Utah

where N is the normal probability density function of I_c, with mean = $\overline{I_c}$ and variance = s^2_{Ic}, for the particular $SI = i$. Zhang and Tumay (1999) found this equation rigorously for the soil classification index, U, rather than for I_c.

Figure 3.7 displays the recommended normal probability density functions of I_c for each *SI* based on the data from Weber County, Utah. Figure 3.8 depicts the graphical solution of eqn. (3.9)for each *SI* using the normal probability density functions in Figure 3.7.

Eqn. (3.9) (or Figure 3.8) provides a method to estimate the probability of each soil type or *SI* for a specific I_c value from the associated conditional probability density functions. For example, if a CPT datum has a corresponding value of $I_c = 2.0$, then $P_1 = 0.01$, $P_3 = 0.42$, $P_4 = 0.47$, $P_5 = 0.10$, and $P_6 = 0.00$, where P_i is the conditional probability that $SI = i$.

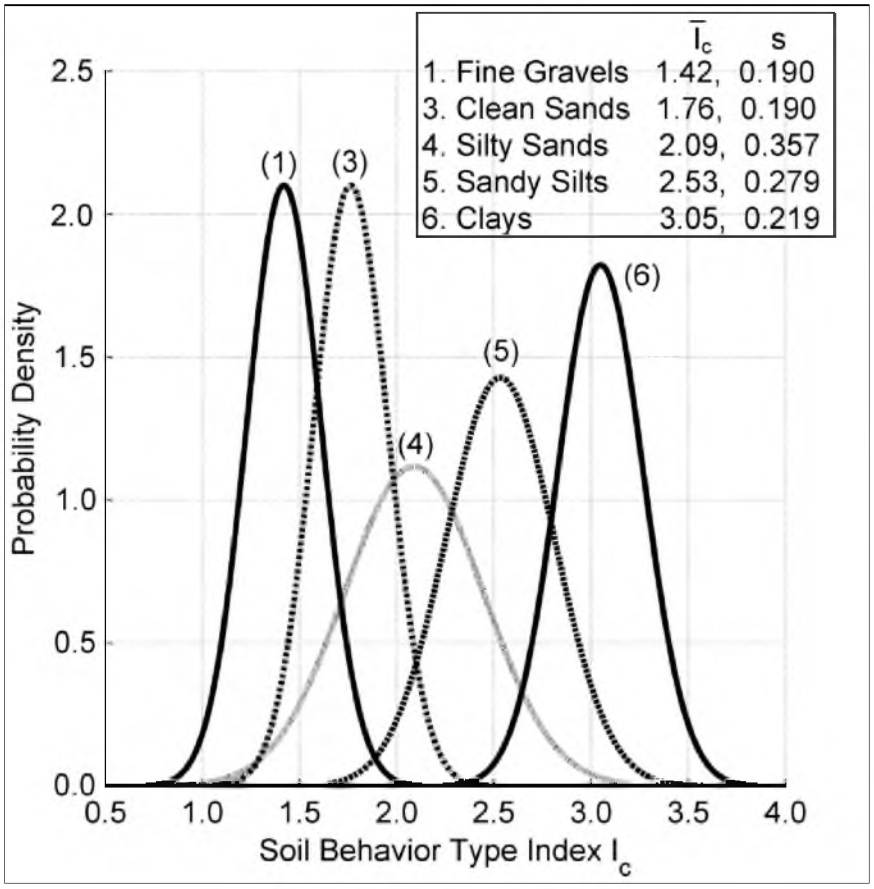

Figure 3.7. Recommended normal probability density functions for I_c, grouped by *SI*; Weber County, Utah

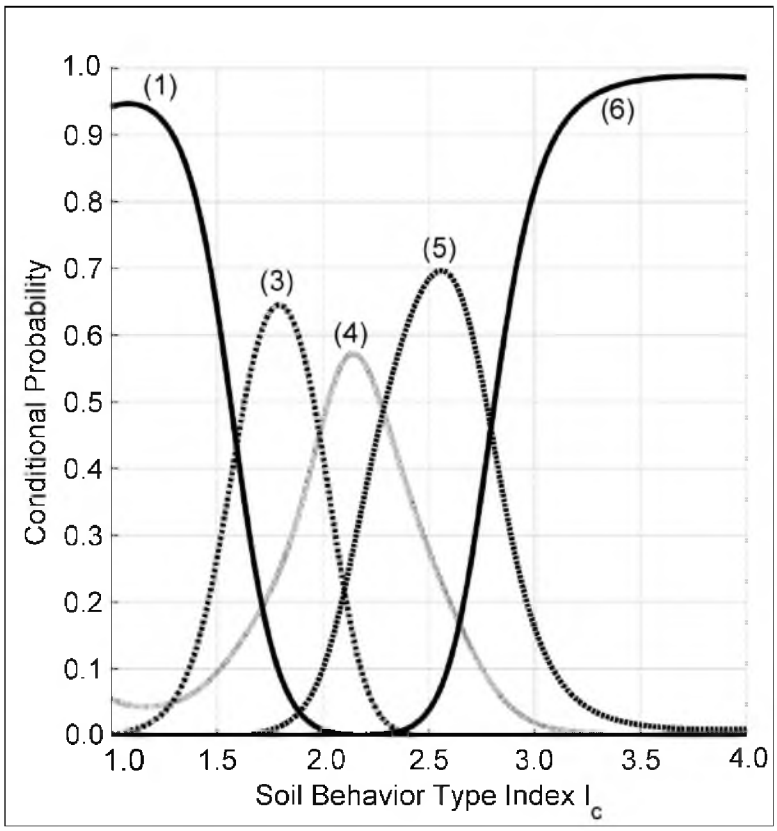

Figure 3.8. CPT point estimation chart for *SI* given I_c; Weber County, Utah

If that same soil was considered susceptible to liquefaction- induced lateral spread (e.g., for that soil, $T_{15} > 0$), then the values of P_1, P_3, P_4, and P_5, could be inserted into eqn. (3.4) as variables x_1, x_3, x_4, and x_5, respectively, for that datum.

Once again, soils with $SI = 6$ were not considered to be susceptible to liquefaction.

Estimating T_{15} with CPT Data

Numerous researchers have found a correlation between SPT-N values and CPT cone tip resistance, q_t (e.g., Robertson et al. 1983, Robertson and Campanella 1986,

Kulhawy and Mayne 1990, Jefferies and Davies 1993). In the aforementioned SPT-CPT "pairs" database for Weber County, Utah, there are 327 samples with SPT-N values corrected to an energy ratio of 60%, N_{60}. Across the 0.3 meters of depth where these blow counts were measured, we found the median values of q_t, and I_c from the adjacent CPT soundings. These points are plotted in Figure 3.9.

Values of q_t are made dimensionless by dividing by the atmospheric pressure, P_a. As can be seen, there is a negative correlation between the $Log\ [(q_t / P_a) / N_{60})]$ versus I_c. Linear regression of the data gives the relationship shown in eqn. (3.10).

$$Log[(q_t / P_a) / N_{60})] = 1.26 + 0.295 \cdot I_c \tag{3.10}$$

This regression model has a value of R^2 equal to 61.6%, and a standard deviation of the predicted variable equal to 0.156. Although a high R^2 value would be preferable, we observe less scatter about the regressed line when $I_c < 2.60$.

Robertson and Wride (1998) suggested that the approximate boundary between cohesionless and cohesive behavior for a soil is around $I_c = 2.60$. Perhaps the additional scatter in the cohesive area is due to small and thus less reliable values of SPT-N measured in the soft and cohesive clays. Since T_{15} is defined as the thickness of saturated, *cohesionless* soil, we recommend eqn. (3.10) to predict values of N_{60} from CPT data for liquefaction studies.

After finding N_{60} from eqn. (3.10) and correcting it for overburden stress to $N_{1,60}$, we identify layers in the upper 15 meters of the CPT logs that are saturated, cohesionless, and have values of $N_{1,60} \leq 15$. T_{15} is found by summing the thickness of these layers.

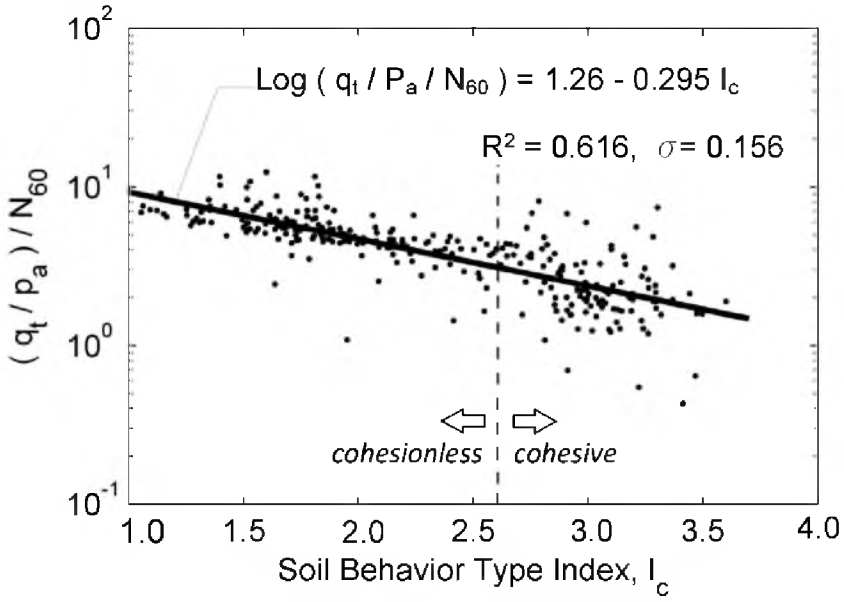

Figure 3.9. Relationship between CPT-data and SPT N_{60}; Weber County, Utah

We then use eqn. (3.9) to compute the conditional probabilities of SI (P_1, P_3, P_4, and P_5) from values of I_c for each of these layers. The averages of these conditional probabilities are inserted into eqn. (3.4) as the variables x_1, x_3, x_4, and x_5 (per eqn. (3.11)).

$$x_i = \frac{T_{15}}{\sum_{j=1}^{m} \frac{t_j}{P_i}} \tag{3.11}$$

where t_j is the thickness of the j-th layer that comprises T_{15} at the CPT sounding (m); P_i is the conditional probability that $SI = i$ for the j-th layer; and, x_i is the average ratio of T_{15} at a CPT sounding that has $SI = i$.

Conclusions

1. The Youd et al. (2002) model for predicting liquefaction-induced lateral spread requires specific inputs from laboratory testing, namely mean grain size, $D50_{15}$, and average fines content, F_{15}. Often in regional studies, these data are not available. By replacing these two soil factors with the soil description, a new model is developed which can use data routinely collected in the field and reported on the borehole logs. This modified MLR model (eqn. (3.4)) has a coefficient of determination, R^2, equal to 80.0%, only 3.6% less than R^2 for the Youd et al. (2002) empirical model (eqn. (3.1)). Therefore, Eqn. (3.4) is recommended for engineering practice as the most parsimonious model for predicting liquefaction-induced lateral spread when using existing data. The proposed empirical model shows that seismic, topographic, and geotechnical factors are highly correlated with liquefaction-induced lateral spread displacement.
2. Fine to medium-grained sands with low fines content are associated with larger lateral spread displacement than coarse grained sands, silty sands, sandy silts, or fine gravels. This can be seen from the partial regression coefficients of the soil description variables of eqn. (3.4).
3. CPT data can be used in conjunction with the proposed empirical model (eqn. (3.4)) because it is possible to use CPT data to estimate the required soil inputs. We have presented a method to calculate the probabilities of each soil type (or index) given the CPT soil behavior type index, I_c (eqn. (3.9)). Because of the structure of proposed empirical model, these probabilities can be input directly into eqn. (3.4). In addition, SPT-N values corrected to an energy ratio of 60% are correlated with

CPT cone tip resistance and I_c (eqn. (3.10)). Eqn. (3.10) provides a method to estimate the thickness of soil susceptible to liquefaction-induced lateral spread.

4. We recommend researchers compile and analyze side-by-side SPT borings and CPT soundings in their area of interest, in order to verify that their data follow the same relationships as presented in Figure 3.8 and eqn. (3.10). If necessary, the methodology presented herein can be readily modified to fit a different dataset.

References

Bardet, J. P., Tobita, T., Mace, N., and Hu, J., 2002. Regional modeling of liquefaction-induced ground deformation, *Earthquake Spectra* **18**(1), 19-46.

Bartlett, S. F., and Youd, T. L., 1992. *Empirical Analysis of Horizontal Ground Displacement Generated by Liquefaction-Induced Lateral Spreads, Technical Report NCEER-92-0021*, National Center for Earthquake Engineering Research, Buffalo, NY.

Bartlett, S. F., and Youd, T. L., 1995. Empirical prediction of liquefaction-induced lateral spread, *J. Geotech. Eng.* **121**(4), 316-328.

Baska, D. A., 2002. *An Analytical/Empirical Model for Prediction of Lateral Spreading Displacements, Ph.D. Dissertation*, University of Washington, Seattle, WA, 539 pp.

Douglas, B. J., and Olsen, R. S., 1981. Soil classification using electric cone penetrometer. in *Cone Penetration Testing and Experience, Proc. of a Session, ASCE National Convention*, G. M. Norris and R. D. Hotz (editors), St. Louis, MO, pp. 209–227.

Faris, A. T., Seed, R. B., Kayen, R. E., and Wu, J., 2006. A Semiempirical Model for the Estimation of Maximum Horizontal Displacement due to Liquefaction-Induced Lateral Spreading, in *Proc. 8th U.S. Conference on Earthquake Engineering*, vol. 3, paper no. 1323, San Francisco, CA, pp. 1584-1593.

Hamada, M., Yasuda, S., Isoyama, R., and Emoto, K., 1986. Study on liquefaction induced permanent ground displacements, in *Report for the Association for the Development of Earthquake Prediction in Japan,* Tokyo, Japan, 87 pp.

Jefferies, M. G., and Davies, M. P., 1991. Soil classification by the cone penetration test: discussion, *Canadian Geotechnical Journal* **28**(1), 173–176.

Jefferies, M. G., and Davies, M. P., 1993. Use of CPTU to estimate equivalent SPT N60, *Geotechnical Testing Journal* **16**(4), 458–468.

Kulhawy, F. H., and Mayne, P. H., 1990. *Manual on Estimating Soil Properties for Foundation Design, EL-6800, Research Project 1493-6*, Electric Power Research Institute (EPRI), Palo Alto, CA.

Molle, J., 2005. *The Accuracy of the Interpretation of CPT-Based Soil Classification Methods in Soft Soils, M.Sc. Thesis*, Delf University of Technology, Delft, the Netherlands.

Olsen, M. J., Bartlett, S. F., and Solomon, B. J., 2007. Lateral spread hazard mapping of the Northern Salt Lake Valley, Utah for a M7.0 scenario earthquake, *Earthquake Spectra* **23**(1), 95-113.

Olsen, R. S., and Malone, P. G., 1988. Soil Classification and site characterization using the cone penetrometer test, in *Penetration Testing 1988, Proc. of the 1st Int. Conf on Penetration Testing, ISOPT-l*, J. de Ruiter (editor), vol. II, Orlando, FL, pp. 887-893.

Rauch, A. F., and Martin, J. R., 2000. EPOLLS model for predicting average displacements on lateral spreads, *J. Geotech. Geoenviron. Eng.* **126**(4), 360-371.

Robertson, P.K., 1990. Soil classification using the cone penetration test, *Canadian Geotechnical Journal* **27**(1), 151–158.

Robertson, P. K., and Campanella, R. G., 1983. Interpretation of the cone penetrometer test: parts I-II, *Canadian Geotechnical Journal* **20**(4), 718-745.

Robertson, P. K., Campanella, R. G., Gillespie, D., and Greig, J., 1986. Use of piezometer cone data, in *Proc. of In Situ '86, a Specialty Conf Sponsored by the Geotechnical Eng. Division of the ASCE*, GSP No. 6, S. P. Clemence (editor), Blacksburg, VA, pp. 1263-1280.

Robertson, P.K., and Wride, C.E., 1998. Evaluating cyclic liquefaction potential using the cone penetration test, *Canadian Geotechnical Journal* **35**(3), 442–459.

Schmertmann, J. H., 1978. *Guidelines for Cone Penetration Test, Performance and Design, Report FHWA-TS-78-209*, US Federal Highway Administration, Washington D.C., 145 pp.

Youd, T. L., Hansen, C. M., and Bartlett S. F., 2002. Revised multilinear regression equations for prediction of lateral spread displacement, *J. Geotech. Geoenviron. Eng.* **128**(12), 1007-1017.

Youd, T.L., and Perkins, D. M., 1987. Mapping of liquefaction severity index, *J. Geotech. Eng.* **113**(11), 1374-1392.

Zhang, G., Robertson, P. K., and Brachman, R. W. I., 2002. Estimating liquefaction-induced ground settlements from CPT for level ground, *Canadian Geotechnical Journal* **39**(5), 1168-1180.

Zhang, G., Robertson, P. K., and Brachman, R. W., 2004. Estimating liquefaction-induced lateral displacements using the standard penetration test or cone penetration test, *J. Geotech. Geoenviron. Eng.* **130**(8), 861-871.

Zhang, Z., and Tumay, M., 1999. Statistical to fuzzy approach toward CPT soil classification, *J. Geotech. Geoenviron. Eng.* **125**(3), 179-186.

CHAPTER 4

A RELIABILITY-BASED APPROACH TO MAPPING THE PROBABILITY OF LIQUEFACTION AND LATERAL SPREAD

Abstract

This paper presents a method to map the probability of liquefaction-induced ground failure for a seismic event. The proposed method incorporates geotechnical and geologic data, and accounts for variations in soil conditions, age, topography, spatial distribution, and other major sources of uncertainty. For an example of implementation of this method, liquefaction hazards are assessed in a study area in Weber County, Utah. This study explored the necessary geotechnical properties to assess liquefaction, and grouped these properties according to geologic unit. Analysis of the dispersion of the geotechnical properties between geologic units of similar depositional environment revealed that it is appropriate to combine these data from a statistical standpoint. These property distributions were then assigned to grid points spaced in a manner so as to capture topographic variations in the mapped domain. Then, at each grid point, numerous Monte Carlo simulations were performed to randomly sample the geotechnical distributions and output distributions of probabilities of liquefaction triggering and lateral

spread displacement exceeding specified thresholds. Solving all grid points in the study area produced the final liquefaction hazard maps. It is hoped that such maps will be useful for probabilistic-based hazard calculations and risk assessment.

Introduction

Liquefaction-induced ground failures, particularly lateral spread displacements from major earthquakes, can cause significant damage to infrastructure and other facilities. Thus, many researchers have developed methods to map areas of significant liquefaction risk (e.g., Olsen et al. 2007). In general, these methods begin with making reasonable estimates of the necessary input variables, and then computing expected values of liquefaction-induced ground failure based on these estimates. These expected values are then generalized to an area of interest. However, almost all of these types of methods do not formally quantify the uncertainty associated with the liquefaction hazard mapping process.

Liquefaction-induced ground failure is a complex phenomenon, and the uncertainties associated with predicting and modeling such hazard is further compounded when mapped at a regional scale. The mapping procedure presented herein accounts for the primary sources of uncertainty in the estimation process. By preserving the uncertainty in the analyses rather than removing it, we can define the median estimate and its distribution. This will aid investigators in deciding if there is a need to perform site-specific analyses to better characterize subsurface conditions and thereby reduce uncertainties in the mapped estimates of liquefaction hazards.

As is usually done in geotechnical engineering, we treat the uncertainties in liquefaction analysis inductively. We begin with limited observations of a large and complex subsurface, and infer behavior based on engineering judgment, geologic information, and statistical reasoning. Numerous sources of uncertainty exist, such as natural variability over time and space, and knowledge uncertainty due to insufficient data and limitations of our current models to represent real processes. Often during engineering analyses, we despair that there are insufficient data or the models are too complex to calculate the associated uncertainty. Ironically, it is when these limitations are present that uncertainties should be fully addressed in a systematic manner.

Therefore, this paper describes a method to map the probability of liquefaction triggering and the probability of lateral spread displacements exceeding specified thresholds for a scenario seismic event. Primary uncertainty is preserved and modeled throughout the process by using Monte Carlo random sampling and other statistical techniques. As an example of implementation of this method, we map the liquefaction hazards in Weber County, Utah, for a 2,500-year return period earthquake and its associated strong motion.

Geologic Mapping

The proposed mapping procedure begins with surficial geologic maps. For Weber County, the Utah Geological Survey (UGS) has published numerous surficial geologic maps, including three 7.5-minute quadrangle maps: Ogden quadrangle (Yonkee and Lowe 2004), Roy quadrangle (Sack 2005), and Plain City quadrangle (Harty and Lowe 2005). The majority of the North Ogden quadrangle in the study area incorporates a map

of Harty and Lowe (2003). To complete the North Ogden quadrangle, we filled in a few areas with an earlier U.S. Geological Survey (USGS) map by Crittenden and Sorensen (1985). We decided to assess liquefaction hazards in these four quadrangles in Weber County, Utah, because the majority of the development in the county is found within these areas.

Using tools in ArcGIS®, we georeferenced each of the geologic maps in the study area, and digitized each geologic unit into a polygon feature class. We attributed each polygon feature with its geologic unit symbol and age. We then converted these polygon attributes into raster images. Raster data are advantageous because we can readily extract their cell values at any point feature using the "latticespot" tool in ArcGIS®.

The geology of the study area is dominated by Holocene and late Pleistocene sediments deposited primarily by the Weber and Ogden Rivers, Lake Bonneville and its successor, the Great Salt Lake. These deposits can be divided primarily into eight groups: stream alluvium, delta, alluvial fan, fluvial terrace, fine-grained lacustrine, coarse-grained lacustrine, landslide (mass-movement), and springs and marshes. We classify three additional groups for mixed delta, alluvium, and lacustrine deposits, and the North Ogden landslide complex. The UGS geologic maps further subdivide many of these groups into units by approximate age. Table 4.1 lists these 11 groups, the map symbols for each of the geologic units within every group, and the approximate age of the units. The ages shown in the table are from the UGS maps.

Figure 4.1 is a composite map of the surficial geology in the study area. As can be seen, the study area is bounded on the east by the Wasatch Mountains.

Table 4.1. Geologic units in study area, descriptions, approximate age, and sample size

Deposit Symbol	Description	Age	#SPT/ CPT
1. Stream Alluvium			
Qal_1	Modern stream alluvium, currently or recently active	< 3,000	79
Qal_2	Modern stream alluvium	3,000 - 10,000	92
Qal_3 - Qal_4	Stream alluvium	10,000 - 12,500	0
2. Delta			
Qd_1	Modern fine-grained delta, currently or recently active	< 200	0
Qd_2	Modern fine-grained delta	9,500 - 10,000	20
Qd_3	Fine-grained delta of Gilbert shoreline age	10,000 -11,000	19
Qd_4	Fine-grained delta from Lake Bonneville's regressive phase	12,000 - 12,100	22
Qd_5	Sand dominated delta from Lake Bonn.'s regressive phase	12,100 - 12,300	18
Qd_6 - Qd_{11}	Deltaic sand from early regressive phase of Lake Bonn.	12,300 - 14,500	3
3. Alluvial Fan			
Qaf	Modern alluvial fan	< 5,000	12*
4. Fluvial Terrace			
Qat_1 - Qat_9	Fluvial terrace, below the Gilbert shoreline	12,000 - 13,300	15
5. Fine-Grained Lacustrine			
Qlf	Mixed from Lake Bonneville and Great Salt Lake lacustrine	2,500 - 14,500	6
Qlf_3	Fine-grained lacustrine from Lake Bonn.'s regressive phase	10,000 - 14,500	271*
Qlf_4	Fine-grained lacustrine from Bonn.'s transgressive phase	14,500 - 28,000	2
6. Coarse-Grained Lacustrine			
Qls	Lacustrine sand from Lake Bonneville's regressive phase	12,200 - 12,500	8*
Qlg_3	Lacustrine gravel from Lake Bonneville's regressive phase	10,000 - 14,500	29*
Qlg_4	Lacustrine gravel from Lake Bonn.'s transgressive phase	14,500 - 28,000	30*
7. Landslide			
Qms_1	Modern landslide, currently or recently active	< 5,000	0
Qms_2	Modern landslide	5,000 - 10,000	22
Qms_3	Liquefaction- induced landslide (East Ogden slide complex)	10,000 - 14,500	6
8. Springs & Marshes			
Qsm	Springs and marshes, undivided	< 12,000	9
9 - 11. Others			
Qda	Undifferentiated delta and alluvium, sand-dominated	< 12,500	14
Qla	Undifferentiated lacustrine and alluvium	< 12,500	43
Qmq_2	Liquefaction-induced landslide (N. Ogden slide complex)	3,000 - 10,000	11

* = To increase the sample size, we analyzed geotechnical data from Salt Lake and Weber Counties of the same geologic description. The sample size listed is for both counties.

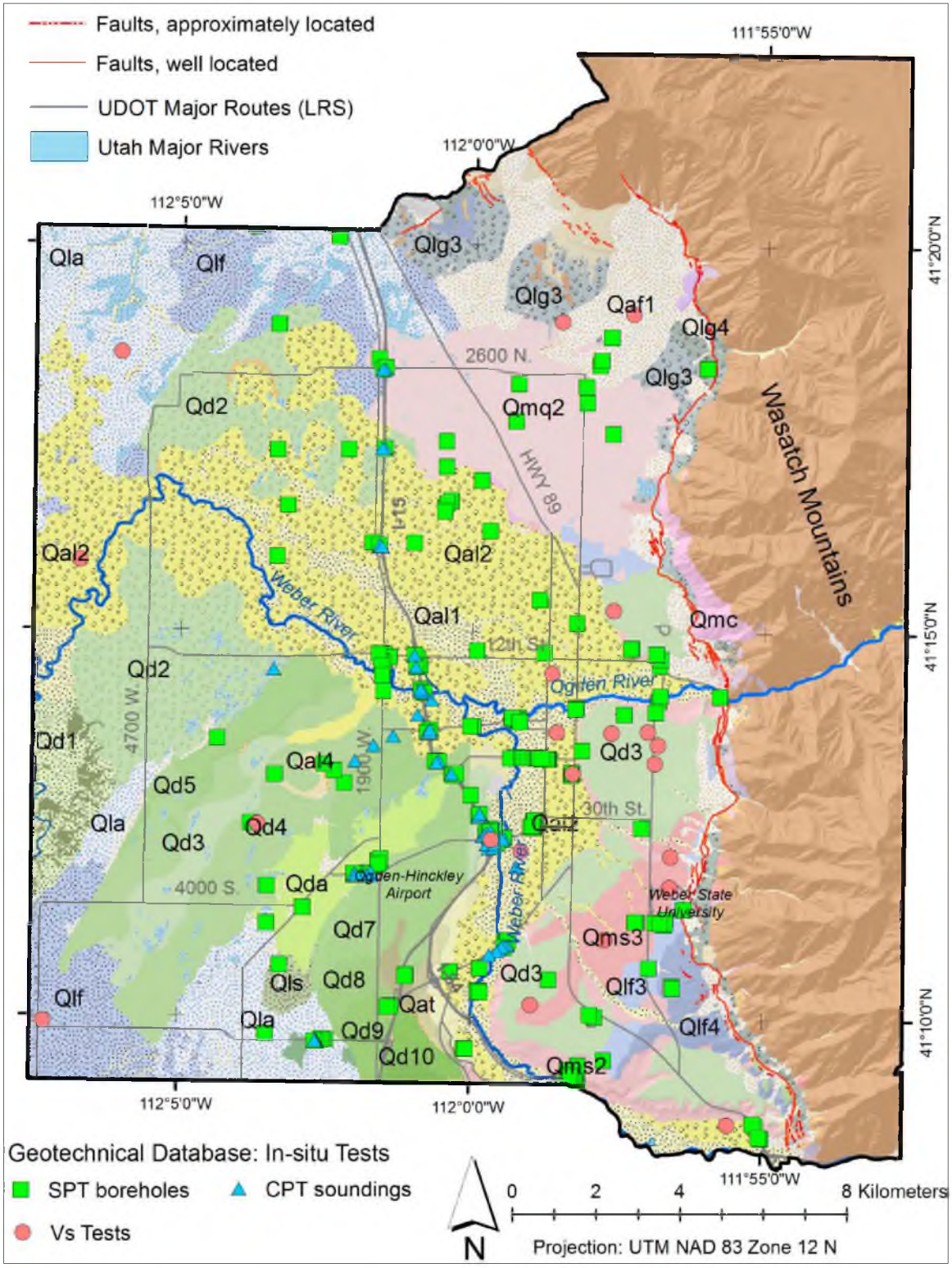

Figure 4.1. Study area, surficial geology, and location of a sample of the geotechnical investigations; Weber County, Utah (See Table 4.1 for description of geologic units)

We consider the deposits on the mountains as non-liquefiable because they are very dense, and the groundwater table is very deep. Figure 4.1 also depicts the location of the Wasatch fault zone, which is a segmented normal fault that extends along the Wasatch Front. The Weber segment of the Wasatch fault is the primary seismic threat to Weber County.

Geotechnical Database

We gathered all available geotechnical data in Weber County, Utah, and input them into an electronic database. This was done to define distributions of geotechnical properties for every geologic deposit listed in Table 4.1 and to assess possible data gaps. A large portion of the geotechnical data came from the Utah Department of Transportation (UDOT). Overall, the geotechnical database for this study contains data from 251 Standard Penetration Test (SPT) boreholes and 157 Cone Penetrometer Test (CPT) soundings. In general, we screened out subsurface tests that did not extend to depths greater than 10 meters. Although deeper tests are preferred, Bartlett and Youd (1992) found that the depth to the lowest factor of safety against liquefaction in numerous case histories is typically (about 90% of the time) within the upper 10 meters of a site profile. We also extracted data from 21 shear wave velocity tests (V_s) in a database published by McDonald and Ashland (2008).

The SPT boreholes provide mostly soil descriptions and classifications for each subsurface layer, depths to groundwater, and uncorrected SPT blow counts, *N*, with depth. In addition, some of the boreholes contained recorded measurements of fines contents, Atterberg limits, unit weights, and moisture contents. To keep track of the

quality of the data, we assigned data ranking fields for each measured soil property. We gave data a value of "1" if it was recorded in the borehole log of the original report. We gave data a value of "2" if it could be estimated from a nearby borehole log in the same report. Remaining estimates of missing data are filled in from Monte Carlo methods, as described later in this paper.

All of the CPT soundings have measurements of cone tip resistance, sleeve friction, and friction ratio. Nearly all of the soundings also have measurements of pore water pressure behind the tip of the cone, and cone tip resistance corrected for pore-pressure effects, at increments of 5 cm with depth. In addition, we found at least one pore-water pressure dissipation test in each sounding. These tests allow reasonable estimation of the depth to the groundwater table at each sounding location.

We used the data from the V_s tests to assist in determining the site soil response of a geologic unit, based on the upper 30 meters of the site profile, according to procedures described in Chapter 20 of ASCE 7 (2010).

Figure 4.1 shows a sampling of the SPT, CPT, and V_s data in this database. (Although we used all of the gathered subsurface data for the analyses, we do not have permission from the owner to release the locations of some of the borehole and CPT data provided by the local utilities.) Table 4.1 lists the number of SPT and CPT investigations in each of the geologic units. As can be seen, some of the units have a small sample size, and there are no SPT/CPT investigations in some of the very small units in the study area.

Probabilistic Framework

This paper presents a method to map the probabilities of liquefaction hazards for a seismic event. Although beyond the scope of this paper, it is certainly possible to extend the methodology presented herein to consider the uncertainty in the seismic inputs, and produce fully probabilistic liquefaction triggering and lateral spread hazard maps in an area of interest. To estimate the probability of liquefaction-induced lateral spread displacement exceeding certain thresholds for a scenario seismic event, we solve the probability chain listed in eqn. (4.1).

$$P[D_H > y] = P[D_H > y \mid L] \cdot P_L \tag{4.1}$$

where D_H is the predicted lateral spread displacement given the scenario seismic inputs, y is a specified displacement threshold, L is the triggering of liquefaction, and P_L is the probability of liquefaction triggering given the scenario seismic inputs.

The probability of liquefaction triggering, P_L, can be computed using the liquefaction potential curves developed by Cetin et al. (2004) for SPT-based data, and Moss et al. (2006) for CPT-based data. Both of these methods require identification of the critical layer in the site profile that is most susceptible to liquefaction. After identification of this layer, we solve for the probability of liquefaction triggering based on the geotechnical properties of the critical layer. For SPT-based data, the necessary geotechnical data describing the critical layer are: clean sand-equivalent corrected SPT blow counts, $N_{1,60,cs}$, the effective stress, σ'_v, total stress σ_v, and depth to the critical layer, *d*. For CPT-based data, the necessary geotechnical data describing the critical layer are:

normalized cone tip resistance, $q_{c,1}$, friction ratio, R_f, stress normalization coefficient, c, σ'_v, σ_v, and d. These SPT and CPT factors are discussed later.

To estimate the probability of lateral spread displacement exceeding a specified threshold given liquefaction ($P[D_H > y \mid LJ]$) from available data, we found it necessary to develop a new empirical lateral spread model (Gillins and Bartlett 2012). We developed the new model by revising the Youd et al. (2002) empirical model such that it is more parsimonious and implementable for regional hazard analysis. This new model is shown as two equations. Eqn. (4.2) is for gently sloping ground conditions, and eqn. (4.3) is for free-face conditions (e.g., presence of a river channel or steep topographical depression, Bartlett and Youd 1992).

$$\overline{Log(D_H)} = \begin{pmatrix} -8.453 + 1.348 \cdot M_w - 1.068 \cdot Log(R^*) - 0.017 \cdot R + 0.334 \cdot Log(S) + \\ +0.588 \cdot Log(T_{15,cs}) + 0.278 \end{pmatrix} \quad (4.2)$$

$$\overline{Log(D_H)} = \begin{pmatrix} -8.795 + 1.348 \cdot M_w - 1.068 \cdot Log(R^*) - 0.017 \cdot R + 0.453 \cdot Log(W) + \\ +0.588 \cdot Log(T_{15,cs}) + 0.278 \end{pmatrix} \quad (4.3)$$

where $\overline{Log(D_H)}$ is the mean value of the logarithm (base 10) of the lateral spread displacement (D_H is in meters), M_w is the moment magnitude of the earthquake, R is the nearest mapped distance from the site to the seismic energy source (km), W is the ratio of the height of the free-face to the horizontal distance between the base of the free-face and the point of interest (%), S is the ground slope (%), and R^* is a nonlinear magnitude-distance function calculated by $R^* = R + 10^{0.89 \cdot M_w - 5.64}$.

As can be seen, the model listed in eqns. (4.2) and (4.3) is a function of one geotechnical variable: $T_{15,cs}$, which can be defined by eqn. (4.4).

$$T_{15,cs} = T_{15} \cdot 10^{\wedge}\left(\frac{-0.647 \cdot x_1 - 0.176 \cdot x_2 + 0.278 \cdot x_3 + 0.032 \cdot x_4 - 0.571 \cdot x_5 - 0.278}{0.588}\right) \quad (4.4)$$

where T_{15} is the cumulative thickness in the upper 15 meters of the site profile that is susceptible to lateral spread (i.e., saturated, cohesionless, and with corrected SPT blows counts, $N_{1,60} \leq 15$), and x_n is the respective ratios of T_{15} with a soil indices, SI, equal to n. Table 4.2 defines SI as a function of the description or classification of a layer of soil. For example, if a T_{15} layer is 30% coarse, gravelly sand and 70% clean sand, then x_2 is 0.3 and x_3 is 0.7. (Note that we consider soil with $SI \geq 6$ as not susceptible to liquefaction; thus, x_6 and x_7 do not appear in eqn. 4.4.)

There are several advantages to using this new empirical model for analysis of lateral spread hazards at a regional scale. First, it uses data routinely collected in the field and reported on the borehole logs. Second, it has a coefficient of determination, R^2 = 80.0%, which is only 3.6% less than that found for the model of Youd et al. (2002). Finally, CPT data can be used in conjunction with the new model, as described in greater detail in Gillins and Bartlett (2012).

Based on eqns. (4.2) and (4.3), we solve for the probability of lateral spread exceeding a displacement threshold, y, given liquefaction, by eqn. (4.5).

Table 4.2. Definition of soil indices and their modeled distributions of dry unit weight, specific gravity, and water content

SI	Soil Description from Borehole Log	$\overline{Log(w)}$ (w in %)	$\sigma_{Log(w)}$	$\overline{G_s}$	σ_{G_s}	$\overline{\gamma_d}$ (pcf)	σ_{γ_d}
1	Silty gravel, gravel with fines	0.998	0.075	2.67	0.01	107.5	7.3
2	Very coarse to coarse sand, gravelly sand	1.294	0.075	2.67	0.01	98.4	7.3
3	Medium to fine clean sand, sand with some silt	1.294	0.075	2.67	0.01	98.4	7.3
4	Very fine sand, silty sand, sand with silt, dirty sand, silty/clayey sand	1.384	0.075	2.67	0.01	98.4	7.3
5	Sandy silt, silt with sand, silt	1.424	0.075	2.65	0.02	93.3	7.3
6	Silty clay, lean clay	1.467	0.183	2.72	0.02	93.3	7.3
7	Fat clay	1.531	0.183	2.62	0.02	86.2	7.3

$$P[D_H > y \mid L] = \Phi\left(-\frac{Log(y) - \overline{Log(D_H)}}{\sigma_{Log(D_H)}}\right) \tag{4.5}$$

where Φ is the standard cumulative normal distribution; and, $\sigma_{Log(DH)}$ is the standard deviation of the predicted variable for eqns. (4.2) and (4.3), which equals 0.218.

In summary, we solve eqn. (4.1) as a function of certain geotechnical properties. For SPT-based data, it is a function of. ($N_{1,60,cs}$, σ'_v, σ_v, d, $T_{15,cs}$). For CPT-based data, it is a function of ($q_{c,1}$, R_f, c, σ'_v, σ_v, d, $T_{15,cs}$). We name these geotechnical variables the "critical datasets", and solve for them at each SPT borehole and CPT sounding. Then, we

group each critical dataset according to their corresponding geologic unit. Since σ'_v, σ_v, and d, are strongly correlated, we will treat each individual critical dataset as an equally likely outcome when sampling within its geologic unit. The next two sections of this paper describe how we solved for the critical datasets, and accounted for their uncertainty.

SPT Data

Cetin et al. (2004) developed probabilistic liquefaction potential curves based on SPT data and a Bayesian framework, and produced a composite equation (eqn. (4.6)) to model these curves. We used this equation to estimate P_L for every layer in an SPT borehole, and then set the layer with the largest value of P_L as the critical layer for the site. After identification of the critical layer, we solved for its critical dataset: ($N_{1,60,cs}$, σ'_v, σ_v, d, $T_{15,cs}$).

$$P_L = \Phi\left(-\frac{N_{1,60,cs} - 13.32\cdot\ln(CSR) - 29.53\cdot\ln(M_w) - 3.70\cdot\ln(\sigma'_v) + 16.85}{2.70}\right) \qquad (4.6)$$

where a_{max} is the peak horizontal ground surface acceleration (in units of gravity), CSR is the equivalent uniform cyclic stress ratio, and σ'_v is in units of atmospheres (atm).

We used definitions by Cetin et al. (2004) to correct raw SPT blow counts, N, to values of $N_{1,60,cs}$ (eqns. (4.7) and (4.8)).

$$N_{1,60,cs} = \begin{cases} N_{1,60} & \text{for } FC < 5\% \\ N_{1,60} \cdot (1 + 0.004 \cdot FC) + 0.05 \cdot FC & \text{for } 5 \le FC \le 35\% \\ 1.14 \cdot N_{1,60} + 1.75 & \text{for } FC > 35\% \end{cases} \quad (4.7)$$

$$N_{1,60} = N \cdot C_n \cdot C_R \cdot C_s \cdot C_B \cdot C_E \quad (4.8)$$

where FC is the fines content (%), C_n is the correction for overburden pressure, C_R is the correction for rod length, C_S is the correction for sampler configuration, C_B is the correction for borehole diameter, and C_E is the correction for hammer energy ratio.

We identified C_E as a major source of uncertainty. The hammer energy ratio is the ratio of the actual versus theoretical SPT impact hammer energy transmitted to the sampler. This ratio is a function of actual hammer drop distance, sliding friction between the hammer and the rods, number of loops of the rope around the cathead, rope conditions, etc. It is best practice to directly measure the impact energy transmitted with each blow of the hammer during the SPT, or to use a well calibrated mechanical hammer release system. Unfortunately, even if these practices were used, they are not mentioned in the reports of the SPT data in Weber County. Hence, we defined C_E for each borehole as a normally distributed random variable with mean, $\overline{C_E}$, and standard deviation, σ_{CE}. For the safety hammer, we set $\overline{C_E}$ = 1.0 and σ_{CE} = 0.1; and for the automatic hammer, we set $\overline{C_E}$ = 1.1 and σ_{CE} = 0.1. These parameters are based on the recommended range of values from Cetin et al. (2004).

Another major source of uncertainty is FC. Often, many of the cohesionless layers in each borehole lacked measurements of FC. To fill in these missing data, we

estimated distributions of FC according to soil type (or SI). Distributions of FC according to SI from data in Weber County are approximately uniform and conformed well to definitions from the Unified Soil Classification System (USCS). Therefore, we modeled the following uniform distributions: for $SI = 1 - 3$, $FC = 0 - 12\%$; for $SI = 4$, $FC = 12 - 50\%$, and for $SI = 5$, $FC = 50 - 95\%$. Since we consider layers with $SI \geq 6$ as not susceptible to liquefaction, we did not fill in their missing FC data.

In addition to many of the layers lacking FC, numerous layers within the boreholes lacked measurements of soil unit weight and water content. We find that these properties can be estimated reasonably well, resulting in minor uncertainty in the stress profile. We filled in these missing data by estimating distributions of dry unit weight, γ_d, water content, w, and specific gravity, G_s, according to values of SI for the layer. Distributions of γ_d per SI in Weber County are normally distributed with equal variance, according to statistical F-tests. Table 4.2 lists normal parameters fitted to these distributions. Distributions of w per SI in Weber County are lognormally distributed with unequal variance, according to statistical F-tests. Table 4.2 lists lognormal parameters fitted to these distributions. Although there are limited G_s data in Weber County, the variability of G_s is typically small. Bowles (1996) lists typical ranges of values for G_s according to soil type. Based on these ranges, we modeled G_s according to the normal parameters listed in Table 4.2.

Due to the uncertainty of several of the input variables (specifically C_E, FC, γ_d, w, and G_s), we solved for the critical dataset in an SPT borehole by the Monte Carlo method. In this method, we randomly sample from all of the distributions of the input variables and compute the result. We then repeat this process numerous times until we have used

enough combinations of the input random variables to define the distribution of the results. We model the random sampling of a uniformly distributed random variable, R_u, by eqn. (4.9).

$$R_u = a + (b - a) \cdot rand(1) \tag{4.9}$$

where a and b are the lower and upper bounds of the uniform distribution of a random variable, respectively, and *rand* is a function that generates random values between 0 and 1.

Similarly, we model the random sampling of a normally distributed random variable, R_n, by eqn. (4.10).

$$R_n = \mu + \sigma \cdot randn(1) \tag{4.10}$$

where μ and σ are the mean and standard deviation parameters of the normal distribution of the random variable, respectively, and *randn* is a function that generates random values from the standard normal distribution.

We found that after 300 Monte Carlo simulations, we have adequately defined the distribution of each variable in the critical dataset at a borehole. Figure 4.2 depicts empirical cumulative distribution functions (CDFs) of each variable in the critical dataset at SPT borehole no. 11 of the Weber County geotechnical database. This figure shows CDFs after 10, 100, 300, 500, and 1000 Monte Carlo random sampling simulations. As can be seen, the CDFs converge after 300 simulations. Therefore, we set 300 as the

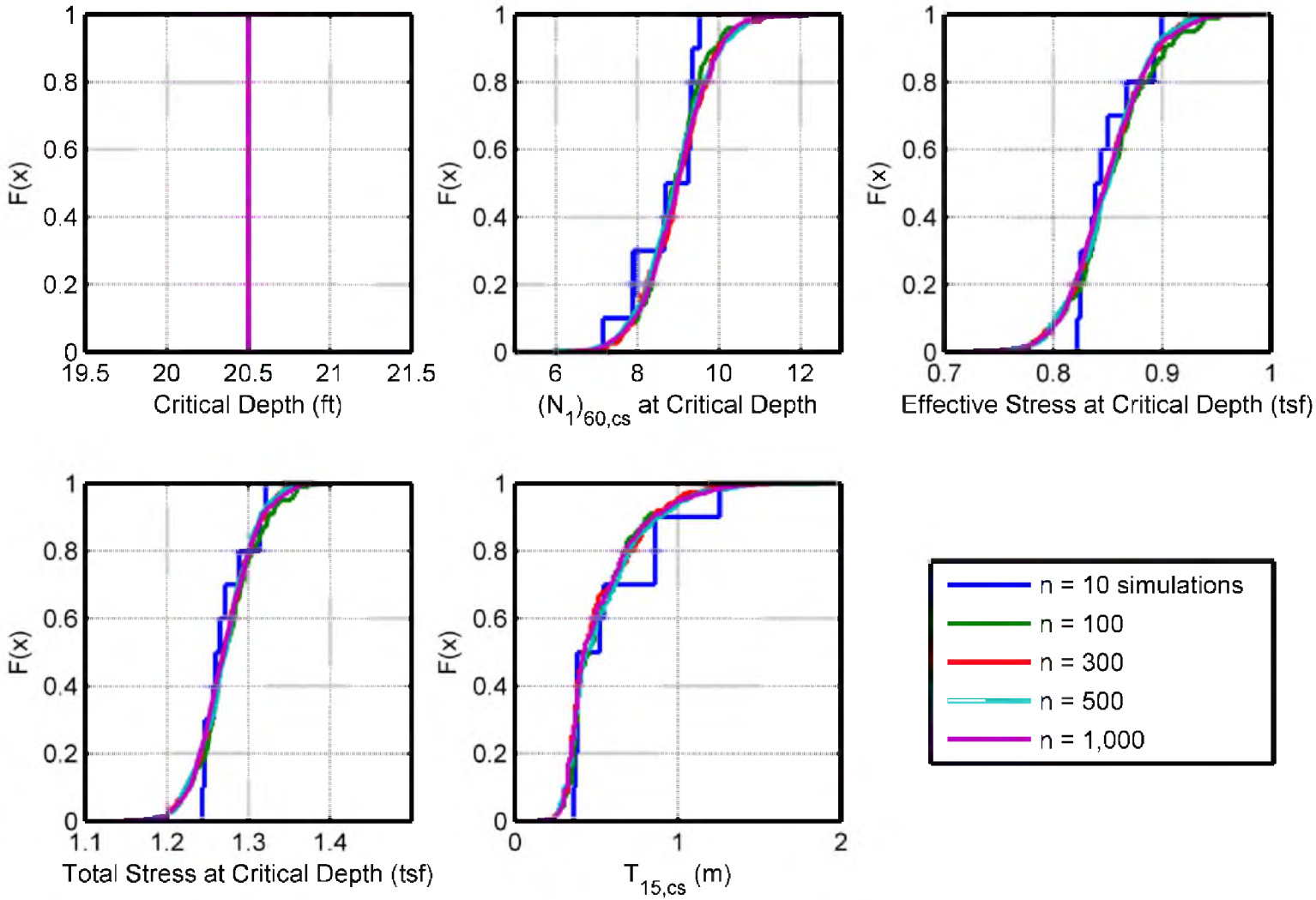

Figure 4.2. Cumulative distribution functions of the critical dataset at SPT site no. 11. The distributions converge after 300 Monte Carlo simulations

necessary number of simulations to ensure definition of the uncertainty of the critical dataset at each SPT borehole. Since σ'_v, σ_v, and d are strongly correlated, we treat each of the 300 individual critical datasets as an equally likely outcome at the SPT borehole.

CPT Data

Moss et al. (2006) developed probabilistic liquefaction potential curves based on CPT data and a Bayesian framework, and produced a composite equation (eqn. (4.11)) to model these curves. Similar to methods presented herein for SPT data, we used this equation to estimate P_L for every layer in a CPT sounding, and then set the layer with the largest value of P_L as the critical layer for the site. After identification of the critical layer, we solve for the critical dataset of the layer: ($q_{c,1}$, R_f, c, σ'_v, σ_v, d, $T_{15,cs}$).

$$P_L = \Phi\left(-\frac{\begin{array}{c} q_{c,1}^{1.045} + q_{c,1}(0.110 \cdot R_f) + (0.001 \cdot R_f) + c(1 + 0.850 \cdot R_f) + \\ -7.177 \cdot \ln(CSR) - 0.848 \cdot \ln(M_w) - 0.002 \cdot \ln(101.325 \cdot \sigma'_v) - 20.923 \end{array}}{1.632}\right) \quad (4.11)$$

where q_c and $q_{c,1}$ are in MPa, R_f is in %, and σ'_v is in atm.

Moss et al. (2006) presented a method to iterate for the stress normalization exponent, c, as a function of $q_{c,1}$ and R_f. Their procedure is based on cavity expansion models used in conjunction with field and laboratory test data. We use their method to find c, and correct raw values of CPT tip resistance, q_c, to values of $q_{c,1}$.

To solve for the stress profile in a CPT sounding, we must estimate soil unit weights. As mentioned in the analysis of SPT data, we found that this type of data can be

estimated reasonably well, and has little uncertainty. However, to conform to SPT-based methods, we model this minor uncertainty by relating the in situ soil behavior measured by the CPT (termed the Soil Behavior Type, SBT) to values of *SI*. Numerous researchers have found that soil classification or type relates well with CPT-based SBT (e.g., Molle 2005). Robertson (2009) introduced a non-normalized chart to estimate SBT based on raw measurements of q_c and R_f. The boundaries of the non-normalized SBT chart can be modeled by concentric circles with radius equal to the soil behavior type index, I_{SBT}, defined by eqn. (4.12).

$$I_{SBT} = [(3.47 - Log(q_c))^2 + (Log(R_f) + 1.22)^2]^{0.5} \tag{4.12}$$

where q_c is in atm and R_f is in %.

Robertson (2009) states that in general, normalized SBT charts provide more reliable identification of SBT than non-normalized charts. However, he also reports that, when the in situ vertical effective stress is between 50 kPa to 150 kPa, there is little difference. Since liquefaction is a shallow phenomenon, and since we are only accounting for the minor uncertainty in the stress profile, we use values of non-normalized SBT to model distributions of γ_d, w, and G_s. Table 4.3 lists how to compute SBT from I_{SBT}, and describes each SBT zone. We linked values of SBT to *SI* according to similar descriptions. Then, using these links, we assigned the distribution parameters for γ_d, w, and G_s to corresponding layers of sediment. We only used these links to estimate the uncertainty in the stress profile at each CPT sounding.

Table 4.3. Definition of SBT by I_{SBT}, and approximate correlation to *SI* for estimating soil parameters

I_{SBT}	SBT Zone	SBT Description	$\approx SI$
$I_{SBT} \leq 1.31$	7	Gravelly sand	2
$1.31 < I_{SBT} \leq 2.05$	6	Sands-clean sand to silty sand	3
$2.05 < I_{SBT} \leq 2.60$	5	Sand mixtures- silty sand to sandy silt	4
$2.60 < I_{SBT} \leq 2.95$	4	Silt mixtures – clayey silt to silty clay	5
$2.95 < I_{SBT} \leq 3.60$	3	Clays	6
$I_{SBT} > 3.60$	2	Organic soils - peats	7

Gillins and Bartlett (2012) provide a general equation (eqn. (4.13)) and method to compute the probability of *SI* given values of normalized soil behavior type index, I_c. We recommend this equation for developing most relationships between *SI* and CPT-based SBT. There are many advantages to calculating the probabilities of soil type from CPT-based data. For one, we can define the major uncertainty in estimating soil type by CPT. The probabilities found from eqn. (4.13) can also be used directly as values of $x_1 - x_5$ in eqn. (4.4) to find $T_{15,cs}$ at a CPT sounding.

$$P[SI = i \mid I_c] = \frac{\mathrm{N}(\overline{I_{ci}}, s^2_{Ici})}{\sum_{i=1}^{M} \mathrm{N}(\overline{I_{ci}}, s^2_{Ici})} \tag{4.13}$$

where N is the normal probability density function of I_c, with mean, $\overline{I_c}$, and variance, s^2_{Ic}, for a value of *SI* equal to *i*.

To implement eqn. (4.13), we recommend developing distributions of I_c per *SI* using data specific to the study area. For example, in this mapping project, we compiled

available "pairs" of side-by-side SPT borings and CPT soundings in Weber County into a database. From this, there are 205 samples that were classified according to the USCS from laboratory measurements. Based on these evaluations, we assigned the samples a value of *SI*. In addition, at the depth intervals where these samples were taken, we found the median value of I_c from the adjacent CPT soundings. From statistical tests, the distributions of I_c per *SI* are normally distributed with unequal means and unequal variances (except for *SI* = 1 and 3). We fit normal probability density functions to these distributions for each *SI*, and found their mean, $\overline{I_c}$, and variance, s^2_{Ic}. For a full description of this process, refer to Gillins and Bartlett (2012). Since the database lacked samples with *SI* = 2 and *SI* = 7 (these soil types are very sparse in the Weber County geotechnical database), it was not possible to develop their probability density functions.

Zhang et al. (2002) most recently defined I_c based on the normalized $Q_t - F_R$ SBT chart of Robertson (1990). Similar to I_{SBT}, I_c is the radius of concentric circles that approximate the boundaries of the normalized SBT chart (eqn. (4.14)).

$$I_c = [(3.47 - Log(Q_{tn}))^2 + (Log(F_R) + 1.22)^2]^{0.5} \tag{4.14}$$

where Q_{tn} is the normalized cone tip resistance (in atm), and F_R is the normalized friction ratio (%).

In addition to the uncertainty with estimating soil type from CPT, another major source of uncertainty is from estimating SPT blow counts, $N_{1,60}$, from CPT. Per eqn. (4.4), $T_{15,cs}$ is a function of T_{15} (i.e., the thickness of saturated, cohesionless soil in the upper 15 meters of a site profile with $N_{1,60} \leq 15$) As described in Gillins and Bartlett

(2012), we found a linear relationship between SPT blow counts and CPT data in Weber County (eqn. (4.15)).

$$\overline{Log(q_t / N_{60})} = 1.26 - 0.295 \cdot I_c \tag{4.15}$$

where q_t is the cone tip resistance corrected for pore-pressure effects (atm), and N_{60} = $N_{1,60}$ / C_n. For this relationship, R^2 = 61.6% and the standard deviation of the predicted variable, $\sigma_{Log(qt / N60)}$ = 0.156.

Similar to the SPT-based approach, we solved for the critical dataset at each CPT sounding by the Monte Carlo method. We modeled the variables with uncertainty (specifically γ_d, w, G_s, and $Log(q_t / N_{60})$) as normally distributed random variables with normal parameters μ and σ (eqn. (4.10)). Like the SPT-based approach, we found that 300 Monte Carlo simulations adequately defined the distribution of each variable in the critical dataset at a CPT sounding. Again, since σ'_v, σ_v, and d are strongly correlated, we treat each of the 300 individual critical datasets as an equally likely outcome at the CPT sounding.

Critical Dataset Distributions by Geologic Unit

Previous researchers (Youd and Perkins 1978, Bartlett and Olsen 2005, Holzer 2006) found that general engineering properties of soils are similar within geologic units. The reduction of SPT and CPT data enables quantitative description of the distribution of geotechnical properties for a geologic unit. This improves understanding of the susceptibility of a unit to liquefaction-induced ground failure.

Aforementioned models to estimate probabilities of liquefaction hazards are functions of certain geotechnical variables we call "critical datasets". In the previous two sections, we described how we solved for the distribution of each variable in the critical dataset at an individual SPT borehole or CPT sounding. To define the distribution of each variable in the critical dataset for a geologic unit, we simply pool the critical datasets of the SPT and CPT investigations within the unit. Since variables in each critical dataset are correlated, and since we simulated 300 possible outcomes of datasets by the Monte Carlo method at each SPT and CPT investigation, pooling data by geologic unit results in very long lists of datasets.

To visualize and analyze the dispersion of the pooled geotechnical data by geologic unit, it is desirable to relate the CPT data ($q_{c,1}$, R_f, *and* c) to the SPT data ($N_{1,60,cs}$). We accomplish this by first, rearranging eqns. (4.6) and (4.11) for *CSR*. We then set these two rearranged equations equal to each other, and solve for $N_{1,60,cs}$ – thereby relating CPT-based data for liquefaction analysis to SPT-based data. Eqn. (4.16) is the complete solution for $N_{1,60,cs}$, as a function of $q_{c,1}$, R_f, c, σ'_v, M_w, and P_L.

$$N_{1,60,cs} = \frac{1.856\left[q_{c,1}^{1.045} + q_{c,1}(0.110 \cdot R_f) + 0.001 \cdot R_f + c(1 + 0.850 \cdot R_f)\right] + }{+3.696 \cdot \ln(\sigma'_v) + 27.956 \cdot \ln(M_w) - 55.712 + 0.329 \cdot \Phi^{-1}(P_L)} \qquad (4.16)$$

To simplify eqn. (4.16) for this study, we found the controlling earthquake magnitude for a 2,500-year return period event is approximately equal to 7, with small variation. In addition, the $\Phi^{-1}(P_L)$ term in eqn. (4.16) has a small coefficient; hence, the total variability of P_L will result in only small variability in $N_{1,60,cs}$. Varying P_L from 0.01

– 0.99 results in a total variability of only 1.530 blows. By inserting M_w = 7, and an average value of P_L into eqn. (4.16), we approximated $N_{1,60,cs}$ from CPT-based data by eqn. (4.17).

$$N_{1,60,cs} \approx \begin{array}{c} 1.856\left[q_{c,1}^{1.045} + q_{c,1}(0.110 \cdot R_f) + 0.001 \cdot R_f + c(1 + 0.850 \cdot R_f) \right] + \\ +3.696 \cdot \ln(\sigma'_v) - 1.294 \pm 0.765 \end{array} \quad (4.17)$$

We used eqn. (4.17) to convert the CPT data to SPT data, and produced frequency histograms of geotechnical properties according to geologic unit. Figure 4.3 is an example of such histograms for modern stream alluvium, Qal_1 in Weber County.

We produced the same set of histograms for each geologic unit listed in Table 4.1 that has a minimum SPT/CPT sample size of 9 (note: a complete set of histograms are available in the appendix of Gillins 2012). The histograms like in Figure 4.3 allow visual exploration of the data: enabling recognition of patterns or trends, and comparison between geologic units. Visual analysis is often better than any kind of statistical test of the dispersion of the data. For instance, Figure 4.3a depicts two sets of frequency plots for quick interpretation of the susceptibility of Qal_1 to liquefaction-induced lateral spread. The first set shows that 98.7% of the SPT and CPT investigations within this unit found a critical layer – a layer that is saturated and cohesionless in the upper 15 meters of the site profile. Only a small percentage of the investigations could not identify a critical layer because either the site profile was entirely cohesive, or the groundwater table was too deep (below 15 meters). The second set of histograms in Figure 4.3a show that 51.4% of the critical datasets had a value of $T_{15} > 0$. In other words, just under half of the datasets

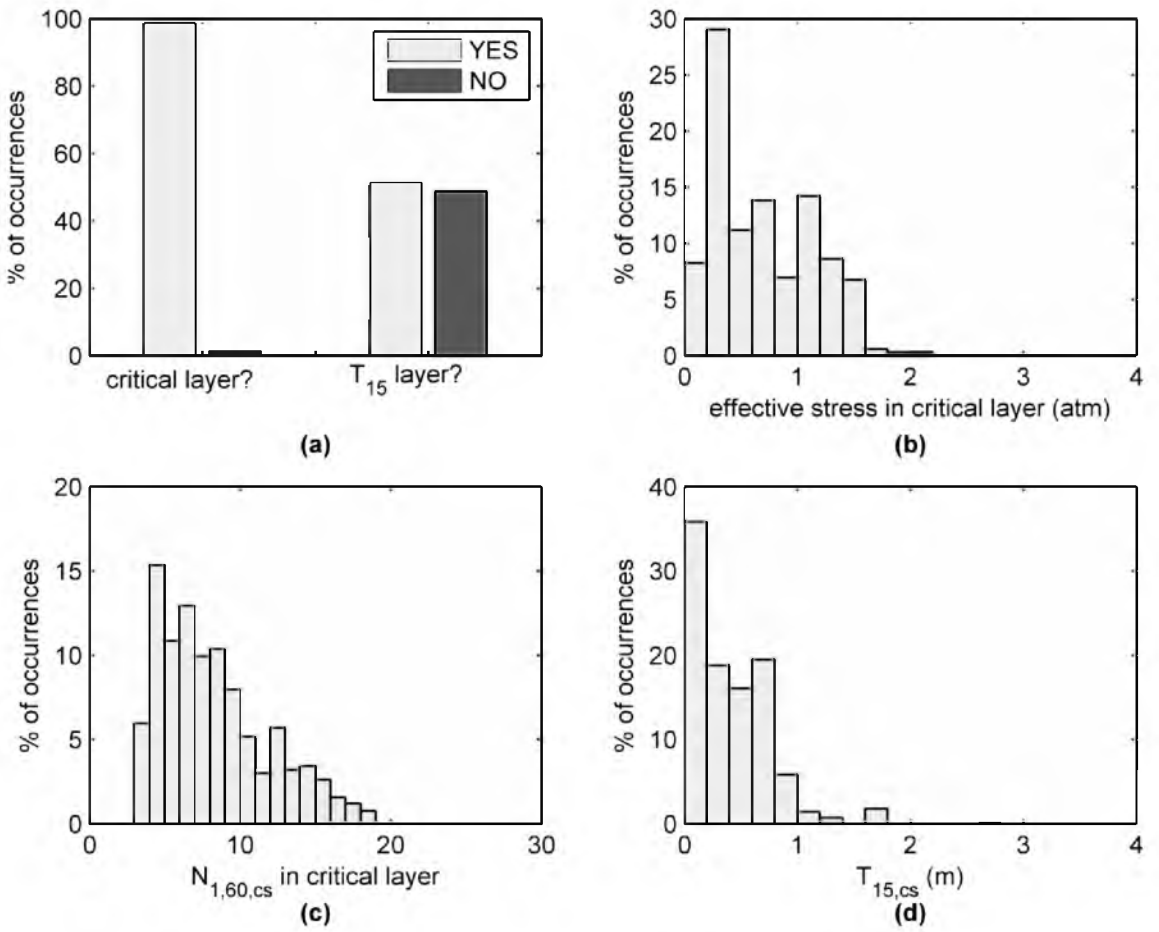

Figure 4.3. Histograms of critical dataset variables for Qal_1; Weber County, Utah. Note subplots (b) – (d) are for critical datasets where $T_{15} > 0$

from the investigations have $T_{15} = 0$. Of course, we are most concerned with that portion of the datasets with $T_{15} > 0$; hence, Figure 4.3b – d shows frequency histograms of values of σ'_v, $N_{1,60,cs}$, and $T_{15,cs}$ for critical datasets where $T_{15} > 0$, respectively. As can be seen, each of these three distributions is approximately lognormally distributed. Most of the values (96.0%) of $T_{15,cs}$ are between 0 – 1 meter, with a median value equal to 0.3 meters. Based on these quantitative geotechnical properties, it appears that Qal_1 is susceptible to liquefaction and lateral spread. On the other hand, similar to Figure 4.3a, Figure 4.4 depicts frequency histograms for (a) alluvial fan, Qaf; and (b), North Ogden landslide

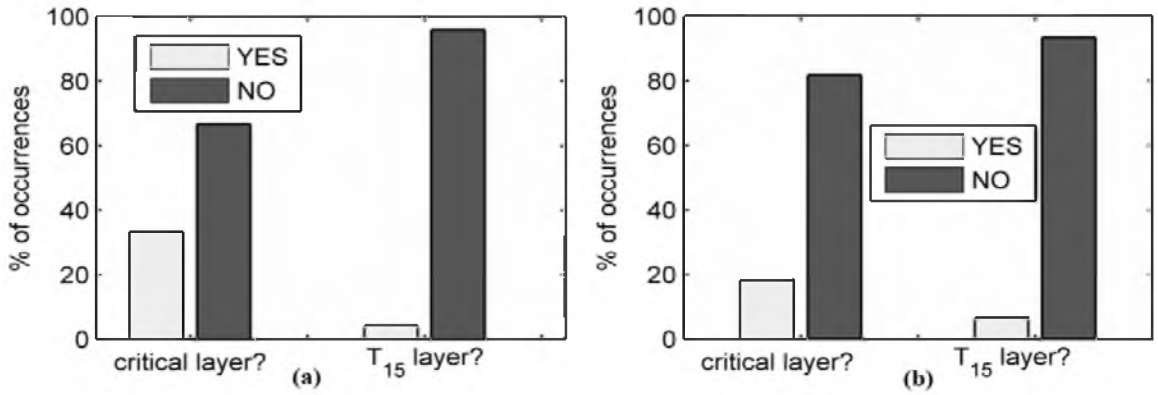

Figure 4.4. Frequency of occurrences of $T_{15} > 0$ for (a) Qaf, and (b) Qmq_2; Weber County, Utah

complex deposits, Qmq_2. As can be seen, neither of these units have a significant percentage of critical datasets with $T_{15} > 0$. Mostly, this is due to very dense, fine, or cohesive sediments found in the borehole studies in these units. Therefore, based on these data, it appears that the Qaf and Qmq_2 units have little to no susceptibility to lateral spread.

Analysis of Dispersion by Geologic Deposit

In the previous section, we described a method to pool and visually explore geotechnical data from individual SPT and CPT tests according to geologic unit. In addition, we described how to convert CPT-based data to approximately equivalent SPT-based data. With a sufficient amount of SPT and CPT investigations, it is possible to quantitatively describe the distribution of geotechnical properties within a geologic unit. Unfortunately, when mapping liquefaction hazards at a regional scale, especially from available data, there is often insufficient sampling of every geologic unit in a study area. To account for insufficient sampling, it is desirable to pool data for geologic units with

similar geotechnical properties. Pooling data increases the robustness of the sampling, thereby improving estimates of the variability of the geotechnical properties within a geologic unit.

We pool data by inductive reasoning, starting with the hypothesis that geologic units of similar depositional environment have similar critical datasets. Then, we analyze the dispersion of the critical datasets for each unit within a depositional environment, and examined visually and through statistical tests (such as multivariate analysis of variance, MANOVA) if our hypothesis cannot be rejected. If our hypothesis cannot be rejected at a certain significance level, then we conclude that it is appropriate to pool the data.

We found through such reasoning, that it is appropriate to pool critical datasets from geologic units of similar depositional environment. Table 4.1 lists how we pooled data from similar geologic units into 11 deposit classes. As can be seen, pooling data into these 11 classes greatly increases the sample size of SPT and CPT investigations for each unit and the robustness of the statistical analysis. The rest of this section describes the methodology for analyzing the dispersion of critical datasets within units of similar deposit type.

First, for each deposit, we compared the frequency histograms of $T_{15} = 0$ versus $T_{15} > 0$ between geologic units (e.g., Figure 4.3a or Figure 4.4). For the delta units, there are similarly high percentages of occurrences in the critical datasets where $T_{15} > 0$: 100% for Qd_2, 85.2% for Qd_3, 95.5% for Qd_4, and 100% for Qd_5. For stream alluvium units, there are similarly medium percentages of occurrences where $T_{15} > 0$: 51.4% for Qal_1, and 65.1% for Qal_2. And for coarse-grained lacustrine units, there are similarly low percentages of occurrences where $T_{15} > 0$: 16.1% for Qlg_3, and 25.8% for Qlg_4.

Second, we compared the distribution of geotechnical variables for critical datasets with $T_{15} > 0$. Figure 4.5 depicts scatter plots in log-log scale of median values of $N_{1,60,cs}$ (or approximate $N_{1,60,cs}$ from CPT data per eqn. (4.17)) versus $T_{15,cs}$ from SPT and CPT investigations (with $T_{15} > 0$). The data points are plotted in subplots according to deposit class, and symbolized according to geologic unit. Figure 4.5a shows that stream alluvium data from the Qal_1 and Qal_2 units in Weber County are very similar, since there are not any distinct patterns separating them.

Similarly, Figure 4.5b shows that deltaic data plot in the same region, without distinctness between the units in Weber County. Figure 4.5c – d depicts data for fine-grained and coarse-grained lacustrine, respectively, from investigations in both Weber and Salt Lake Counties. There are insufficient sample sizes for some of the lacustrine units; however, it appears from the small samples that they could be similar. We postulate that these units are similar based on the finding that the stream alluvium and delta units are similar.

Finally, because there are adequate sample sizes of numerous units within the stream alluvium and delta deposits, it is possible to perform one-way MANOVA of each unit to statistically test our hypothesis. One-way MANOVA compares the mean vectors of two or more groups of multivariate data, and tests the null hypothesis that the means are the same. The test assumes the independent variables are approximately normally distributed and not heavily correlated. Therefore, we analyzed the following geotechnical variables for a geologic unit: Log($N_{1,60,cs}$), Log($T_{15,cs}$), and Log(σ'_v). We compared 16^{th}, 50^{th}, and 84^{th} percentile values at all subsurface investigations where $T_{15} > 0$. The 50^{th} percentile value is the median value of these three variables at a SPT or CPT.

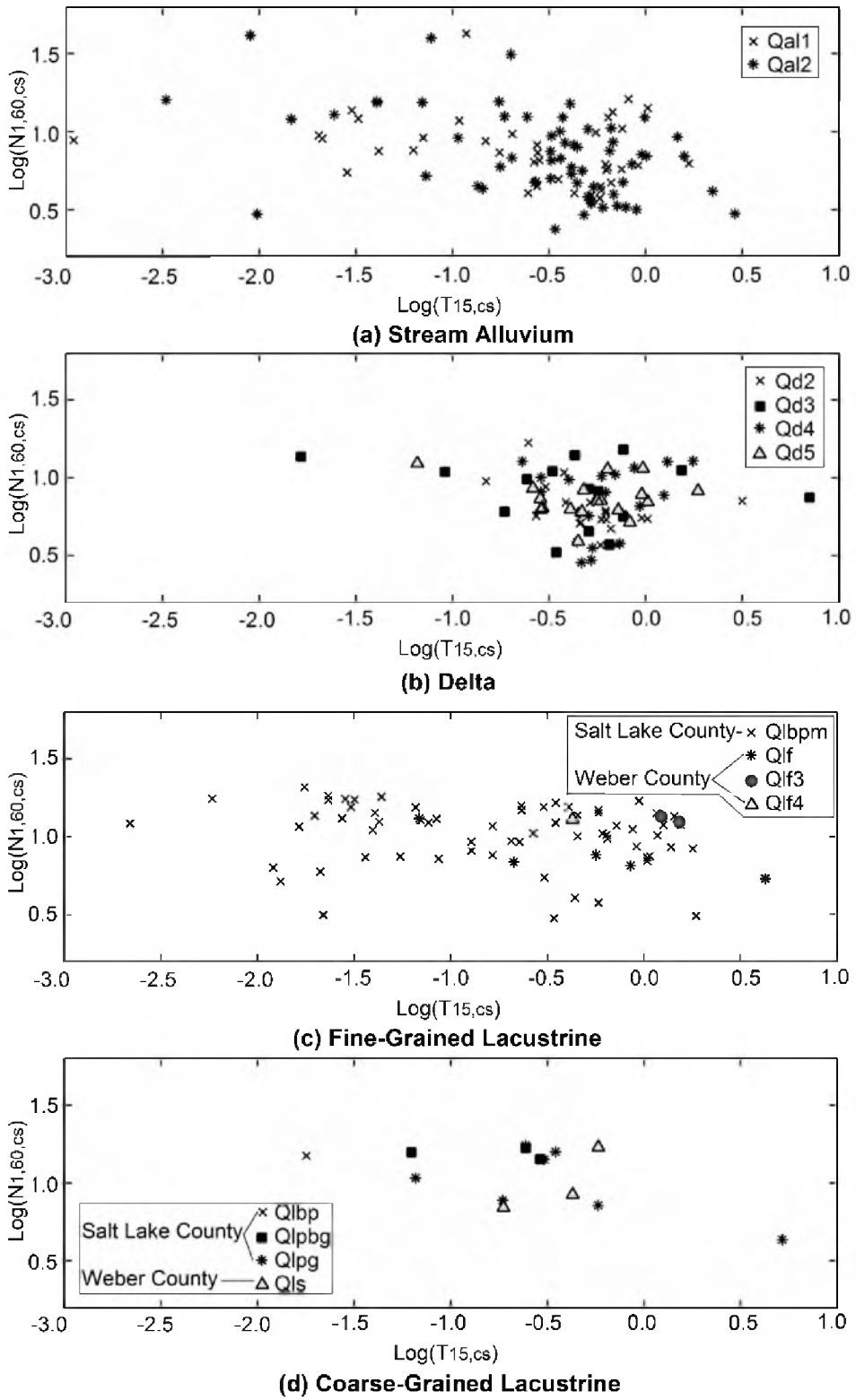

Figure 4.5. Scatter plots of median values of $N_{1,60,cs}$ vs. $T_{15,cs}$ according to geologic deposit, at sites where $T_{15} > 0$, for (a) stream alluvium and (b) delta in Weber County only, (c) fine-grained lacustrine and (d) coarse-grained lacustrine in shown counties

The 16th and 84th percentile values approximate the mean minus and mean plus one standard deviation values, respectively.

Table 4.4 summarizes the results of the MANOVA tests for the stream alluvium units, Qal_1 and Qal_2. As can be seen, results are similar for all 3 percentile values from the SPT and CPT investigations. At every percentile, the determinant of the within-unit dispersion, $|\mathbf{W}|$, is approximately equal to the determinant of the total dispersion of both units, $|\mathbf{T}|$. The ratio of these determinants, $|\mathbf{W}| / |\mathbf{T}|$, is equal to Wilks's Criterion (Wilks 1932), L. If L is equal to 1, then **W** and **T** are the same and there are no differences between the units. We find $L = 0.99$ at every percentile. From Wilks's work, we transform L such that it is distributed approximately as χ^2 with 3 degrees of freedom, enabling estimation of the significance of L. For every percentile, we find large significance values ($P = 0.71 - 0.77$) that the null hypothesis cannot be rejected. For additional interest, the Mahalanobis distance between the units, D, is only equal to 0.05-0.06. Hence, we conclude that the subclassification of the two units, Qal_1 and Qal_2, achieves nearly nothing in terms of the critical datasets. Therefore, we pooled the critical datasets from Qal_1 and Qal_2 into a single dataset.

Table 4.4. Summary of MANOVA results with 3 degrees of freedom for Qal_1, Qal_2; Weber County, Utah.

	Percentile variables from SPT/CPT		
	16th	50th	84th
$\|\mathbf{W}\|$	1.27×10^3	1.34×10^3	1.93×10^3
$\|\mathbf{T}\|$	1.29×10^3	1.35×10^3	1.95×10^3
L	0.99	0.99	0.99
χ^2	1.26	1.12	1.38
P	0.74	0.77	0.71
D	0.06	0.05	0.05

Figure 4.6 displays graphically the results of the MANOVA tests for stream alluvium and delta deposits at the 50^{th} percentile. Figures of this type aid in visually examining how similar or different the units are from one another. To produce this figure, we rotated the axes of the independent variables into canonical axes. In canonical space, confidence ellipses that represent the distributions within the units become circles. For this figure, we plotted 90% confidence circles of the data on the first two canonical axes. As can be seen from Figure 4.6a, the confidence circles nearly perfectly overlap for the stream alluvium units, at the 50^{th} percentile. We find the same results at the 16^{th} and 84^{th} percentile; thus, there is nearly no distinctness between the two units. Similarly, Figure 4.6b shows significant overlap of the circles for all of the delta units. It appears that Qd_3 is the most different unit; however, it is not significantly different than the other units. We conclude that the classification of the 4 delta units achieves little in terms of the critical datasets. Therefore, we pooled the critical datasets from $Qd_2 - Qd_5$.

Accounting for the Influence of Age

Several investigators have noted that liquefaction resistance of soils increases with age. Youd and Perkins (1978) noted that older Holocene sediments are generally less susceptible to liquefaction than sediments deposited within the past few thousand years, and Pleistocene sediments are even less susceptible. Although these increases have been noted, factors causing increased liquefaction with age are poorly understood (Youd et al. 2001). Researchers have not found explicit evidence to fully explain the mechanisms behind the phenomenon known as aging (Leon et al. 2006). Past research has focused primarily on chemical and mechanical mechanisms (Leon et al. 2006).

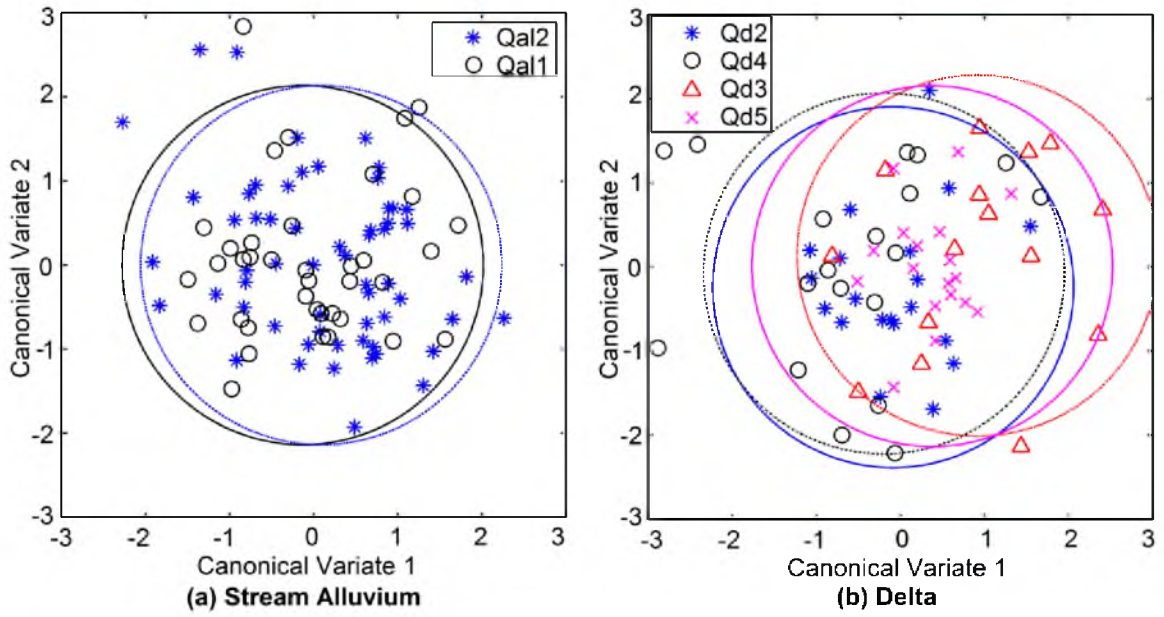

Figure 4.6. Scatter of median values of σ'_v, $N_{1,60,cs}$, and $T_{15,cs}$ at sites where $T_{15} > 0$, on planes of canonical axes for (a) stream alluvium and (b) delta, with 90 % confidence circles; Weber County

Mitchell and Solymar (1984) suggested that aging is a result of chemical mechanisms such as the formation of silica acid gel on particle surfaces and silica precipitates from the water table over time. These precipitates may cause cementing bonds at interparticle contacts. Schmertmann (1987) suggested that aging is a result of mechanical mechanisms such as processes that take place during secondary consolidation. During this consolidation phase, soil particles gradually rearrange to a more stable system resulting in an increase in the number of interparticle contacts, in macro-interlocking of sand grains, and in micro-interlocking of grain surface roughness. Olsen et al. (2001) proposed that in the first few thousand years after sediment is deposited, the majority of the aging process is explained by the rearrangement of soil

particles during secondary consolidation. However, over geologic time, cementation from chemical mechanisms may become significant.

In the previous section, we found that the critical datasets of geologic units of similar depositional environment are similar, regardless of their age. For instance, we did not find significant statistical differences in measurements of $N_{1,60,cs}$, or $T_{15,cs}$ in early Holocene or late Pleistocene delta units. This leads to the conclusion that data from high-strain penetration resistance tests, like the SPT or CPT, do not adequately identify the influence of soil aging. Instead, some researchers have found more success detecting the influence of age from low-strain tests, like the V_s (e.g., Andrus et al. 2009). Unfortunately, there are little available V_s data in the study area.

To account for the influence of age using SPT-based or CPT-based liquefaction analysis techniques, researchers suggest applying an age correction factor, K_{DR}, to *CSR*. Hayati and Andrus (2009) combined 24 previous cases studies based on laboratory and/or field tests of age strength gain factors, and proposed eqn. (4.18) from linear regression of the data.

$$\overline{K_{DR}} = 0.13 \cdot Log(t) + 0.83 \tag{4.18}$$

where t is the time since initial deposition or critical disturbance (i.e., liquefaction), in years. Eqn. (4.18) suggests an average reference age (when $K_{DR} = 1$) of approximately 23 years (Hayati and Andrus 2009). A reference age of 23 years seems logical because the liquefaction potential curves were developed primarily with liquefaction case history data

that occurred in the past 1 – 100 years. For eqn. (4.18), R^2 is 62% and the standard deviation of the model, σ_{KDR}, is 0.24.

To apply eqn. (4.18), one must carefully estimate the age of the sediment (i.e., time since initial deposition or last critical disturbance) at the point of interest. Table 4.1 lists approximate ages of the geologic units in the study area from the UGS surficial geology maps. Next, one computes K_{DR}, and then divides it into values of *CSR* that are uncorrected for age, per eqn. (4.19). Finally, one uses this reduced *CSR* in eqns. (4.6) or (4.11) to estimate the probability of liquefaction triggering.

$$CSR = 0.65 \cdot (a_{\max}) \cdot \left(\frac{\sigma_v}{\sigma'_v}\right) \cdot \left(\frac{r_d}{K_{DR}}\right) \tag{4.19}$$

where r_d is the nonlinear shear mass participation factor. Cetin et al. (2004) proposed a model to estimate r_d, with mean, $\overline{r_d}$, and standard deviation, σ_{r_d}. This model is a function of the average shear wave velocity in the upper 12 meters of the site profile ($V^*_{s,12}$). Moss et al. (2006) proposed a new regression model for r_d without $V^*_{s,12}$. Since $V^*_{s,12}$ data are sparse, we use these equations (instead of estimating $V^*_{s,12}$ and introducing additional uncertainty).

Spatial Dependence and Weights

The first law of geography states that everything is related to everything else, but near things are more related than distant things. Likewise, geotechnical properties at sites that are close together are more correlated than properties at sites that are further apart.

In this paper, we described a method to develop distributions of geotechnical properties, specifically critical datasets, according to geologic deposit. When developing these distributions, we treated results from each SPT or CPT investigation as independent and equally likely to occur when sampling within a geologic unit. However, geotechnical properties at a point in space are more likely to be similar to properties found from nearby investigations than properties found from investigations that are further away.

A common way to describe the degree of variation of properties in space is through a semivariogram. Cressie (1993) defined a semivariogram function as the variance of the difference between field values at two locations across the realizations of the field. Semivariance analysis is optimal when data are normally distributed and stationary (i.e., the mean and variance do not vary significantly in space). In the study area, we found that the median values of $Log(T_{15,cs})$ from SPT and CPT investigations are approximately normally distributed and stationary. We computed the average semi-variance of these values, $\gamma(\mathbf{h})$, at numerous lags (distance and direction), $\mathbf{h}$, according to eqn. (4.20).

$$\gamma(\mathbf{h}) = \frac{1}{2m}\sum_{i=1}^{m}\left[z(\mathbf{x}_i) - z(\mathbf{x}_i + \mathbf{h})\right]^2 \tag{4.20}$$

where $z(\mathbf{x})$ is the median value of $Log(T_{15,cs})$ for a point at vector coordinate $\mathbf{x}$, $z(\mathbf{x} + \mathbf{h})$ is the median value of $Log(T_{15,cs})$ for a point at vector coordinate $\mathbf{x} + \mathbf{h}$, i is a pair of points separated by $\mathbf{h}$, and m is the number of pairs separated by $\mathbf{h}$.

Figure 4.7 depicts the average semivariance of median values of $Log(T_{15,cs})$, from the SPT and CPT investigations in the study area, versus lag distances. We found the data were approximately isotropic; thus, the lag **h** becomes the scalar h, which is simply equal to the horizontal distance between pairs of points. As shown, we fit a theoretical bounded linear semivariogram model through the data. Eqn. (4.21) lists the formula for this theoretical model.

$$\gamma(h) = \begin{cases} 0.277\left(\dfrac{h}{94.6}\right) & \text{for } h \le 94.6 \text{ m} \\ 0.277 & \text{for } h > 94.6 \text{ m} \end{cases} \tag{4.21}$$

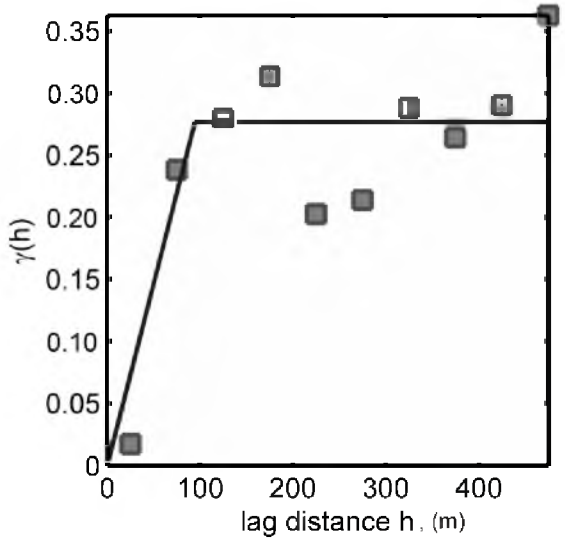

Figure 4.7. Semivariogram of median values of Log($T_{15,cs}$); Weber County, Utah.

As can be seen in Figure 4.7, the data within 20 meters of another (h = 20 meters) are heavily correlated, because their semivariance is nearly equal to zero. As the lag distance between data points increases, the semivariance also increases until reaching a limit (or sill) where the semivariance flattens and becomes roughly constant with lag distance. The semivariance at the sill represents the total semivariance of the variable. The lag at which the semivariogram reaches its sill is the range. The range is the limit of spatial dependence; beyond it the semivariance bears no relation to the separating distance. From eqn. (4.21), we found that the range is approximately 95 meters, and the sill variance is approximately 0.28. Therefore, if a point of interest is within 95 meters of a geotechnical investigation, then we expect that its value of $Log(T_{15,cs})$ will be more correlated to values found from that investigation than to values found from investigations that are more than 95 meters away. On the other hand, if a point of interest is not within 95 meters of any geotechnical investigation, then we have no spatial dependence, and we model the total variance, and thus increased uncertainty, of $Log(T_{15,cs})$ from all geotechnical investigations in the corresponding deposit.

We performed the same semivariance analysis for the median values of $Log(N_{1,60,cs})$, from SPT and CPT investigations in the study area. We found that the range of spatial dependence for this variable is also roughly 95 meters. Therefore, we set 95 meters as the rough limit of spatial dependence for critical datasets in the study area, and modeled the critical datasets as random regional variables, weighted according to their proximity to a point of interest. We used ordinary kriging theory to find these weights.

In ordinary kriging, the vector of weights for each data point, $\boldsymbol{\lambda}$, is a function of the semivariogram model. This vector of weights is set such that it sums to 1. Webster and Oliver (1990) succinctly define the weights from ordinary kriging by eqn. (4.22).

$$\begin{bmatrix} \boldsymbol{\lambda} \\ \psi \end{bmatrix} = \mathbf{A}^{-1}\mathbf{b} \tag{4.22}$$

For isotropic conditions, eqn. (4.23) defines **A** and **b**.

$$\mathbf{A} = \begin{bmatrix} \gamma(d_{1,1}) & \gamma(d_{1,2}) & \dots & \gamma(d_{1,n}) & 1 \\ \gamma(d_{2,1}) & \gamma(d_{2,2}) & \dots & \gamma(d_{2,1}) & 1 \\ \vdots & \vdots & \vdots & \vdots & \vdots \\ \gamma(d_{n,1}) & \gamma(d_{n,2}) & \dots & \gamma(d_{n,n}) & 1 \\ 1 & 1 & \dots & 1 & 0 \end{bmatrix}; \quad \mathbf{b} = \begin{bmatrix} \gamma(d_{1,p}) \\ \gamma(d_{2,p}) \\ \vdots \\ \gamma(d_{n,p}) \\ 1 \end{bmatrix} \tag{4.23}$$

where ψ is the Lagrange multiplier needed to ensure the weights sum to 1, n is the total number of data points in the dataset, p is the point of interest, and $\gamma(d_{i,j})$ is the model semivariogram evaluated at a lag equal to the distance between points i and j.

Calculating weights based on the semivariogram enables modeling of the spatial dependence of the critical datasets. For example, suppose we are interested in estimating the distribution of the critical dataset at a point in the stream alluvium deposits where there are three geotechnical investigations within the range of the semivariogram. Say SPT A is 11.3 meters, SPT B is 26.3 meters, and CPT C is 60.6 meters from the point of interest. Calculating the weights to every geotechnical investigation in the stream alluvium deposit, by eqn. (4.22), finds that the weights to SPT A, SPT B, and CPT C are

0.71, 0.17, and 0.11, respectively. The weights to the other 168 investigations in the stream alluvium deposits are nearly zero in comparison. As expected, the weights decrease as the distance from the point of interest to the geotechnical investigation increases. With the weights defined, we can treat each of the possible critical datasets for the stream alluvium deposit as a weighted random variable. By weighted random sampling, there is a higher probability of selecting critical datasets from SPT A, a lower probability of selecting from SPT B or CPT C, and essentially no probability of selecting critical datasets for any of the other investigations in the stream alluvium deposit.

Of course, if at a point of interest there are no geotechnical investigations within the range of the semivariogram, then the weights to the critical datasets at each investigation in the corresponding geologic deposit are equal. If the point of interest is at a geotechnical investigation, then the weight for the critical datasets at that investigation will equal 1.

Accounting for the Influence of Topography

Numerous researchers found that the magnitude of lateral spread displacement is highly correlated with the degree of ground slope, or the distance and height of a nearby free-face (e.g., Bartlett and Youd 1992, Youd et al. 2002, Zhang et al. 2004, Faris et al. 2006, Gillins and Bartlett 2012). Therefore, when mapping liquefaction hazards, it is important to account for variations in topography. For this study, we selected the Gillins and Bartlett (2012) empirical model for estimating lateral spread displacement (eqns. (4.2) and (4.3)). This model is a function of the free-face ratio, W, and the ground slope, S. To compute these variables in space, we obtained both a 1/3 arcsecond (about 10

meters resolution) and 1 arcsecond (about 30 meters resolution) Digital Elevation Model (DEM) of Weber County from the USGS National Elevation Dataset.

We identified two significant free-face features in the study area: the channels of the Weber and Ogden rivers. Based on the 1/3 arcsecond DEM, and river data from the USGS National Hydrography Dataset, it is possible to estimate the alignment and elevation of the bottom of these channels throughout the study area. Since this DEM has a resolution of approximately 10 meters, we assigned a uniform grid spaced at 10 meters along the influential zone of the channels. Bartlett and Youd (1992) defined the minimum value of W as 1%; hence, we set the influential zone as that area where $W >$ 1%. We then extracted elevation values from the DEM at each grid point, and calculated the perpendicular (or shortest) distance from the grid point to the river channel. Finally, we computed W at each grid point by: first, differencing the elevations of the grid point and the river channel at the point of intersection; and then, dividing by the distance between the two points. Figure 4.8 shows values of W at numerous grid points along the deepest portion of the Weber River in the study area. As expected, W is largest along the edges of the river channel, and then decreases as the distance from the channel increases. For this portion of the Weber River, we see the influential zone is approximately 0.6 to 0.8 km from the channel.

Similar to the method to find W, we estimated S by extracting ground slope values at each point of a uniform grid. The ground slope term in the Gillins and Bartlett (2012) empirical model is based on regression of case history data originally compiled by Bartlett and Youd (1992). For those case history data, Bartlett and Youd used slightly different techniques to measure S for nonuniform slopes than for uniformly long and

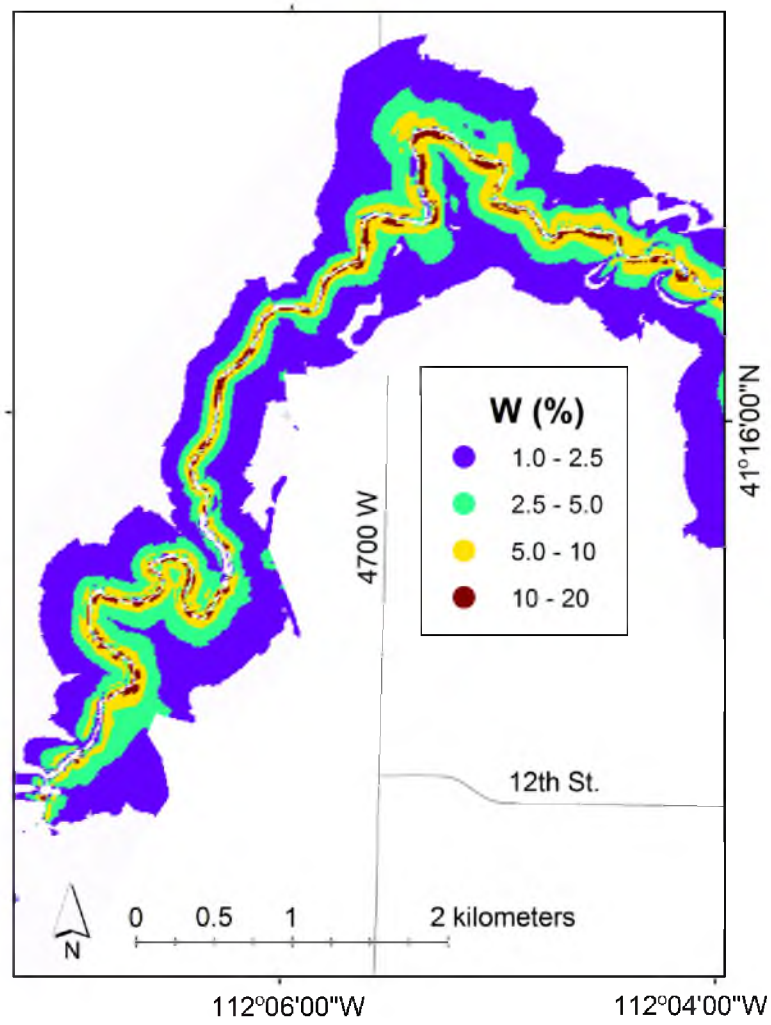

Figure 4.8. Variation of *W* along a portion of the Weber River; Weber County, Utah.

gentle slopes. From the observed displacement pattern in the case histories, they noted that the zone of increased displacement near undulated slopes extended above and below the toe and crest of the undulations. Thus, their measurements of *S* for displacement vectors within this zone were steepened to either the crest or to the toe of the undulations.

In an effort to be more consistent with this definition of *S*, we found *S* using the 1 arc-second DEM of Weber County, as opposed to finding *S* from higher-resolution data.

Using the "slope" tool in ArcGIS®, we converted this DEM raster to a percent ground slope raster. This slope tool determines the slope at each cell of a raster by finding the maximum change in elevation from the eight neighboring cells. Since the cell size of the input DEM raster is approximately 30 meters, the slope at each cell of the raster is smoother and more uniform over that area. To account for the variation of S in the study area, we assigned a uniform grid, spaced at 30 meters (or 10 meters if the grid point is within the influential zone of a free-face feature). We then extracted percent ground slope values from the slope raster at each grid point.

Implementation of the Mapping Method

We implemented the hazard mapping process by assigning and solving a uniform grid, spaced in a manner to capture topographic variations in the study area. At each grid point, we solved the probability chain shown in eqn. (4.1). This section of the paper summarizes how to solve this probability chain at an individual grid point. Ultimately, this process is repeated for all grid points in the study area to produce final probabilistic liquefaction hazard maps.

The previous section of this paper explained how to extract raster data from DEMs to compute W and S at a grid point. At each grid point, we also extracted values of geologic deposit and age from the raster data developed from the geologic mapping. We extracted values from raster data using the "latticespot" tool in ArcGIS®.

Next, we input the mean seismic variables, a_{max}, M_w, and R, based on interactive deaggragation (using the USGS website: https://geohazards.usgs.gov/deaggint/2008) of the 2,500-year return period seismic hazard at the grid point. The interactive

deaggragation website uses the 2008 source and attenuation models of the National Seismic Hazard Mapping Project (Peterson et al. 2008). These attenuation models provide estimates of values of peak ground acceleration (a_{max}) by accounting for soil effects via direct input of the average shear wave velocity in the upper 30 meters of the site profile ($V_{s,30}$). We estimated values of $V_{s,30}$ in the study area according to midrange site classification values, defined by ASCE 7 (2010). Interactive deaggragation revealed that the Weber segment of the Wasatch fault zone is the controlling seismic source for this seismic event.

The subsequent step is to input the geotechnical variables (specifically the critical datasets) from the corresponding geologic deposit. As discussed, we treat the geotechnical data from each SPT or CPT investigation in the geologic deposit as weighted random regional variables. We compute the weights to the data for each of these investigations by eqn. (4.22). For example, for this study, there are 82 SPT and CPT investigations in the delta deposits. When solving a grid point within this deposit, we calculate the weights for each of these 82 investigations. The weights will be larger for data from investigations within the range of the semivariogram, as defined by eqn. (4.21).

After computing the weights to every SPT or CPT investigation in the corresponding geologic deposit, we used the Monte Carlo method to input the necessary random variables and output resulting probabilities of liquefaction hazards. First, we randomly selected an SPT or CPT investigation in the corresponding geologic deposit. This random sampling was weighted (or nonuniform). Second, within the selected investigation, we randomly selected one of its individual critical datasets. (Earlier, we

described it takes roughly 300 Monte Carlo simulations to define the distribution of each variable in the critical dataset at an SPT or CPT investigation.) Third, we randomly sampled a value of K_{DR}, which is modeled as a normally distributed random variable with mean, $\overline{K_{DR}}$ (eqn. (4.18)), and standard deviation, σ_{KDR}. Fourth, we randomly sampled a value of r_d, which is likewise modeled as a normally distributed random variable with mean, $\overline{r_d}$, and standard deviation, σ_{rd}. Fifth, we computed CSR using the previously selected random variables (eqn. (4.19)). Sixth, we calculated P_L. If a critical dataset from an SPT borehole is selected, we found P_L using the SPT-based probabilistic liquefaction potential curves (eqn. (4.6)). Likewise, if a critical dataset from a CPT sounding is selected, we found P_L using the CPT-based liquefaction potential curves (eqn. (4.11)). Seventh, we calculated $\overline{D_H}$ according to the controlling topographic conditions (eqns. (4.2) and (4.3)). For cases where the grid point has a value of S and W, we found $\overline{D_H}$ for both conditions and selected the maximum value. Finally, we found the probability that the lateral spread displacement exceeds a specified threshold (eqn. (4.1)). We repeat these eight steps numerous times until we have defined a distribution of outcomes (i.e., probabilities of liquefaction hazard) at a grid point. We found that 3,000 Monte Carlo simulations adequately defined the distribution of outcomes at a grid point.

Figure 4.9 shows histograms of resulting probabilities of liquefaction hazards at a sample grid point in the stream alluvium. At this particular grid point, there are no geotechnical investigations within the range of the semivariogram; hence, there is large uncertainty in the probabilities. The distribution for the probability of liquefaction triggering is bimodal. Figure 4.9a indicates that 28.1% of the critical datasets from SPT

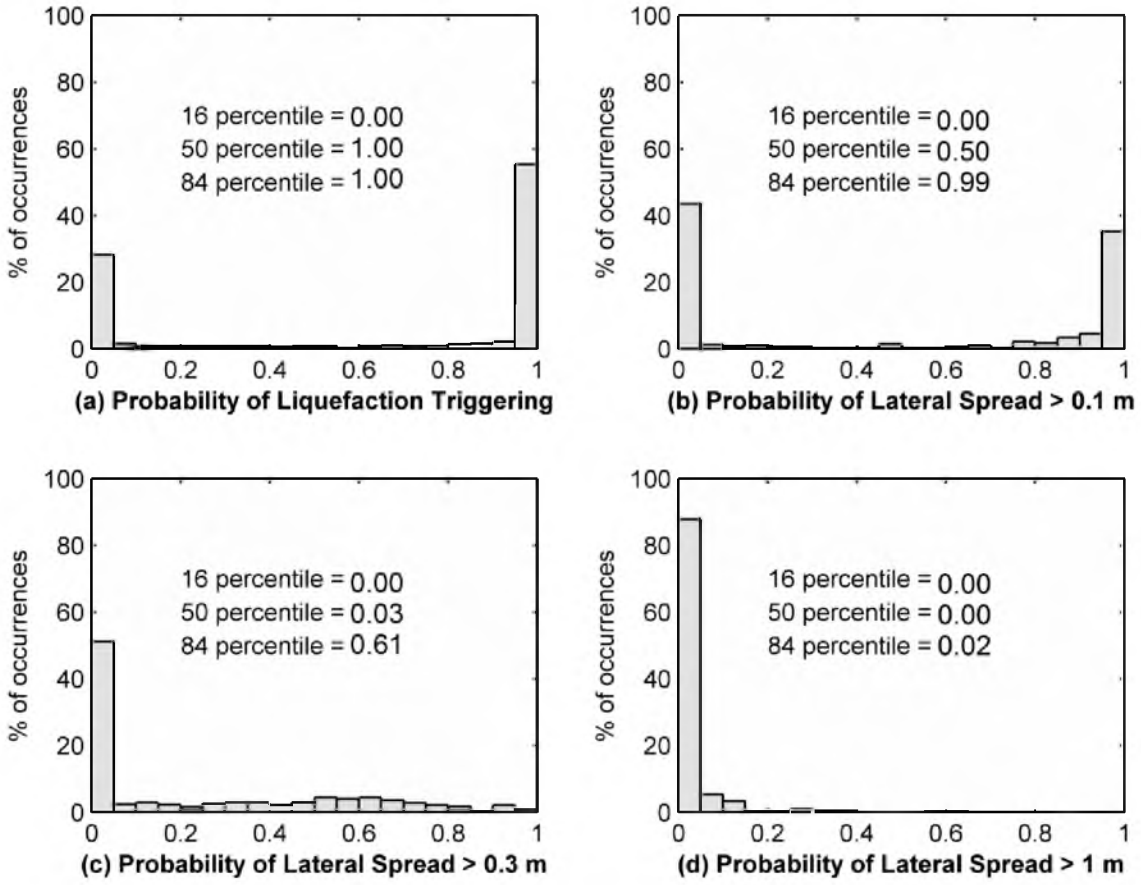

Figure 4.9. Example of a distribution of probabilities at a grid point in the stream alluvium, for (a) liquefaction triggering, (b) lateral spread exceeding 0.1 m, (c) lateral spread exceeding 0.3 m, (d) lateral spread exceeding 1 m.

and CPT investigations in the stream alluvium did not find a layer susceptible to liquefaction; thus, for those datasets, $P_L = 0$. On the other hand, due to the strong ground motion from a 2,500-year return period event, nearly all critical datasets with a liquefiable layer have $P_L = 100\%$.

The distribution for the probability of lateral spread displacement exceeding 0.1 meters is also bimodal. Figure 4.9b indicates that 41.3% of the critical datasets in the stream alluvium have $T_{15} = 0$. For those datasets with $T_{15} > 0$, there is a high probability

that the lateral spread will exceed 0.1 meters. However, Figure 4.9c – d indicate low probability that the lateral spread at this point will exceed 0.3 or 1.0 meters. Since the distributions in Figure 4.9 are either bimodal or heavily skewed and non-normal, this figure lists the 16^{th}, 50^{th}, and 84^{th} percentile probability values.

We solved for the probability distributions (like in Figure 4.9) for every grid point in the study area. Figure 4.10 depicts a map of the 50^{th} percentile (or median) probability of lateral spread displacement exceeding 0.3 meters given a 2,500-year return period event.

Conclusions

In this paper, we proposed a method to map the probabilities of liquefaction hazards for a scenario seismic event. The method uses geologic, topographic, and geotechnical inputs, and accounts for major sources of uncertainty. Such uncertainties include variability over space, lack of data, and limitations of the empirical models to estimate liquefaction phenomena. After gathering available data, we implemented this method to produce liquefaction hazard maps in a study area in Weber County, Utah.

Empirical models that predict the probability of liquefaction triggering and lateral spreads exceeding specified displacement thresholds are functions of certain geotechnical properties. We found these particular geotechnical properties (we call "critical datasets") at each available SPT and CPT investigation in Weber County, Utah. When reducing borehole data, we identified and accounted for two major sources of uncertainty: the energy of the SPT impact hammer transmitted to the sampler, and missing laboratory measurements of fines content for numerous layers in the site profile. When reducing

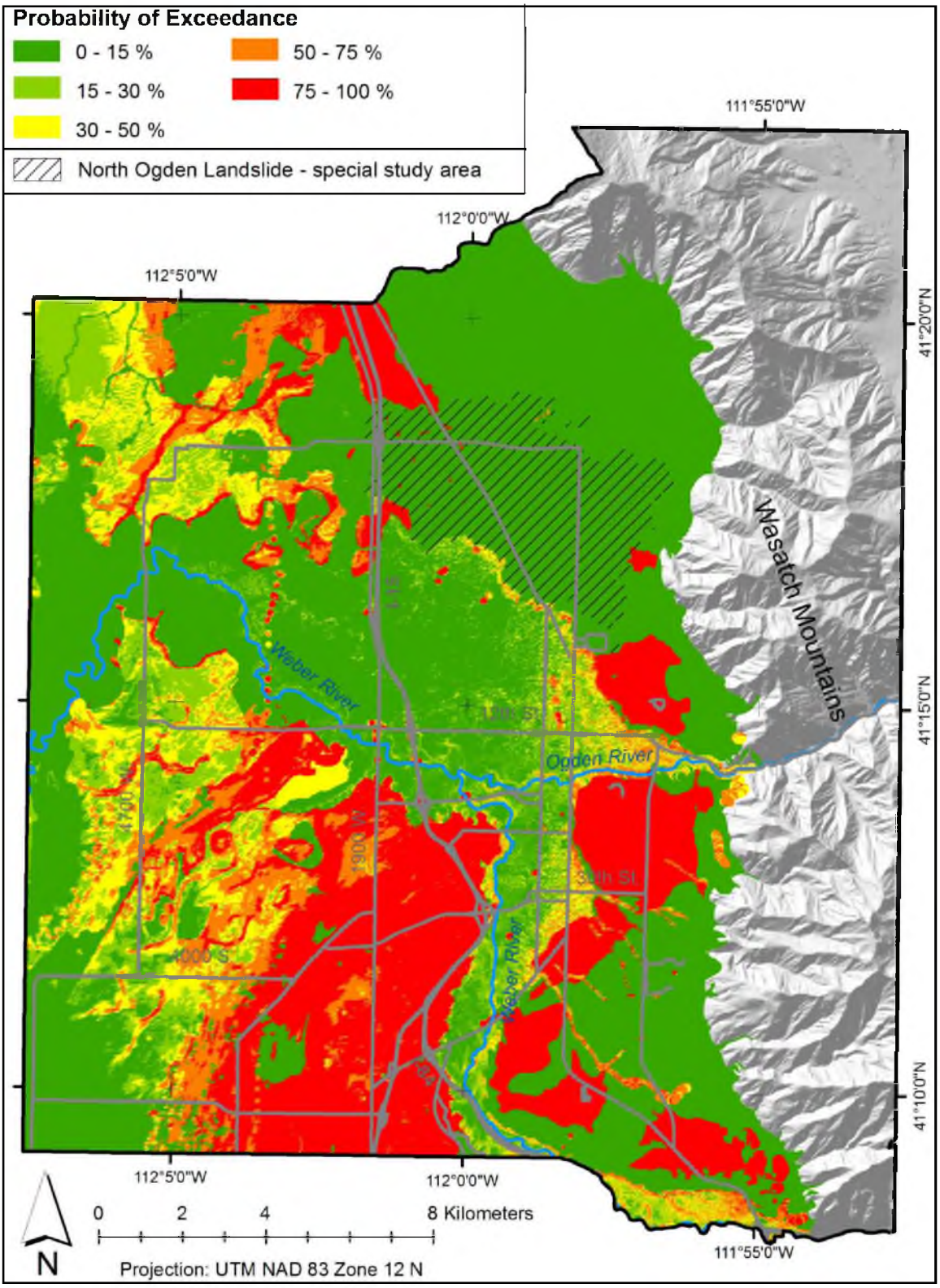

Figure 4.10. 50th percentile probabilities of lateral spread displacement exceeding 0.3 meters for a 2,500-year seismic event; Weber County, Utah

CPT sounding data, we accounted for two major sources of uncertainty: estimating soil type or classification, and converting CPT penetration resistance to SPT blow counts.

We found that the dispersions of the critical datasets are statistically similar between geologic units of similar depositional environment. Therefore, in this study of Weber County, we pooled data into 11 deposit classes, as shown in Table 4.1. Pooling data increases the robustness of the sampling, thereby improving estimates of the total variability of the geotechnical properties for each geologic unit.

Previous investigators noted that liquefaction resistance of soils increase with age. However, we are unable to identify differences in the critical datasets according to the age of the soil. This indicates that penetration resistance data from high-strain tests like the SPT or CPT are poor detectors of the influence of the age of the soil. Hence, we accounted for liquefaction resistance due to increased age by applying an age correction factor, as defined by Hayati and Andrus (2009).

From semivariance analysis, we found that critical datasets from nearby geotechnical investigations are spatially correlated, but only for a small range. To model this spatial dependence, we fit a theoretical semivariogram to the critical data. We then treated the critical datasets as weighted random regional variables; weighted according to the semivariogram model and ordinary kriging theory. For the data in the study area of Weber County, the range of this semivariogram is only approximately 95 meters. Since this range is so small, and there are a somewhat limited number of geotechnical investigations in the study area, we found large uncertainty in the estimates of the probabilities of liquefaction hazards.

We accounted for variations in topography by solving for probabilities of liquefaction hazards at points in a finely spaced grid. We spaced the grid according to the resolution of the topographic data from the DEMs (i.e., 10 or 30 meters).

At a grid point, we found that 3,000 Monte Carlo simulations are necessary to define the total distribution of the resulting probabilities of liquefaction hazards. We identified large uncertainty in the empirical models for K_{DR}, r_d, P_L, and D_H. We accounted for these uncertainties by treating their results as normally distributed random variables. Because of the large number of necessary simulations at each point of a very fine grid, there is a large amount of calculations. Therefore, further research is needed in Monte Carlo variance reduction methods—such as use of correlated and/or stratified sampling.

We implemented this procedure to map probabilistic liquefaction hazards in a study area in Weber County, Utah. Figure 4.10 depicts 50^{th} percentile (median) probabilities of lateral spread displacement exceeding 0.3 meters for a 2,500-year return period seismic event. We recommend producing maps at other percentile values, such as the 16^{th} and 84^{th} percentile values, in order to quantify the uncertainty in the estimates.

References

ASCE 7, 2010. *Minimum Design Loads for Buildings and Other Structures*, Structural Engineering Institute of the American Society of Civil Engineers, Danvers, MA, Chapter 20.

Andrus, R. D., Hayati, H., and Mohanan, N. P., 2009. Correcting liquefaction resistance for aged sands using measured to estimated velocity ratio, *J. Geotech. Geoenviron. Eng.* **135**(6), 735 – 744.

Bartlett, S. F., and Youd, T. L., 1992. *Empirical Analysis of Horizontal Ground Displacement Generated by Liquefaction-Induced Lateral Spreads, Technical Report NCEER-92-0021*, National Center for Earthquake Engineering Research, Buffalo, NY.

Bartlett S. F., Olsen, M. J., and Solomon, B. J., 2005. *Probabilistic Liquefaction Potential and Liquefaction-Induced Ground Failure Maps for the Urban Wasatch Front: Collaborative Research with the University of Utah, Utah State University and the Utah Geological Survey, Phase I, FY2004, U.S.G.S. Research Award No. 04HQGR0026*, Reston, VA.

Bowles, J. E., 1996. *Foundation Analysis and Design,* 5th edition, The McGraw-Hill Companies, Inc., New York, NY, Chapter 2, p. 29.

Cetin, K. O., Seed, R. B., Kiureghian, A. D., Tokimatsu, K., Harder, L. F., Jr., Kayen, R. E., and Moss, R. E., 2004. Standard Penetration Test-based probabilistic and deterministic assessment of seismic soil liquefaction potential, *J. Geotech. Geoenviron. Eng.* **130**(12), 1314 – 1340.

Cressie, N. A. C., 1993. *Statistics for Spatial Data Revised Edition*, John Wiley & Sons, Inc., Hoboken, NJ, Chapter 2.

Crittenden, M. D., Jr., and Sorenson, M. L., 1985. *Geologic Map of the North Ogden Quadrangle and Part of the Ogden and Plain City Quadrangles, Box Elder and Weber Counties, Utah, U.S. Geological Survey Miscellaneous Investigations Series Map I-1606*, Reston, VA, scale 1:24,000.

Faris, A. T., Seed, R. B., Kayen, R. E., and Wu, J., 2006. A semiempirical model for the estimation of maximum horizontal displacement due to liquefaction-induced lateral spreading, in *Proc. 8th U.S. Conference on Earthquake Engineering*, vol. 3, paper no. 1323, San Francisco, CA, pp. 1584-1593.

Gillins, D.T., 2012. *Mapping the Probability and Uncertainty of Liquefaction-Induced Ground Failure*, *Ph.D. Dissertation,* Department of Civil and Environmental Engineering, University of Utah, Salt Lake City, UT.

Gillins, D. T., and Bartlett, S. F., 2012. Multilinear regression equations for predicting lateral spread displacements from soil type and CPT data, *J. Geotech. Geoenviron. Eng.*, under review.

Harty, K. M., and Lowe, M., 2003. *Geologic Evaluation and Hazard Potential of Liquefaction-Induced Landslides along the Wasatch Front, Utah, Utah Geological Survey Special Study 104*, Salt Lake City, UT, 40 pp., 16 pl.

Harty, K. M., and Lowe, M., 2005. *Interim Geologic Map of the Plain City Quadrangle, Weber and Box Elder Counties, Utah, Utah Geological Survey Open-File Report 451*, Salt Lake City, UT, 2 pl., scale 1:24,000.

Hayati, H., and Andrus, R. D., 2009. Updated liquefaction resistance correction factors for aged sands, *J. Geotech. Geoenviron. Eng.* **135**(11), 1683-1692.

Holzer, T. L., Bennett, M. J., Noce, T. E., Padovani, A. C., and Tinsley, J. C., 2006. Liquefaction hazard mapping with LPI in the greater Oakland, California, area, *Earthquake Spectra* **22**(3), 693-708.

Lenz, J., and Baise, L. G., 2007. Variability of LPI across geologic units for regional liquefaction mapping, in *Geo-Denver 2007: New Peaks in Geotechnics, Dynamic Response and Soil Properties (GSP 160)*, M. M. Dewoolkar and J. P. Koester (editors), ASCE, Denver, CO, 10 pp.

Leon, E., Gassman, S. L., and Talwani, P., 2006. Accounting for soil aging when assessing liquefaction potential, *J. Geotech. Geoenviron. Eng.* **132**(3), 363-377.

McDonald, G. N., and Ashland, F. X., 2008. *Earthquake Site Conditions in the Wasatch Front Urban Corridor, Utah, Utah Geological Survey Special Study 125,* Salt Lake City, UT, 41 pp., 1 pl., scale 1:50,000.

Mitchell, J. K., and Solymar, Z. V., 1984. Time-dependent strength gain in freshly deposited or densified sand, *J. Geotech. Eng.* **110**(11), 1559-1576.

Molle, J. 2005. *The Accuracy of the Interpretation of CPT-Based Soil Classification Methods in Soft Soils, M Sc. thesis*, Delf University of Technology, Delft, the Netherlands.

Moss, R. E. S., Seed, R. B., Kayen, R. E., Stewart, J. P., Kiureghian, A. D., and Cetin, K. O., 2006. CPT-based probabilistic and deterministic assessment of in situ seismic soil liquefaction potential, *J. Geotech. Geoenviron. Eng.* **132**(8), 1032 – 1051.

Olsen, M. J., Bartlett, S. F., and Solomon, B. J., 2007. Lateral spread hazard mapping of the Northern Salt Lake Valley, Utah for a M7.0 scenario earthquake, *Earthquake Spectra* **23**(1), 95-113.

Olsen, S. M., Obermeier, S. F., and Stark, T. D., 2001. Interpretation of penetration resistance for back-analysis at sites of previous liquefaction, *Seismological Research Letters* **72**(1), 46-59.

Petersen, M. D., Frankel, A. D., Harmsen, S. C., Mueller, C. S., Haller, K. M., Wheeler, R. L., Wesson, R. L., Zeng, Y., Boyd, O. S., Perkins, D. M., Luco, N., Field, E. H., Wills, C. J., and Rukstales, K. S., 2008. *Documentation for the 2008 Update of the United States National Seismic Hazard Maps, U.S. Geological Survey Open-File Report 2008–1128*, Reston, VA, 61 pp.

Robertson, P. K., 1990. Soil classification using the cone penetration test, *Canadian Geotechnical Journal* **27**(1), 151–158.

Robertson, P. K., 2009. *Soil Behaviour Type from the CPT: an Update,* Gregg Drilling & Testing Inc., Signal Hill, CA, 8 pp.

Robertson, P. K., 2009b. Interpretation of cone penetration tests – a unified approach, *Canadian Geotechnical Journal* **46**, 1337-1355.

Sack, D., 2005. *Geologic Map of the Roy 7.5-Minute Quadrangle, Weber and Davis Counties, Utah, Utah Geological Survey Miscellaneous Publication 05-03*, Salt Lake City, UT, 22 pp., scale 1:24,000.

Schmertmann, J. H., 1987. Discussion of 'Time-dependent strength gain in freshly deposited or densified sand' by James K. Mitchell and Zoltan V. Solymar, *J. Geotech. Eng.* **113**(2), 173-175.

Webster, R., and Oliver, M. A., 1990. *Statistical Methods in Soil and Land Resource Survey*, Oxford University Press, New York, NY, chapter 12.

Wilks, S. S., 1932. Certain generalizations in the analysis of variance, *Biometrika* **24**, 471-494.

Yonkee, A., and Lowe, M., 2004. *Geologic Map of the Ogden 7.5-Minute Quadrangle, Weber and Davis Counties, Utah, Utah Geological Survey Map 200*, Salt Lake City, UT, 42 pp., scale 1:24,000.

Youd, T.L., and Perkins, D.M., 1978. Mapping liquefaction-induced ground failure potential, *Journal of the Geotechnical Engineering Division* **104**, No. GT4, 433-446.

Youd, T. L., Hansen, C. M., and Bartlett S. F., 2002. Revised multilinear regression equations for prediction of lateral spread displacement, *J. Geotech. Geoenviron. Eng.* **128**(12), 1007-1017.

Youd, T. L., Idriss, I. M., Andrus, R. D., Arango, I., Castro, G., Christian, J. T., Dobry, R., Finn, W. D. L., Harder, L. F., Jr., Hynes, M. E., Ishihara, K., Koester, J. P., Liao, S. S. C., Marcuson, W. F., III, Martin, G. R., Mitchell, J. K., Moriwaki, Y., Power, M. S., Robertson, P. K., Seed, R. B., Stokoe, K. H., II, 2001. Liquefaction resistance of soils: summary report from the 1996 NCEER and 1998 NCEER/NSF workshops on evaluation of liquefaction resistance of soils, *J. Geotech. Geoenviron. Eng.* **127**(10), 817-833.

Zhang, G., Robertson, P. K., and Brachman, R. W. I., 2002. Estimating liquefaction-induced ground settlements from CPT for level ground, *Canadian Geotechnical Journal* **39**(5), 1168-1180.

Zhang, G., Robertson, P. K., and Brachman, R. W., 2004. Estimating liquefaction-induced lateral displacements using the standard penetration test or cone penetration test, *J. Geotech. Geoenviron. Eng.* **130**(8), 861-871.

CHAPTER 5

PROBABILISTIC LIQUEFACTION GROUND FAILURE MAPS FOR WEBER COUNTY, UTAH

Abstract

This paper presents probabilistic liquefaction-induced ground failure maps for Weber County, Utah. The mapping project presented herein better defines the liquefaction hazard areas in this county over previous mapping efforts. The new maps are produced from mapping techniques based on geologic and geotechnical inputs and a rigorous quantification of uncertainty in the mapped domain. The proposed method accounts for variations in soil conditions, age, topography, spatial distribution and major sources of aleatory uncertainty. The degree of ground slope significantly influences the amount of lateral spread potential. To illustrate the uncertainty associated with the mapped estimates, the probability of horizontal displacements exceeding specified thresholds are produced for 50^{th} and 84^{th} percentiles. This approach allows for estimates of the median and approximately the median plus one standard deviation probabilities. The maps identify a significant zone with relatively high probability of liquefaction triggering for either a 500-year or a 2,500-year return period event. In addition, the new ground failure maps identify zones with moderate probability of liquefaction-induced

lateral spread displacement exceeding 0.3 meters for a 500-year seismic event, and high probability of exceeding 0.6 meters for a 2,500-year seismic event.

Introduction

Soil liquefaction is a general loss of shear resistance in saturated, cohesionless sediments caused by a rapid increase in excess pore water pressure usually generated by major earthquakes. Liquefaction-induced ground failure can cause severe and costly damage to infrastructure and other facilities. Such damage from recent earthquakes in Japan and New Zealand raise questions about our ability to assess, delineate and quantify the hazard in vulnerable locations. For example, a preliminary report indicates that much of the estimated $309 billion (2011 USD estimate, BBC News, March 23) in damage to infrastructure in the 2011 Tohoku, Japan earthquake was from liquefaction (Ashford et al. 2011). In this report, investigators noted liquefaction damage that included tilted and settled structures, crippled utility lines, and lateral spread displacement of levees and small water channels.

To aid in identifying and quantifying the hazard in areas vulnerable to liquefaction-induced ground failure, we proposed a probabilistic-based approach to map the liquefaction hazard for a region, such as a municipal county (Gillins and Bartlett 2012b). The proposed method allows for the quantification of the probability of lateral spread displacement exceeding specified thresholds. The method is based on geologic mapping and available geotechnical data, and accounts for variations in topography, sediment age, spatial dependence and other major sources of uncertainty. This is done using random sampling methods and Monte Carlo simulations.

In the 1980s to early 1990s, researchers developed liquefaction triggering maps for urban areas located along the Wasatch Front in Utah using a relatively small geotechnical database and strong ground motion studies that were available at that time (e.g., Anderson et al. 1994). In their time, these maps were useful to government agencies and consultants for delineating zones with high, moderate, or low liquefaction hazards. However since then, the geotechnical database and liquefaction methods have significantly improved and liquefaction prone areas should be reevaluated. In addition, the urban Wasatch Front is one of the fastest growing areas in the United States and is home to approximately 2 million people. It is located in a relatively deep intermountain basin filled with potentially liquefiable sediments and is prone to relatively large-magnitude earthquakes ($7 < M < 7.5$) from the nearby Wasatch fault zone, thus this mapping project is important for improving seismic safety and preserving economic development.

This paper presents liquefaction hazard mapping results for Weber County, Utah, for two scenario earthquake events: (1) 500-year return period, and (2) 2,500-year return period. The new maps we present in this study are based on state-of-the-art probabilistic liquefaction analysis techniques, current seismic hazard data, extensive geotechnical investigations, and recently published surficial geologic maps. In addition to identifying zones with high probability of liquefaction, the new maps provide estimates of the probabilities of lateral spread displacements exceeding specified thresholds. Such maps are useful for probabilistic-based hazard calculations and risk assessment. In addition, these maps are the first of their kind to formally quantify the uncertainty associated in the mapped estimates.

Setting and Geology

Continental sediments from Holocene (and possibly late Pleistocene) unconsolidated fluvial, floodplain, deltaic, lacustrine, playa, colluvial, dunes, loess, tephra, and sebkha depositional environments may be moderately to highly susceptible to liquefaction (Youd and Perkins 1978). Saturated, cohesionless soils found in these environments consist mainly of interbedded layers of loosely deposited sand, gravel, and silt. In the study area in Weber County, Utah, there is a large amount of these soils deposited in widespread fluvial, deltaic, and lacustrine environments. Since these sediments are also located in a zone that is prone to large-magnitude earthquakes, the study area has high potential for liquefaction-induced ground failures.

The geology of Weber County is dominated by Holocene and late Pleistocene sediments, deposited primarily by the Weber and Ogden Rivers, Lake Bonneville and its successor, the Great Salt Lake. Figure 5.1 displays a map of the extent and topography of the study area which encompasses most of the urban development in Weber County, Utah. Figure 4.1 displays a map of the surficial geology of the study area. Table 4.1 lists the description and approximate age of the geologic units shown in Figure 4.1. The mapped units shown in this figure are from a combination of recently published surficial geologic maps at the 7.5-minute (1:24,000) scale (Crittenden and Sorenson 1985, Harty and Lowe 2003, Yonkee and Lowe 2004, Sack 2005, Harty and Lowe 2005). See Gillins and Bartlett (2012b) for more details on the production of Figure 4.1.

The study area is located within the Lake Bonneville hydrologic basin, a closed basin dominated by evaporation and filled with a few tens to several hundred meters of Quaternary deposits. The basin has been an area of internal drainage for much of the past

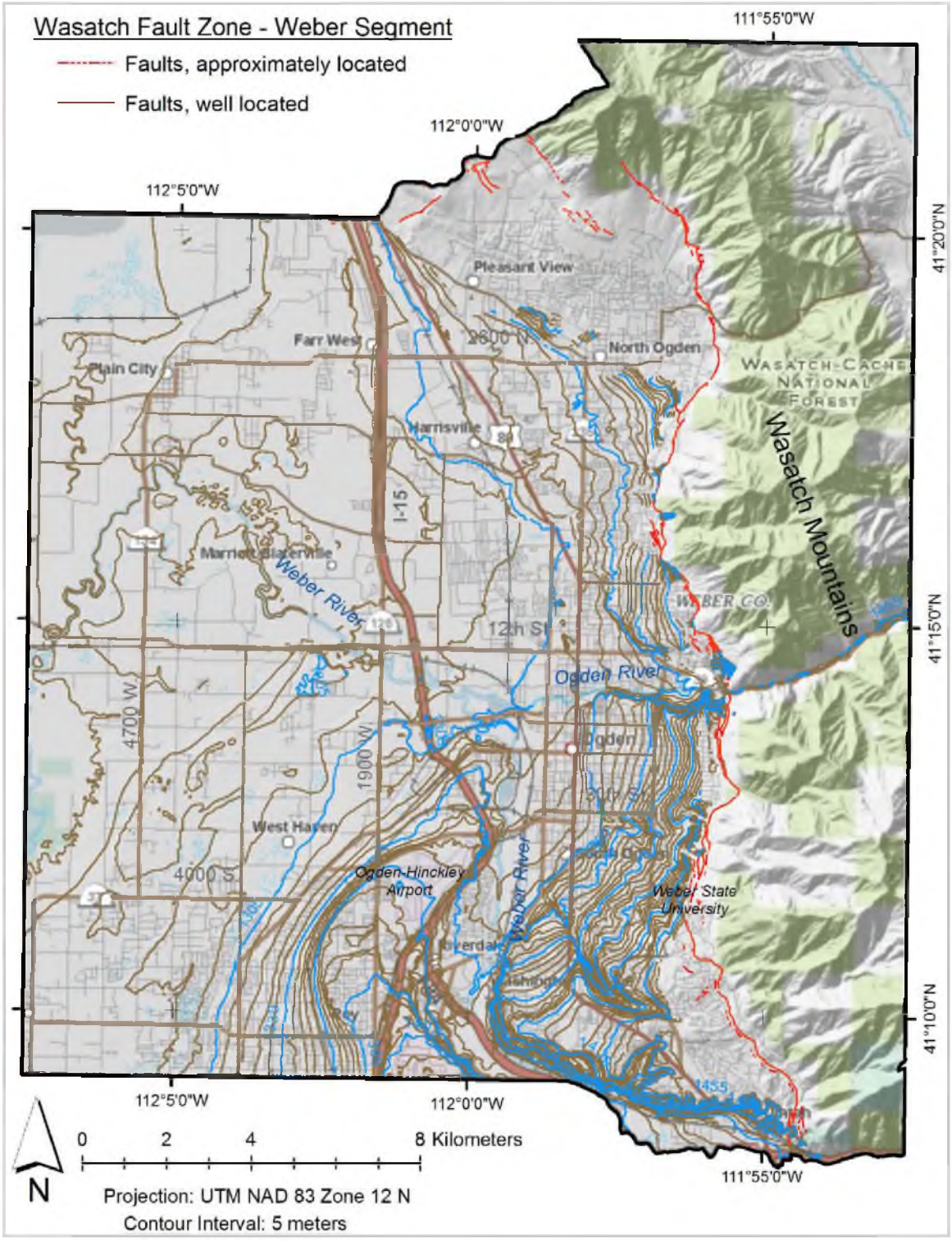

Figure 5.1. Vicinity map and topography of study area (contours not shown for mountainous land where ground slopes exceed 6%); Weber County, Utah (base map from Utah AGRC)

15 million years, and lakes of varying sizes likely existed in the area during all of that time (Currey et al. 1984). Lake Bonneville occupied the basin in the late Pleistocene, from about 12,000 to 28,000 years ago (Oviatt et al. 1992). This lake underwent phases of transgression (lake expands in size) and regression (lake contracts in size). Near the end of its final transgression, about 15,000 years ago, the lake reached its highest elevation (the Bonneville Shoreline with approximate elevation equal to 1552 meters), covered most of the study area, and deposited gravel-dominated lacustrine sediments along its shoreline. Approximately 14,500 years ago, catastrophic threshold failure caused sudden regression of the lake until it stabilized at 1,444 meters, where it formed the Provo shoreline (Malde 1968). When the lake fell to the Provo level, much of the study area remained submerged, and sand-dominated sediment supplied to the lake from the then westerly-bearing Weber River began accumulating in the south-central most part of Figure 4.1, forming the Provo-level delta (Sack 2005). Lake Bonneville began its climatically-induced rapid regression from the Provo shoreline about 14,000 years ago, causing the Weber River to incise its Provo-level delta and to construct, then incise, a downward-stepping and northerly trending series of regressive, sand-dominated, deltaic components (Sack 2005). About 12,200 years ago, additional regression of the lake allowed the river to flow around the north end of the abandoned deltas and shift the deltaic environment to the westerly portion of the study area (Sack 2005). It appears that transgression and regression of the Great Salt Lake, and erosion due to the Weber River floodplain, deposited Holocene sediments on the ground surface in the westerly portion of the study area.

Although there are not any records of historical liquefaction or lateral spread in the study area, previous researchers have mapped two prehistoric liquefaction-induced landslide complexes. The North Ogden landslide (first identified by Miller 1980) covers approximately 25 square kilometers in the northeasterly portion of the study area, mostly southwesterly of North Ogden City (labeled Qmq_2 in Figure 4.1). The East Ogden landslide (first identified by Pashley and Wiggins 1972) covers approximately 10 square kilometers in the southeasterly portion of the study area, mostly in the eastern Ogden City area (labeled Qms_3 in Figure 4.1). Other deposits related to liquefaction-induced ground oscillation and lateral spreads may be present, but have not been recognized due to limited geomorphic expression (Yonkee and Lowe 2004).

Geotechnical Database

As discussed in Gillins and Bartlett (2012b) we gathered and input all available geotechnical data into a database for Weber County, Utah. This geotechnical database contains data from 251 Standard Penetration Testing (SPT) boreholes and 157 Cone Penetrometer Testing (CPT) soundings. We also extracted data from 21 shear wave velocity tests (V_s) in a database published by McDonald and Ashland (2008). Figure 4.1 shows a sampling of the SPT, CPT, and V_s data in this database. (Although we used all of the gathered subsurface data for the analyses, we do not have permission to release the locations of some of the test data provided by the local utilities.) Table 4.1 lists the number of SPT and CPT investigations in each of the surficial geologic units. In Gillins and Bartlett (2012b) we described in detail: (1) how we reduced these data for

liquefaction analysis; and, (2) how we developed distributions of geotechnical data for each of the 11 geologic deposits listed in Table 4.1.

Seismicity and Faulting

The magnitude of liquefaction and lateral spread displacement decreases markedly for $M < 6.0$ earthquakes (Bartlett and Youd 1992). Hence, when analyzing liquefaction, we are particularly concerned with areas prone to moderate to large magnitude earthquakes ($M > 6.0$). The study area lies in the Intermountain seismic belt, a region of historical seismic activity that extends from northwestern Montana, through Utah, to southern Nevada and northwestern Arizona (Smith and Arabasz 1991). This belt contains major normal faults capable of generating $7 < M < 7.5$ earthquakes, such as the Wasatch fault zone, as well as numerous other faults capable of generating moderate-sized earthquakes. The largest historical earthquake in the study area occurred in 1914, had an estimated magnitude of 5.5, and caused local damage (Arabasz et al. 1979).

The Wasatch fault zone is the primary seismic threat to inducing liquefaction because of its potential for generating large earthquakes, its recency of movement, and its proximity to the study area. In the study area, this zone strikes north to northwest, and is interpreted to dip about 40 to 45 degrees west (Yonkee and Lowe 2004, Crittenden and Sorenson 1985). Based on paleoseismic data for the past 6,000 years, the average recurrence interval for a large-magnitude earthquake ($M > 6.5$) along the combined five most-active segments (Brigham City, Weber, Salt Lake City, Provo, and Nephi) of the zone is about 320 years; and, the average recurrence interval for a large-magnitude

earthquake on an individual segment, such as the Weber, is about 1,600 years (Pechmann and Arabasz 1995).

The Weber segment of the Wasatch fault zone is nearest to the study area, trending 60 kilometers from its southern end near North Salt Lake City to its northern end in Pleasant View, Utah (Machette et al. 1992). The faults depicted in Figure 5.1 are nearly entirely of the Weber segment of the Wasatch fault zone. This segment has had 4 surface-rupturing events over roughly the past 6,000 years, including its most recent major event approximately 1,016 years ago (McCalpin and Nishenko 1996). Some of its surface rupturing events produced 0.6 to 3.5 meters of vertical ground offset, giving estimated paleoearthquake magnitudes of 7 to 7.5 (Nelson and Personious 1993).

For the study, we mapped liquefaction hazards based on two scenario seismic events: a 500-year return period event (10% probability of exceedance in 50 years), and a 2,500-year return period event (2% probability of exceedance in 50 years). Engineers often consider seismic design loading based on these two events because they closely represent an "expected earthquake" and a "maximum considered earthquake (MCE)," respectively. We found, by interactive deaggragation at numerous points in the study area (using the USGS website: https://geohazards.usgs.gov/deaggint/2008), that the M for both of these scenario events is greater than 6; and, that the Weber segment of the Wasatch fault zone is primarily the contributing seismic source. For the 500-year return period event, the mean M from contributing seismic sources is approximately 6.68 to 6.73 in the study area; and, for the 2,500-year return period event, the mean M is approximately 6.85 to 7.00. Thus, for both of these scenario earthquakes, the

corresponding strong motions are sufficiently high to induce liquefaction in susceptible soils.

For strong motion evaluations located on soil profiles, it is important to consider soil effects. Soft and/or deep soil profiles will either amplify or deamplify the strong motion depending on the nature and frequency content of the strong motion and the characteristics of the soil profile. The study area is a relatively deep intermountain basin filled with interbedded alluvium, delta, and lacustrine deposits. Undoubtedly, soft soil effects will play a role in modifying the strong ground motion in this area. The USGS interactive deaggragation website uses the 2008 source and attenuation models of the National Seismic Hazard Mapping Project (Peterson et al. 2008). These attenuation models provide estimates of values of peak ground acceleration (PGA) by accounting for soil effects via direct input of the average shear wave velocity in the upper 30 meters of the site profile ($V_{s,30}$). Unfortunately, there are only 21 available V_s tests in the study area.

However, McDonald and Ashland (2008) have produced a $V_{s,30}$ map along the urban corridor of the Wasatch Front including the study area in Weber County. Because this map is based on limited V_s data, and because we can supplement these V_s data with additional SPT and CPT data from the geotechnical database, we decided to produce an updated map. Figure 5.2 shows this map, shaded according to National Earthquake Hazards Reduction Program (NEHRP) site classes. This map is based on knowledge of geology, V_s, SPT, and CPT data of sufficient depth. Figure 5.2 depicts the location of these geotechnical tests, colored per the definitions of the NEHRP site classes.

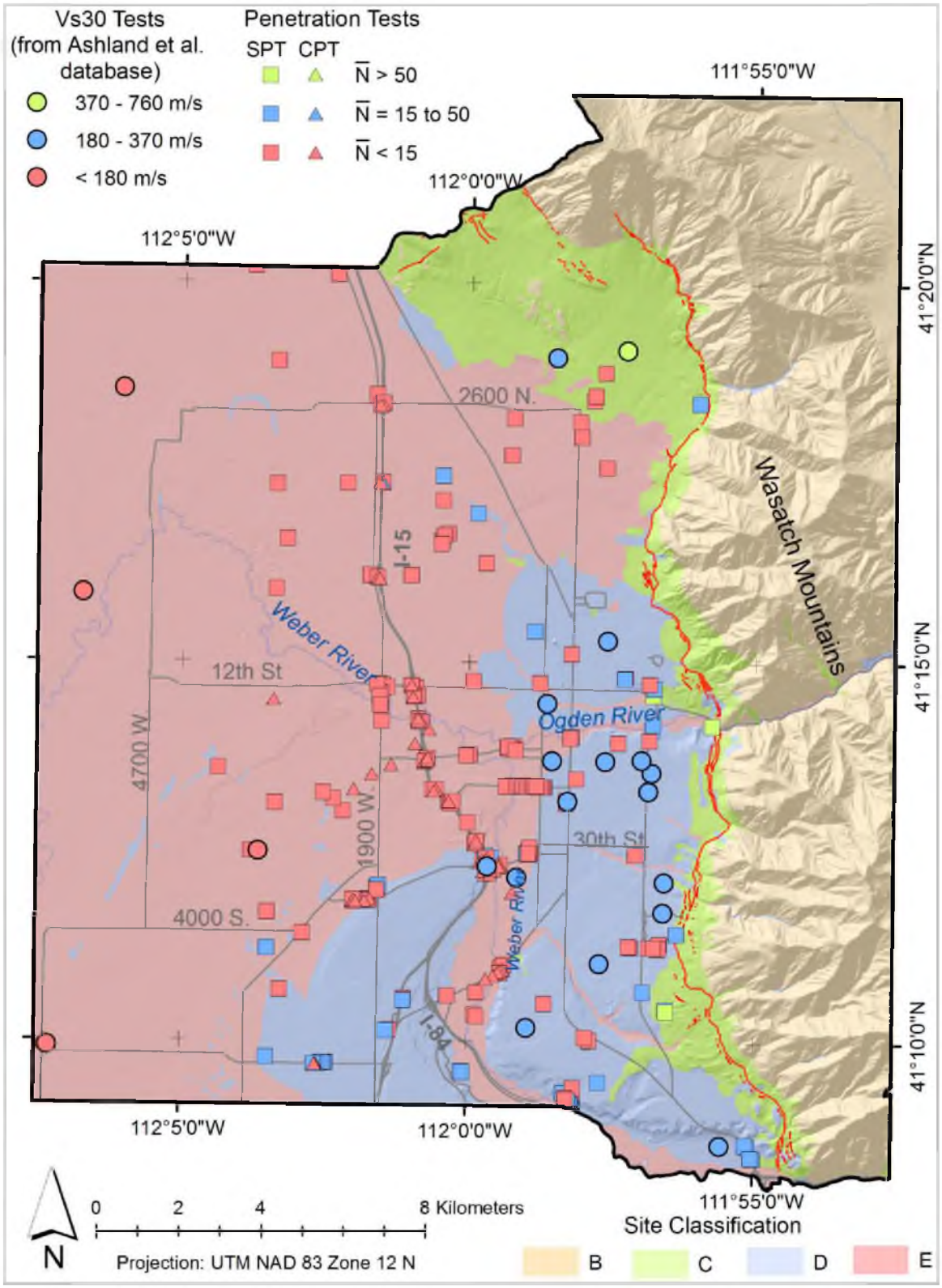

Figure 5.2. NEHRP site classification map and location of a sample of the geotechnical investigations; Weber County, Utah

ASCE 7 (2010) defines the site classes by measurements of $V_{s,30}$, or average SPT blow counts in the upper 30 meters of the site profile, $\overline{N}$ (see Table 5.1). Of course, we found $V_{s,30}$ at each V_s test location and considered these data as the best type for classifying the site soil response of a geologic unit. Due to the sparse amount of V_s data, we calculated $\overline{N}$ at each SPT and CPT to further assist in classifying geologic units. We followed empirical models developed in Gillins and Bartlett (2012a) to estimate SPT blow counts from CPT penetration resistance data.

Figure 5.2 shows that the majority of the study area consists of site class E soil. Holocene fine-grained lacustrine sediments, stream alluvium, the North Ogden landslide complex, and very late Pleistocene to modern deltaic deposits are either soft or very loosely deposited (site class E). Late Pleistocene deltaic deposits and the East Ogden landslide complex appear somewhat stiffer (site class D). Although there are limited geotechnical data in this area, alluvial fans deposited from mountain canyon streams, and gravel-grained lacustrine sediments deposited along the upper-most shoreline of Lake Bonneville are typically dense, with shallow deposits overlying mountain bedrock. Hence, we map these units as site class C which conformed to the class mapped by McDonald and Ashland (2008).

Table 5.1. NEHRP site class definitions (from ASCE 7 2010)

Site Class	Description	$V_{s,30}$ (m/s)	$\overline{N}$
B	Rock	760 to 1520	N/A
C	Very dense soil and soft rock	370 to 760	> 50
D	Stiff soil	180 to 370	15 to 50
E	Soft clay soil	< 180	< 15

We used a midrange $V_{s,30}$ value in the aforementioned new attenuation models within each mapped soil site class zone. More specifically, we input: $V_{s,30}$ = 537 m/s for site class C, 259 m/s for site class D, and 180 m/s for site class E.

Because site class C sediments have low to no susceptibility to liquefaction, we were mostly concerned with site class D and E soils. For a 500-year return period event for the study area, the new attenuation models returned PGA values varying from 0.24 to 0.26 units of gravity (g) in areas classified as site class E; values were just slightly lower (0.22 to 0.24g) in areas classified as site class D. For a 2,500-year return period event, the new attenuation models returned PGA values which were significantly larger: 0.42 to 0.52g in areas classified as site class E, and 0.52 to 0.59g in areas classified as site class D. These larger PGA values (particularly from the 2,500-year return period seismic event) greatly increase the likelihood of triggering liquefaction in susceptible sediments.

Brief Review of the Mapping Method

We implemented our proposed method (Gillins and Bartlett 2012b) to map the median estimate of the probability of liquefaction triggering and the probability of lateral spread displacement exceeding specified thresholds (i.e., 0.3 or 0.6 meters) for the two scenario earthquake events. To estimate the probability of liquefaction-induced lateral spread displacement exceeding certain distances given a scenario event, we solve the probability chain shown in eqn. (5.1).

$$P[D_H > y] = P[D_H > y \mid L] \cdot P_L \tag{5.1}$$

where D_H is the predicted lateral spread displacement given the scenario seismic inputs, y is a specified displacement threshold, L is the triggering of liquefaction, and P_L is the probability of liquefaction triggering given the scenario seismic inputs.

In this paper, we briefly review our method to map the probabilities in eqn. (5.1). Refer to Gillins and Bartlett (2012b) for more details on analysis of the data in Weber County and a full description of the mapping method. We began our analysis by reducing available SPT and CPT data in the geotechnical database. For each of the investigations, we found the necessary geotechnical variables for liquefaction assessment (along with their uncertainty), and grouped these variables according to their mapped geologic unit. Due to the somewhat limited number of available geotechnical investigations in the study area, we analyzed the dispersion of the geotechnical variables between geologic units of similar depositional environment. This analysis revealed it was appropriate to pool the data into 11 deposit classes, as shown in Table 4.1. Pooling data increases the sampling size of SPT/CPT investigations within each geologic unit, thereby improving estimates of the total variability of geotechnical properties within a given unit.

Subsequently, we input gridded topographical points to capture topographic variations in the study area. In general, the grid points were evenly spaced every 30 meters. However, near the Ogden and Weber Rivers, we decreased the grid spacing to 10 meters to capture the influence of the river channels. Bartlett and Youd (1992) found it important to model topographic conditions because the magnitude of lateral spread displacement was highly correlated with the degree of ground slope, or the distance and height of a nearby free-face, such a river channel. At each grid point, we extracted the

following mapped values: (1) ground slope and/or distance and height of a nearby free-face (based on Digital Elevation Models from the USGS National Elevation Dataset); (2) surficial geologic deposit and age (Figure 4.1); and, (3) site classification (Figure 5.2). For each grid point, we input the mean seismic variables at the ground surface based on the site classification and the interactive deaggragation of the seismic hazard at the point.

Finally, we solved eqn. (5.1) at each gridded point using the Monte Carlo random sampling method. In this method, we randomly sampled geotechnical variables for a grid point corresponding to its associated geologic deposit. This random sampling was weighted (or nonuniform based on semivariance analysis) according to the proximity of the grid point to an SPT or CPT borehole or sounding. Next, we computed P_L from the liquefaction potential curves developed by Cetin et al. (2004) for SPT-based data, and Moss et al. (2006) for CPT-based data. We accounted for the influence of age by applying an age correction factor (Hayati and Andrus 2009). We also accounted for uncertainty in the empirical models by treating their results as normally distributed random variables. Afterwards, we calculated $P[D_H > y \mid L]$ for a desired threshold, y, based on our empirical model to predict lateral spread displacement from available data (Gillins and Bartlett 2012a). Lastly, we repeat the random sampling process numerous times until we have defined a distribution of outcomes (i.e., probabilities of liquefaction hazard) at a gridded point. Ultimately, we solved all grid points in the study area to produce the liquefaction hazard maps for both a 500-year return period seismic event and a 2,500-year return period seismic event.

Probabilistic Liquefaction Triggering Maps

At most gridded points, the mapping method returned probabilities of liquefaction triggering that were bimodally distributed. For example, Figure 5.3 shows histograms of resulting probabilities of liquefaction triggering at a sample grid point in the deltaic deposits. As can be seen, most of the values of P_L equal either 0 or 100%. There are several reasons for this bimodality in the liquefaction triggering probability as seen in Figure 5.3.

First, as is often the case, there were not any SPT/CPT investigations near the gridded point; hence, we modeled the total variability of geotechnical data from all investigations in the corresponding geologic deposit. Semivariance analysis indicates that the geotechnical data were spatially correlated, but only for a range equal to about 95 meters (Gillins and Bartlett 2012b). The combination of small range of spatial dependence, limited number of geotechnical investigations, and large total variability of geotechnical properties for many geologic deposits increases the uncertainty in the estimated probabilities.

Second, a major contributor to the bimodality of the distributions results from the strong ground motion of the two scenario seismic events. Over 90% of the equivalent cyclic stress ratio (*CSR*) values from PGA values for the 500-year return period earthquake are between 0.15 and 0.30, and for the 2,500-year return period earthquake are 0.30 to 0.60. Such large values of *CSR* for the latter event dramatically increase the probability of triggering liquefaction in loosely deposited, saturated, sandy soils. Thus, when assessing liquefaction for a relatively low SPT N value for a particular geologic

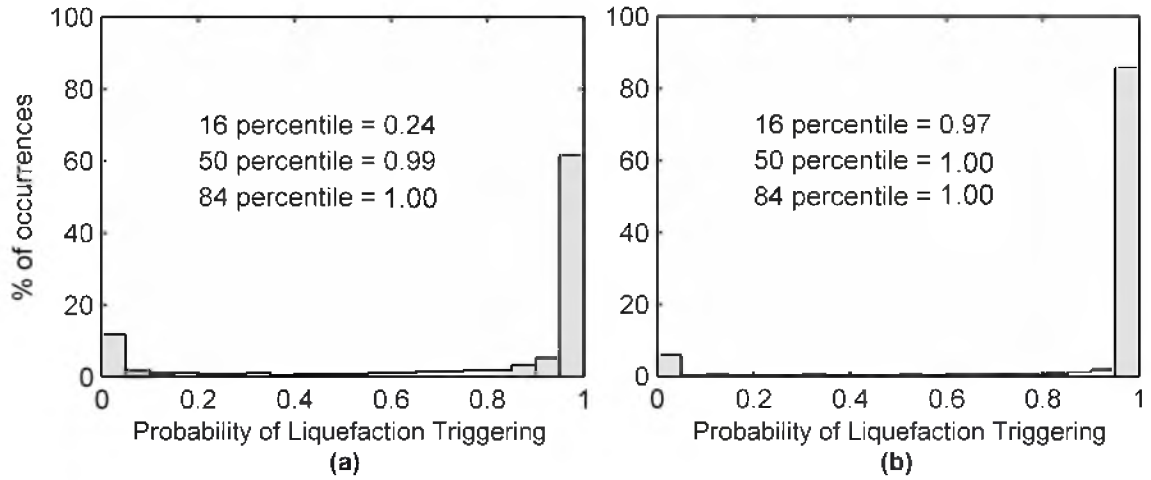

Figure 5.3. Histograms of the probability of liquefaction triggering at a grid point in the delta environment for: (a) a 500-year return period seismic event; and, (b) a 2,500-year return period seismic event

deposit, often we found that P_L equals 100%, especially for the 2,500-year return period seismic event. On the other hand, when assessing nonliquefiable sediments (e.g., clayey soils) from geotechnical tests in that same geologic deposit, P_L, of course equaled 0%.

Finally another reason for the bimodality of the distributions is due to the shape of the probabilistic liquefaction potential curves of Cetin et al. (2004) or Moss et al. (2006). Because these curves of equal probability plot relatively close together (i.e., not differential by large changes in $N_{1,60,cs}$) small variation in SPT penetration resistance can significantly affect estimates of P_L. This underscores the importance of obtaining high quality geotechnical data when performing liquefaction analyses.

Because the probability distributions like those shown in Figure 5.3 are non-normal, we mapped the median or 50th percentile probabilities instead of the mean probabilities. The median value represents a typical value at a given location and has a 50% probability of exceedance.

Figure 5.4 shows the 50th percentile probability of triggering liquefaction for a 500-year return period seismic event in the study area. Because there is a 10% probability of PGA values exceeding the critical value for this seismic event in a 50 year window, we must conclude that the study area has a relatively high risk of experiencing liquefaction, especially in the zones where P_L = 75 to 100%.

Figure 5.5 shows 50th percentile probabilities of liquefaction triggering for the 2,500-year return period seismic event. This figure indicates that such a large (or maximum considered) event could induce widespread liquefaction in the study area. It is anticipated that such severe liquefaction would likely cause significant and costly damage to large portions of the infrastructure in the study area.

Probabilistic Lateral Spread Ground Failure Maps

Liquefaction-induced damage is strongly correlated with the amount of horizontal displacement resulting from lateral spread. Lateral spread displacement on gently sloping ground is generally the most pervasive type of liquefaction-induced ground failure generated by earthquakes (NRC 1985). Structures at the head of lateral spread ground failures are commonly pulled apart; those at the toe are compressed or buckled. Buried objects, such as pipelines and piles, are often sheared by differential movement (Bartlett and Youd 1992). Accordingly, when analyzing liquefaction susceptibility, it is important to assess the potential amount of lateral spread displacement.

During lateral spread, blocks of mostly intact, surficial soil displace down slope or towards a free-face (i.e., channel or abrupt depression), along a shear zone formed by liquefaction (Bartlett and Youd 1992). This type of displacement typically occurs on

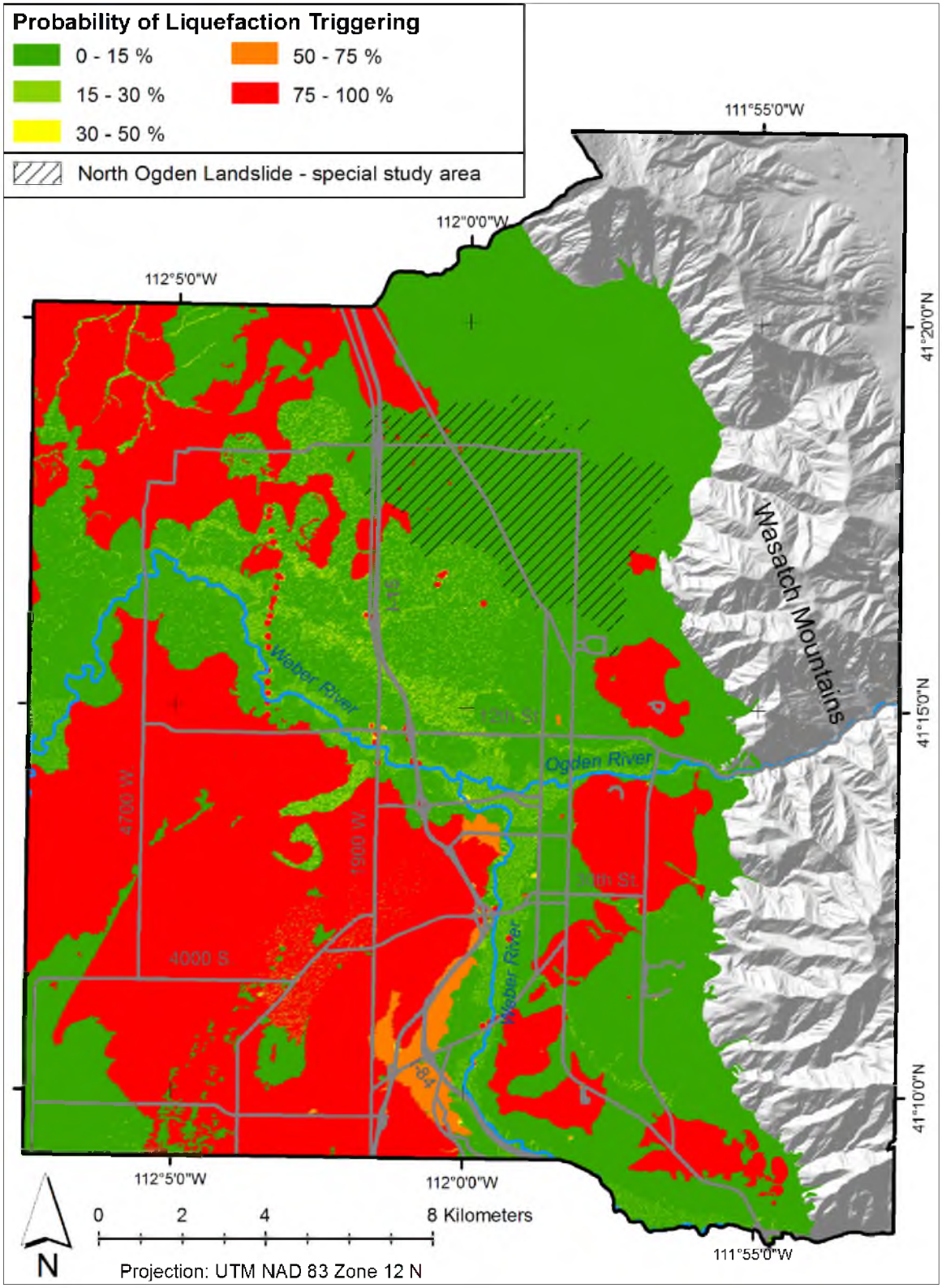

Figure 5.4. 50th percentile probabilities of liquefaction triggering for a 500-year seismic event; Weber County, Utah

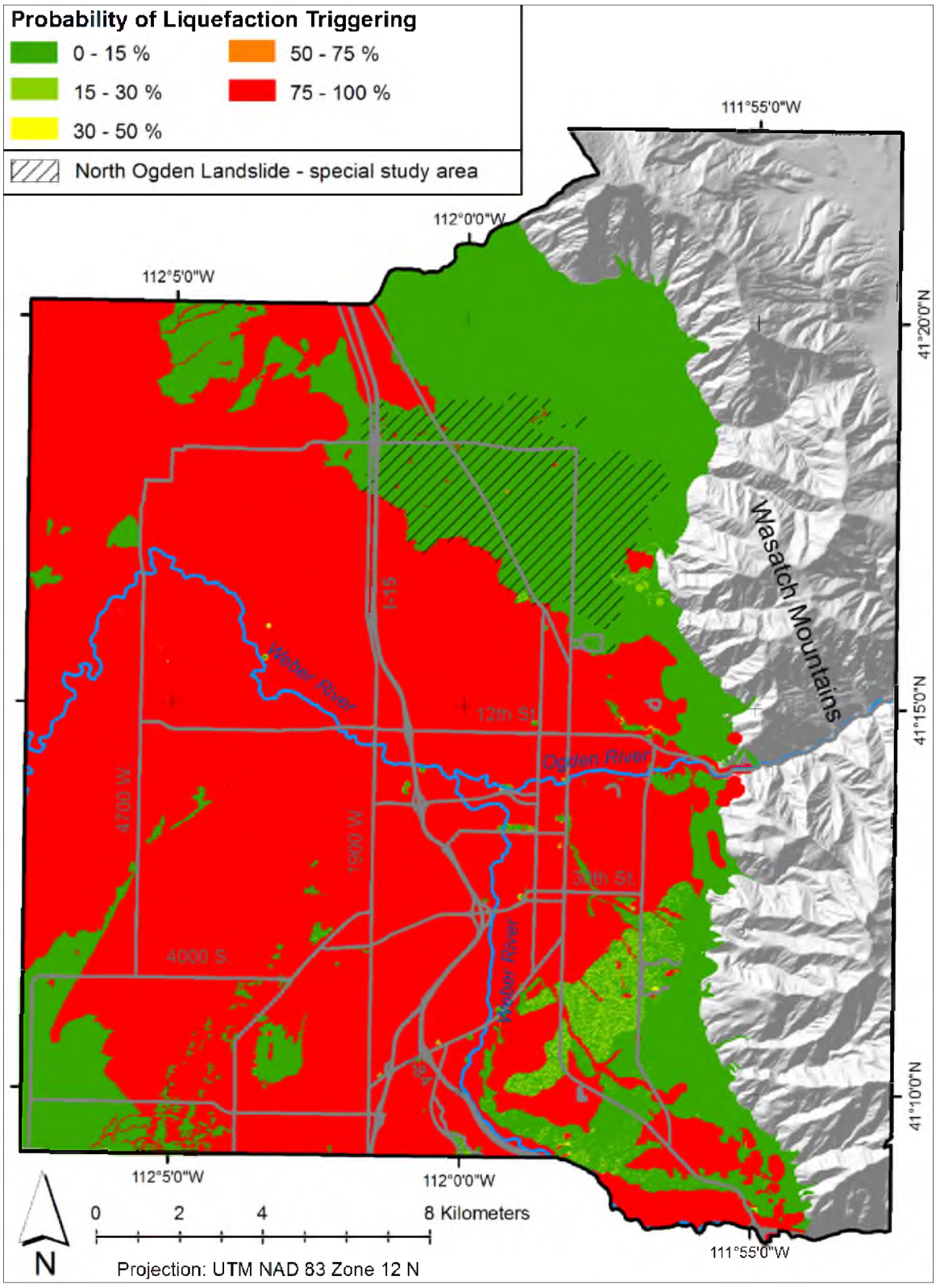

Figure 5.5. 50th percentile probabilities of liquefaction triggering for a 2,500-year seismic event; Weber County, Utah

gentle slopes that range from 0.3 to 5% (Youd 1978). Consequently, probabilistic lateral spread ground failure maps should include topographic conditions in the mapping methodology. Currently, it is popular to map the Liquefaction Potential Index, LPI (Iwasaki et al. 1978). Although LPI maps can indicate liquefaction-induced ground failure potential, they do not directly incorporate the influence of topography, nor do they provide estimates of the expected amount of lateral spread displacement in the mapped domain. The proposed method herein directly incorporates topographical effects by use of a digital elevation model (DEM).

The topographic factors (i.e., percent ground slope, S, and free-face ratio, W) in the Gillins and Bartlett (2012a) empirical model for estimating lateral spread displacement are based on multilinear regression of case history data originally compiled in Bartlett and Youd (1992) and further expanded in Youd et al. (2002). For most of the lateral spread ground failures in these case histories, S ranged from 0.1 to 6%; and, for most of the free-face ground failures, W ranged from 1 to 20%. Hence, the Gillins and Bartlett (2012a) empirical model is only valid for conditions within these ranges. Liquefaction on steeper slopes or larger free-face values may induce flow failures rather than lateral spreads. Flow failures usually travel farther distances than lateral spreads, and, in certain cases, can displace materials by tens of kilometers at velocities of tens of kilometers per hour (Youd 1984). For the study area, over 95% of the area susceptible to liquefaction has gentle sloping ground ($S \leq 5\%$) or small free-face ratio values ($W \leq 5\%$). Free-face ratio values generally begin to reach 20% only when within 35 meters of the channels of the Ogden or Weber Rivers.

Resulting lateral spread displacement hazard maps in Weber County show that estimates of the amount of horizontal displacement are highly correlated with the degree of ground slope. Similar to the probabilistic liquefaction triggering maps, the mapping method returns probabilities of lateral spread displacement that are not normally distributed (i.e., the distributions are bimodal or skewed). Thus, similar to the liquefaction triggering maps, we chose to map the median or 50^{th} percentile probability of lateral spread displacement exceeding specified thresholds. To show the uncertainty or variation of estimates in the mapped domain, we also mapped the 16^{th} and 84^{th} percentile probabilities. We selected these additional percentiles because they approximate the mean minus and mean plus one standard deviation critical values, respectively, in normally distributed populations. In non-normal distributions, the 84^{th} percentile value represents a conservative value in that it has only a 16% chance of being exceeded. Refer to the appendix of Gillins (2012) for maps of the 16^{th} percentile probabilities.

Figure 5.6 and Figure 5.7 show the 50^{th} and 84^{th} percentile probabilities of liquefaction-induced lateral spreads displacing more than 0.1 meters for a 500-year return period seismic event, respectively. These figures indicate moderate to high probabilities (i.e., 50 to 100%) that the horizontal displacements will exceed 0.1 meters for this event in numerous zones in the study area. However, the probabilities that the horizontal displacements will exceed larger thresholds (i.e., $y \geq 0.3$ meters) for this event are significantly smaller. Figure 5.8 and Figure 5.9 show the 50^{th} and 84^{th} percentile probabilities of liquefaction-induced lateral spreads displacing more than 0.3 meters for the same seismic event, respectively. As can be seen, only in the very late Pleistocene

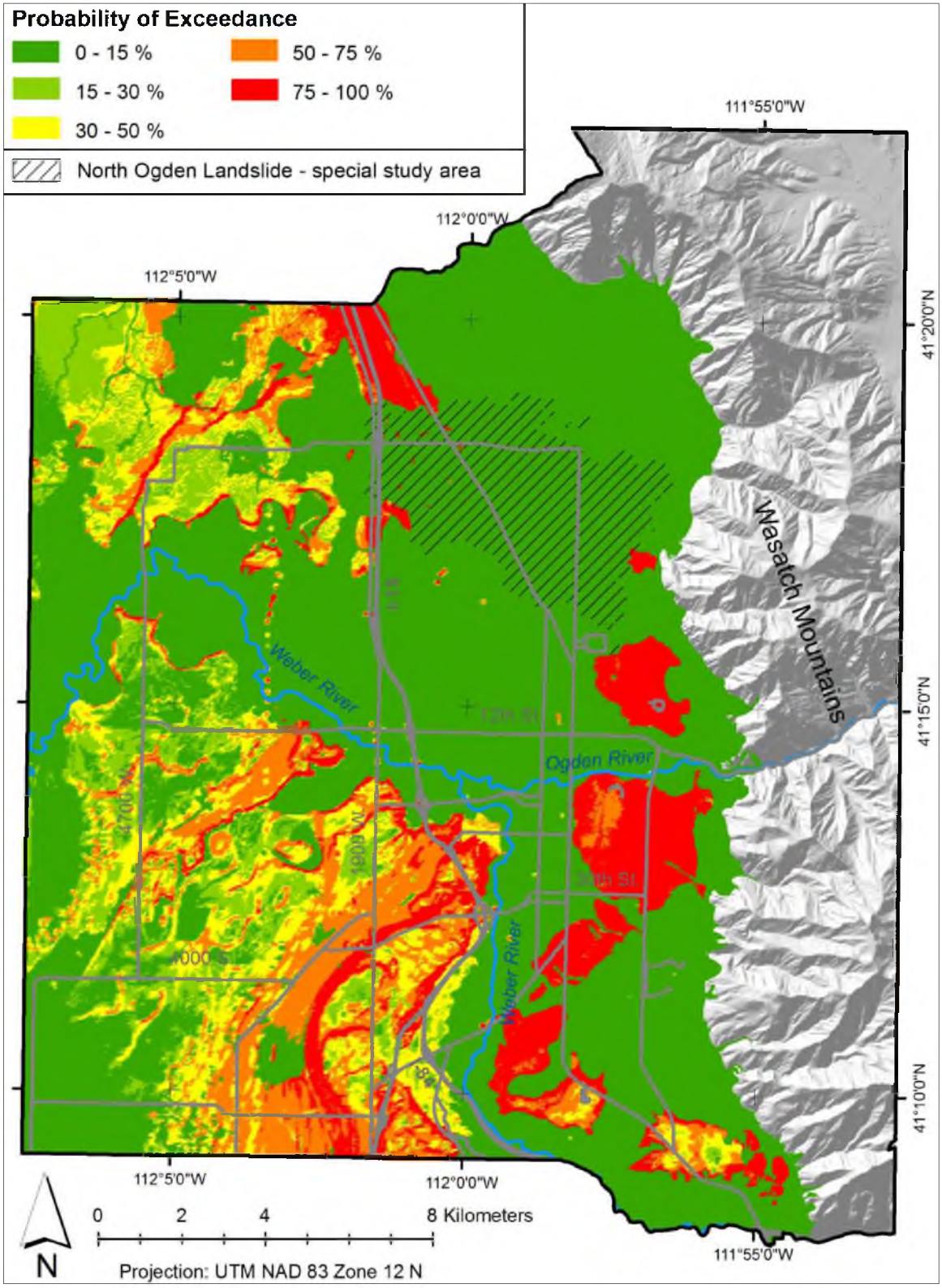

Figure 5.6. 50th percentile probabilities of lateral spread displacement exceeding 0.1 meters for a 500-year seismic event; Weber County, Utah

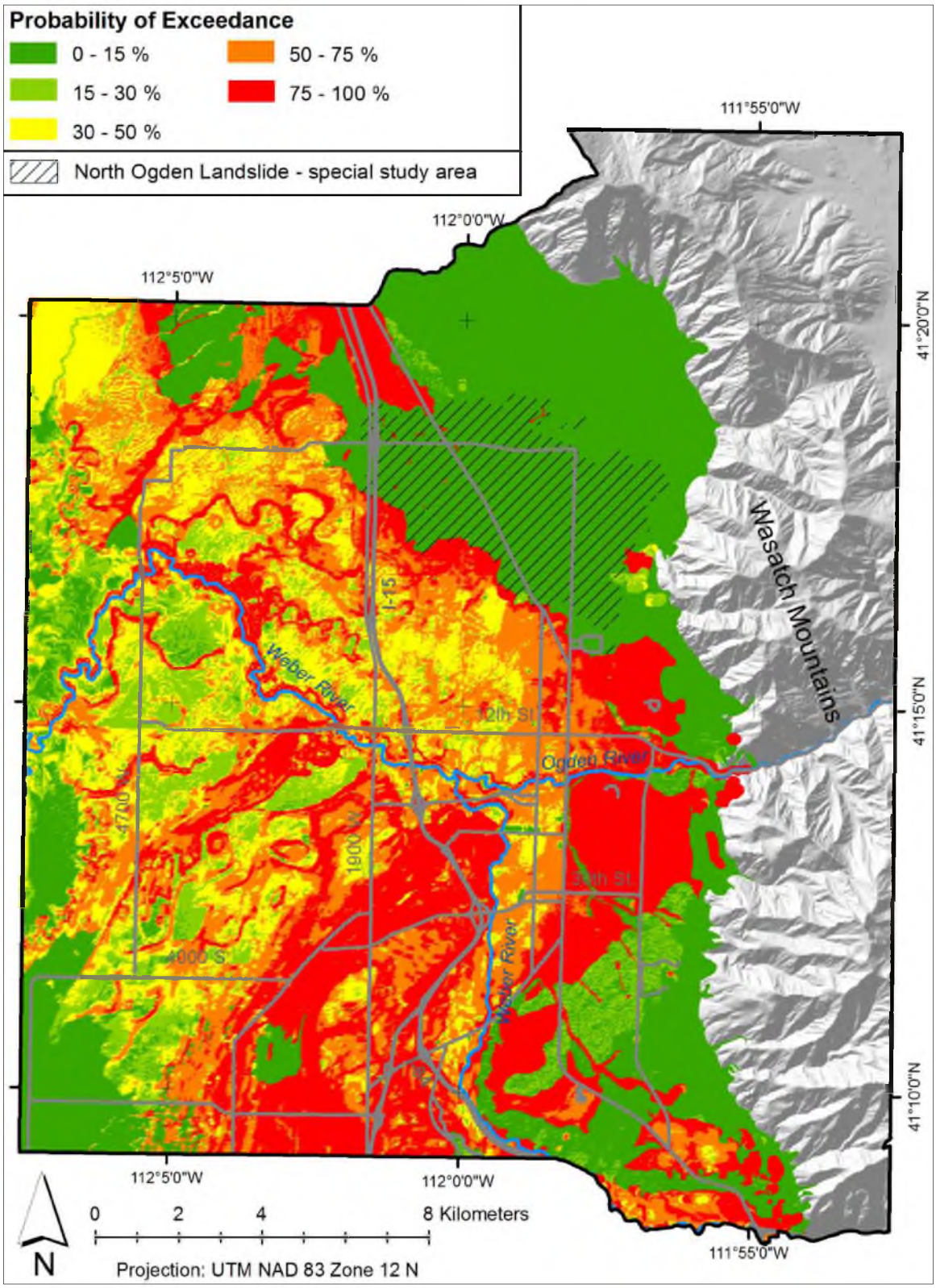

Figure 5.7. 84th percentile probabilities of lateral spread displacement exceeding 0.1 meters for a 500-year seismic event; Weber County, Utah

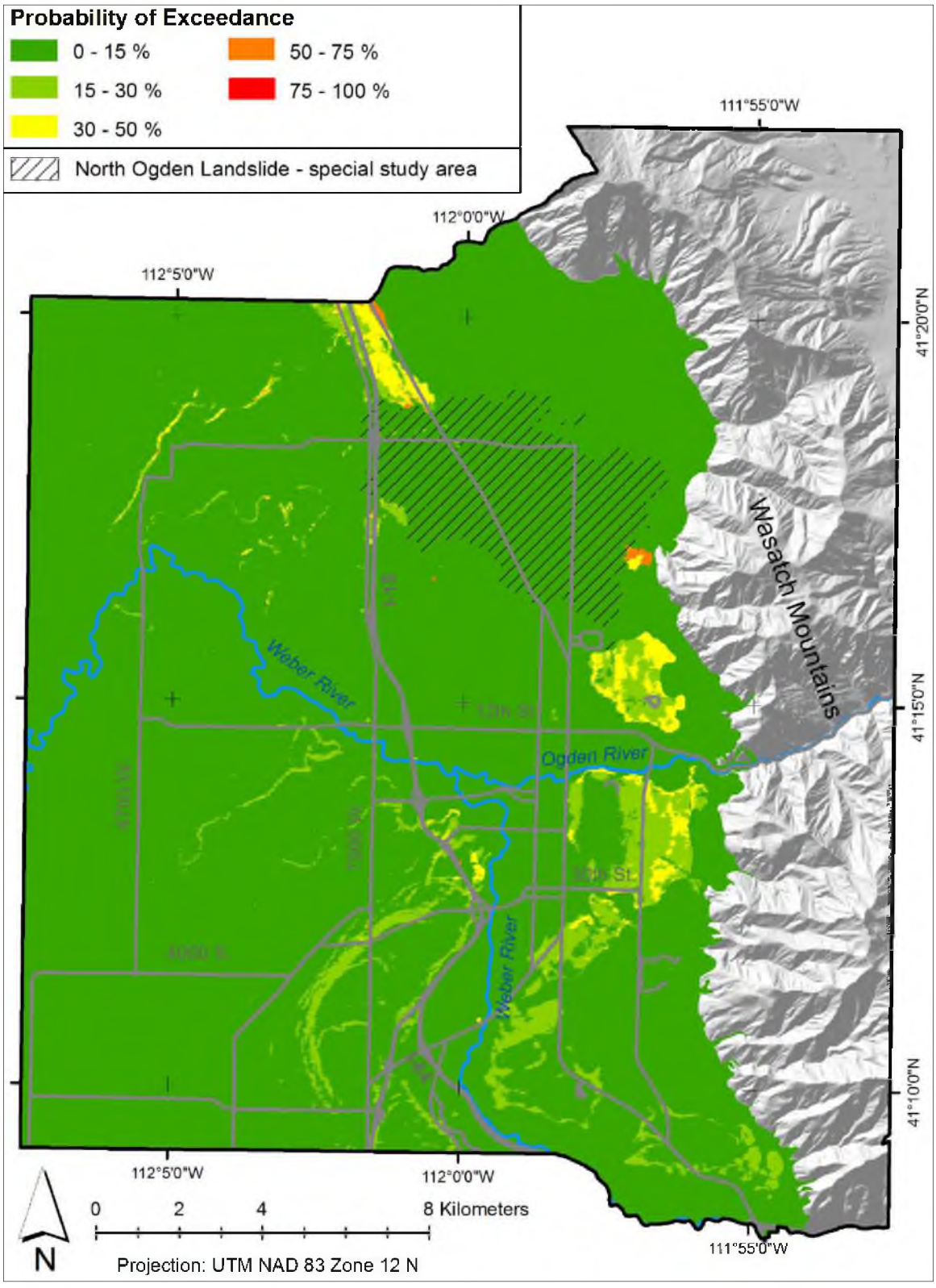

Figure 5.8. 50th percentile probabilities of lateral spread displacement exceeding 0.3 meters for a 500-year seismic event; Weber County, Utah

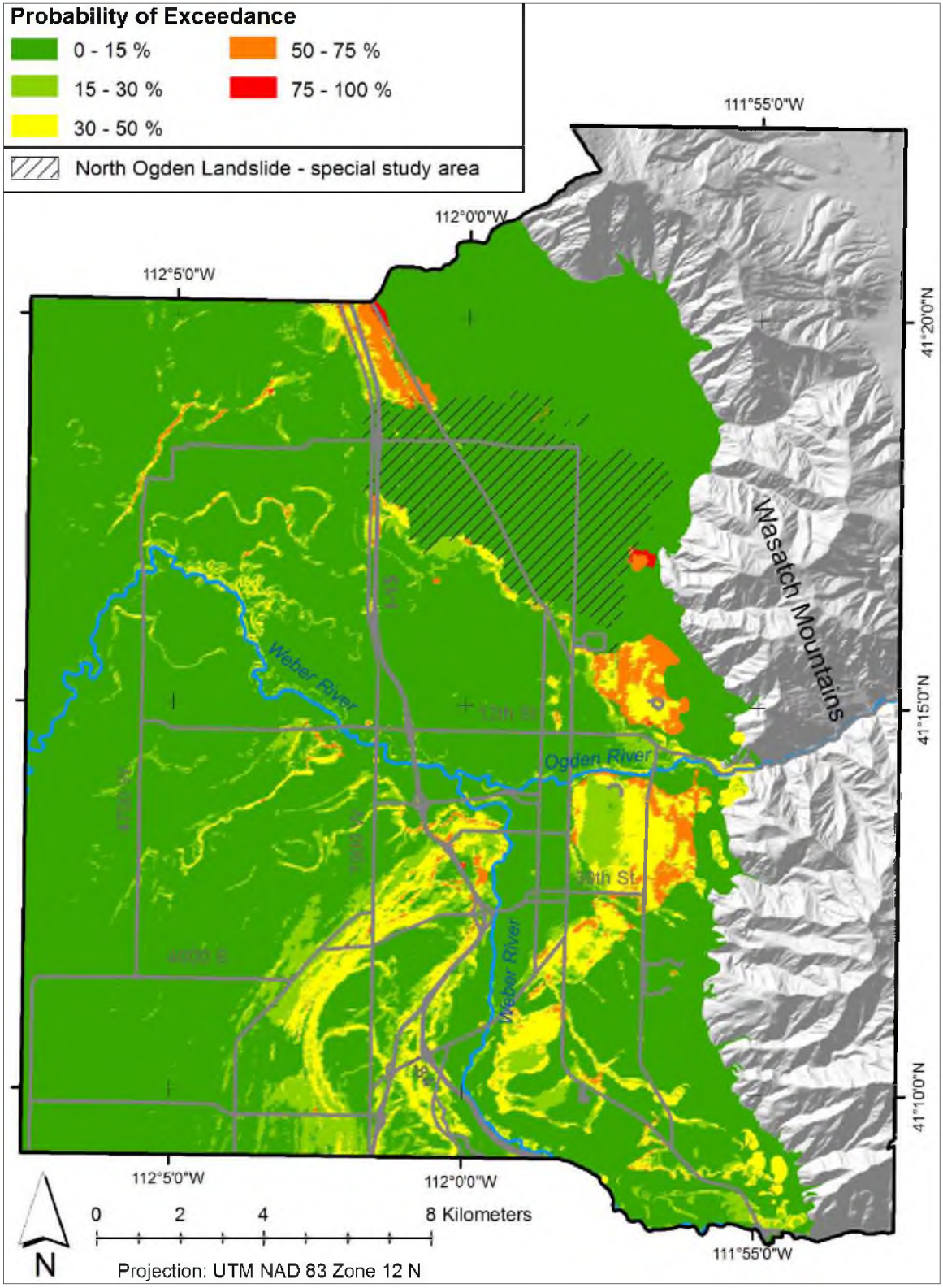

Figure 5.9. 84th percentile probabilities of lateral spread displacement exceeding 0.3 meters for a 500-year seismic event; Weber County, Utah

deltas where the ground slope is between 3 to 6% are values of exceedance probabilities greater than 30%.In these deltas where ground slope is between 1.5 to 3%, exceedance probabilities are only about 15 to 30%. Interestingly, for all zones in the study area with slopes less than 1.5%, there is low to no probability of lateral spreads exceeding 0.3 meters. This leads to the conclusion that the 500-year return period seismic event is not strong enough to induce lateral spreads greater than 0.3 meters in areas where ground slope is less than 1.5%. From mapping greater thresholds, we also find that 0.4 meters roughly represents the maximum probable displacement due to lateral spreading. In other words, we believe the probability of lateral spreads exceeding 0.4 meters in any of the study area is relatively low for the 500-year return period seismic event.

Unlike the 500-year return period event, we find that the 2,500-year return period event is capable of generating lateral spreads that exceed displacements of 0.6 meters in the study area, even for zones where ground slope is as little as 0.3%. Figure 5.10 and Figure 5.11 show the 50^{th} and 84^{th} percentile probabilities of lateral spreads displacing more than 0.1 meters for a 2,500-year return period seismic event, respectively. These figures indicate high probabilities that the horizontal displacements will exceed 0.1 meters for this large event in most of the study area susceptible to liquefaction. Figure 5.12 and Figure 5.13 depict the 50^{th} and 84^{th} percentile probabilities of lateral spreads displacing more than 0.3 meters for the same event, respectively. As can be seen, the exceedance probabilities are somewhat smaller. Finally, Figure 5.14 and Figure 5.15 show the 50^{th} and 84^{th} percentile probabilities of lateral spreads displacing more than 0.6 meters for the same event, respectively. These figures indicate that the most susceptible

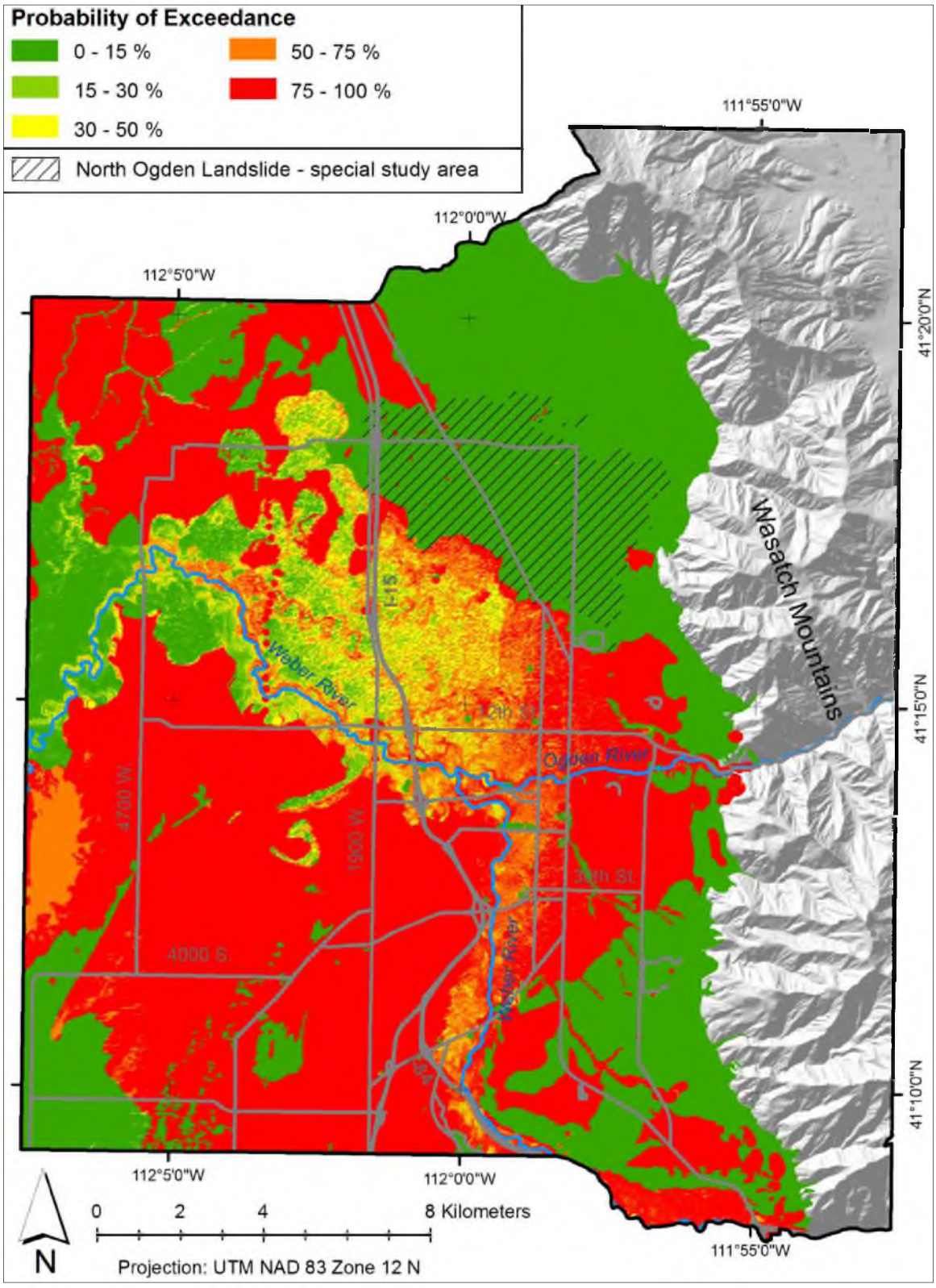

Figure 5.10. 50th percentile probabilities of lateral spread displacement exceeding 0.1 meters for a 2,500-year seismic event; Weber County, Utah

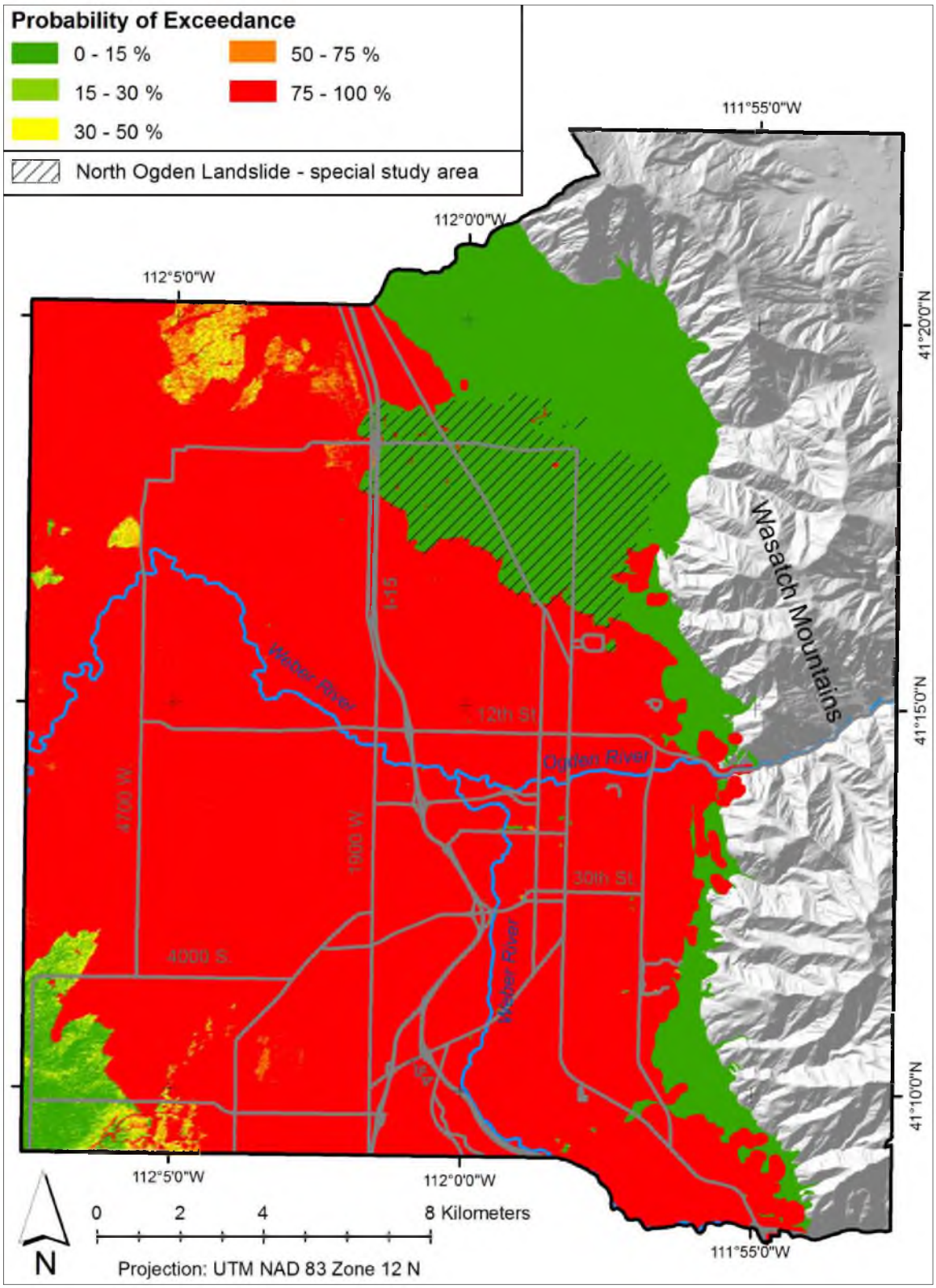

Figure 5.11. 84th percentile probabilities of lateral spread displacement exceeding 0.1 meters for a 2,500-year seismic event; Weber County, Utah

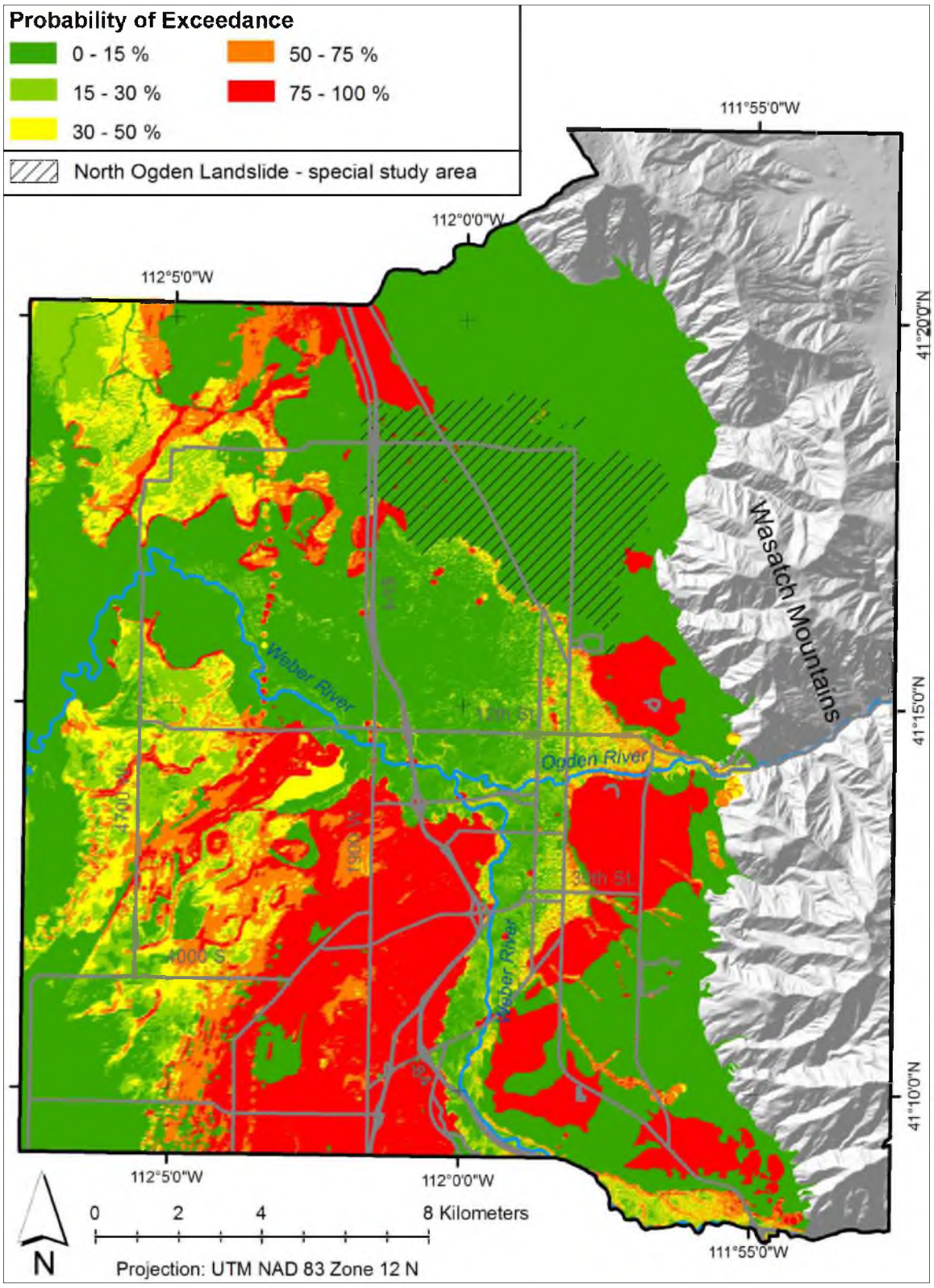

Figure 5.12. 50th percentile probabilities of lateral spread displacement exceeding 0.3 meters for a 2,500-year seismic event; Weber County, Utah

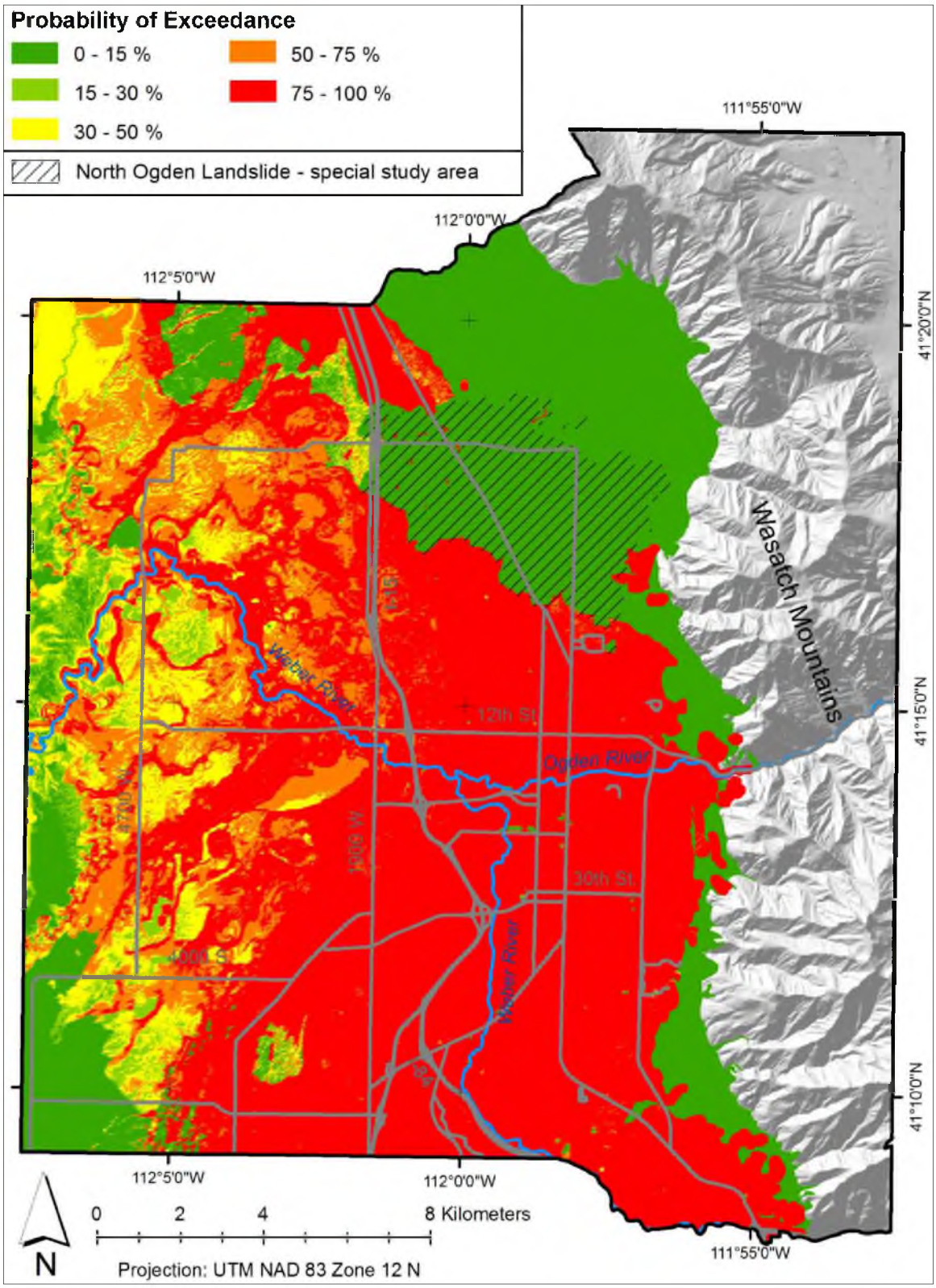

Figure 5.13. 84th percentile probabilities of lateral spread displacement exceeding 0.3 meters for a 2,500-year seismic event; Weber County, Utah

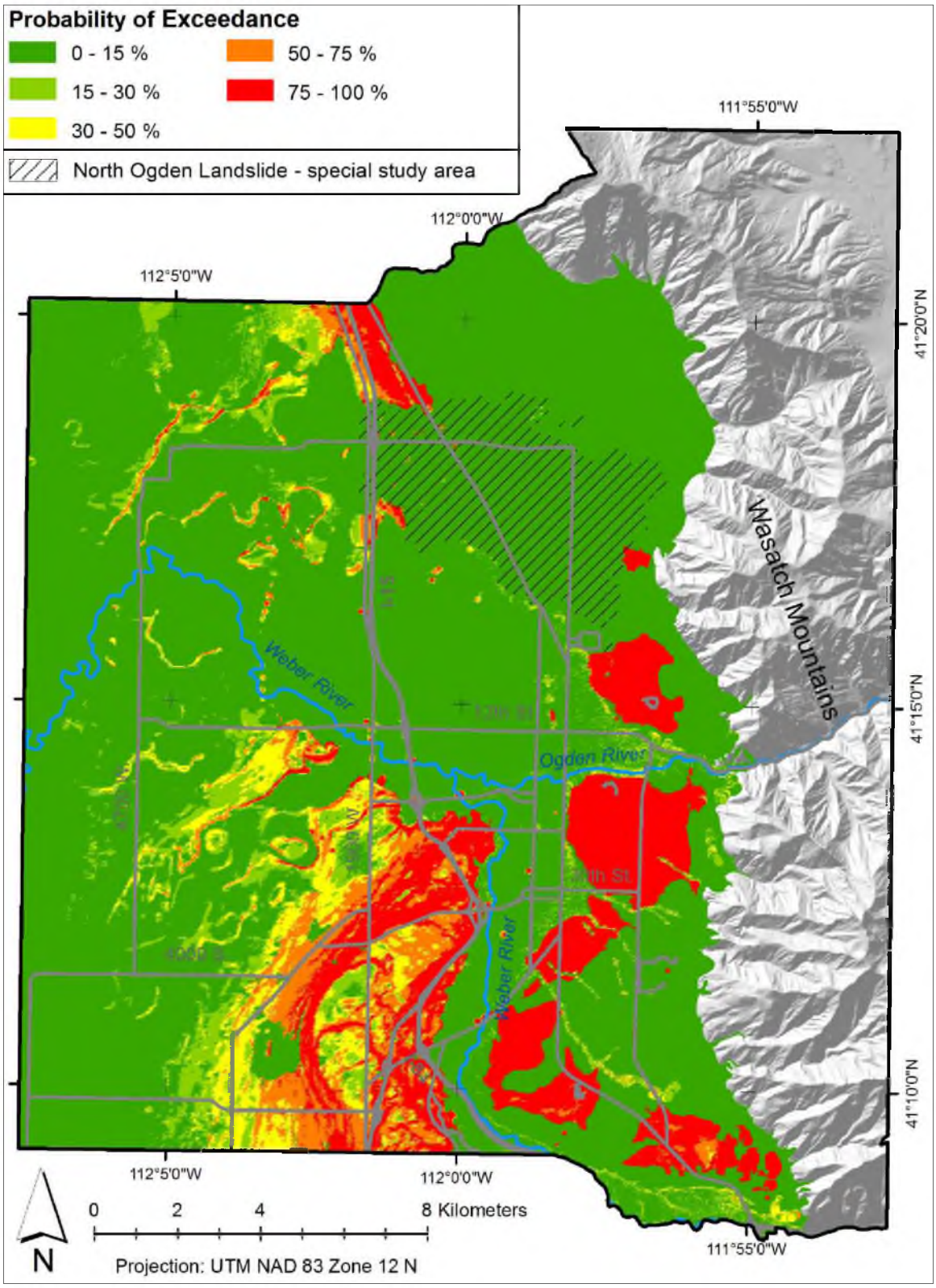

Figure 5.14. 50th percentile probabilities of lateral spread displacement exceeding 0.6 meters for a 2,500-year seismic event; Weber County, Utah

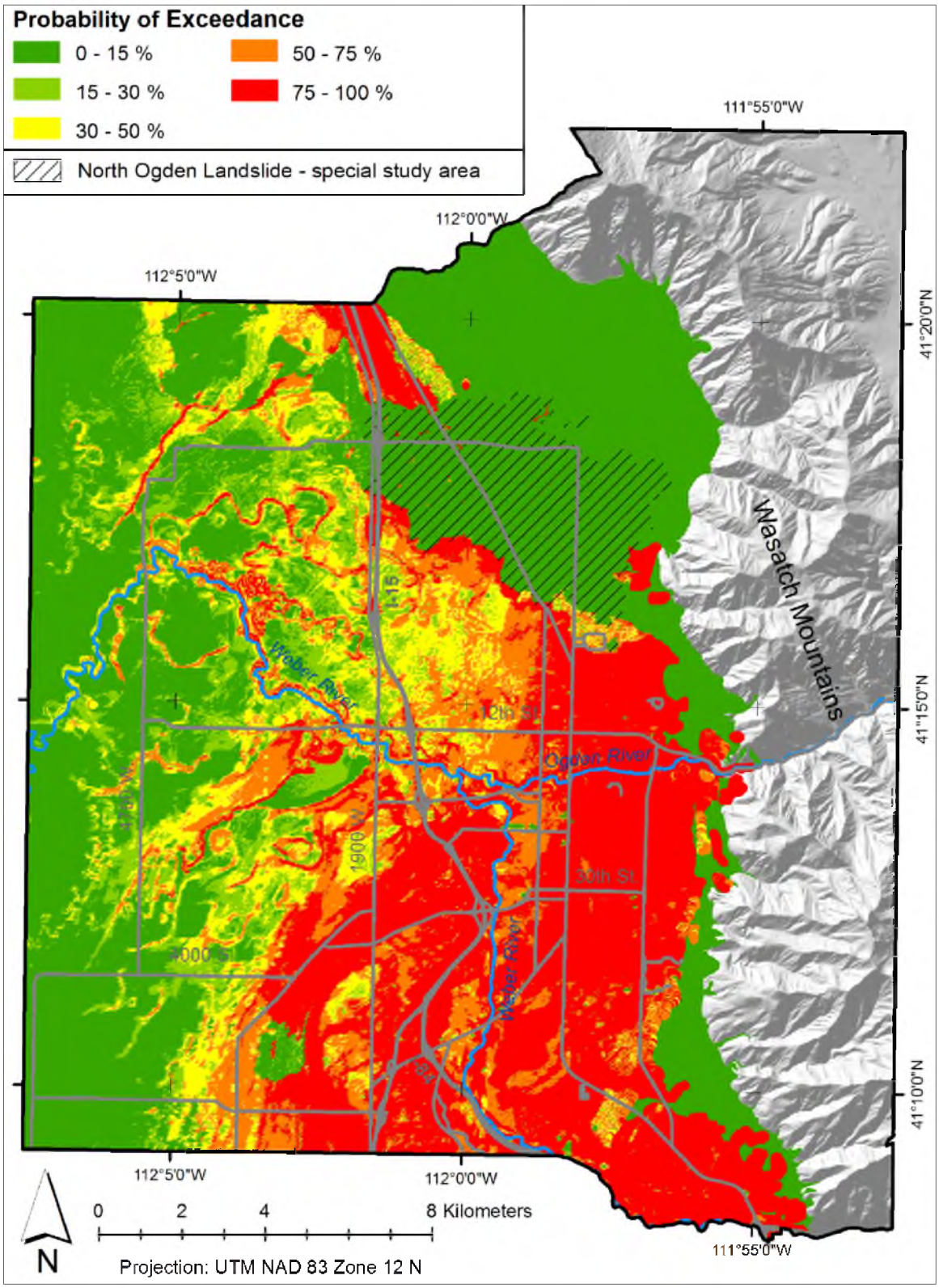

Figure 5.15. 84th percentile probabilities of lateral spread displacement exceeding 0.6 meters for a 2,500-year seismic event; Weber County, Utah

zones for large lateral spread displacement are within the very late Pleistocene deltas with ground slopes greater than 1.5%.Due to the higher ground motion near the fault, deltas within 3.5 kilometers of the Wasatch fault zone (mostly within the Ogden City area) have the highest and most uniform probability of lateral spreads exceeding 0.6 meters. Consequently, these zones have the highest risk of damage due to liquefaction-induced ground failures.

Discussion of Liquefaction Hazards by Geologic Deposit

Deltaic Deposits

Approximately 35% of the surficial geology of the study area consists of deltaic sediments deposited since the late Pleistocene by the Ogden and Weber Rivers. Almost all of these sediments were deposited roughly 9,500 to 14,500 years ago during and shortly after the final regression of Lake Bonneville (Qd_2 – Qd_{11}). Due to erosion of the shorelines of the lake, these deltaic sediments are dominated with loosely deposited, fine to medium-grained sands. Unfortunately, such saturated sands are highly susceptible to liquefaction. Investigators have found uniformly thick layers of these sands in much of the deltaic environments. For instance, considerable quantities of deltaic sand have been quarried in the southwestern portion of the study area, and there remain some active sand quarry sites (Sack 2005).

Seventy-seven of the available 82 SPT/CPT investigations in the deltaic deposits also discovered relatively thick layers of loosely deposited and saturated clean to silty sands. These 77 investigation sites have "typical values" of $T_{15,cs}$ ranging from 0.3 to 0.9 meters; and, the liquefiable layers have typical values of $N_{1,60,cs}$ ranging from 5 to 11. We

define "typical values" as values between the 16th and 84th percentiles of the dataset. Refer to Gillins and Bartlett (2012b) for development of the geotechnical distributions for each geologic deposit and definitions of these geotechnical variables. Briefly, $T_{15,cs}$ is the clean-sand equivalent cumulative thickness of soil in the upper 15 meters of the site profile that is susceptible to liquefaction and lateral spread (i.e., saturated, cohesionless, and with corrected SPT blow counts, $N_{1,60} \leq 15$). The variable $N_{1,60,cs}$ is defined as clean-sand equivalent corrected SPT blow counts. Young, saturated, cohesionless soils with $N_{1,60,cs} \leq 15$ have high probability for liquefaction during strong seismic events (Cetin et al. 2004). Gently sloping sites with $T_{15,cs}$ greater than 0.3 meters are highly susceptible to liquefaction-induced lateral spreads (Gillins and Bartlett 2012a).

The deltaic deposits in the study area appear highly susceptible to liquefaction due to the near-consistent observation of loosely deposited, saturated, sandy soils at each geotechnical investigation. Probabilistic liquefaction triggering maps indicate uniformly high probabilities (i.e., 100%) of liquefaction triggering in the deltaic deposits for either the 500-year or 2,500-year return period seismic event. As mentioned, almost all of the surficial deltaic sediments in the study area were deposited during the very late Pleistocene to the very early Holocene. Several investigators have noted that liquefaction resistance of soils increases with age. For example, Youd and Perkins (1978) noted that sediments deposited within the past few thousand years are generally more susceptible to liquefaction than older Holocene sediments; and, older Holocene sediments are generally more susceptible than Pleistocene sediments. Our mapping method accounted for the influence of age by applying an age correction factor, as defined by Hayati and Andrus (2009). Despite applying this age correction factor (which is approximately equal to 1.5

for the age of the surficial deltaic sediments), the probabilities of liquefaction triggering in the deltaic deposits remain high.

Probabilistic lateral spread displacement hazard maps show that gently sloping deltaic zones may have low to moderately high probabilities (i.e., 15 to 75%) of lateral spreads exceeding 0.3 meters for the 500-year return period seismic event, and uniformly high probabilities (i.e., 100%) of lateral spreads exceeding 0.6 meters for the 2,500-year return period event. The deltaic zones at risk of large lateral spread displacement are best illustrated in Figure 5.14. As can be seen, these zones are mostly within the Ogden City area, along the outer-most foothills of the Wasatch Mountains; or, in the south-central portion of the study area, in the deltaic components formed to the north of the Provo-level delta. In these zones, ground slopes range from 1.5 to 6%. In the higher elevations of these zones, it is probable that depths to groundwater are much deeper than recorded depths to groundwater at the lower elevation deltaic zones. Deeper groundwater depths at a site result in lesser amounts of saturated soils; hence, modeled values of $T_{15,cs}$ within these higher elevation zones might be somewhat conservative. However, based on the recorded groundwater depths from the available SPT and CPT investigations, we are unable to detect consistently deeper groundwater depths in these higher elevation zones. This may be explained by large fluctuations in groundwater depth from year to year, and season to season; and/or by localized areas containing perched groundwater. Investigators have noted perched groundwater at many locations in the study area, particularly along bluffs above streams incised in the river deltas, and even at higher elevations in the eastern Ogden City area (Yonkee and Lowe 2004).

Stream Alluvium Deposits

Approximately 30% of the study area consists of stream alluvium deposited mostly during the Holocene by the Ogden and Weber Rivers (Qal_1, Qal_2). Grain size and sorting of the stream alluvium sediments vary with the location of an exposure as well as with depositional sub-environments. At lower map elevations, such as near the Weber River west of Interstate 15, finer grained sizes predominate and the river channel is narrow and deep (Sack 2005). Farther upstream, along the Weber and Ogden River in the eastern and south-central parts of the study area, wider and shallower channels tend to reflect coarser loads, predominately of cobbles, gravels, and gravelly sands (Yonkee and Lowe 2004). This leads to the hypothesis that geotechnical variables describing the stream alluvium sediments should be divided into two groups: one group for finer sediments at lower elevations, and another group for coarser sediments at higher elevations. Although SPT investigations in stream alluvium deposits near the Ogden River tend to reveal denser and coarser sediments than elsewhere in the study area, there are insufficient data to support this hypothesis. Instead, geotechnical data from the SPT and CPT investigations in the stream alluviums seem highly variable with little spatial distinction.

Due to the high variability in geotechnical data, mapped probabilities of liquefaction ground failure in the stream alluvium deposits have large uncertainties. Of the available 171 SPT/CPT investigations in the stream alluvium deposits, 101 (or 59%) discovered a layer of loosely deposited, saturated, and cohesionless soil. These 101 investigation sites have typical values of $T_{15,cs}$ ranging from 0.1 to 0.7 meters; and, the liquefiable layers have typical values of $N_{1,60,cs}$ ranging from 4 to 13. Hence, although

only three-fifths of the investigations identified a liquefiable layer of sediment, these identified layers are very loosely deposited (thus, highly susceptible to liquefaction) and potentially thick enough for lateral spread ground failures in zones with sufficient slope, given large-magnitude seismic events.

The high and localized variability of geotechnical variables highlight the need to carefully characterize site conditions when assessing liquefaction hazards in the stream alluvium deposits. Some zones contain loosely deposited, sandy sediments that are highly susceptible to liquefaction-induced ground failures. Other zones contain dense and very coarse sediments that are not susceptible to liquefaction.

Fine-Grained Lacustrine Deposits

Approximately 8% of the study consists of thin layers of mixed lacustrine sediments of Lake Bonneville and the Great Salt Lake which were deposited in near-shore and offshore settings below an elevation of 1,300 meters (Qlf). Unfortunately, there are a limited number of available geotechnical investigations in the lacustrine deposits in Weber County. To improve estimates of the total variability of geotechnical properties in these deposits, we combined the limited geotechnical data in Weber County with data from investigations in similar lacustrine in Salt Lake County. We postulate that lacustrine sediments from Lake Bonneville and the Great Salt Lake are similar in both of these counties. However, we recognize the need for more geotechnical investigations in Weber County to fully validate this postulate.

Fine-grained lacustrine deposits from both counties appear hardly susceptible to liquefaction, and likely not susceptible to lateral spreads. Geotechnical investigations in

these deposits commonly found silty clays, with some thin layers of silts and fine sands. Seventy-three percent of the geotechnical investigations found only cohesive sediments. Consequently, mapped probabilities of liquefaction triggering in the fine-grained lacustrine sediments are generally low. However, since slightly more than one-quarter of the investigations found relatively thin layers of liquefiable soil, there is some probability of liquefaction in localized areas for the larger 2,500-year return period seismic event. Nearly 60% of these liquefiable layers have values of $T_{15,cs}$ less than 0.4 meters. The majority of the fine-grained lacustrine deposits are located on flat ground (i.e., slopes < 0.3%) in the western portion of the study area. These flat surfaces further increase the resistance of the fine-grained lacustrine deposits to liquefaction-induced lateral spreads. Hence, the probability of significant lateral spread displacement in these flat lying locales is very low.

Undifferentiated Lacustrine and Alluvium Deposits

Approximately 9% of the study consists of complexly inter-lain sediments of fine-grained lacustrine and alluvium, deposited over approximately the past 12,500 years (Qla). Sheet wash, gullies, small alluvial fans, and shallow ephemeral channels have re-worked the lake sediments such that neither depositional signature dominates (Sack 2005). These fluvial processes have partially eroded and buried shoreline bluffs, resulting in predominantly loosely deposited, fine sands to sandy silts.

The Qla deposits are highly susceptible to liquefaction due to the near-consistent observation of loosely deposited, saturated, cohesionless soils at each geotechnical investigation. Forty-two of the available 43 SPT/CPT investigations in the Qla deposits

discovered thick layers of loosely deposited and saturated clean sands, silty sands, and sandy silts. These 42 investigation sites have typical values of $T_{15,cs}$ ranging from 0.4 to 1.1 meters; and, the liquefiable layers have typical values of $N_{1,60,cs}$ ranging from 5 to 10. All of these geotechnical investigations found depths to groundwater less than 5 meters. Probabilistic liquefaction triggering maps indicate uniformly high probabilities (i.e., nearly 100%) of liquefaction triggering in the Qla deposits for either the 500-year or 2,500-year return period seismic event.

Fortunately, the majority of the Qla deposits are located on flat ground (i.e., slopes < 0.3%); and, these flat grounds are generally not susceptible to significant lateral spreads for the scenario events. However, two zones of Qla deposits have gentle slopes: (1) southwesterly of Pleasant View City in the north central portion of the study area (with ground slopes between 1 to 2%); and (2) near the center of Roy City in the south-central portion of the study area (with ground slopes between 0.5 to 1.5%). Probabilistic lateral spread displacement hazard maps show that zone 1 has low to moderately high probabilities (i.e., 15 to 75%) of lateral spreads exceeding 0.3 meters for the 500-year return period seismic event; and, both zones have moderate to high probabilities (i.e., 30 to 100%) of lateral spreads exceeding 0.6 meters for the 2,500-year return period seismic event.

Landslide Deposits

The surficial geology of the study area includes two prehistoric liquefaction-induced landslides: the East Ogden complex (Qms_3) which makes-up less than 5% of the surficial geology of the study area; and the North Ogden complex (Qmq_2) which makes-

up roughly 8%. Geomorphic features within these two landslides, such as scarps, hummocks, closed depressions, and transverse lineaments, suggest complex flow failures, lateral spreads, translational slides, and slumps (Harty and Lowe 2003). These complexes contain mixtures of clay, silt, fine sand, and gravel, redeposited after ground failures. Hence, geotechnical properties in these landslides are likely locally variable.

Geologic evidence indicates that liquefaction-induced land-sliding occurred at least once in the eastern Ogden City area, approximately 13,000 to 13,500 years ago (Harty and Lowe 2003). At that time, the area was likely close to the shoreline of the lake. Although groundwater levels are deeper today, perched groundwater is common in the eastern Ogden City area. Forty-two percent of the geotechnical investigations in the landslides east of Ogden City identified groundwater levels less than 3 meters deep; furthermore, 77% identified groundwater levels less than 6 meters deep.

Due to the high variability of geotechnical properties in the East Ogden landslide complex and apparent shallow groundwater levels, there is some probability for liquefaction-induced ground failures in localized zones. Only 40% of the SPT investigations in the landslides east of Ogden City found a layer susceptible to liquefaction. Most of these liquefiable layers are very fine sands and silts. Nearly 60% of these layers have values of $T_{15,cs}$ less than 0.2 meters. The small values of $T_{15,cs}$ suggest low probability of large-magnitude lateral spreads due to liquefaction in this complex. However, perched groundwater and steep slopes within this complex may result in localized lateral spread ground failures for the larger 2,500-year return period seismic event.

Recent mass movement and shallow groundwater levels recorded from geotechnical investigations (i.e., mostly less than 5 meters) within the North Ogden landslide complex demonstrates that there is some likelihood of future liquefaction-induced ground failures in localized areas. Geomorphic and geologic evidence indicates that the North Ogden landslide complex may have initially moved as a single mass during a large earthquake in the early Holocene or late Pleistocene, and since then, parts of the landslide may have moved three or four more times (Harty and Lowe 2003). Radiocarbon dating suggests initial flow failures deposited sediments approximately 7,860 years ago (Harty and Lowe 2003).

However, only one of the available 11 SPT investigations in the North Ogden landslide complex found a layer of liquefiable soil. Since the geotechnical investigations consistently encountered cohesive sediments, mapped probabilities of liquefaction ground failures in the North Ogden complex are generally very low. This leads to the conclusion that there are insufficient geotechnical data to fully characterize this large landslide complex. Hence, we hatch this complex as a special study area in the probabilistic liquefaction hazard maps.

Since the two landslide complexes have locally variable geotechnical properties, we recommend collecting additional geotechnical data to carefully characterize site conditions during assessment of liquefaction hazards.

Conclusions

This mapping project better defines liquefaction hazards in Weber County over previous mapping efforts. The new maps incorporate: (1) state-of-the-art probabilistic

liquefaction analysis techniques (Cetin et al. 2004, Moss et al. 2006, Gillins and Bartlett 2012b); (2) strong ground motion estimates from the current (2008) USGS National Seismic Hazard Mapping Project (Peterson et al. 2008); (3) a larger geotechnical database—allowing more robust characterization of the various geologic deposits; and, (4) recently published surficial geologic maps at the 7.5-minute (1:24,000) scale (Crittenden and Sorenson 1985, Harty and Lowe 2003, Yonkee and Lowe 2004, Sack 2005, Harty and Lowe 2005). In addition, these new liquefaction hazard maps account for variations in topography, influence of age, spatial dependence, and major sources of uncertainty. Due to the large uncertainties, we produced maps for 16^{th}, 50^{th} and 84^{th} percentile probabilities and identified zones with high probability of liquefaction triggering. In addition, the new maps also estimate probabilities of lateral spread displacement exceeding specified thresholds. Such displacement hazard maps are useful for identifying areas susceptible to damaging liquefaction-induced ground failure.

Unfortunately, the probabilistic liquefaction triggering maps indicate high probability of widespread liquefaction along the Wasatch Front in Weber County during a 500-year return period seismic event; and, exceptionally widespread liquefaction during the larger 2,500-year return period seismic event. This is because: (1) the study area is filled with loose, cohesionless sediments deposited in deltaic, fluvial, and lacustrine environments since the late Pleistocene; (2) Of the 408 available SPT/CPT investigations in the study area, 390 (or 96%) identified shallow groundwater depths (i.e., less than 9 meters); and, (3) the study area is near the seismically active Wasatch fault zone, which is capable of generating earthquakes of M = 7, or greater (Nelson and Personious 1993). Because geotechnical investigations consistently found relatively thick, loose,

cohesionless layers in the sand-dominated deltaic (Qd_2 – Qd_{11}) and undifferentiated lacustrine/alluvium sediments (Qla), these geologic deposits appear to have uniformly high probabilities of liquefaction triggering for either of the two scenario seismic events. Additionally, stream alluvium and landslide deposits apparently have some probability for liquefaction triggering in localized areas. Geotechnical properties of the stream alluvium and landslide deposits are highly variable.

Zones of liquefiable sediments with sufficient slope have low to moderately high probabilities of lateral spreads exceeding 0.3 meters for the 500-year return period seismic event; and high probabilities of lateral spreads exceeding 0.6 meters for the 2,500-year return period seismic event. In general, if ground slopes are less than 1.5%, there is no probability of lateral spreads exceeding 0.3 meters for the 500-year event. However, even in areas where ground slope is as little as 0.3%, the 2,500-year event appears capable of generating large lateral spreads exceeding 0.6 meters.

The results shown in the new liquefaction displacement hazard maps lead to two conclusions. First, the magnitude of liquefaction-induced displacements is highly correlated to the degree of ground slope. Therefore, it is important to capture variations in topography when mapping liquefaction-induced ground failure hazards. There is high probability for significant lateral spread displacement in deposits that are both susceptible to liquefaction and have ground slopes between 3 to 6% in the study area. Second, the high probability of widespread liquefaction and the potential for large lateral spread displacement in various gently sloping zones indicates substantial risk for liquefaction-induced ground failures in the study area during large-magnitude seismic events. Due to this substantial risk, we recommend additional work, such as performing site-specific

analyses, where appropriate, to further characterize subsurface conditions and thereby reduce uncertainties in the mapped liquefaction hazards. The new hazard maps are based on available and varying quality geotechnical data. Certainly, performing additional and more specific geotechnical investigations will improve understanding of groundwater conditions, site profiles, soil properties, etc.

In addition, we encourage communities to develop a strategic emergency plan to mitigate potential damage due to liquefaction ground failure in high hazard areas. Such plans should identify provisions to protect or retrofit critical infrastructure and lifelines. Furthermore, the plan should establish alternatives or redundancies should crucial infrastructure become inoperable. We also encourage the design and construction of communities that are resistant to liquefaction. We hope the new liquefaction hazard maps presented herein will aid and encourage local governments, planners, and engineers to improve the resiliency of their respective communities to earthquake hazards.

References

Anderson, L. R., Keaton, J. R., and Bay, J. A., 1994. *Liquefaction Potential Map for the Northern Wasatch Front, Utah, Complete Technical Report, Utah Geological Survey Contract Report 94-6*, Salt Lake City, UT.

Arabasz, W. J., Smith, R. B., and Richins, W. D. (editors) 1979. *Earthquake Studies in Utah, 1850-1978*, Special Publication, University of Utah Seismograph Stations, Salt Lake City, UT, 552 pp.

ASCE 7, 2010. *Minimum Design Loads for Buildings and Other Structures*, Structural Engineering Institute of the American Society of Civil Engineers, Danvers, MA, Chapter 20.

Ashford, S. A., Boulanger, R. W., Donahue, J. L., and Stewart, J. P., 2011. *Geotechnical Quick Report on the Kanto Plain Region During the March 11, 2011, Off Pacific Coast of Tohoku Earthquake, Japan, Report No. GEER-025a*, Geotechnical Extreme Events Reconnaissance (GEER) Association, Berkeley, CA, 20 pp.

Bartlett, S. F., and Youd, T. L., 1992. *Empirical Analysis of Horizontal Ground Displacement Generated by Liquefaction-Induced Lateral Spreads, Technical Report NCEER-92-0021*, National Center for Earthquake Engineering Research, Buffalo, NY.

Cetin, K. O., Seed, R. B., Kiureghian, A. D., Tokimatsu, K., Harder, L. F., Jr., Kayen, R. E., and Moss, R. E., 2004. Standard Penetration Test-based probabilistic and deterministic assessment of seismic soil liquefaction potential, *J. Geotech. Geoenviron. Eng.* **130**(12), 1314 – 1340.

Crittenden, M. D., Jr., and Sorenson, M. L., 1985. *Geologic Map of the North Ogden Quadrangle and Part of the Ogden and Plain City Quadrangles, Box Elder and Weber Counties, Utah, U.S. Geological Survey Miscellaneous Investigations Series Map I-1606*, Reston, VA, scale 1:24,000.

Currey, D. R., Atwood, G., and Mabey, D. R., 1984. *Major Levels of Great Salt Lake and Lake Bonneville, Utah Geological and Mineral Survey Map 73,* Salt Lake City, UT, scale: 1:750,000.

Gillins, D.T., 2012. *Mapping the Probability and Uncertainty of Liquefaction-Induced Ground Failure, Ph.D. Dissertation,* Department of Civil and Environmental Engineering, University of Utah, Salt Lake City, UT.

Gillins, D. T., and Bartlett, S. F., 2012. Multilinear regression equations for predicting lateral spread displacements from soil type and CPT data, *J. Geotech. Geoenviron. Eng.*, under review.

Gillins, D. T., and Bartlett, S. F., 2012b. A reliability-based approach to mapping the probability of liquefaction and lateral spread, *Earthquake Spectra*, under review.

Harty, K. M., and Lowe, M., 2003. *Geologic Evaluation and Hazard Potential of Liquefaction-Induced Landslides along the Wasatch Front, Utah, Utah Geological Survey Special Study 104*, Salt Lake City, UT, 40 pp., 16 pl.

Harty, K. M., and Lowe, M., 2005. *Interim Geologic Map of the Plain City Quadrangle, Weber and Box Elder Counties, Utah, Utah Geological Survey Open-File Report 451*, Salt Lake City, UT, 2 pl., scale 1:24,000.

Hayati, H., and Andrus, R. D., 2009. Updated liquefaction resistance correction factors for aged sands, *J. Geotech. Geoenviron. Eng.* **135**(11), 1683-1692.

Iwasaki, T., Tatsuoka, F., Tokida, K., and Yasuda, S., 1978. A practical method for assessing soil liquefaction potential based on case studies at various sites in Japan, in *Proc. 2nd Int. Conf on Microzonation,* San Francisco, CA, pp. 885-896.

Machette, M. N., Personious, S. F., and Nelson, A. R., 1992. Paleoseismology of the Wasatch fault zone – A summary of recent investigations, interpretations, and conclusions, in *Assessment of Regional Earthquake Hazards and Risk along the Wasatch Front, Utah, U.S. Geological Survey Professional Paper 1500-A-J,* P. L. Gori and W. W. Hays (editors), Reston, VA, pp. A1-A71.

Malde, H. E., 1968. *The Catastrophic Late Pleistocene Bonneville Flood in the Snake River Plain, Idaho, U S. Geological Survey Professional Paper 596,* Reston, VA, 52 pp.

McCalpin, J. P., and Nishenko, S. P., 1996. Holocene paleoseismicity, temporal clustering, and probabilities of future large (M > 7) earthquakes on the Wasatch fault zone, Utah, *Journal of Geophysical Research* **101**(B3), 6233-6253.

McDonald, G. N., and Ashland, F. X., 2008. *Earthquake Site Conditions in the Wasatch Front Urban Corridor, Utah, Utah Geological Survey Special Study 125,* Salt Lake City, UT, 41 pp., 1 pl., scale 1:50,000.

Miller, R. D., 1980. *Surficial Geologic Map along Part of the Wasatch Front, Great Salt Lake Valley, Utah, U.S. Geological Survey Miscellaneous Field Investigations Map MF-1198*, Salt Lake City, UT, 13 pp., scale 1:100,000.

Moss, R. E. S., Seed, R. B., Kayen, R. E., Stewart, J. P., Kiureghian, A. D., and Cetin, K. O., 2006. CPT-based probabilistic and deterministic assessment of in situ seismic soil liquefaction potential, *J. Geotech. Geoenviron. Eng.* **132**(8), 1032 – 1051.

National Research Council (NRC), 1985. *Liquefaction of Soils During Earthquakes*, National Academy Press, Washington D. C., 240 pp.

Nelson, A. R., and Personious, S. F., 1993. *Surficial Geologic Map of the Weber Segment, Wasatch Fault Zone, Weber and Davis Counties, Utah, U.S. Geological Survey Miscellaneous Investigations Series Map I-2199*, Salt Lake City, UT, scale 1:50,000.

Oviatt, C. G., Currey, D. R., and Sack, D, 1992. Radiocarbon chronology of Lake Bonneville, eastern Great Basin, USA, *Paleogeography, Paleoclimatology, Paleoecology* **99**, 225-241.

Pashley, E. F., Jr., and Wiggins, R. A., 1972. Landslides of the northern Wasatch Front, in *Environmental Geology of the Wasatch Front, 1971, Utah Geological Association Publication 1*, L. S. Hilpert (editor), Salt Lake City, UT, pp. K1 – K16.

Pechmann, J. C., and Arabasz, W. J., 1995. The problem of the random earthquake in seismic hazard analysis – Wasatch Front region, Utah, in *Environmental and Engineering Geology of the Wasatch Front Region, Utah Geological Association Publication 24*, W. R. Lund (editor), Salt Lake City, UT, pp. 77 – 94.

Petersen, M. D., Frankel, A. D., Harmsen, S. C., Mueller, C. S., Haller, K. M., Wheeler, R. L., Wesson, R. L., Zeng, Y., Boyd, O. S., Perkins, D. M., Luco, N., Field, E. H., Wills, C. J., and Rukstales, K. S., 2008. *Documentation for the 2008 Update of the United States National Seismic Hazard Maps, U.S. Geological Survey Open-File Report 2008–1128*, Reston, VA, 61 pp.

Sack, D., 2005. *Geologic Map of the Roy 7.5-Minute Quadrangle, Weber and Davis Counties, Utah, Utah Geological Survey Miscellaneous Publication 05-03*, Salt Lake City, UT, 22 pp., scale 1:24,000.

Smith, R. B., and Arabasz, W. J., 1991. Seismicity of the intermountain seismic belt, in *Neotectonics of North America*, Geological Society of America, D. B. Slemmons and E. R. Engdahl (editors), Boulder, CO, pp. 185-228.

Yonkee, A., and Lowe, M., 2004. *Geologic Map of the Ogden 7.5-Minute Quadrangle, Weber and Davis Counties, Utah, Utah Geological Survey Map 200*, Salt Lake City, UT, 42 pp., scale 1:24,000.

Youd, T. L., 1978. Major cause of earthquake damage is ground failure, *Civil Engineering—ASCE* **48**(4), 47-51.

Youd, T. L., 1984. Geologic effects—liquefaction and associated ground failure, in *Proc. of the Geologic and Hydrologic Hazards Training Program, U.S. Geological Survey Open-File Report 84-760*, C. Kitzmiller (compiler), Reston, VA, pp. 210-232.

Youd, T.L., and Perkins, D.M., 1978. Mapping liquefaction-induced ground failure potential, *Journal of the Geotechnical Engineering Division* **104**, No. GT4, 433-446.

CHAPTER 6

CONCLUSIONS

Major Findings from this Research

Liquefaction-induced ground failure can cause severe and costly damage to the built-up environment during major earthquakes. The first step of defense against such damage is to identify areas at significant risk. Once these areas are identified, planners, developers, and engineers can strategize approaches to mitigate the risk. This dissertation presented statistically-based methods to map estimates of the probability of liquefaction triggering and the probability of lateral spread displacements exceeding specified thresholds for a scenario seismic event. This method can be applied to assess hazard levels for other areas throughout the United States with significant risk of damage from liquefaction.

The mapping method uses the following: (1) a newly developed empirical model for probabilistic lateral spread analysis; (2) state-of-the-art probabilistic liquefaction triggering analyses (Cetin et al. 2004, Moss et al. 2006); (3) probabilistic strong ground motion estimates from the current USGS National Seismic Hazard Mapping Project (Petersen et al. 2008); (4) recently published surficial geologic maps at the 7.5-minute (1:24,000) scale (e.g., Yonkee and Lowe 2004, Sack 2005, Harty and Lowe 2005); (5)

Digital Elevation Models (DEMs) from the USGS National Elevation Dataset; and, (6) available SPT, CPT, and V_s data compiled into a spatial database—enabling more robust characterization of various geologic units. This mapping method accounts for: (1) changes in the degree of ground slope or the size of a free-face; (2) influence of the age of the geologic deposit; (3) proximity to a geotechnical investigation; and, (4) other major sources of uncertainty. The mapping method was implemented to produce new probabilistic liquefaction-induced ground failure maps for a study area in Weber County, Utah. The new maps are for a 500-year or a 2,500-year return period seismic event. To illustrate the uncertainty associated with the mapped estimates, the probability of horizontal displacements exceeding specified thresholds are produced for 16^{th}, 50^{th} and 84^{th} percentiles.

This work proposed a new empirical model for predicting liquefaction-induced lateral spread displacement by significantly revising the widely-used empirical model of Youd et al. (2002). The Youd et al. (2002) empirical model requires specific inputs from laboratory testing, namely mean grain size and average fines content. Often in regional studies, these data are not readily available. By replacing these two soil factors with the soil description, the new empirical model uses data routinely collected in the field and reported on the borehole logs. Such replacement makes the new model more parsimonious and implementable for regional hazard analyses while preserving much of its original predictive power.

In addition, CPT data can be used in conjunction with the proposed empirical model because it is possible to use CPT data to estimate the required soil inputs. Based on side-by-side borehole and CPT data in Weber County, this research found the

following,: (1) it is possible to calculate the probabilities of each soil type (or index) from the CPT-based soil behavior type index, I_c; and, (2) SPT corrected blow count values, N_{60}, are correlated with CPT penetration resistance data. Such correlations/relationships make it possible to estimate the required soil inputs in the new empirical model using the CPT, and define the uncertainty of the estimates.

Fine to medium-grained clean sands are associated with larger lateral spread displacements than coarser sediments or sediments with higher fines content. Therefore, a new geotechnical variable is introduced: $T_{15,cs}$. This new variable is the equivalent value of T_{15} for fine to medium-grained clean sand only. $T_{15,cs}$ shows how soil type and thickness jointly affect lateral spreading. For example, 1 meter of saturated, clean, fine to medium-grained sand with $N_{1,60} \leq 15$ has about the same displacement potential as 15 meters of saturated soil that is either gravel or silt with $N_{1,60} \leq 15$. Hence, it is important to assess lateral spread hazards at locales with fine to medium-grained clean sand.

The empirical models used in the proposed mapping method are functions of certain geotechnical properties. This research found that the distributions of these geotechnical properties are statistically similar between geologic units of similar depositional environment. Therefore, in the study of Weber County, it was appropriate to pool data into 11 depositional classes. Pooling data increases the robustness of the sampling, thereby improving estimates of the total variability of the geotechnical properties for each geologic unit.

Previous investigators noted that liquefaction resistance of soils increase with age (e.g., Youd and Perkins 1978). Unfortunately, the factor(s) causing increased liquefaction resistance with age is poorly understood (Youd et al. 2001). This research

was unable to identify differences in the geotechnical properties according to the age of the soil. This leads to the conclusion that high-strain tests like the SPT or CPT are poor discriminators of the influence of the age of the soil on liquefaction susceptibility. Thus, the proposed mapping method accounts for the influence of age by applying an age correction factor, K_{DR}, as defined by Hayati and Andrus (2009).

Semivariance analysis found that geotechnical properties from nearby investigations are spatially correlated, but only up to roughly 95 meters. Since this range is relatively small, and available geotechnical investigations are relatively sparsely spaced in Weber County, there are large uncertainties in the estimates of the probability of liquefaction hazards. These large uncertainties are also due to poor quality or missing data in numerous borehole investigations (e.g., lacking measurements of the energy of the SPT impact hammer transmitted to the sampler or the fines content of a layer of soil), and error in the empirical models for estimating: K_{DR}; the nonlinear shear mass participation factor, r_d; the probability of liquefaction triggering; the lateral spread displacement; and, soil type and SPT blow counts from the CPT. The proposed mapping method accounts for these major uncertainties by applying Monte Carlo random sampling.

Results shown in the new liquefaction hazard maps for Weber County lead to two conclusions. First, the magnitude of liquefaction-induced ground displacement is highly correlated to the degree of ground slope. Therefore, it is important to capture variations in topography when mapping liquefaction-induced ground failure hazards. There is high probability for significant lateral spread displacement in deposits that are both susceptible to liquefaction and have ground slopes between 3 to 6% in the study area. The proposed mapping method accounts for variations in topography by solving for probabilities of

liquefaction hazards at points in a finely spaced topographical grid. The grid is spaced according to the resolution of the topographic data from the DEMs (i.e., 10 – 30 meters). Generally, about 3,000 Monte Carlo simulations at each grid point are necessary to define the total uncertainty in the resulting probabilities of liquefaction hazards. Because of the large number of simulations at each point of a very fine grid, there is a need for further research in the use of Monte Carlo variance reduction methods (e.g., correlated and/or stratified sampling). Second, the high probability of widespread liquefaction and the potential for large lateral spread displacement in various gently sloping zones indicates substantial risk for liquefaction-induced ground failures in the study area during large-magnitude seismic events. This is because: (1) the study area is filled with loose, sand-dominated sediments deposited in deltaic, fluvial, and lacustrine environments since the late Pleistocene; (2) 96% of the 408 available SPT/CPT investigations in the study area found shallow groundwater depths (i.e., less than 9 meters); and, (3) the study area is near the seismically active Wasatch fault zone, which is capable of generating earthquakes of magnitude equal to 7 or greater (Nelson and Personious 1993). Several zones of liquefiable sediments with sufficient slope have: (1) low to moderately high probabilities of lateral spreads exceeding 0.3 meters for the 500-year return period seismic event; and, (2) high probabilities of lateral spreads exceeding 0.6 meters for the 2,500-year return period seismic event.

Unfortunately, many of the zones with high probability of significant lateral spread displacement are also areas with high population density and infrastructure. Figure 6.1 depicts the population density (in units of people per km^2) in the study area, based on data from the 2010 U.S. Census. As can be seen, most of the population in the

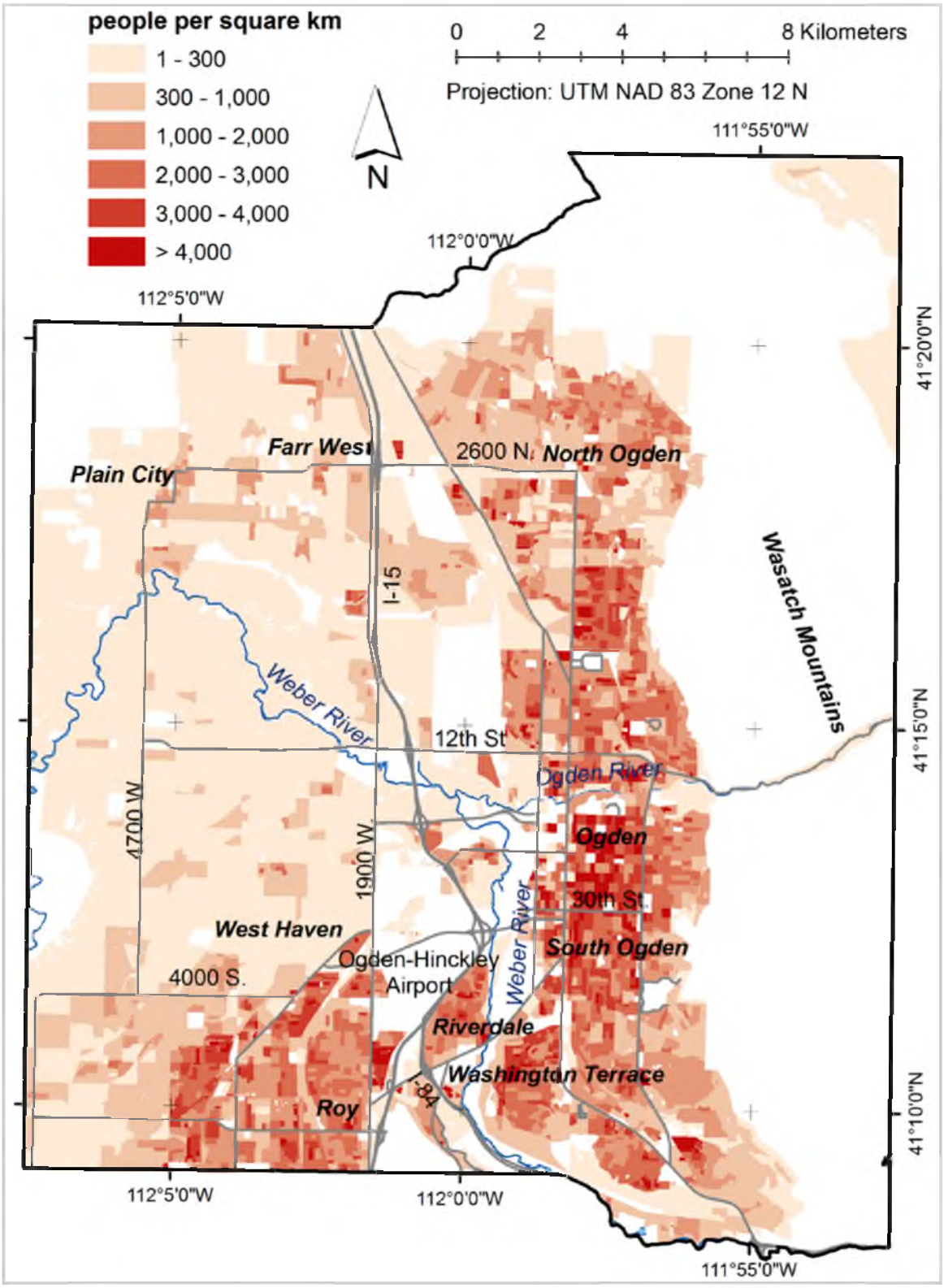

Figure 6.1. Population density map based on 2010 Census; Weber County, Utah

study area resides either along a north-south corridor easterly of Interstate 15 (from North Ogden City to Washington Terrace), or in the south-southwestern portion of the figure (near Roy City). Some areas in the center of Figure 6.1 have a population density equal to zero, indicating no one resides in these zones. However, many of these zones are filled with large facilities, infrastructure, or business buildings. For instance, the zone with zero population density northwesterly of Riverdale City is the Ogden-Hinckley Airport. Hence, Figure 6.2 is shown to depict the development in the study area (from 2009 aerial photography). Accordingly, Figure 5.12 shows that most of the zones with 75 – 100% probability of lateral spread displacements exceeding 0.3 meters given a 2,500-year return period seismic event are located in zones with extensive development or with population density greater than 2,000 people per km^2. This substantial risk for liquefaction-induced ground failure underscores the need to perform site-specific analyses in the study area, where appropriate, to further characterize subsurface conditions and also reduce uncertainties in the mapped liquefaction hazards.

Figure 6.2. 2009 High Resolution Orthophotography (HRO); Weber County, Utah

References

Cetin, K. O., Seed, R. B., Kiureghian, A. D., Tokimatsu, K., Harder, L. F., Jr., Kayen, R. E., and Moss, R. E., 2004. Standard Penetration Test-based probabilistic and deterministic assessment of seismic soil liquefaction potential, *J. Geotech. Geoenviron. Eng.* **130**(12), 1314 – 1340.

Harty, K. M., and Lowe, M., 2005. *Interim Geologic Map of the Plain City Quadrangle, Weber and Box Elder Counties, Utah, Utah Geological Survey Open-File Report 451*, Salt Lake City, UT, 2 pl., scale 1:24,000.

Hayati, H., and Andrus, R. D., 2009. Updated liquefaction resistance correction factors for aged sands, *J. Geotech. Geoenviron. Eng.* **135**(11), 1683-1692.

Moss, R. E. S., Seed, R. B., Kayen, R. E., Stewart, J. P., Kiureghian, A. D., and Cetin, K. O., 2006. CPT-based probabilistic and deterministic assessment of in situ seismic soil liquefaction potential, *J. Geotech. Geoenviron. Eng.* **132**(8), 1032 – 1051.

National Research Council (NRC), 1985. *Liquefaction of Soils During Earthquakes*, National Academy Press, Washington D. C., 240 pp.

Nelson, A. R., and Personious, S. F., 1993. *Surficial Geologic Map of the Weber Segment, Wasatch Fault Zone, Weber and Davis Counties, Utah, U.S. Geological Survey Miscellaneous Investigations Series Map I-2199*, Reston, VA, scale 1:50,000.

Petersen, M. D., Frankel, A. D., Harmsen, S. C., Mueller, C. S., Haller, K. M., Wheeler, R. L., Wesson, R. L., Zeng, Y., Boyd, O. S., Perkins, D. M., Luco, N., Field, E. H., Wills, C. J., and Rukstales, K. S., 2008. *Documentation for the 2008 Update of the United States National Seismic Hazard Maps, U.S. Geological Survey Open-File Report 2008–1128*, Reston, VA, 61 pp.

Sack, D., 2005. *Geologic Map of the Roy 7.5-Minute Quadrangle, Weber and Davis Counties, Utah, Utah Geological Survey Miscellaneous Publication 05-03*, Salt Lake City, UT, 22 pp., scale 1:24,000.

Yonkee, A., and Lowe, M., 2004. *Geologic Map of the Ogden 7.5-Minute Quadrangle, Weber and Davis Counties, Utah, Utah Geological Survey Map 200*, Salt Lake City, UT, 42 pp., scale 1:24,000.

Youd, T.L., and Perkins, D.M., 1978. Mapping liquefaction-induced ground failure potential, *Journal of the Geotechnical Engineering Division* **104**, No. GT4, 433-446.

Youd, T. L., Hansen, C. M., and Bartlett S. F., 2002. Revised multilinear regression equations for prediction of lateral spread displacement, *J. Geotech. Geoenviron. Eng.* **128**(12), 1007-1017.

Youd, T. L., Idriss, I. M., Andrus, R. D., Arango, I., Castro, G., Christian, J. T., Dobry, R., Finn, W. D. L., Harder, L. F., Jr., Hynes, M. E., Ishihara, K., Koester, J. P., Liao, S. S. C., Marcuson, W. F., III, Martin, G. R., Mitchell, J. K., Moriwaki, Y., Power, M. S., Robertson, P. K., Seed, R. B., Stokoe, K. H., II, 2001. Liquefaction resistance of soils: summary report from the 1996 NCEER and 1998 NCEER/NSF workshops on evaluation of liquefaction resistance of soils, *J. Geotech. Geoenviron. Eng.* **127**(10), 817-833.

APPENDIX A

GEOTECHNICAL DATABASE STRUCTURE

Brief Explanation

We compiled all available geotechnical data in Weber County, Utah, and input them into an electronic database. A large portion of the geotechnical data came from the Utah Department of Transportation (UDOT), the Weber County Recorder's office, and local engineering firms. Overall, the geotechnical database for Weber County contains data from 251 standard penetration test (SPT) boreholes and 157 cone penetrometer test (CPT) soundings. There are also 21 shear wave velocity tests (V_s) from a database published by McDonald and Ashland (2008).

The SPT and CPT data are stored in a Microsoft® Access database, which is available online at the Utah Liquefaction Advisory Group (ULAG) webpage (http://www.civil.utah.edu/~bartlett/ULAG/). Scanned images of many of the reports and/or logs, and spreadsheets of raw CPT data are also available. The geotechnical database for Weber County is structured similar to the geotechnical database for Salt Lake County (Bartlett and Olsen 2005), enabling compatibility between mapping projects. The database consists of several tables filled with numerous data fields.

The SITE and BLOW tables contain raw SPT data. We assign each borehole a site identification number (SITEIDNO) in order to link together data in the two tables. The SITE table contains information about the borehole site, such as: groundwater depth, approximate address, type of equipment, source of the data, gratitude of the borehole, etc. See Table A.1 for a definition of each field in the SITE table. The BLOW table contains various data for each sample obtained during the SPT, such as: depth of the sample, properties of the sampler, the soil description and classification, uncorrected SPT blow count, dry unit weight, moisture content, etc. In addition, the BLOW table has records that identify the depth to each boundary of a layer of sediment in a borehole. See Table A.2 for a definition of each field in the BLOW table. The SITE and BLOW tables also have several fields to rank the quality of the data. In general, we assigned: a rank of "1" for data extracted directly from the report or soil log; a rank of "2" for data that could be reasonably estimated from other samples in the same borehole or nearby borehole logs; and, a rank of "3" for data estimated from another source. Further details on the ranking system for each data quality field are in Table A.1 and Table A.2.

Similar to the SPT data, the CPT data are stored in two tables: SITECPT and CPTDATA. We assigned each sounding an identification number (CPTIDNO) in order to link together data in the two tables. The SITECPT table for CPT data is similar to the SITE table for SPT data. It contains coordinates of the site and other general information about the CPT sounding. See Table A.3 for a definition of each field in the SITECPT table. The CPTDATA table contains near-continuous measurements from the cone with depth, such as: cone tip resistance, sleeve friction, pore-water pressure behind the tip of the cone, etc. See Table A.4 for a definition of each field in the CPTDATA table.

Table A.1. Description of data fields for SITE table

Field Name	Description	Units
BOREELEV	Surface elevation of SPT borehole	feet
BORING	Identification of borehole listed on SPT log	[text]
BoreDiam	Diameter of borehole	inches
BoreDiamEs	Quality indicator of diameter of borehole: 1 = directly from log; 2 = from log drilled by same rig and driller	
DATE	Date of borehole	[text]
DEPTHGW	Depth to groundwater table	feet
DRILLER	Name of company who drilled the borehole	[text]
DRILLMETH	Drilling method	[text]
ELEVEST	Quality indicator for elevation of borehole: 1 = directly from log; 2 = estimated from nearby log; 3 = from maps	
GWDATE	Date of depth to groundwater measurement	[text]
GWEST	Quality indicator of depth to groundwater measurement; 1 = directly from log at least 24 hours after drilling; 2 = from log but date not listed; 3 = from nearby log	
HAMMER_TYP	Hammer type (i.e., safety, donut, or automatic)	[text]
LATITUDE	NAD 1983 latitude (in decimal degrees)	degree
LATITEST	Quality indicator of measurements of latitude and longitude: 1 = directly from log; 2 = scaled from maps	
LONGITUDE	NAD 1983 longitude (in decimal degrees)	degree
NCORR	True/False whether SPT N-values on logs were already corrected to $N_{1,60}$	
NOTES	Notes and other information	[text]
REFERENCE	Name of folder containing scanned images of SPT logs	
REPORT	Name of report where SPT log can be found	[text]
RIGTYPE	Type of drill rig used by drillers	[text]
SITEIDNO	Identification number assigned to SPT (link to BLOW table)	
SITENAME	Name of facility or address where SPT was performed	[text]
EASTING	NAD 1983, UTM Zone 12 easting	meters
NORTHING	NAD 1983, UTM Zone 12 northing	meters
CE	Mean correction for hammer energy ratio : 1 = safety; 1.1 = automatic. Apply to correct raw SPT blow counts to $N_{1,60}$	
CB	Correction for borehole diameter. Apply to correct raw SPT blow counts to $N_{1,60}$	
GEOLUNIT	Mapped surficial geologic unit where SPT was performed	[text]

Table A.2. Description of data fields for BLOW table

Field Name	Description	Units
BOREIDNO	Identification of boring listed on SPT log	[text]
COMMENTS	Comments or additional information	[text]
DEPTH	Depth to middle of sample or depth to boundary line between layers	feet
DRYUNIT	Dry unit weight of sample	kN/m^3
DRYUNITPCF	Dry unit weight of sample in pounds per cubic foot	pcf
ESTATT*	Quality indicator for Atterberg limits of sample	
ESTDRY*	Quality indicator for dry unit weight of sample	
ESTFINES*	Quality indicator for fines content of sample	
ESTMOIST*	Quality indicator for moisture content of sample	
ESTNM*	Quality indicator for SPT blow counts for bottom 12 inches (0.3 m) of sample	
ESTUSCS*	Quality indicator for classification of sample according to the Unified Soil Classification System	
ESTWET*	Quality indicator for wet unit weight of sample	
FINES	Fines content of sample (percent of sample passing a U.S. Standard No. 200 sieve)	%
LIQUIDLIMIT	Liquid limit of sample	%
MOISTURE_ CONTENT	Moisture content of sample	%
N160	Corrected SPT blow counts ($N_{1,60}$) from borehole log for bottom 12 in. (0.3 m) of sample	
NVALUE	Uncorrected SPT blow counts for bottom 12 in. (0.3 m) of sample (more common than N160)	
PERGRAVEL	Percent of sample retained on a No. 4 sieve	%
PERSAND	Percent of sample passing a No. 4 sieve and retained on a No. 200 sieve	%
PLASTICINDEX	Plastic index of sample	%
PLASTICLIMIT	Plastic limit of sample	%
SAMPLER	Type of sampler: CS or MCAL = modified California; DM = Dames & Moore; SH = thin-walled Shelby tube; SS = split-spoon (standard for SPT)	
SAMPLEREST	Quality indicator for properties of sampler	
SAMPLER-LENGTH	Length sample retained in the sampler	feet
SAMPLER_ OUTSIDE_ DIAMETER	Outside diameter of sampler	inches
SITEIDNO	Identification number assigned to SPT (link to SITE table)	
SOILTYPE	Description of soil sample from log; blank values indicate boundary lines between layers	[text]

Table A.2. (continued)

Field Name	Description	Units
SPGRAV	Specific gravity of sample	
USCS	Unified Soil Classification System	[text]
WETUNIT	Wet unit weight of sample	pcf
WCLASS	Index assigned to sample for estimating its unit weight	
MCLASS	Index assigned to sample for estimating its moisture class	
SGCLASS	Index assigned to sample for estimating its specific gravity	
N60CE	SPT blow counts for bottom 12 in. (0.3 m) of sample, corrected for rod length, sampler liner, sampler type, and borehole diameter (but not for energy ratio, C_E)	
SOIL INDEX	Soil index of sample (*SI*)	

* = A value of: 1 = directly from log; 2 = from nearby log in same report; 3 = from nearby log of different report; 9 = from log but likely inaccurate

Table A.3. Description of data fields for SITECPT table

Field Name	Description	Units
CONEID	Identification number of cone used for test	[text]
CPTIDNO	Identification number assigned to CPT	
DATE_	Date of sounding	[text]
DEPTHGW	Depth to groundwater table	feet
ELEV	Surface elevation of CPT sounding	feet
ELEVEST	Quality indicator for elevation of sounding: 3 = from map	
GWEST	Quality indicator of depth to groundwater measurement; 1 = from pore-water dissipation (PPD) test; 2 = from nearby PPD test ; 3 = interpolated between PPD tests	
LATITUDE	NAD 1983 latitude (in decimal degrees)	degree
LATITEST	Quality indicator of measurements of latitude and longitude: 1 = directly from log; 2 = scaled from maps; 3 = scale from maps of lesser quality	
LONGITUDE	NAD 1983 longitude (in decimal degrees)	degree
PROJECT	Name of folder containing raw CPT data	
REPORT	Name of report where CPT log can be found	[text]
SOUNDING	Identification of CPT sounding from logs	[text]
SOURCE	Name of company who performed the CPT	[text]
AREA_RATIO	Net area ratio of the cone	
EASTING	NAD 1983, UTM Zone 12 easting	meters
NORTHING	NAD 1983, UTM Zone 12 northing	meters
INCREMENT	Change in depth between CPT measurements	meters
GEOLUNIT	Mapped surficial geologic unit where CPT was performed	[text]

Table A.4. Description of data fields for CPTDATA table

Field Name	Description	Units
CPTIDNO	Identification number assigned to CPT (link to SITECPT table)	
DEPTH	Depth below ground surface	feet
PRESSURE	Pore-water pressure behind tip of cone (in feet of head)	feet
QC	Cone tip resistance	tsf
QT	Cone tip resistance corrected for pore-pressure effects	tsf
SLEEVE	Sleeve friction	tsf
SOUNDING	Identification of CPT sounding from logs	[text]
UBT	Pore-water pressure behind tip of cone (in tsf)	tsf
FRATIO	Friction ratio (SLEEVE/QT*100)	%
DEPTHM	Depth below ground surface, in meters	meters

References

Bartlett S. F., Olsen, M. J., and Solomon, B. J., 2005. *Probabilistic Liquefaction Potential and Liquefaction-Induced Ground Failure Maps for the Urban Wasatch Front: Collaborative Research with the University of Utah, Utah State University and the Utah Geological Survey, Phase I, FY2004, U.S.G.S. Research Award No. 04HQGR0026*, Reston, VA.

McDonald, G. N., and Ashland, F. X., 2008. *Earthquake Site Conditions in the Wasatch Front Urban Corridor, Utah*, *Utah Geological Survey Special Study 125,* Salt Lake City, UT, 41 pp., 1 pl., scale 1:50,000.

APPENDIX B

DISTRIBUTIONS OF GEOTECHNICAL PROPERTIES FOR VARIOUS GEOLOGIC UNITS

Chapter 4 discussed production of frequency histograms of particular geotechnical properties (we call "critical datasets") according to geologic unit. For example, Figure 4.3 shows histograms of critical dataset variables for modern stream alluvium, Qal_1 in Weber County. Figure 4.4 depicts frequency histograms for (a) alluvial fan, Qaf; and, (b) North Ogden landslide complex deposits, Qmq_2, in Weber County. Histograms in these figures allow visual exploration of the data: enabling recognition of patterns or trends, and comparison between geologic units.

This appendix contains the same type of histograms for other geologic units listed in Table 4.1 (with a minimum SPT/CPT sample size of 9). See Figure B.1 through Figure B.14 for these histograms. Refer to Chapter 4 for a discussion on how to interpret the histograms in these figures. It is important to note that the data in subplots (b) through (d) of these figures are from critical datasets where $T_{15} > 0$, only.

As discussed in Chapter 4, we pooled critical datasets from geologic units of similar depositional environment into 11 deposit classes (see Table 4.1).

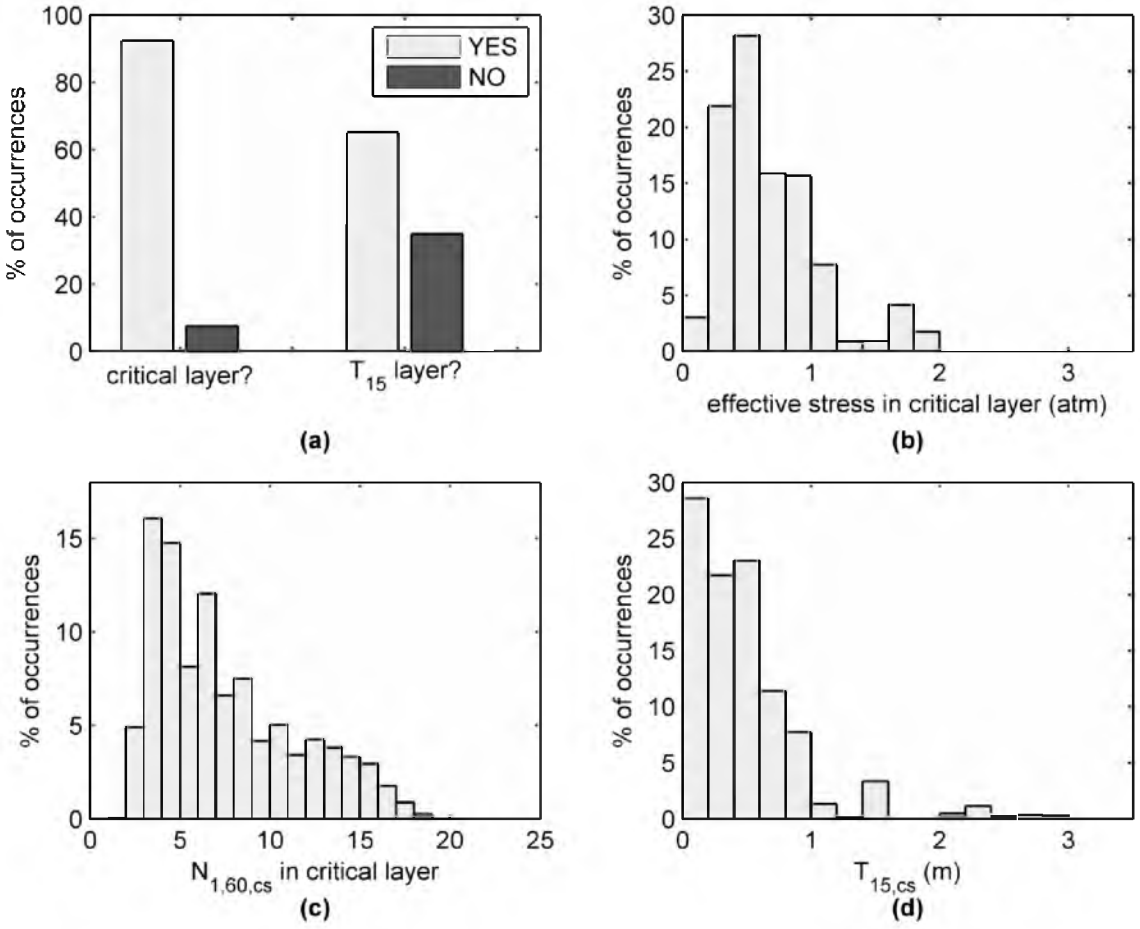

Figure B.1. Histograms of critical dataset variables for Qal_2; Weber County, Utah

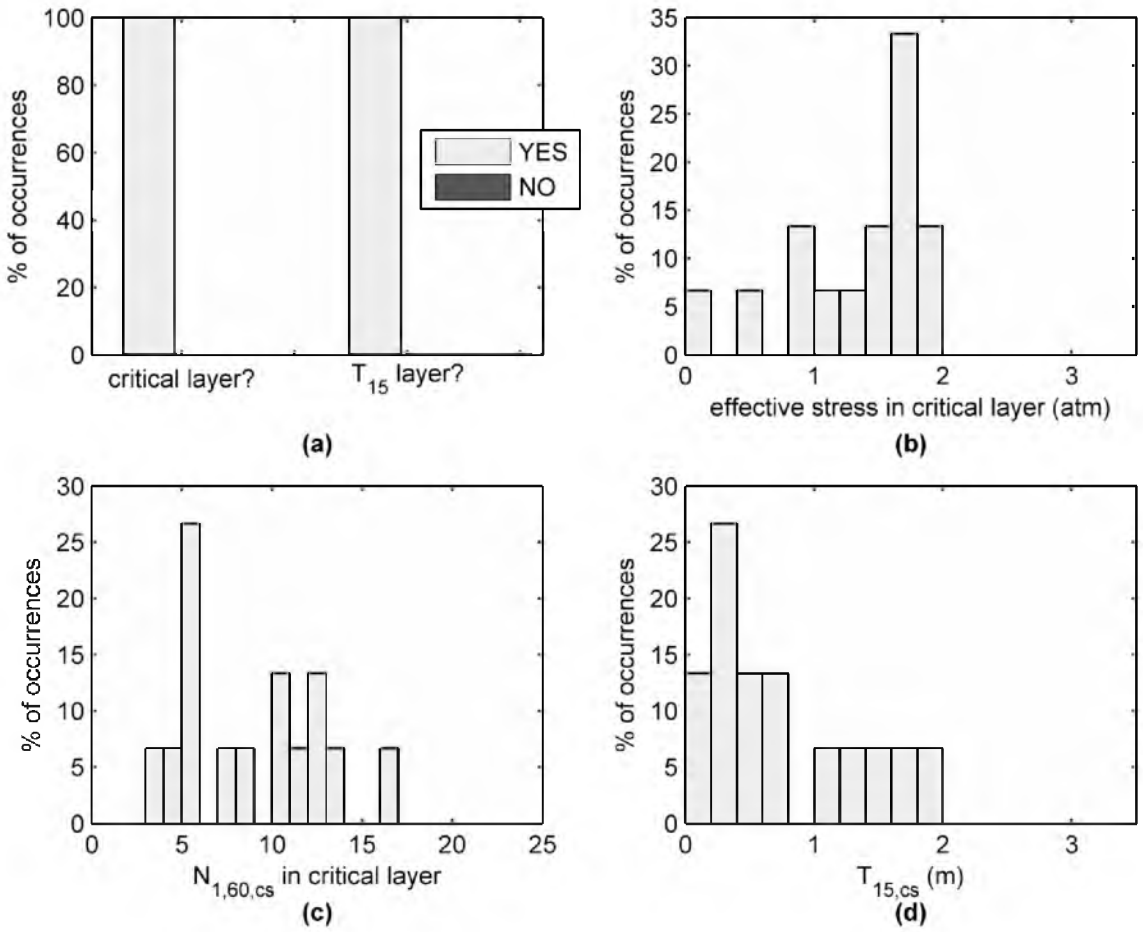

Figure B.2. Histograms of critical dataset variables for Qat; Weber County, Utah

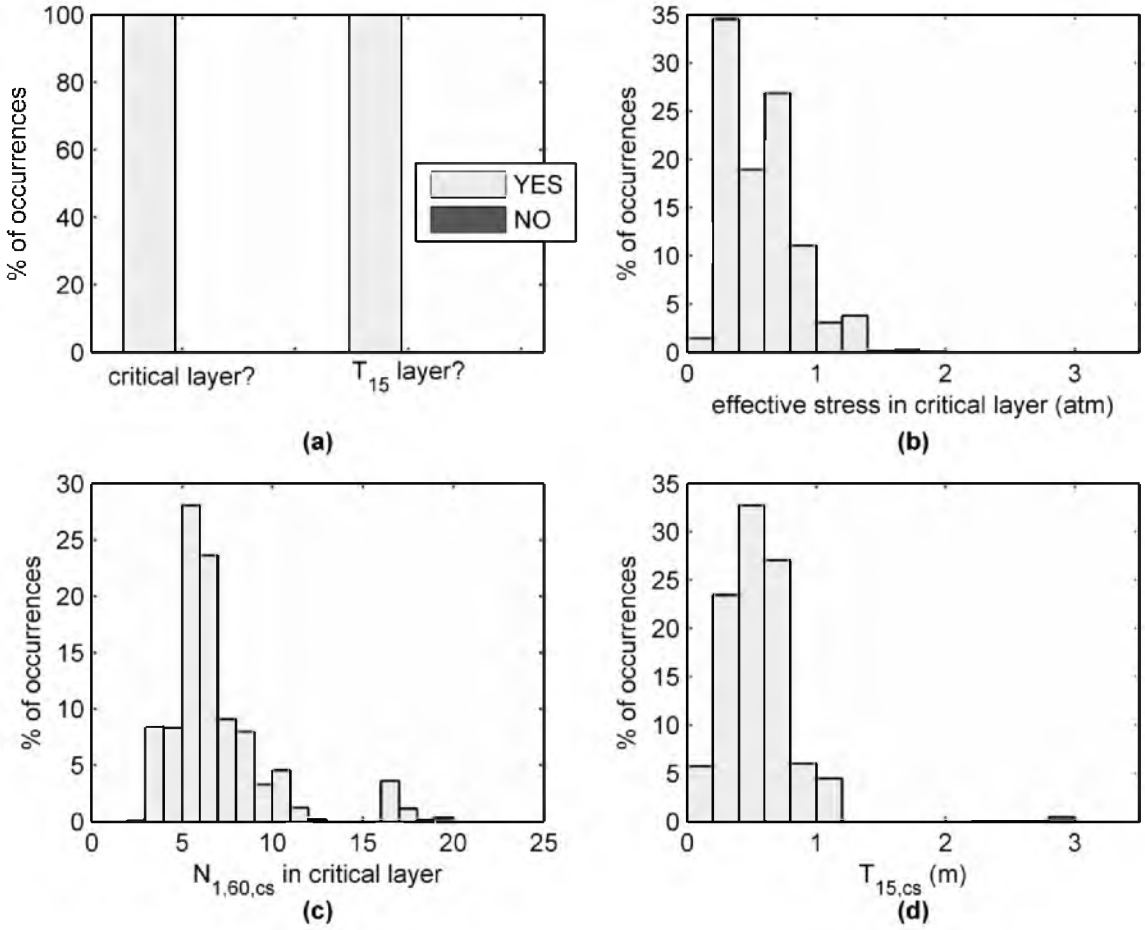

Figure B.3. Histograms of critical dataset variables for Qd_2; Weber County, Utah

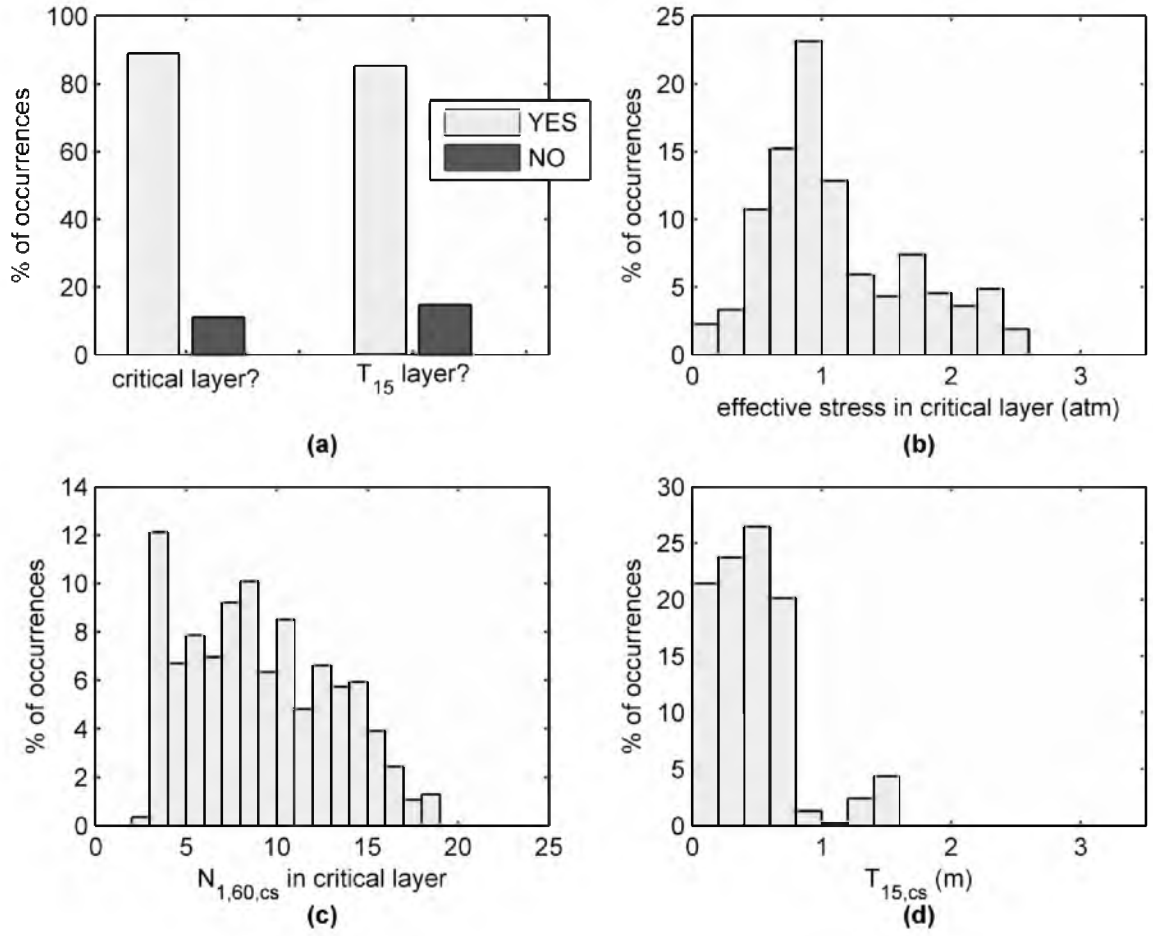

Figure B.4. Histograms of critical dataset variables for Qd_3; Weber County, Utah

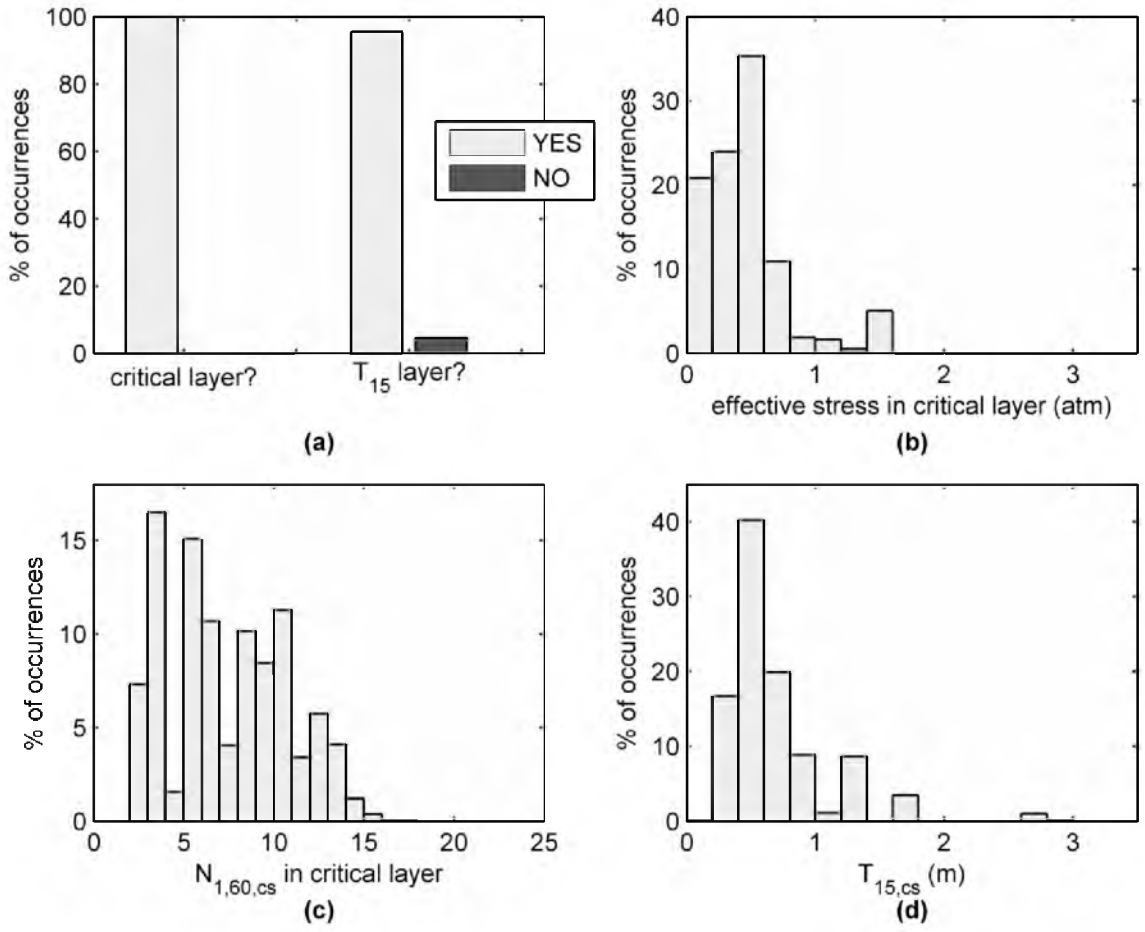

Figure B.5. Histograms of critical dataset variables for Qd_4; Weber County, Utah

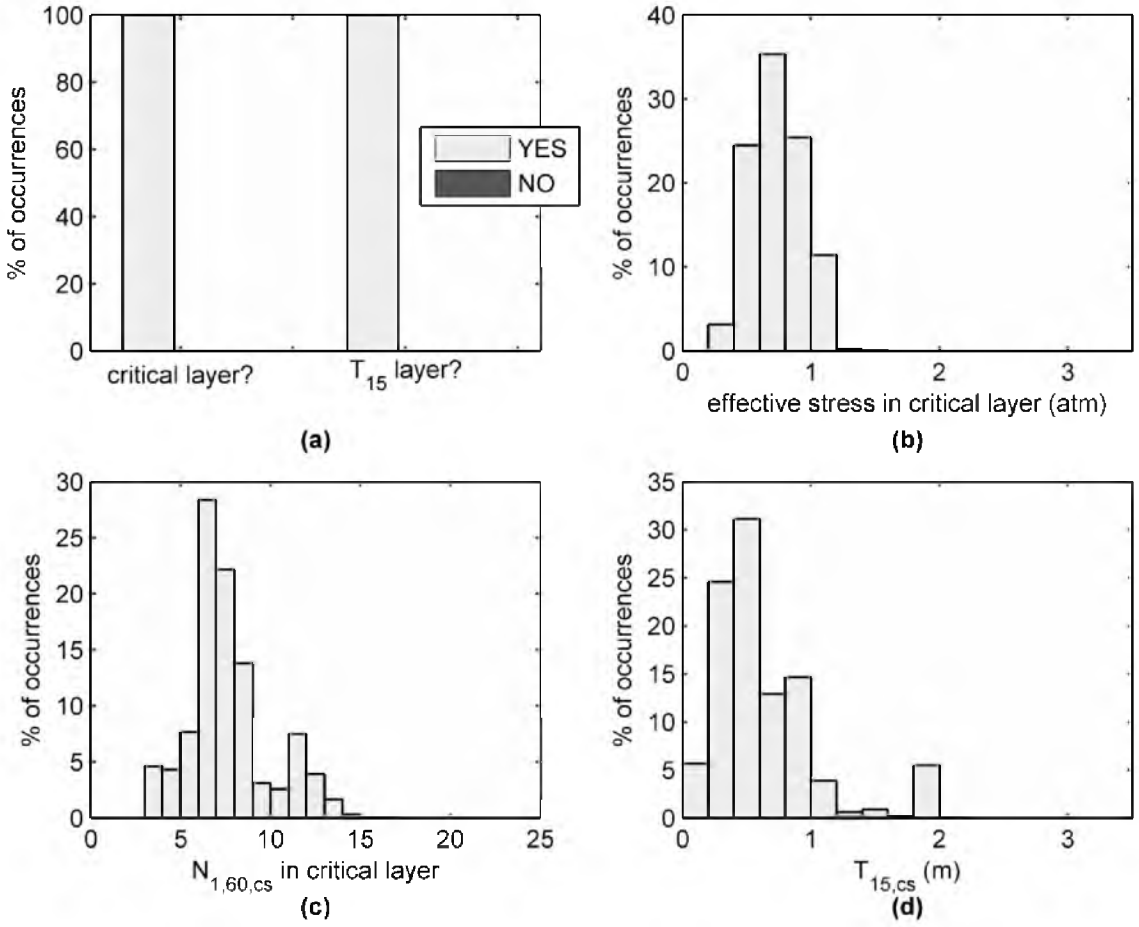

Figure B.6. Histograms of critical dataset variables for Qd_5; Weber County, Utah

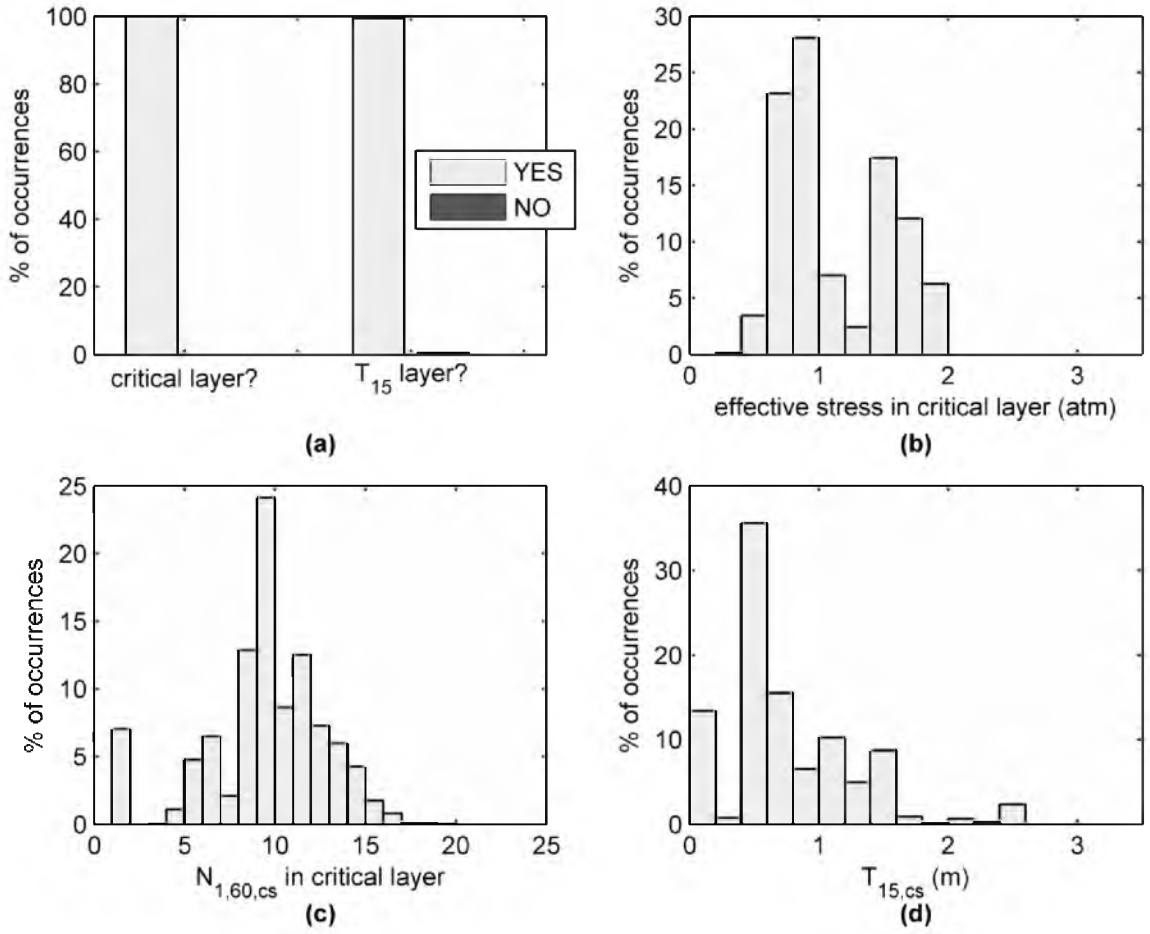

Figure B.7. Histograms of critical dataset variables for Qda; Weber County, Utah

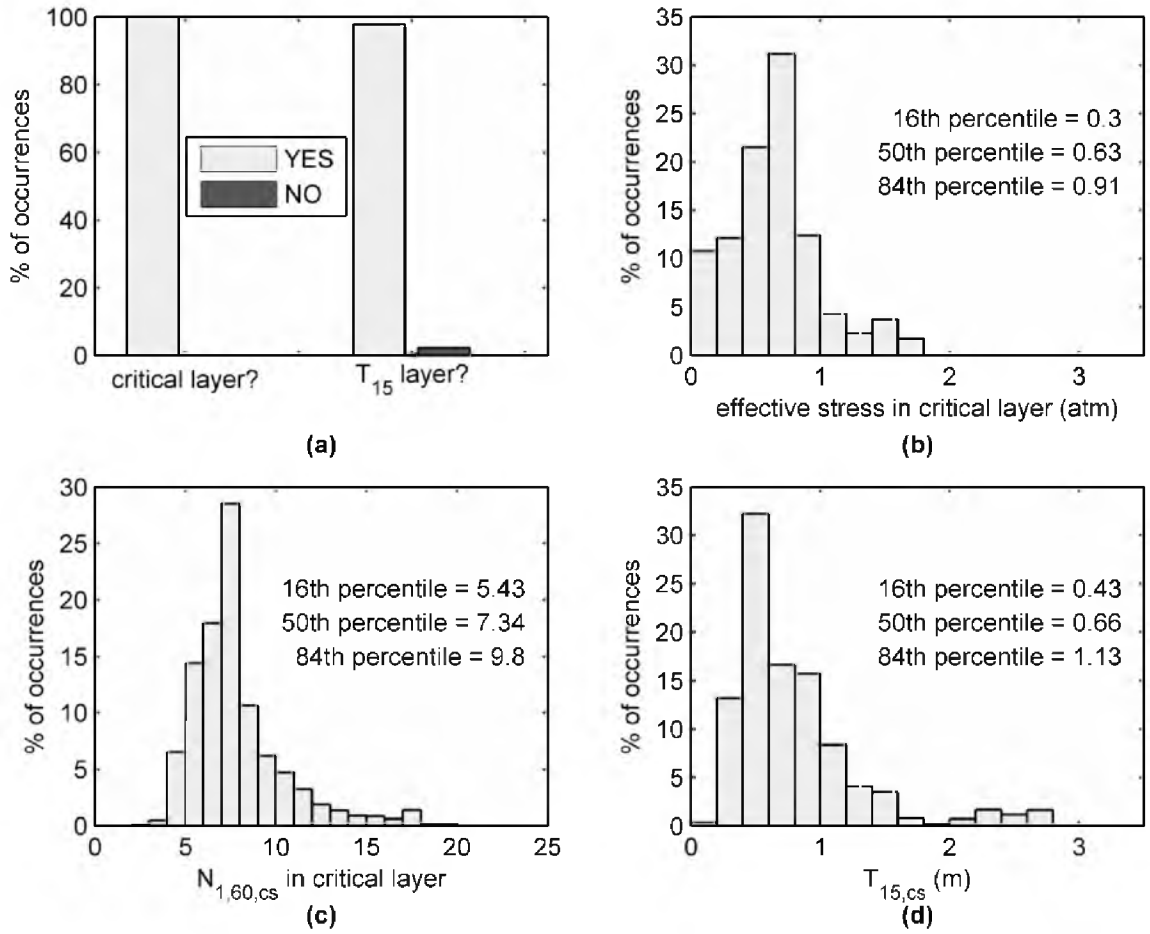

Figure B.8. Histograms of critical dataset variables for Qla; Weber County, Utah

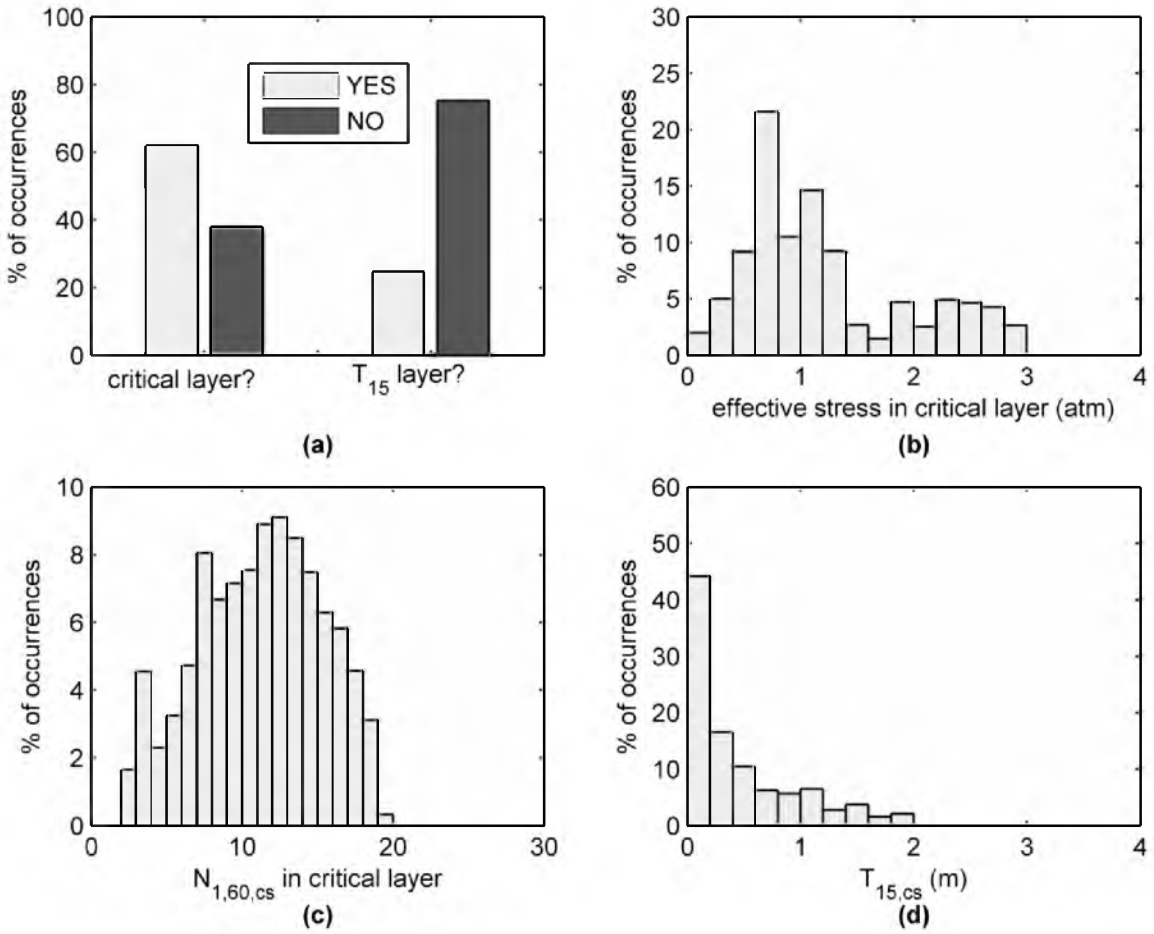

Figure B.9. Histograms of critical dataset variables for Qlf_3; Salt Lake and Weber Counties, Utah

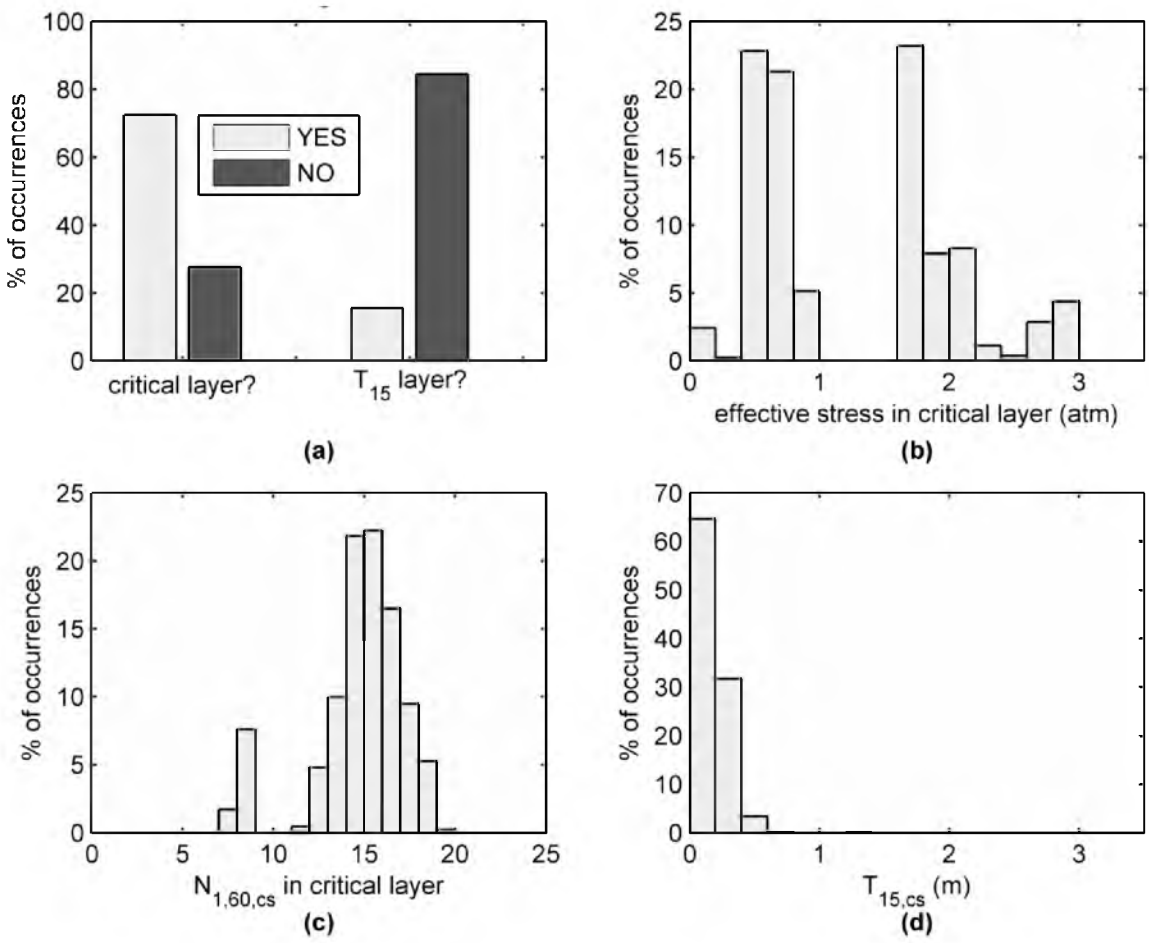

Figure B.10. Histograms of critical dataset variables for Qlg_3; Salt Lake and Weber Counties, Utah

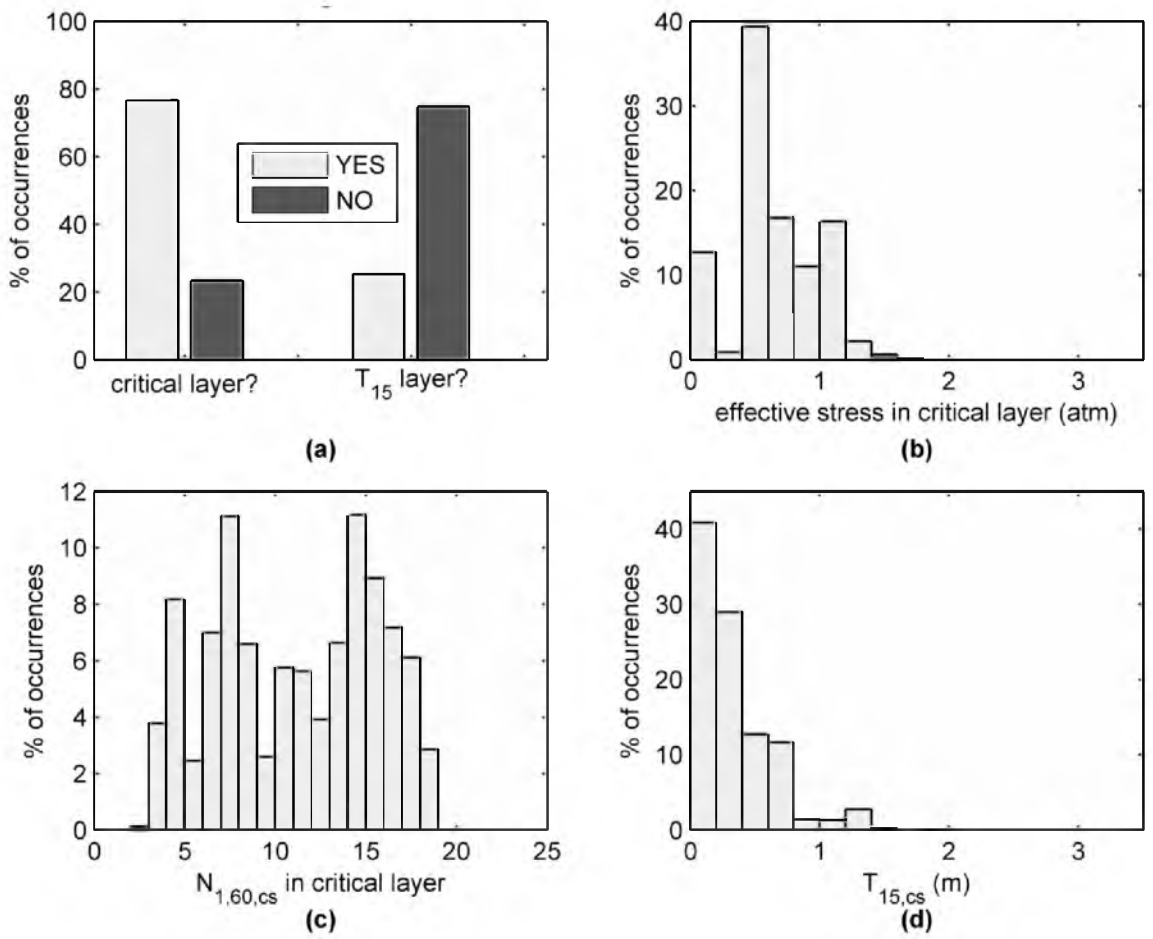

Figure B.11. Histograms of critical dataset variables for Qlg_4; Salt Lake and Weber Counties, Utah

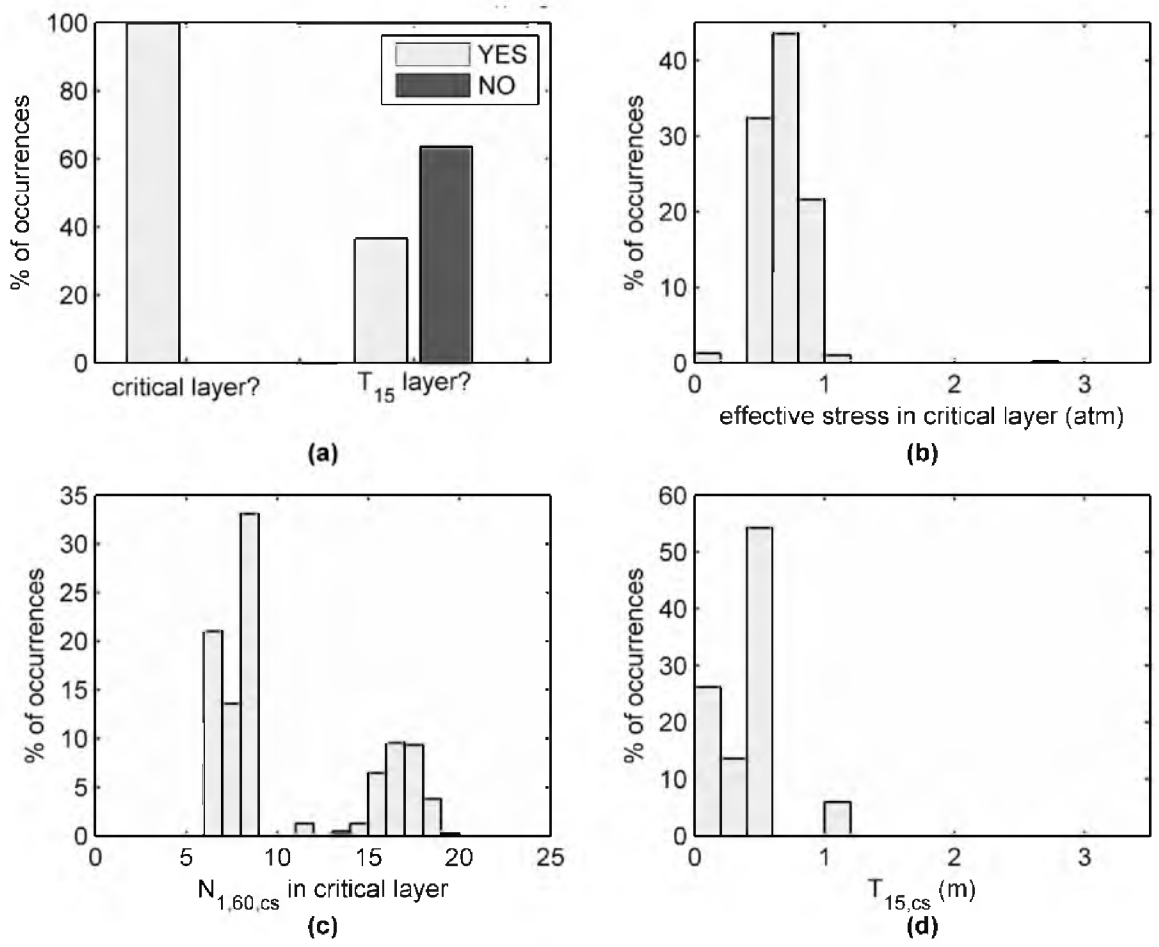

Figure B.12. Histograms of critical dataset variables for Qls; Salt Lake and Weber Counties, Utah

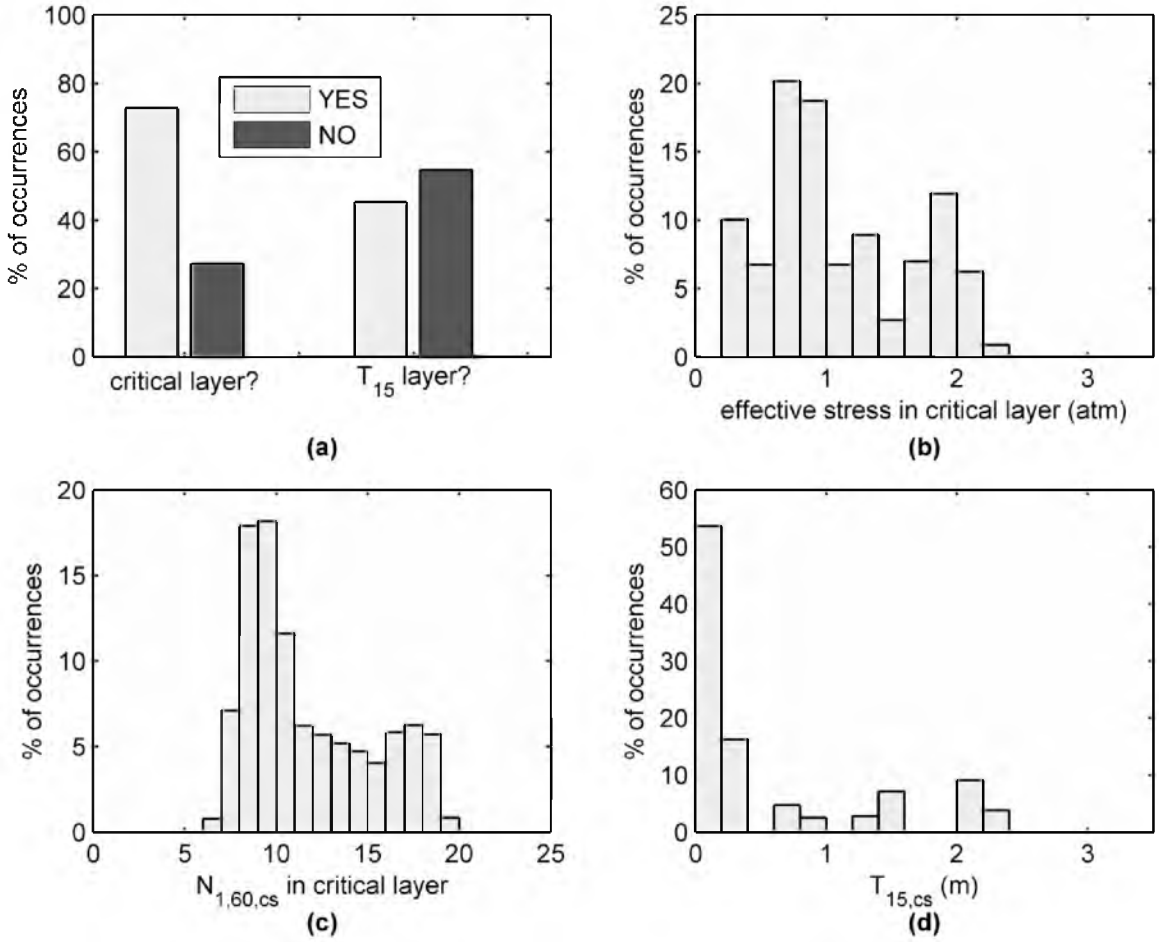

Figure B.13. Histograms of critical dataset variables for Qms_2; Weber County, Utah

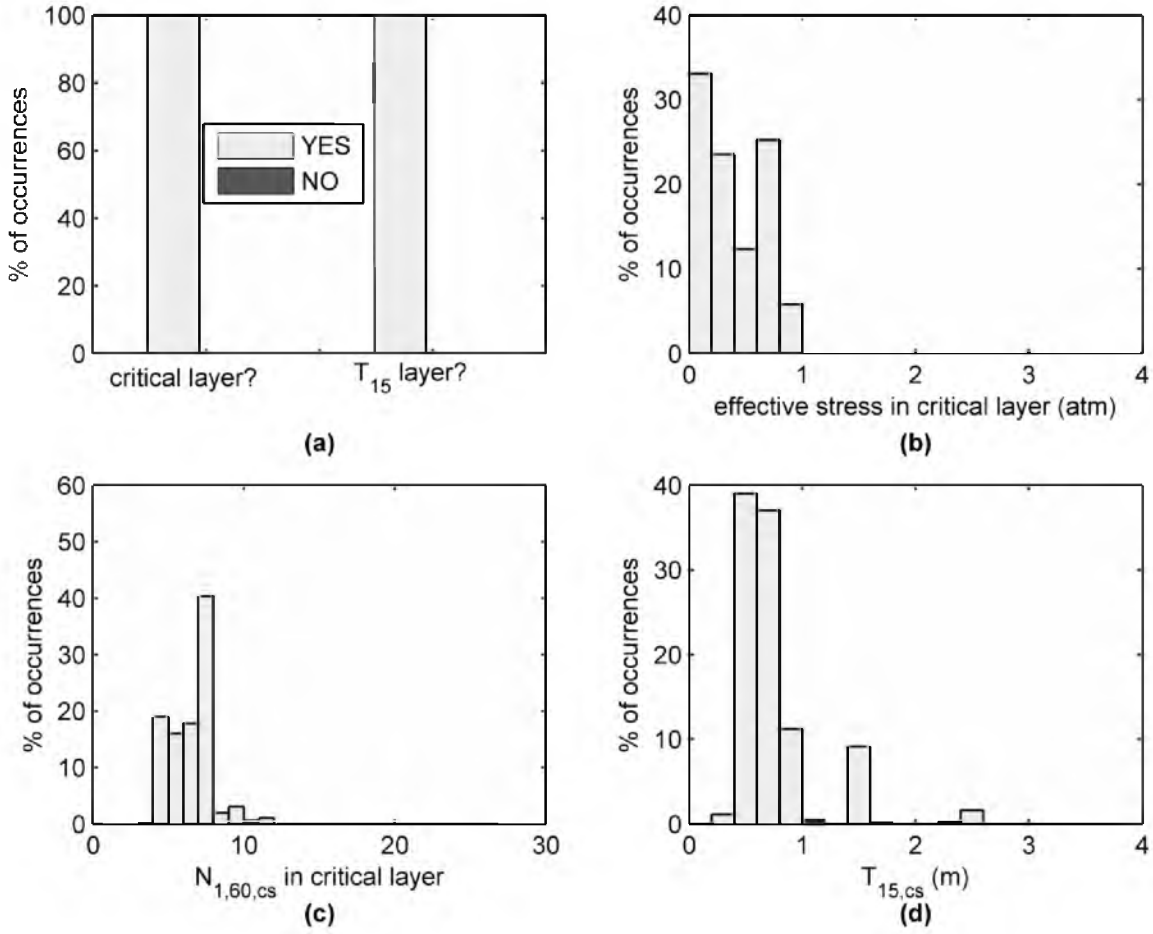

Figure B.14. Histograms of critical dataset variables for Qsm; Weber County, Utah

For the classes with more than one geologic unit, we produced histograms for the pooled critical datasets. These histograms are also in this appendix (see Figure B.15 through Figure B.18). For instance, Figure B.15 shows histograms of pooled data from all SPT and CPT investigations in the deltaic deposits (i.e., Qd_2 – Qd_{11}) of Weber County.

Finally, in Chapter 4 we tested the hypothesis that geologic units of similar depositional environment have similar critical datasets. We presented Figure 4.6, which plots 50^{th} percentile values of critical dataset variables at each SPT/CPT investigation on planes of canonical axes for: (a) stream alluvium deposits; and, (b) delta deposits in Weber County. Figure B.19 and Figure B.20 show the same type of plots for 16^{th} and 84^{th} percentile values, respectively. In canonical space, confidence ellipses that represent the distributions within the units become circles. As can be seen from these figures, there is significant overlap of the circles. This indicates that the subclassification of the units achieves little in terms of 16^{th}, 50^{th}, and 84^{th} percentile values of the critical dataset variables.

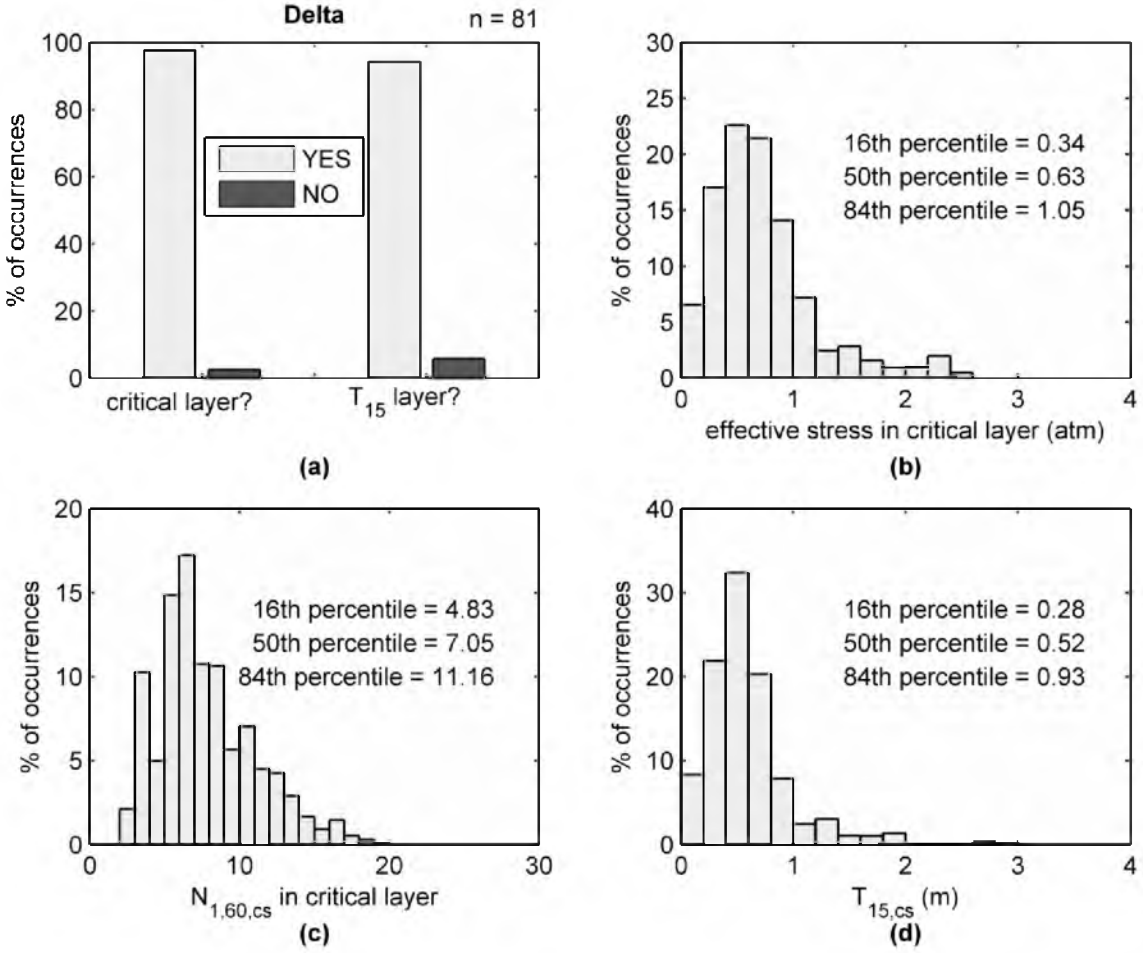

Figure B.15. Histograms of critical dataset variables for deltaic deposits; Weber County, Utah

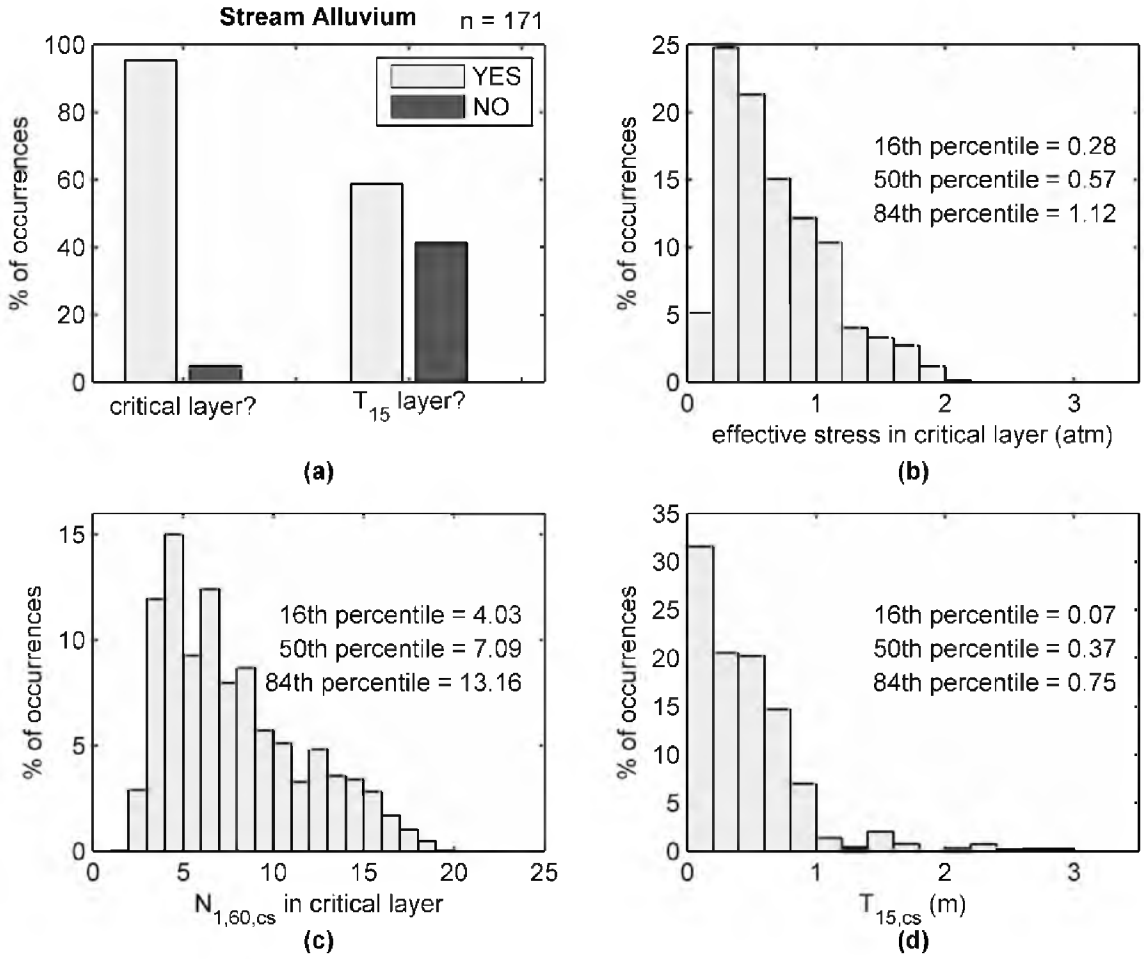

Figure B.16. Histograms of critical dataset variables for stream alluvium deposits; Weber County, Utah

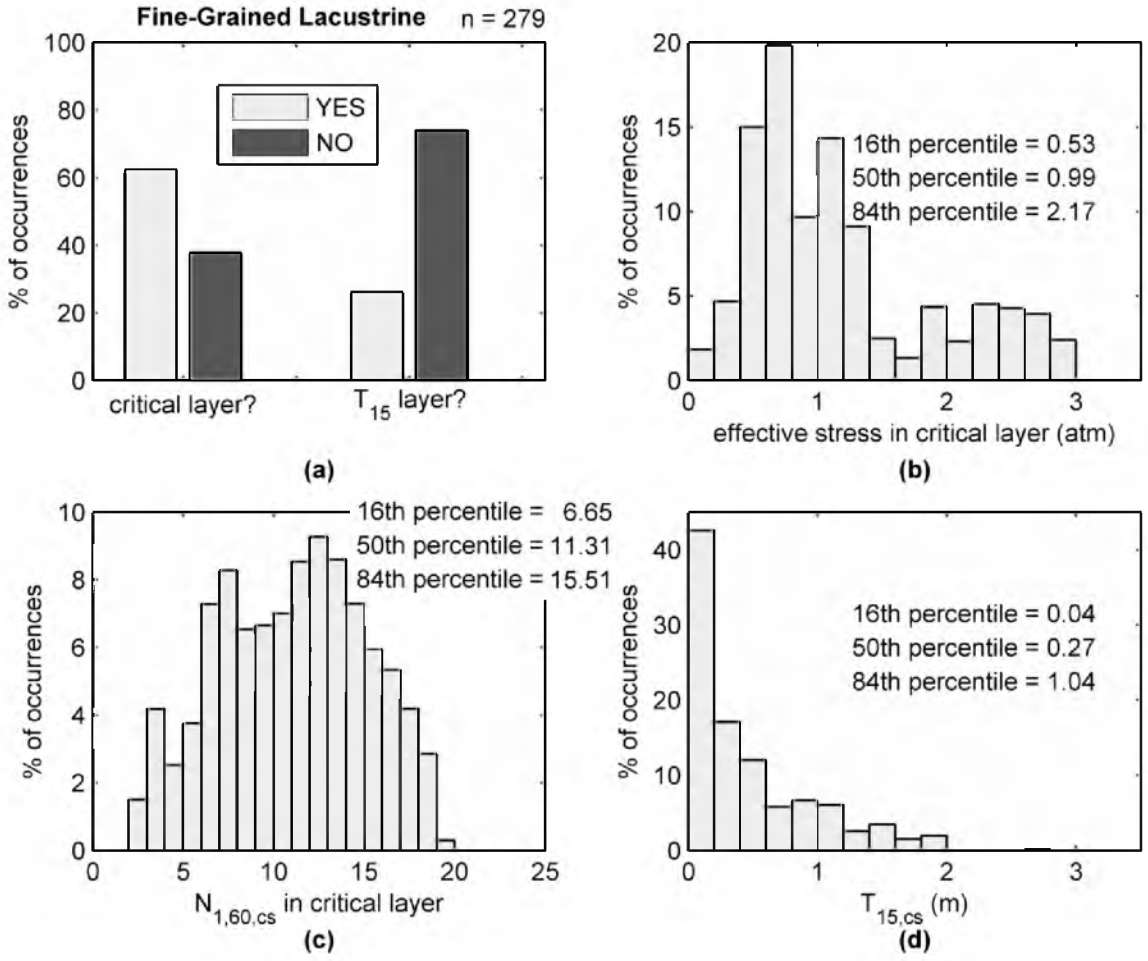

Figure B.17. Histograms of critical dataset variables for fine-grained lacustrine deposits; Salt Lake and Weber Counties, Utah

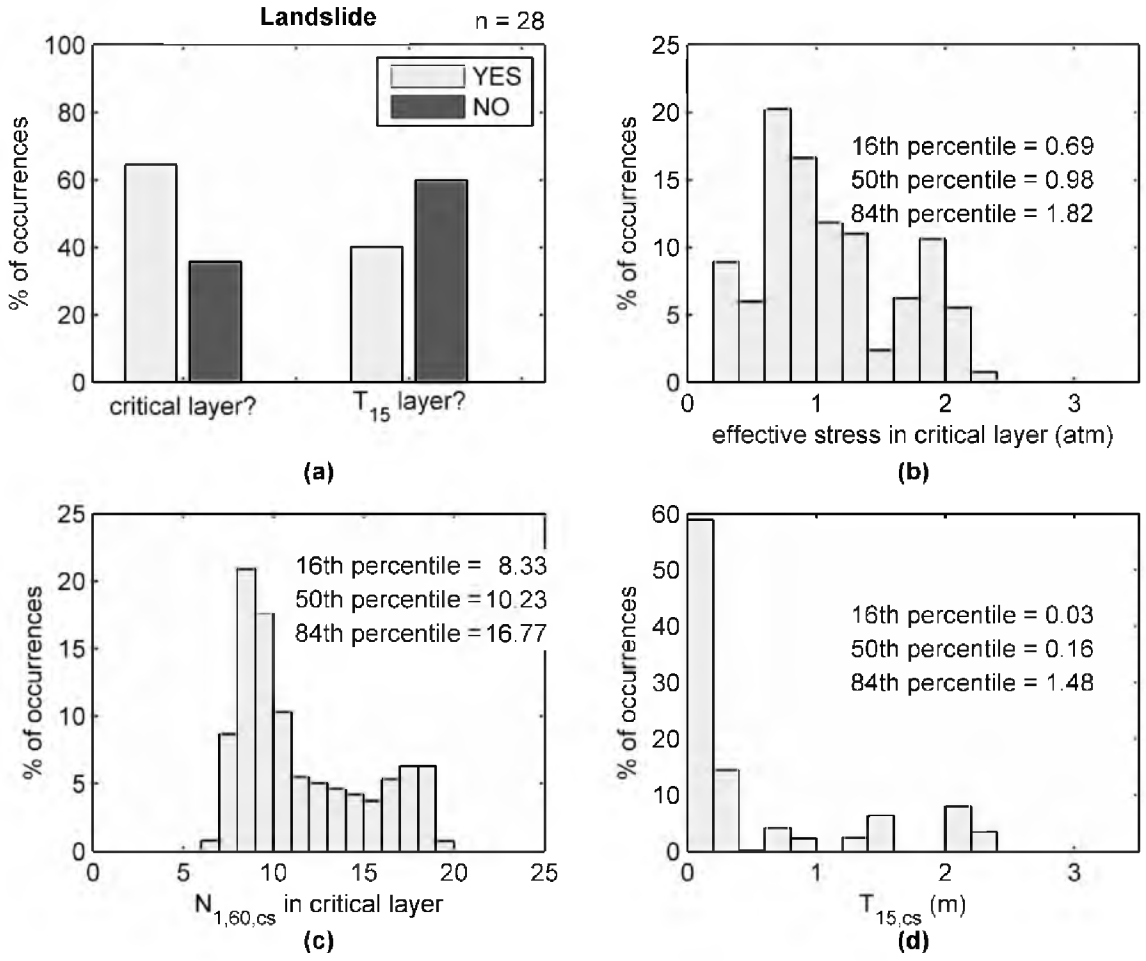

Figure B.18. Histograms of critical dataset variables for landslide deposits in the eastern Ogden City area; Weber County, Utah

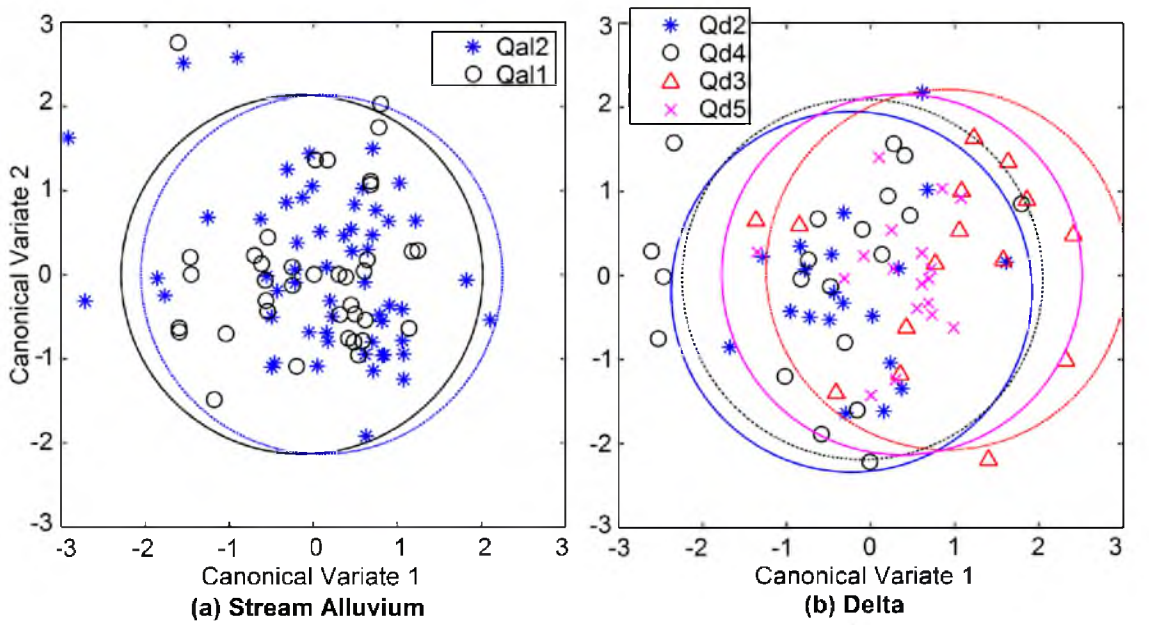

Figure B.19. Scatter of 16th percentile values of σ'$_v$, $N_{1,60,cs}$, and $T_{15,cs}$ at sites where T_{15} > 0 on planes of canonical axes for (a) stream alluvium and (b) delta, with 90 % confidence circles; Weber County

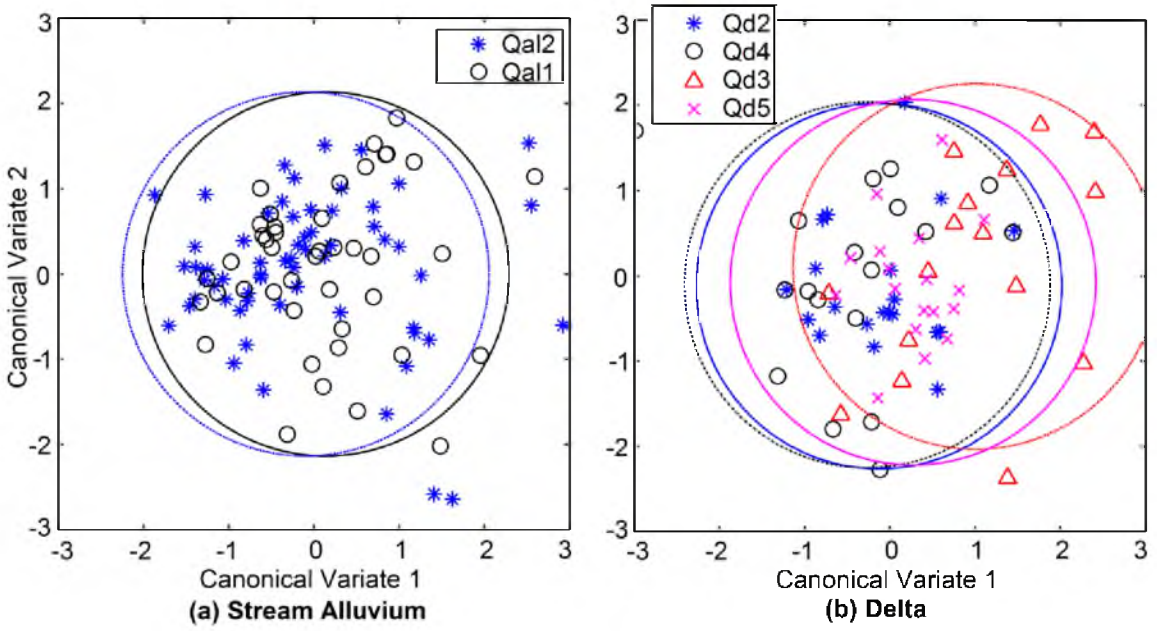

Figure B.20. Scatter of 84th percentile values of σ'$_v$, $N_{1,60,cs}$, and $T_{15,cs}$ at sites where T_{15} > 0 on planes of canonical axes for (a) stream alluvium and (b) delta, with 90 % confidence circles; Weber County

APPENDIX C

CONVERGENCE OF RESULTS FROM MONTE CARLO SIMULATIONS

Figure 4.2 depicts empirical cumulative distribution functions (CDFs) of each variable of the critical dataset for SPT borehole no. 11 of the geotechnical database. This figure shows CDFs after 10, 100, 300, 500, and 1000 Monte Carlo random sampling simulations. As can be seen, the CDFs converge after 300 simulations. Therefore, we set 300 as the necessary number of simulations to ensure definition of the total distribution of the critical dataset at each SPT borehole.

Similarly, Figure C.1 depicts CDFs of each variable of the critical dataset for CPT sounding no. 1 of the geotechnical database. Certainly, after 300 Monte Carlo simulations, the CDFs converge.

Figure C.2 shows CDFs at a grid point for the probability of liquefaction triggering and the probability of lateral spread displacement exceeding various thresholds for a scenario seismic event. This figure shows CDFs after numerous amounts of Monte Carlo random sampling simulations. After thousands of simulations, the CDFs appear to converge. Thus, we set 3,000 as the necessary number of simulations to ensure definition of the distribution of the probabilities of liquefaction hazards at each grid point.

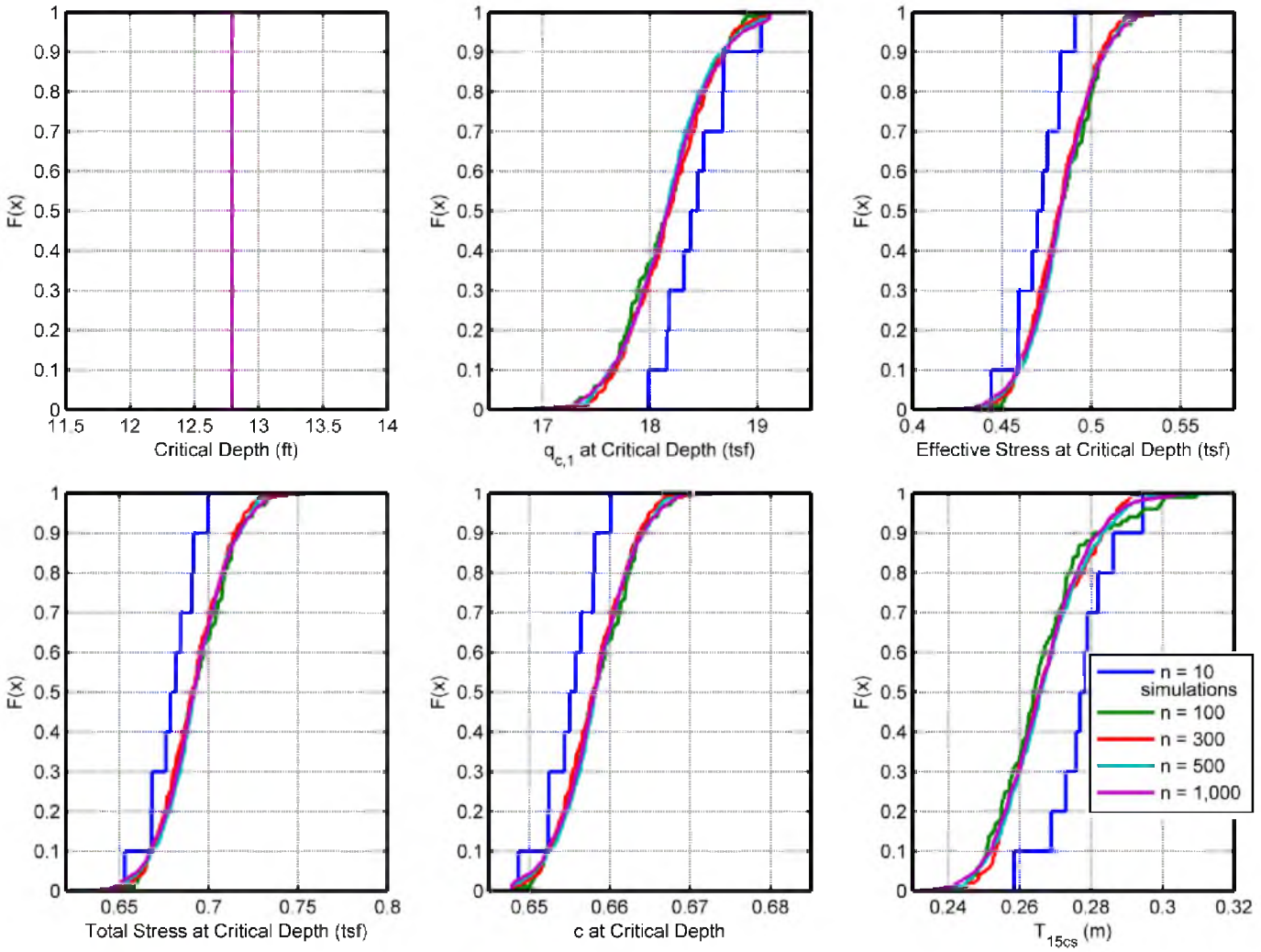

Figure C.1. Cumulative distribution functions of the critical dataset at CPT site no. 1. The distributions converge after 300 Monte Carlo simulations

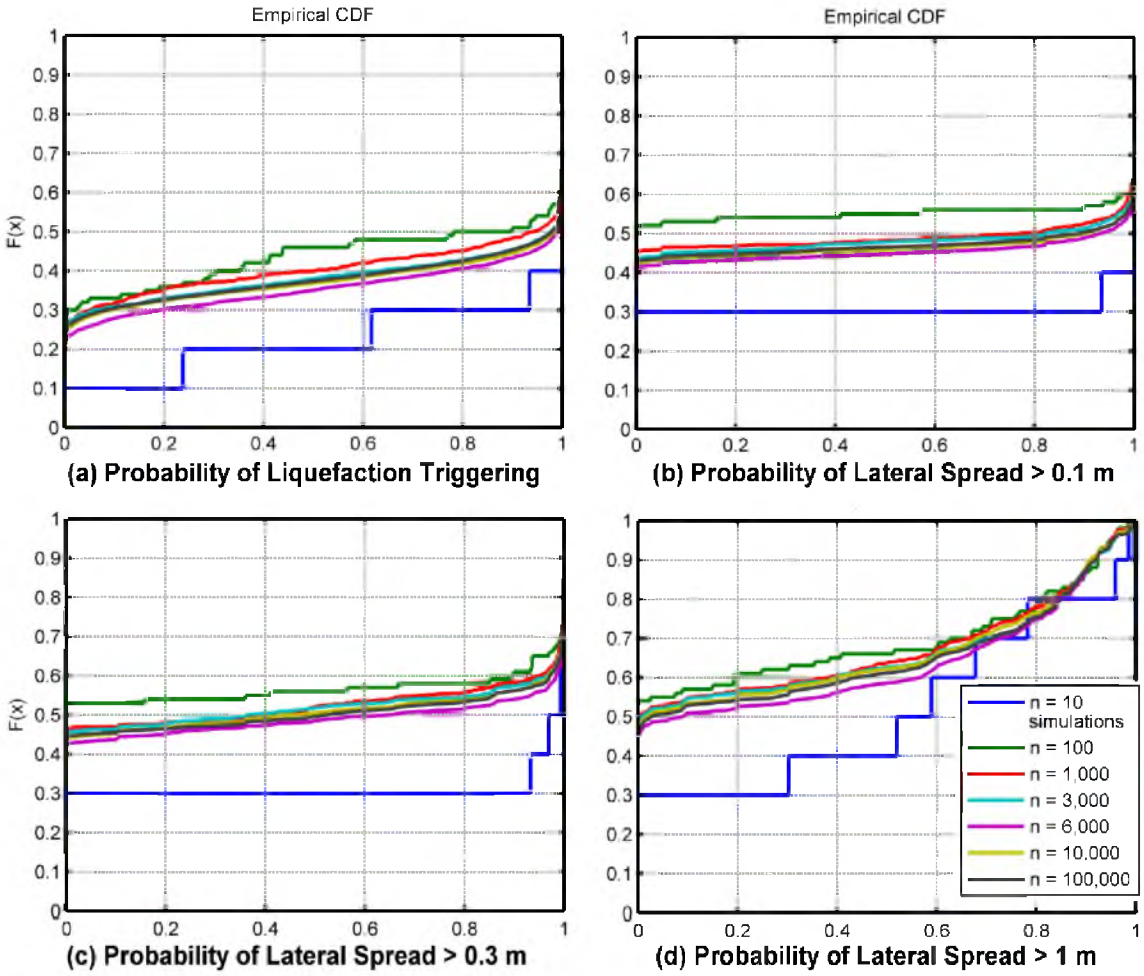

Figure C.2. Cumulative distribution functions of the probability of: (a) liquefaction triggering; and, lateral spread displacements exceeding (b) 0.1 meter, (c) 0.3 meter, and (d) 1.0 meter. The distributions converge after roughly 3,000 Monte Carlo simulations

APPENDIX D

FINES CONTENT ACCORDING TO SOIL INDEX

For many of the layers of sediment in the borehole investigations in Weber County, there is a lack of measurements of fines content, FC (percentage of sediment passing a U.S. Standard No. 200 sieve). This appendix contains distributions of FC for each soil index, SI. Such distributions enable estimation of lacking measurements of FC according to the value of SI for a layer of sediment. The distributions are based on laboratory results of numerous soil samples (i.e., data with a quality rank equal to 1), as listed on the borehole logs in the geotechnical database of Weber County.

Figure D.1 depicts histograms of FC for soil samples assigned a value of SI equal to 1, 3, 4, or 5. The figure also shows the sample size, n, for each SI group. As can be seen, distributions of FC for each SI are approximately uniform. For samples assigned a value of SI equal to 1 or 3, FC is typically (at least 90% of the time) between 0 to 15%. For samples assigned a value of SI equal to 4, FC is typically between 10 to 50%. Finally, for samples assigned a value of SI equal to 5, FC is typically between 50 to 95%.

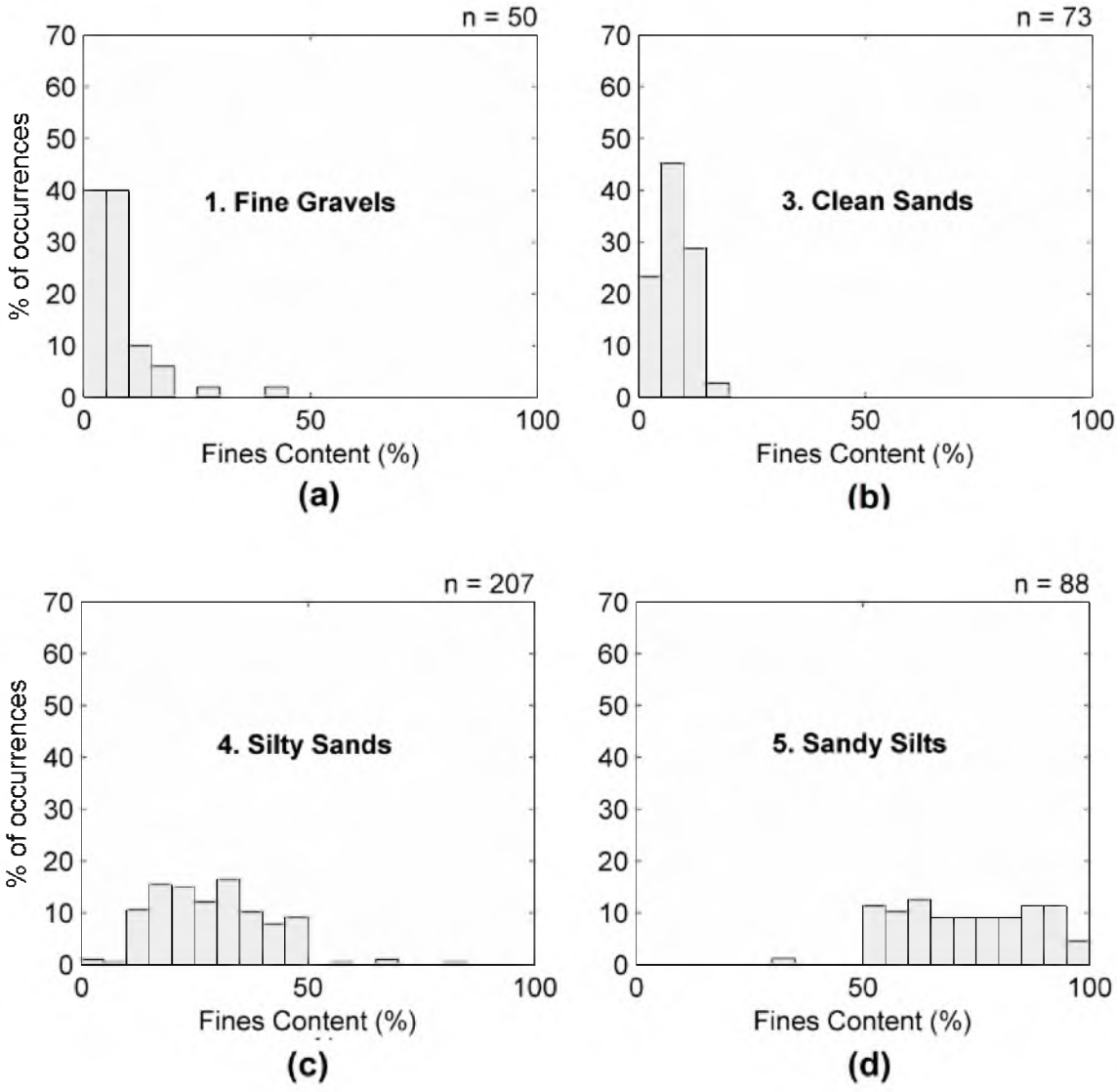

Figure D.1. Histograms of fines content for samples with a value of: (a) *SI* = 1, (b) *SI* = 3, (c) *SI* = 4, and (d) *SI* = 5; Weber County, Utah

APPENDIX E

ADDITIONAL PROBABILISTIC LIQUEFACTION-INDUCED GROUND FAILURE HAZARD MAPS OF WEBER COUNTY, UTAH

Chapter 5 presented probabilistic liquefaction-induced ground failure hazard maps for the Wasatch Front of Weber County, Utah. The maps show the probability of liquefaction triggering or lateral spread displacement exceeding certain thresholds for scenario seismic events. This appendix contains additional maps. Figure E.1 and Figure E.2 show 16^{th} and 84^{th} percentile probabilities of liquefaction triggering for a 500-year return period seismic event, respectively. Similarly, Figure E.3 and Figure E.4 depict 16^{th} and 84^{th} percentile probabilities of liquefaction triggering for a 2,500-year return period seismic event, respectively. Figure E.5 and Figure E.6 show 16^{th} percentile probabilities of lateral spread displacements exceeding 0.1 and 0.3 meters for a 500-year return period seismic event, respectively. Figure E.7 through Figure E.9 show 16^{th} percentile probabilities of lateral displacements exceeding 0.1, 0.3, and 0.6 meters for a 2,500-year return period seismic event, respectively. Finally, Figure E.10 through Figure E.12 depict 16^{th}, 50^{th} and 84^{th} percentile probabilities of lateral spread displacements exceeding 1.0 meters for a 2,500-year return period seismic event, respectively.

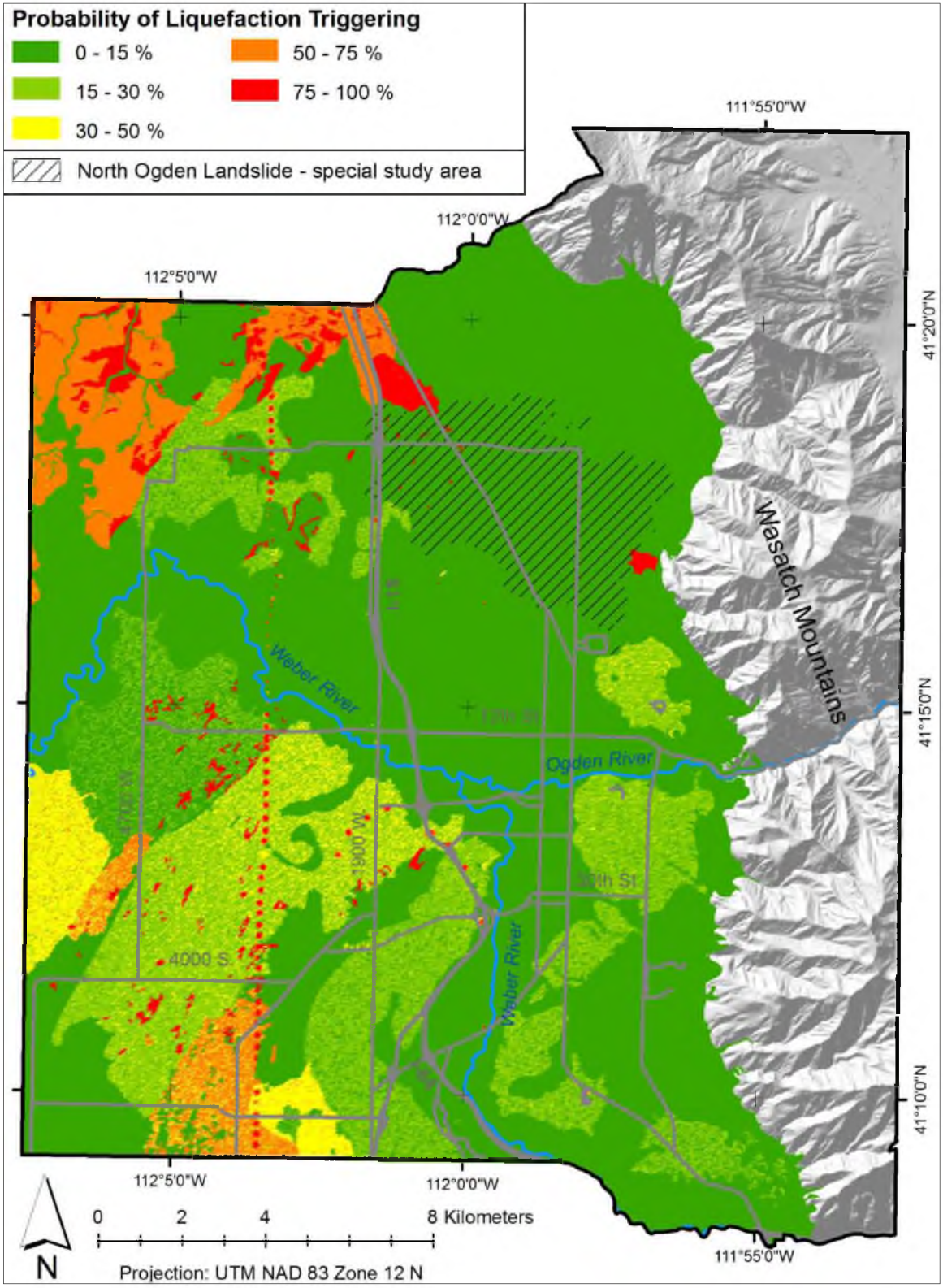

Figure E.1. 16th percentile probabilities of liquefaction triggering for a 500-year seismic event; Weber County, Utah

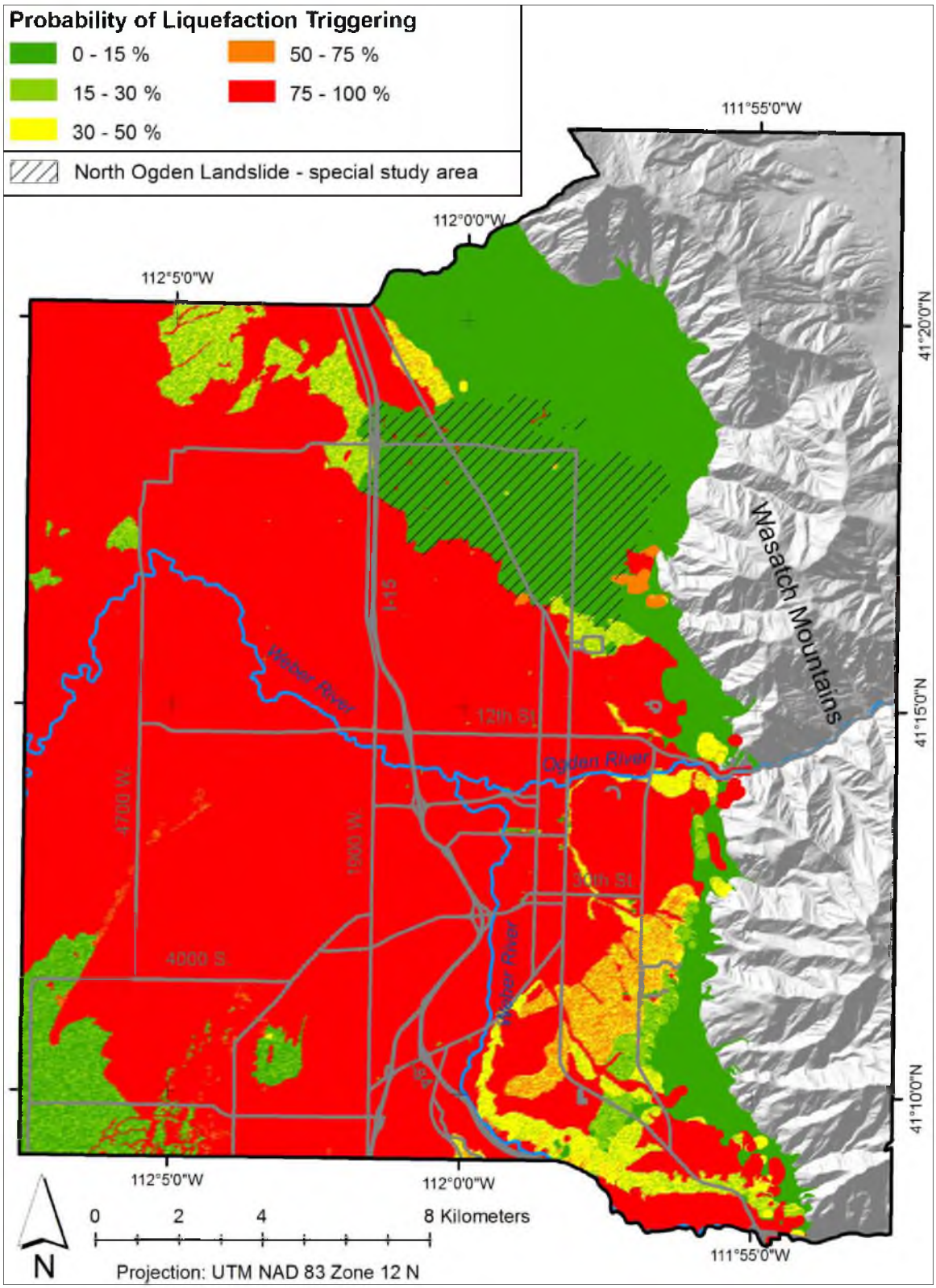

Figure E.2. 84th percentile probabilities of liquefaction triggering for a 500-year seismic event; Weber County, Utah

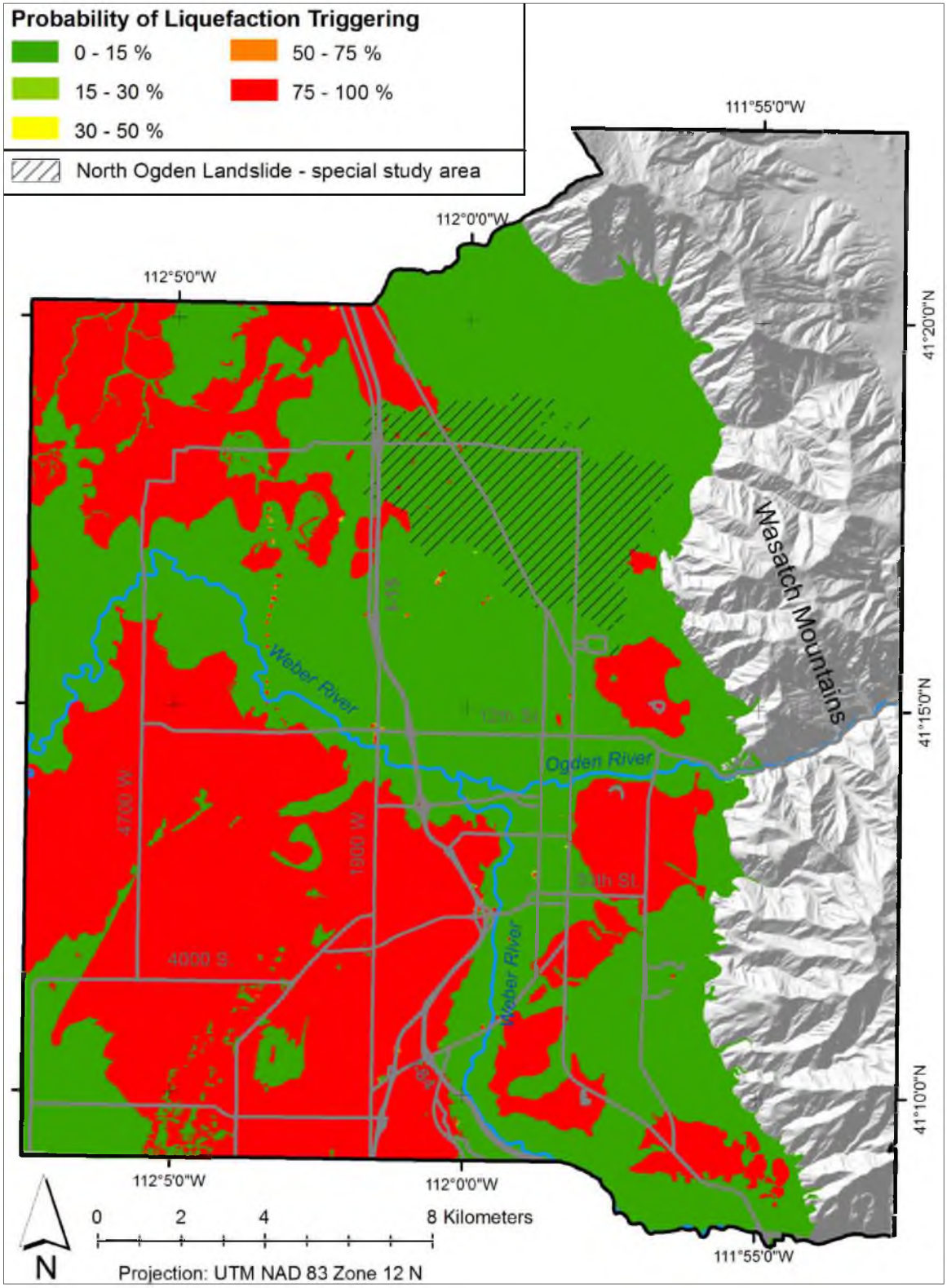

Figure E.3. 16th percentile probabilities of liquefaction triggering for a 2,500-year seismic event; Weber County, Utah

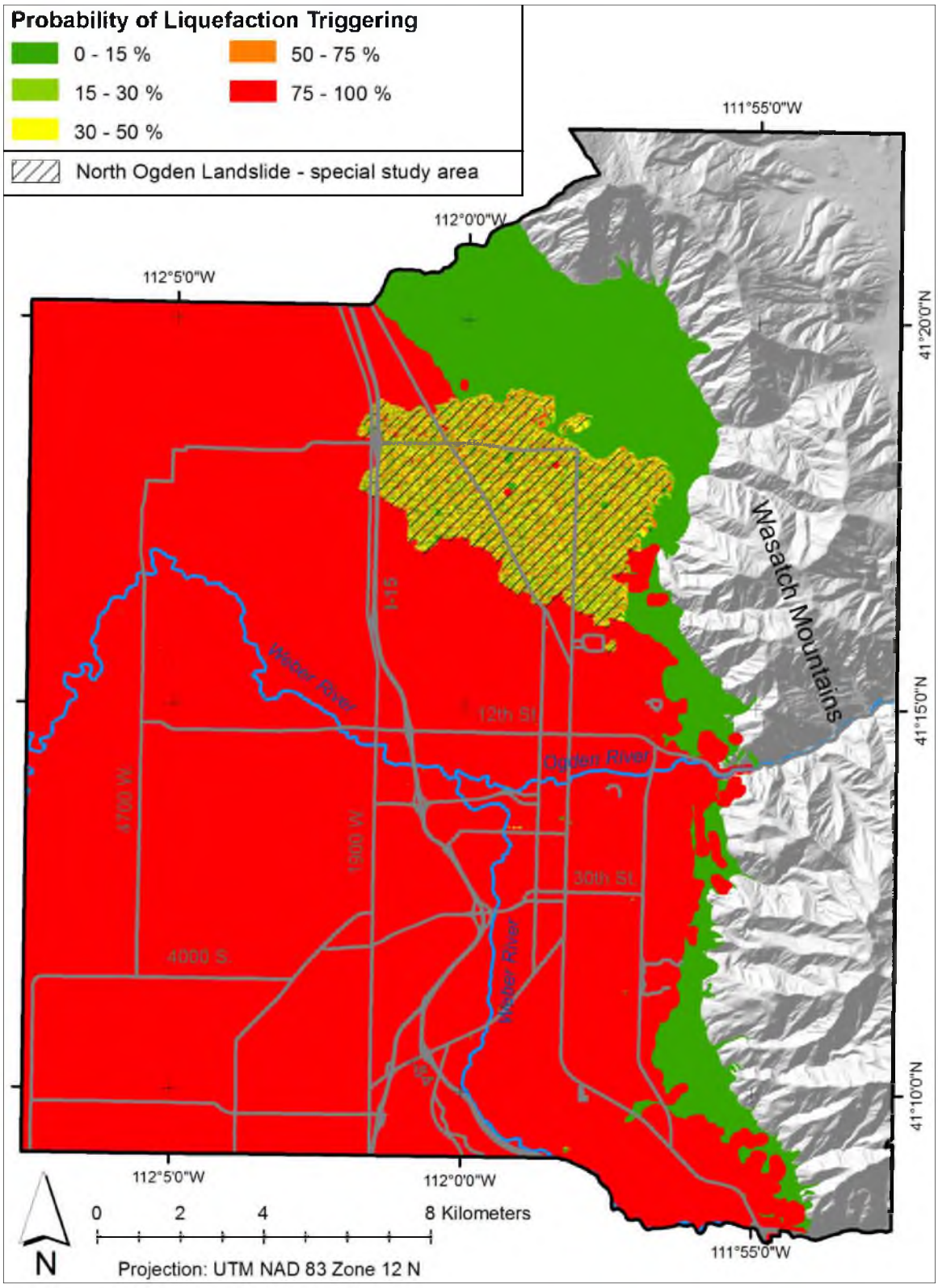

Figure E.4. 84th percentile probabilities of liquefaction triggering for a 2,500-year seismic event; Weber County, Utah

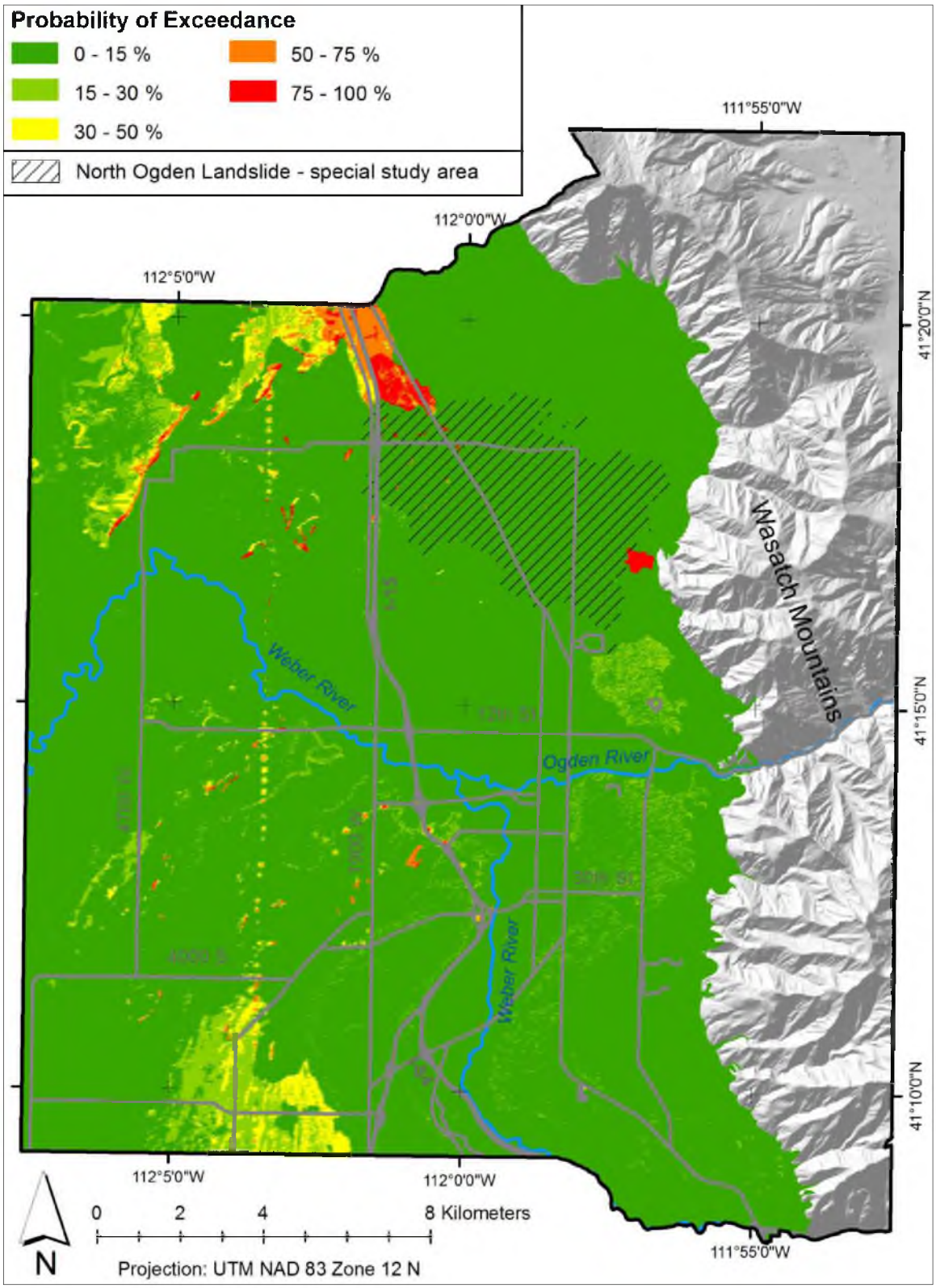

Figure E.5. 16th percentile probabilities of lateral spread displacement exceeding 0.1 meters for a 500-year seismic event; Weber County, Utah

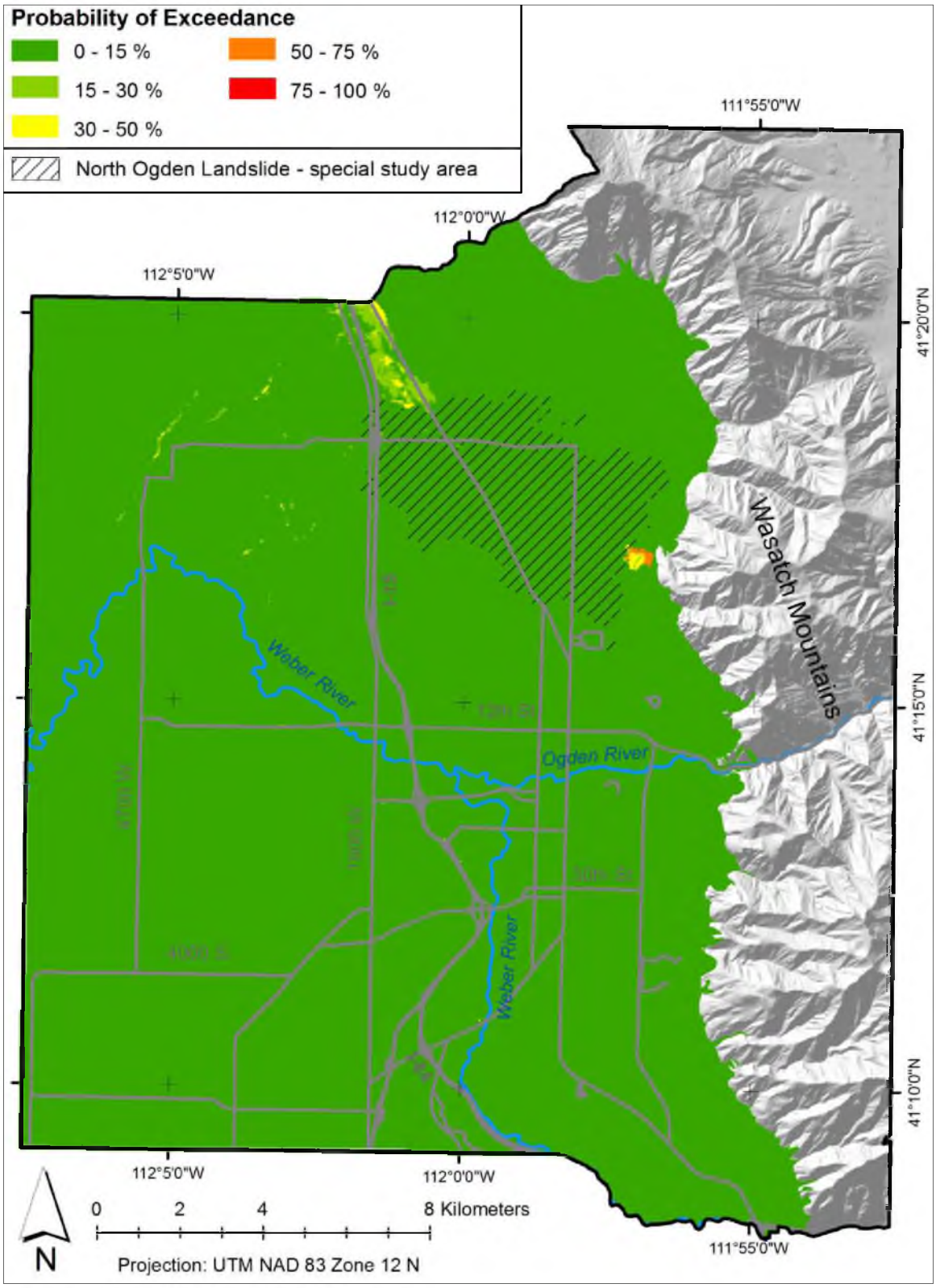

Figure E.6. 16th percentile probabilities of lateral spread displacement exceeding 0.3 meters for a 500-year seismic event; Weber County, Utah

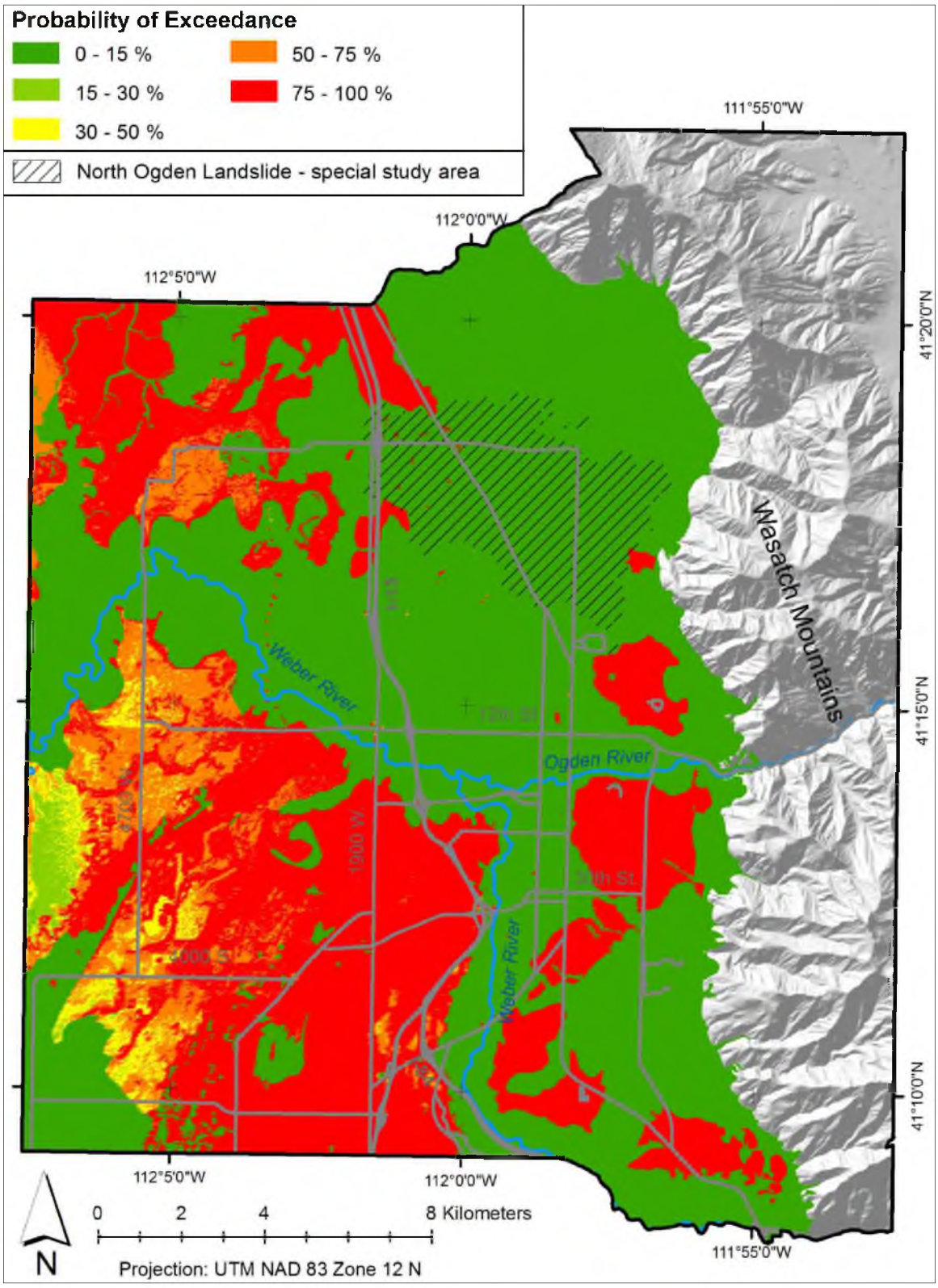

Figure E.7. 16th percentile probabilities of lateral spread displacement exceeding 0.1 meters for a 2,500-year seismic event; Weber County, Utah

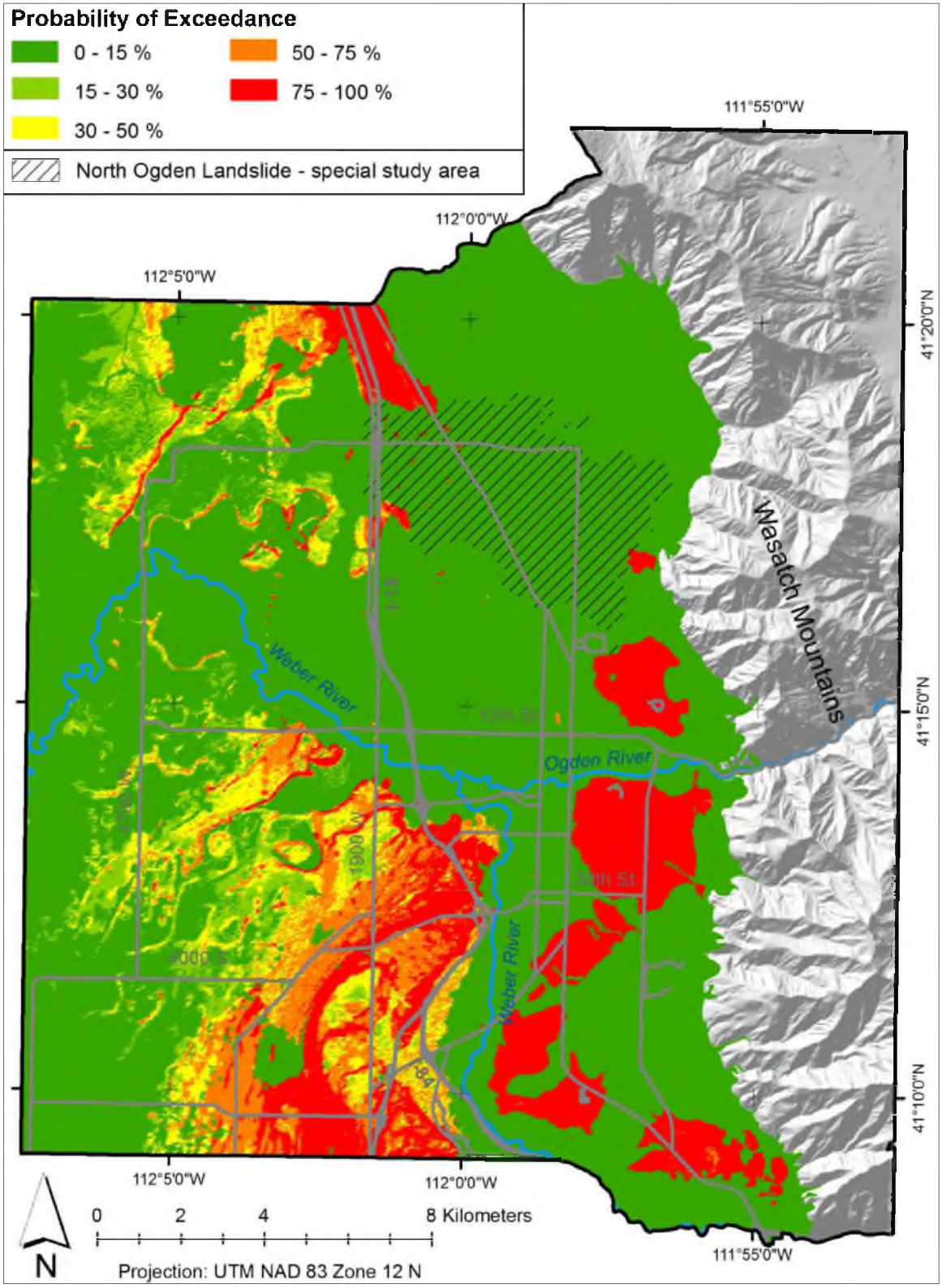

Figure E.8. 16th percentile probabilities of lateral spread displacement exceeding 0.3 meters for a 2,500-year seismic event; Weber County, Utah

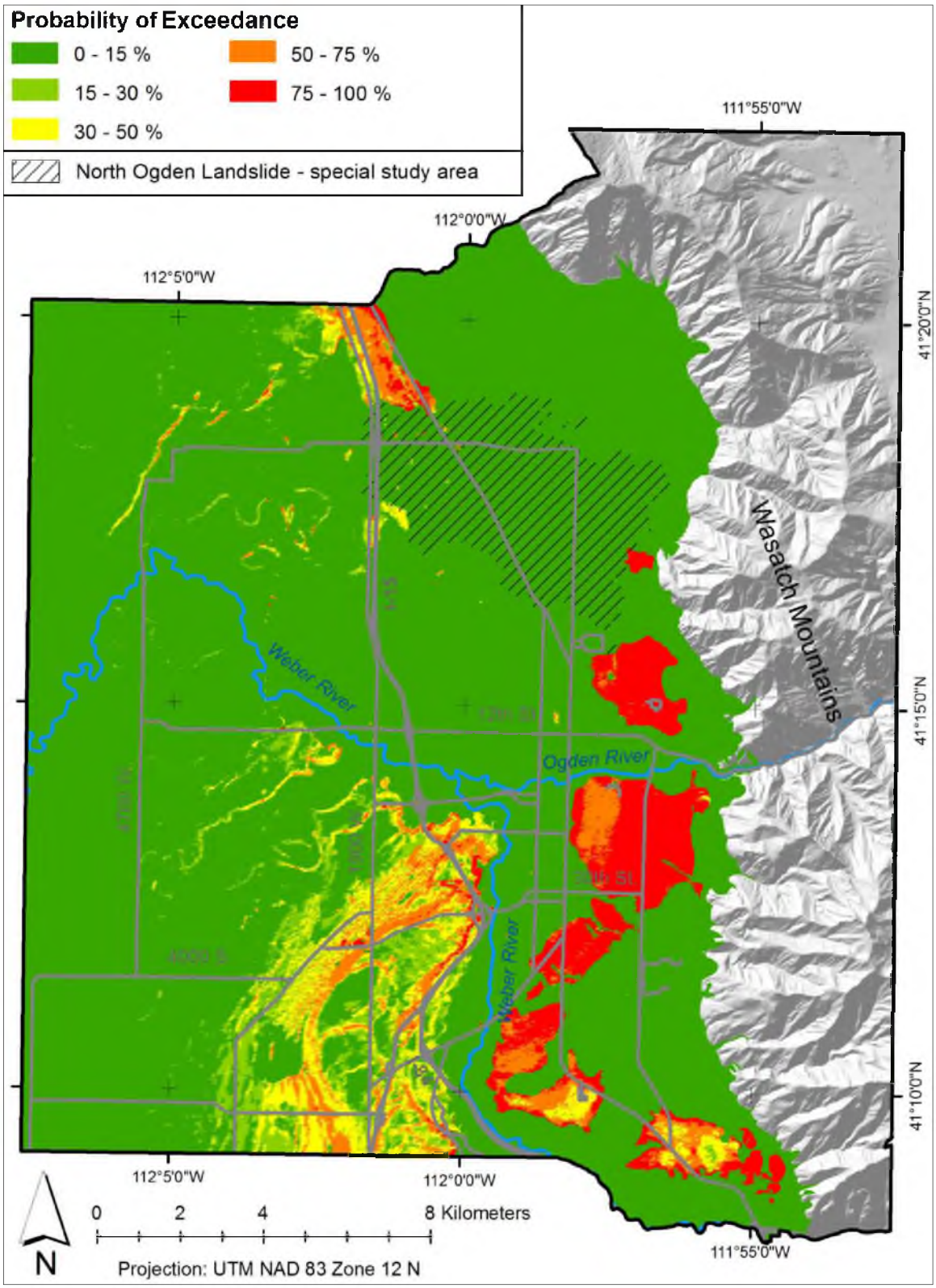

Figure E.9. 16th percentile probabilities of lateral spread displacement exceeding 0.6 meters for a 2,500-year seismic event; Weber County, Utah

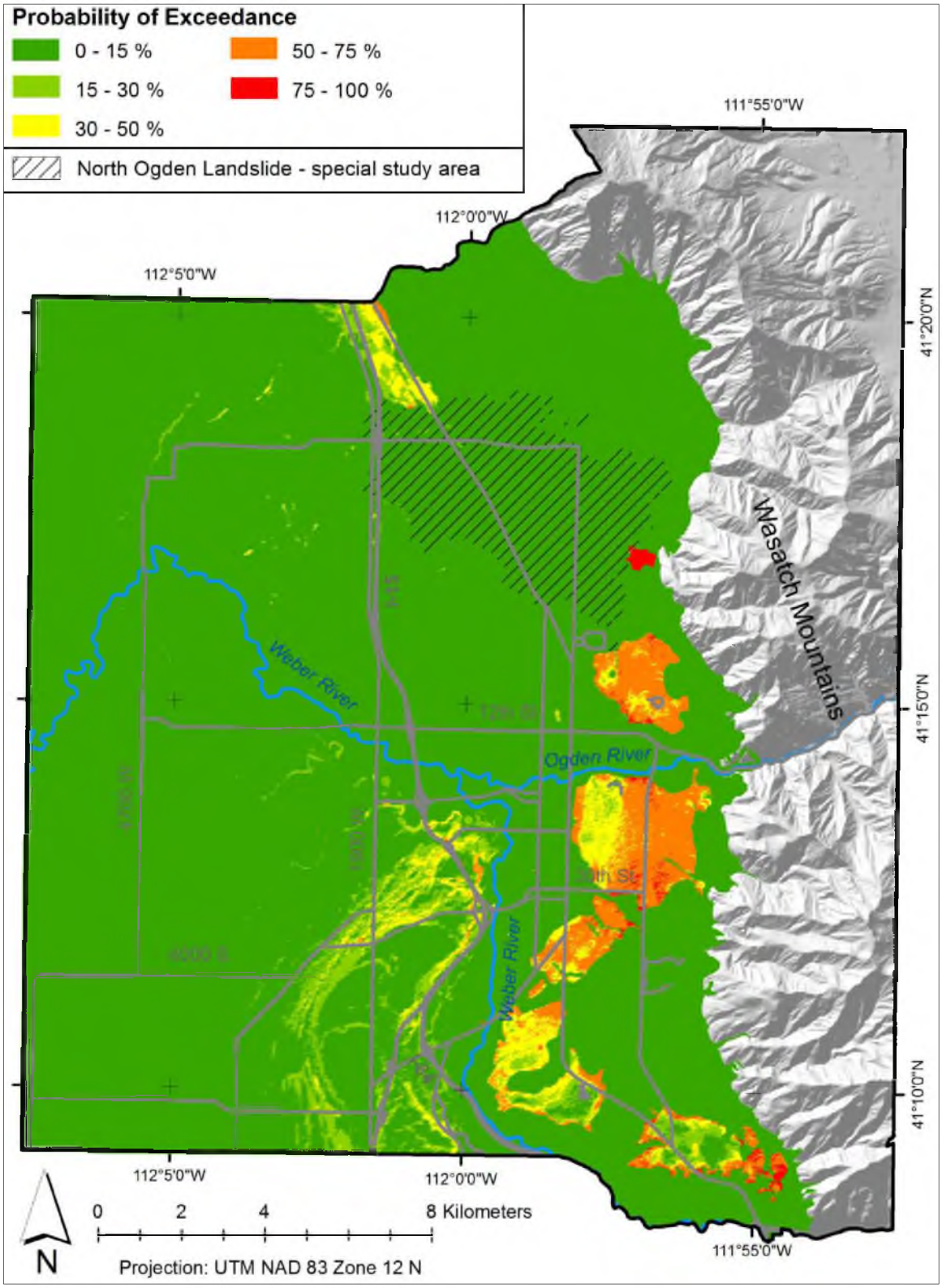

Figure E.10. 16th percentile probabilities of lateral spread displacement exceeding 1.0 meters for a 2,500-year seismic event; Weber County, Utah

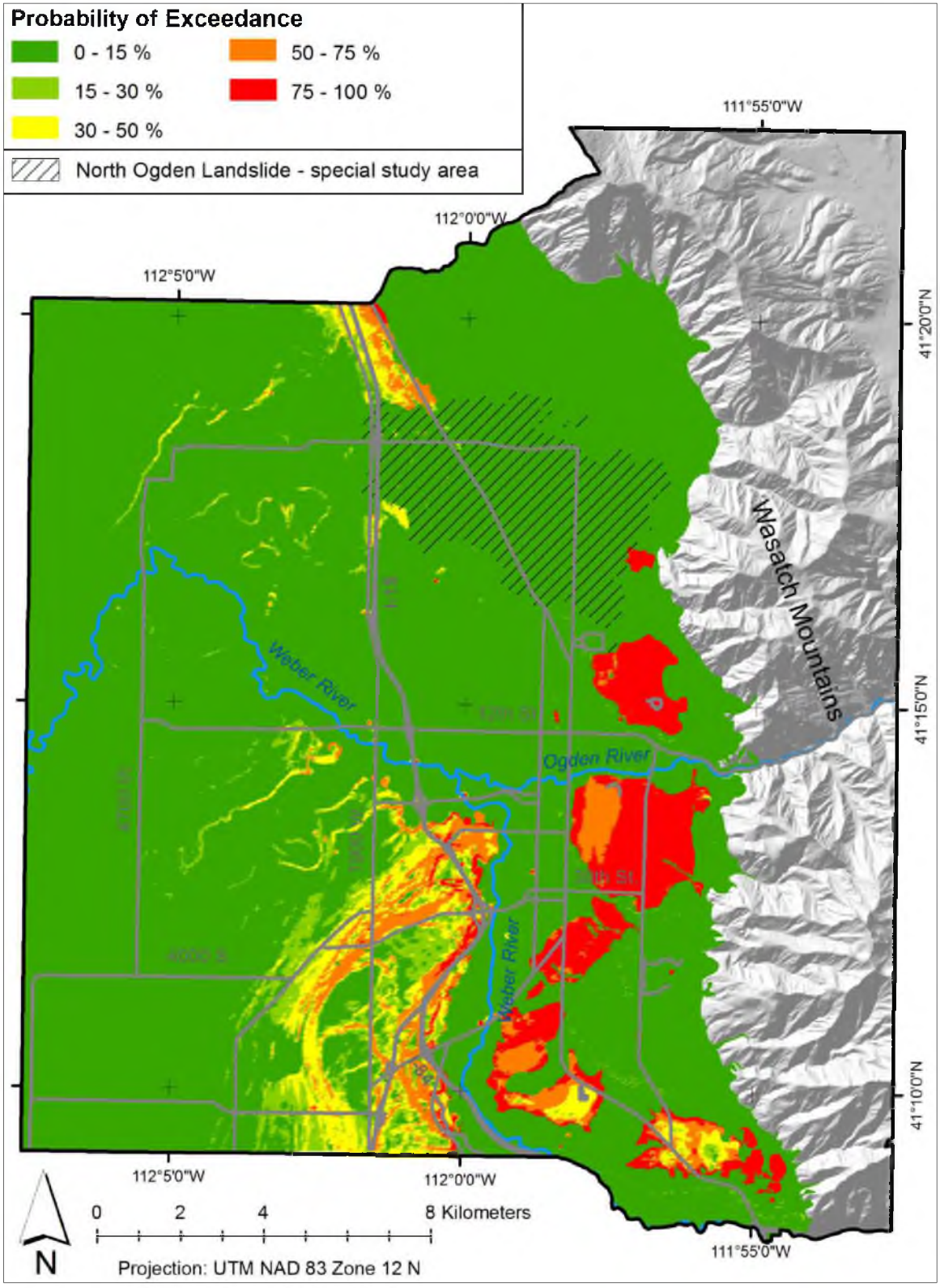

Figure E.11. 50th percentile probabilities of lateral spread displacement exceeding 1.0 meters for a 2,500-year seismic event; Weber County, Utah

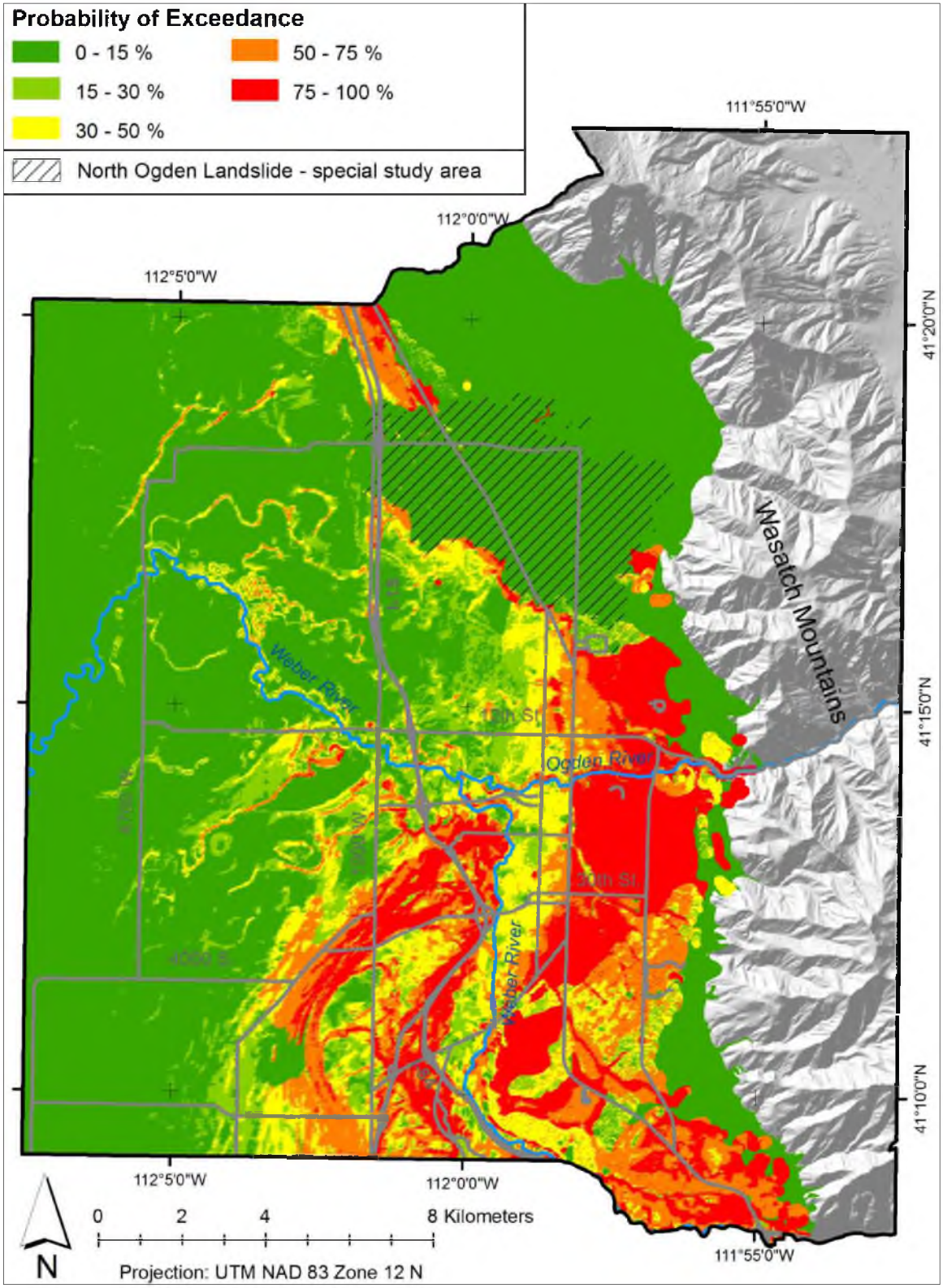

Figure E.12. 84th percentile probabilities of lateral spread displacement exceeding 1.0 meters for a 2,500-year seismic event; Weber County, Utah

APPENDIX F

MATLAB CODE

We wrote Matlab® computer code to perform the necessary computations and Monte Carlo simulations. Matlab® is a programming language as well as an interactive computational environment. Files that contain code in the Matlab® language are called M-files. There are two kinds of M-files: scripts, which operate on data in the workspace and execute commands found in the file; and, functions, which accept input arguments and return output arguments. For the analysis, we wrote 9 scripts and 7 functions. This appendix contains the code for all 16 of these M-files, which can be saved in a directory and added to a Matlab® search path. The percent symbol (%) precedes comments that briefly explain lines of code.

The first 4 M-files in this appendix are scripts that reduce raw SPT and CPT data from the geotechnical database. They are set to run 300 Monte Carlo random sampling simulations at each SPT borehole or CPT sounding, thereby solving for the distributions of all variables in the critical dataset at each investigation. The fifth M-file (BINC_CINC_COMBINER.m) is a script that combines and saves the outputs of the first 4 M-files into a binary file structure (ALLSITE.mat).

The remaining 11 M-files find the distributions of the probability of liquefaction triggering and the probability of lateral spread displacements exceeding certain thresholds for a scenario seismic event. Four of these 11 M-files are scripts that use the 7 functions to solve for these distributions. Each of the 4 scripts must be executed in the order shown in this appendix. Prior to running these scripts, we filled the study area with a grid of point features using GIS tools in ArcMap®. We saved these features into a shapefile. As previously discussed, at each point feature we used the "latticespot" tool in ArcMap® to extract values from the following raster data: the surficial geologic deposit and its age, ground slope, site class, and elevation. The latticespot tool saves these raster values in the attribute table of the point features. After developing the grid, we run the first of the 4 scripts (grid_reader.m) to import the shapefile into Matlab®. The next script (mr_finder.m) loads mapped values of a scenario earthquake and interpolates for the mean seismic variables (i.e., a_{max}, M, and R) at each grid point. The third script (w_finder.m) loads line features that define the free-faces in the study area, and computes the free-face ratio (W) at each grid point. Finally, the fourth script (grid_solver.m) loads the geotechnical data from ALLSITE.mat, and runs 3,000 Monte Carlo random sampling simulations at each grid point in order to calculate the distributions of the probability of liquefaction triggering and the probability of lateral spread displacements exceeding thresholds from 0.1 to 1.0 meters. This final script outputs gridded 16^{th}, 50^{th}, and 84^{th} percentile probabilities of each distribution, as well as the mean and standard deviation of each distribution.

1. SPT_INCREMENTER.m

```
%This Matlab script loads SITE and BLOW tables and merges them into a structure
%for liquefaction analysis.  It interpolates soil properties at increments of 0.1
%ft. It assigns indices to layers of sediment according to description.
%Outputs data into BLOWINC table.

clear all
close all
load BLOW
load SITE

[Bu Iu Ju]=unique(BF.USCS); %all unique USCS classes
ibound = find(Ju==1); %index to all "boundary" lines (not samples)
idata = find(Ju~=1); %index to all samples in database

ifines = find(BF.ESTFINES <= 2); %index to all samples with fines content in
database
idry = find(BF.ESTDRY <= 2);
imoist = find(BF.ESTMOIST <=2);

e = length(SITE.SITEIDNO);

for idx = 1:e;
    isite = SITE.SITEIDNO(idx); %index to individual boring
    ibf = find(BF.SITEIDNO==isite); %index to data in an individual boring
    ibfd = intersect(ibf,idata); %index to sample only data in a boring
```

```
%determine SITEIDNO and GWT
BINC(idx).siteidno = isite;
zgw = SITE.DEPTHGW(idx);
BINC(idx).depthgw = zgw;
BINC(idx).geolunit = SITE.GEOLUNIT(idx);
BINC(idx).easting = SITE.EASTING(idx);
BINC(idx).northing = SITE.NORTHING(idx);
BINC(idx).amax = 0.2; %set temporary values to solve for critical layer
BINC(idx).Mw = 7;

%assign hammer type (CE = 1 is safety, CE = 1.1 is automatic)
BINC(idx).hammer = SITE.CE(idx);

%find the boundaries of each layer in the borehole
ibo=[]; top=[]; bot=[];
ibo = intersect(ibound, ibf);
top = BF.DEPTH(ibo(1:length(ibo)-1)); %depth to top of each layer
bot = BF.DEPTH(ibo(2:length(ibo))); %depth to bottom of each layer

%eliminate layers that begin below 100' (liquefaction is a shallow
%phenomena
itop50 = find(top >= 100);
top(itop50) = [];
bot(itop50) = [];
```

```
%set up depth increment
maxdepth(idx) = max(bot);
BINC(idx).z(:,1) = 0:0.1:maxdepth(idx);

%assign layer numbers to each depth increment, and soil index numbers
for i = 1:length(top);
   ilay = find(BINC(idx).z >= top(i));
   BINC(idx).zlay(ilay,1) = i;
end

%assign layer numbers to each sample in the BLOW database
BF.LAYER(ibfd,1) = interp1q(BINC(idx).z, BINC(idx).zlay,BF.DEPTH(ibfd));

%assign soil index numbers, wclass, mclass, sgclass to each layer
%number
SI = []; WCLASS = []; MCLASS = []; SGCLASS = [];
for i = 1:length(top);
   ilay2 = find(BF.LAYER(ibfd) == i);
   BINC(idx).si(i) = mode(BF.SOIL_INDEX(ibfd(ilay2))); %soil index for a layer
   BINC(idx).wclass(i) = mode(BF.WCLASS(ibfd(ilay2))); %wclass for a layer
   BINC(idx).mclass(i) = mode(BF.MCLASS(ibfd(ilay2))); %mclass for a layer
   BINC(idx).sgclass(i) = mode(BF.SGCLASS(ibfd(ilay2))); %sgclass for a layer
end

%assign FINES to layers with measured data from BLOW database
ifc = [];
```

```
BINC(idx).fines(1:length(BINC(idx).z),1) = NaN;
ifc = intersect(ibfd,ifines); %index to measured fines content in a borehole
if isempty(ifc) == 0;
   [Bf If Jf] = unique(BF.LAYER(ifc)); %layers in boring with known fines
   for i = 1:length(Bf);
      jfines = find(Jf == i);
      ilay3 = find(BINC(idx).zlay == Bf(i));
      if length(jfines) == 1;
         BINC(idx).fines(ilay3,1) = BF.FINES(ifc(jfines));
      else %interpolate to nearest measurement in layers with multiple
measurements
         BINC(idx).fines(ilay3,1) =
interp1(BF.DEPTH(ifc(jfines)),BF.FINES(ifc(jfines)),BINC(idx).z(ilay3),'nearest','extra
p');
      end
   end
end

%assign DRYUNITPCF to layers with measured data from BLOW database
idu = [];
BINC(idx).dryunit(1:length(BINC(idx).z),1) = NaN;
idu = intersect(ibfd,idry); %index to measured dryunits in  a borehole
if isempty(idu) == 0;
   [Bd Id Jd] = unique(BF.LAYER(idu));
   for i = 1:length(Bd);
      jdry = find(Jd == i);
```

```
            ilay3 = find(BINC(idx).zlay == Bd(i));
            if length(jdry) == 1;
               BINC(idx).dryunit(ilay3,1) = BF.DRYUNITPCF(idu(jdry));
            else
               BINC(idx).dryunit(ilay3,1) =
interp1(BF.DEPTH(idu(jdry)),BF.DRYUNITPCF(idu(jdry)),BINC(idx).z(ilay3),'nearest','
extrap');
            end
         end
      end

      %assign MOISTURE_CONTENT to layers with measured data from BLOW
      %database
      iwn = []; ilay5 = [];
      BINC(idx).moisture_content(1:length(BINC(idx).z),1) = NaN;
      iza = find(BINC(idx).z < zgw);
      if isempty(iza) == 0;
         BINC(idx).moisture_content(iza,1) = 0; %assume mc = 0 above GWT unless
otherwise measured and filled in below
      end
      iwn = intersect(ibfd,imoist); %index to measured moisture contents in a borehole
      jabove = find(BF.DEPTH(iwn) < zgw); %index to mc's above GWT (assume moist
or wet)
      jbelow = find(BF.DEPTH(iwn) >= zgw); %index to mc's below GWT (assume
saturated)
      if isempty(jabove) == 0; %assign measured mc's to layers above GWT
```

```
      [Bm Im Jm] = unique(BF.LAYER(iwn(jabove))); %layers of a borehole with
measured mc's above GWT
      for i = 1:length(Bm);
         jmc = find(Jm == i);
         ilay3 = find(BINC(idx).zlay == Bm(i));
         ilay4 = find(BINC(idx).z < zgw);
         ilay5 = intersect(ilay3,ilay4);
         if length(jmc) == 1;
            BINC(idx).moisture_content(ilay5,1) =
BF.MOISTURE_CONTENT(iwn(jabove(jmc)));
         else
            BINC(idx).moisture_content(ilay5,1) =
interp1(BF.DEPTH(iwn(jabove(jmc))),BF.MOISTURE_CONTENT(iwn(jabove(jmc))),BI
NC(idx).z(ilay5),'nearest','extrap');
         end
      end
   end
   if isempty(jbelow) == 0; %assign measured mc's to layers below GWT
      [Bm Im Jm] = unique(BF.LAYER(iwn(jbelow))); %layers of a borehole with
measured mc's below GWT
      for i = 1:length(Bm);
         jmc = find(Jm == i);
         ilay3 = find(BINC(idx).zlay == Bm(i));
         ilay4 = find(BINC(idx).z >= zgw);
         ilay5 = intersect(ilay3,ilay4);
         if length(jmc) == 1;
```

```
            BINC(idx).moisture_content(ilay5,1) =
BF.MOISTURE_CONTENT(iwn(jbelow(jmc)));
         else
            BINC(idx).moisture_content(ilay5,1) =
interp1(BF.DEPTH(iwn(jbelow(jmc))),BF.MOISTURE_CONTENT(iwn(jbelow(jmc))),BI
NC(idx).z(ilay5),'nearest','extrap');
         end
      end
   end

   %fill in measured values of N60/CE from BLOW database to nearest depth
   %in BINC database
   BINC(idx).n60ce(1:length(BINC(idx).z),1) = NaN;
   for i = 1:length(ibfd);
      ila = find(roundn(BINC(idx).z,-1) == roundn(BF.DEPTH(ibfd(i)),-1));
      BINC(idx).n60ce(ila) = BF.N60CE(ibfd(i));
   end



end

save BLOWINC BINC
```

2. SPT_BOREHOLE_SIMULATOR.m

```
%Script uses Monte Carlo techniques to fill in NaN's of important soil inputs
%and then solves for the stress profile, N160, critical layer information,
%and T15cs (file solves for critical dataset at each SPT)

clear all
close all

load BLOWINC;

e = length(BINC);
n = 300; %specify number of simulations.

for idx = 1:e;

    ce = [];
    %simulate energy ratio correction, CE
    if BINC(idx).hammer == 1; %safety hammer
        ce = 1.0 + 0.1.*randn(1,n);
    else %automatic hammer
        ce = 1.1 + 0.1.*randn(1,n);
    end
    ce = repmat(ce,length(BINC(idx).z),1);

    %simulate fines content for layers w/o data (neglect SI = 6 since
    %cohesive layers are not needed for liquefaction analysis)
```

```
fines = []; simfc = [];
afines = [ 0  0  0 15 50]; %lower bound of uniform fines distribution for SI
bfines = [15 15 15 50 95]; %upper bound of fines distribution for SI
ich = find(BINC(idx).si ~=6);
jnan = isnan(BINC(idx).fines) == 1;
inan = unique(BINC(idx).zlay(jnan));
ifines = intersect(ich,inan)'; %index to cohesionless layers w/o fines data

fines = repmat(BINC(idx).fines,1,n);

if isempty(ifines) == 0;
   for i = 1:length(ifines);
      ilay = find(BINC(idx).zlay == ifines(i));
      si = BINC(idx).si(ifines(i));
      simfc(ifines(i),:) = afines(si) + (bfines(si) - afines(si)).*rand(1,n);
      fines(ilay,:) = repmat(simfc(ifines(i),:),length(ilay),1);
   end
end

%simulate dry unit weights for layers w/o data
dryunit = []; simdu = [];
mudry = [86.2 93.3 98.4 107.5]; %means in pcf
sigmadry = 7.3; %pooled standard deviation

jnan = isnan(BINC(idx).dryunit) == 1;
idry = unique(BINC(idx).zlay(jnan)); %index to layers w/o dryunit data
```

```
    dryunit = repmat(BINC(idx).dryunit,1,n);

    if isempty(idry) == 0;
       for i = 1:length(idry);
          ilay = find(BINC(idx).zlay == idry(i));
          wclass = BINC(idx).wclass(idry(i));
          simdu(idry(i),:) = mudry(wclass) + sigmadry.*randn(1,n);
          dryunit(ilay,:) = repmat(simdu(idry(i),:),length(ilay),1);
       end
    end

    %simulate moisture contents for layers w/o data
    moisture_content = []; simmc = [];
    mumoist =    [1.531  1.467  1.424  1.384   1.294 0.998]; %log10 means (log %)
    sigmamoist = [0.0749 0.0749 0.0749 0.0749 0.1826 0.1826]; %log 10 standard
dev.

    jnan = find(isnan(BINC(idx).moisture_content) == 1);
    imoist = unique(BINC(idx).zlay(jnan)); %index to layers w/o m.c. data

    moisture_content = repmat(BINC(idx).moisture_content,1,n);

    if isempty(imoist) == 0;
       for i = 1:length(imoist);
          ilay = find(BINC(idx).zlay == imoist(i));
```

```
            mclass = BINC(idx).mclass(imoist(i));
            simmc(imoist(i),:) = 10.^(mumoist(mclass) +
sigmamoist(mclass).*randn(1,n));
            moisture_content(ilay,:) = repmat(simmc(imoist(i),:),length(ilay),1);
        end
    end

    %simulate specific gravities for all layers
    spgravity = []; simsg = [];
    musg = [2.72 2.65 2.67 2.62]; %mean of s.g. distribution for sgclass
    sigmasg = [0.02 0.02 0.01 0.02]; %sigma of s.g. distribution

    isg = 1:length(BINC(idx).sgclass); %index to each layer in a borehole

    for i = 1:length(isg);
        ilay = find(BINC(idx).zlay == isg(i));
        sgclass = BINC(idx).sgclass(isg(i));
        simsg(isg(i),:) = musg(sgclass) + sigmasg(sgclass).*randn(1,n);
        spgravity(ilay,:) = repmat(simsg(isg(i),:),length(ilay),1);
    end

    %calculate unit weights of soil with depth for every simulation
    unitwt = [];
    iabove = find(BINC(idx).z < BINC(idx).depthgw); %index to depths above GWT
    ibelow = find(BINC(idx).z >= BINC(idx).depthgw); %index to depths below GWT
```

```
    unitwt(iabove,:) = dryunit(iabove,:).*(1+moisture_content(iabove,:)./100);
    unitwt(ibelow,:) =
spgravity(ibelow,:).*62.4.*(1+moisture_content(ibelow,:)./100)./(1+moisture_cont
ent(ibelow,:)./100.*spgravity(ibelow,:));
    unitwt(1,:) = 0; %set to zero at ground surface

    %calculate stress profiles for every simulation
    pwp = []; totalstress = []; effstress = []; dts = [];

    pwp(iabove,:) = 0; %assume pwp = 0 above GWT
    pwp(ibelow,:) = 62.4/2000 .* (BINC(idx).z(ibelow,:)-BINC(idx).depthgw); %in tsf
    pwp = repmat(pwp,1,n);
    pwp(1,:) = 0;

    dts = unitwt./2000.*0.1; %incremental change in total stress
    totalstress = cumsum(dts); %in tsf
    effstress = totalstress - pwp; %in tsf
    i = effstress < 0;
    effstress(i) = 0;

    %calculate CN for every simulation
    cn = [];
    cn = 2.2./(1.2 + effstress);
    i = cn > 1.7;
    cn(i) = 1.7;
```

```
%correct measured blowcounts to N160 based on data from every simulation
n60ce = []; n160 = [];
n60ce = repmat(BINC(idx).n60ce,1,n);
n160 = n60ce .* ce .* cn;

%fill in values of N160 for every depth increment

for i = 1:length(isg);
   inm = find(isnan(n160(:,1)) == 0); %index to measured blowcounts
   ilay = find(BINC(idx).zlay == i); %index to data in a given layer
   idat = intersect(ilay, inm); %index to measured blowcounts in a layer
   if length(idat) == 1;
      n160(ilay,:) = repmat(n160(idat,:),length(ilay),1);
   else  %linearly interpolate between measured values
      n160(ilay,:) =
interp1(BINC(idx).z(idat),n160(idat,:),BINC(idx).z(ilay),'linear');
      inan = find(isnan(n160(ilay,1)) == 1); %extrapolate for points outside of
bounds
      n160(ilay(inan),:) =
interp1(BINC(idx).z(idat),n160(idat,:),BINC(idx).z(ilay(inan)),'nearest','extrap');
   end

end
n60 = []; n160cs = [];
n60 = n160./ce;
FC = [];
```

```
    FC = fines; %use as fines content for correcting N160 to clean sand equivalent
    i = FC < 5;
    FC(i) = 0;
    i = FC > 35;
    FC(i) = 35;  %cap the fines correction to between 5 and 35%
    n160cs = n160.*((1+0.004.*FC)+.05.*(FC./n160));

    %Find average N160 value in the upper 100' per ASCE 7
    nb = n160;
    i = nb == 0;
    nb(i) = 1; %so that won't divide by zero.
    i = nb > 100;
    nb(i) = 100;
    BINC(idx).Nbar =
sum(repmat(BINC(idx).z,1,n))./sum((repmat(BINC(idx).z,1,n))./nb);
    BINC(idx).Nbarmed = median(BINC(idx).Nbar);
    BINC(idx).zmax = max(BINC(idx).z);

    %Find probability of liquefaction (PLINC) for every increment in each simulation.
    %Then calculate the maximum value and set to the PL for each simulation
    SI = []; plinc = []; plmax = []; iz = [];
    for i = 1:length(isg);
        ilay = find(BINC(idx).zlay == i);
        SI(ilay,1) = BINC(idx).si(i);
    end
    SI = repmat(SI,1,n);
```

```
    plinc(1:length(BINC(idx).z),1:n) = NaN;
    ich = find(SI ~= 6); %index to cohesionless increments in a borehole
    isat = find(repmat(BINC(idx).z,1,n) >= BINC(idx).depthgw);
    iliq1 = intersect(ich,isat);
    i50 = find(repmat(BINC(idx).z,1,n) <= 50); %set critical depth to no more than
50 ft.
    iliq = intersect(i50,iliq1);

    Rd = []; sigmard = []; sim_rd = []; csr = [];
    [Rd, sigmard] = rd(0.3048.*BINC(idx).z, BINC(idx).amax, BINC(idx).Mw);
    sim_rd = repmat(Rd,1,n) + repmat(sigmard,1,n) .*
repmat(randn(1,n),length(BINC(idx).z),1); %simulate values of rd
    i = sim_rd > 1;
    sim_rd(i) = 1;
    i = sim_rd < 0.18;
    sim_rd(i) = 0.18;
    csr = 0.65 .* BINC(idx).amax .* totalstress./effstress.*sim_rd;

    plinc(iliq) = probliq(n160cs(iliq), 0, csr(iliq), BINC(idx).Mw, effstress(iliq));
    [plmax,iz] = max(plinc);

    %Determine critical depth (d) by finding the depth for the maximum PL
    %value.
    izs = sub2ind([length(BINC(idx).z) n],iz,[1:n]); %convert index

    BINC(idx).dcr = BINC(idx).z(iz)'; %in ft.
```

```
BINC(idx).n160cr = n160(izs);

BINC(idx).n160cscr = n160cs(izs);

BINC(idx).escr = effstress(izs); %in tsf

BINC(idx).tscr = totalstress(izs); %in tsf


%if liquefaction doesn't occur, set to zero

i = BINC(idx).dcr == 0;

BINC(idx).n160cr(i) = 0;

BINC(idx).n160cscr(i) = 0;


%Find T15 and x's, then T15cs for every simulation

t15i = []; t15 = [];

i15 = find(n160 <= 15);

isat = find(repmat(BINC(idx).z,1,n) >= BINC(idx).depthgw);

i15sat = intersect(i15,isat);

i50 = find(repmat(BINC(idx).z,1,n) <= 50); %clip to upper 15 m.

it15a = intersect(ich,i15sat);

it15 = intersect(it15a, i50); %index to soil susceptible to lateral spread

t15i = zeros(length(BINC(idx).z),n);


t15i(it15) = 0.1;

t15 = sum(t15i).*0.3048; %T15 in meters


XI = []; xthick = []; x = [];

for i = 1:5;

   XI = zeros(length(BINC(idx).z),n);
```

```
        isi = find(SI == i);
        ix = intersect(isi,it15);
        XI(ix) = 0.1;
        xthick(i,:) = sum(XI).*0.3048;
        x(i,:) = xthick(i,:)./t15;
    end
    inan = find(isnan(x) == 1);
    x(inan) = 0; %replace NaN's with zeros (due to T15 = 0)

    BINC(idx).t15cs = t15e(t15,x);

end

save BLOWINC BINC; %save results
```

3. CPT_INCREMENTER.m

```
%Script takes raw CPT data (from SITECPT and CPTDATA tables) and puts it into a
%structure for liquefaction analysis.  Each sounding is clipped to its upper 100 ft.

clear all;
close all;
load CPTDATA;
load SITECPT;
e = length(SITEC.CPTIDNO);

i50 = find(CPT.DEPTH <= 102); %clip to 100 ft. (upper 30 meters)
```

```
for idx = 1:e;
    isite = SITEC.CPTIDNO(idx);
    icpt1 = find(CPT.CPTIDNO == isite);
    icpt = intersect(icpt1,i50);

    CINC(idx).cptidno = isite; %save CPTIDNO to structure
    zgw = SITEC.DEPTHGW(idx);
    CINC(idx).depthgw = zgw; %depth to GWT (in ft.)
    CINC(idx).sounding = SITEC.SOUNDING(idx);
    CINC(idx).geolunit = SITEC.GEOLUNIT(idx);
    CINC(idx).northing = SITEC.NORTHING(idx);
    CINC(idx).easting = SITEC.EASTING(idx);
    CINC(idx).increment = SITEC.INCREMENT(idx); %measurement inc. in meters
    CINC(idx).Mw = 7; %set temporary values to solve for critical layer
    CINC(idx).amax = 0.5;

   %insert raw data into structure
    CINC(idx).z = CPT.DEPTH(icpt); %depth in ft.
    CINC(idx).u2 = CPT.UBT(icpt); %pwp behind tip in tsf
    CINC(idx).qc = CPT.QC(icpt); %tip resistance in tsf
    CINC(idx).qt = CPT.QT(icpt); %corrected tip resistance in tsf
    CINC(idx).fs = CPT.SLEEVE(icpt); %sleeve friction in tsf
    CINC(idx).rf = CPT.FRATIO(icpt); %friction ratio in %
end
save CPTINC CINC; %output results to CPTINC table
```

4. CPT_SOUNDING_SIMULATOR.m

```
%Script uses Monte Carlo techniques to simulate inputs in order to find
%distributions of (d, qc1, Rf, c, sigmav, sigmav', T15cs) at the critical
%layer for each CPT sounding (file solves for critical dataset at each CPT).

clear all;
close all;
load CPTINC

e = length(CINC);
n = 300; %specify number of simulations

%load SBT zones and their approximate boundaries defined by Ic
SBT = [7 7 6 6 5 5 4 4 3 3 2 2];
ZONES = [0 1.31 1.310001 2.05 2.050001 2.60 2.600001 2.95 2.950001 3.60
3.600001 10];

for idx = 1:e;
    %solve for ISBT and SBT vs. depth using Robertson (2009) method
    isbt = []; sbt = [];
    isbt = ((3.47 - log10(CINC(idx).qt)).^2 + (log10(CINC(idx).rf)+1.22).^2).^0.5;
    sbt = interp1(ZONES,SBT,isbt,'nearest');

    %load unit weights, moisture contents, and spec. gravities by SBT
    mudry = [0 86.2 93.3 93.3 98.4 98.4 107.5];
```

```
    sigmadry = 7.3;
    mumoist = [0 1.531 1.467 1.424 1.384 1.294 0.998];
    sigmamoist = [0 0.0749 0.0749 0.0749 0.0749 0.1826 0.1826];
    musg = [0 2.62 2.72 2.65 2.67 2.67 2.67];
    sigmasg = [0 0.02 0.02 0.02 0.01 0.01 0.01];

    %simulate values of unit weights, moisture contents, and spgravity for
    %each SBT
    dryunit = []; moisture_content = []; spgravity = [];
    dryunit(1:length(CINC(idx).z),1:n) = NaN;
    for i = 1:7;
       j = find(sbt == i);
       if isempty(j) == 0;
          dryunit(j,:) = repmat(mudry(i) + sigmadry.*randn(1,n),length(j),1);
          moisture_content(j,:) = repmat(10.^(mumoist(i) +
sigmamoist(i).*randn(1,n)),length(j),1);
          spgravity(j,:) = repmat(musg(i) + sigmasg(i).*randn(1,n),length(j),1);
       end
    end
    iabove = find(CINC(idx).z < CINC(idx).depthgw); %index to depths above GWT
    ibelow = find(CINC(idx).z >= CINC(idx).depthgw); %index to depths below GWT

    moisture_content(iabove,:) = 0; %assume soil is "dry" above GWT

    %calculate unit weights
    unitwt = [];
```

```
    unitwt(iabove,:) = dryunit(iabove,:).*(1+moisture_content(iabove,:)./100);
    unitwt(ibelow,:) =
spgravity(ibelow,:).*62.4.*(1+moisture_content(ibelow,:)./100)./(1+moisture_cont
ent(ibelow,:)./100.*spgravity(ibelow,:));
    unitwt(1,:) = 0; %set to zero at ground surface

    %find incremental change in depth matrix
    inc = [];
    inc = CINC(idx).z(2:length(CINC(idx).z))-CINC(idx).z(1:length(CINC(idx).z)-1);
    inc = vertcat(inc,inc(length(inc)));

    %solve for stress profiles of every simulation
    pwp = []; totalstress = []; effstress = [];
    pwp(iabove,:) = 0; %assume pwp = 0 above GWT
    pwp(ibelow,:) = 62.4/2000 .* (CINC(idx).z(ibelow,:)-CINC(idx).depthgw); %in tsf
    pwp(1,:) = 0;
    pwp = repmat(pwp,1,n);
    dts = unitwt./2000.*repmat(inc,1,n); %incremental change in total stress
    totalstress = cumsum(dts); %in tsf
    effstress = totalstress - pwp; %in tsf
    i = effstress < 0;
    effstress(i) = 0;

    %solve for Ic by iterating for n and finding Qtn and Fr per Robertson (2009)
    nR = []; %overburden stress normalization factor (n)
    nR = ones(length(CINC(idx).z),n); %assume for first iteration
```

```
nj = []; cq = []; Qtn = []; Fr = []; ic = [];
for i = 1:5; %converges for nR after only a few iterations
    ni = nR;
    cq = (1./effstress).^ni;
    j = cq > 1.7;
    cq(j) = 1.7;
    Qtn = (repmat(CINC(idx).qt,1,n) - totalstress).*cq;
    Fr = (repmat(CINC(idx).fs,1,n))./(repmat(CINC(idx).qt,1,n)-totalstress).*100;
    inan = Qtn < 0; %set to a small value so that it's not complex
    Qtn(inan) = 1;
    inan = Fr < 0;
    Fr(inan) = 0.1;
    ic = ((3.47 - log10(Qtn)).^2 + (log10(Fr)+1.22).^2).^0.5;
    nR = 0.381.*ic + 0.05.*effstress - 0.15;
    j = nR > 1;
    nR(j) = 1;
    j =nR < 0.5;
    nR(j) = 0.5;
end

%solve for Moss et al. (2006) overburden stress normalization
%coefficient, and qc,1
c = [];
c = cfind(CINC(idx).qt.*0.09576,CINC(idx).rf); %assume for first iteration
j = c > 1;
c(j) = 1;  %set range for c between 0.25 and 1.0
```

```
    j = c < 0.25;
    c(j) = 0.25;
    cq = [];
    c = repmat(c,1,n);
    ci = []; qc1 = [];
    for i = 1:5; %converges for c after only a few iterations
       ci = c;
       cq = (1./effstress).^ci;
       j = cq > 1.7; %cap correction at 1.7--similar to CN
       cq(j) = 1.7;
       qc1 = cq.*repmat(CINC(idx).qt,1,n); %in tsf
       c = cfind(qc1.*0.09576,repmat(CINC(idx).rf,1,n));
       j = c > 1;
       c(j) = 1;
       j = c < 0.25;
       c(j) = 0.25;
    end

    %solve for Rd with depth
    Rd = []; sigmard = []; sim_rd = [];
    [Rd, sigmard] = rd(0.3048.*CINC(idx).z,CINC(idx).amax,CINC(idx).Mw);
    sim_rd = repmat(Rd,1,n) + repmat(sigmard,1,n) .*
repmat(randn(1,n),length(CINC(idx).z),1); %simulate values of rd
    i = sim_rd > 1;
    sim_rd(i) = 1;
    i = sim_rd < 0.18;
```

```
    sim_rd(i) = 0.18;  %cap rd between 0.18 and 1

    %solve for csr with depth
    csr = [];
    csr = 0.65 .* CINC(idx).amax .* totalstress./effstress.*sim_rd;

    %solve for prob. of liq. with depth. Screen out cohesive soils defined
    %as when Ic > 2.6 (Idriss & Boulanger).  Use method by Moss et al.
    %2006
    ich = find(ic <= 2.6); %index to cohesionless increments in a borehole
    isat = find(repmat(CINC(idx).z,1,n) > CINC(idx).depthgw);
    iliq1 = intersect(ich,isat);
    i50 = find(repmat(CINC(idx).z,1,n) <= 50);
    iliq = intersect(i50,iliq1); %set critical depth to no more than 50'.
    plinc = [];
    plinc(1:length(CINC(idx).z),1:n) = 0;
    RF = [];
    RF = repmat(CINC(idx).rf,1,n);
    plinc(iliq) = probliqcpt(qc1(iliq).*0.09576, RF(iliq), c(iliq), csr(iliq), CINC(idx).Mw,
effstress(iliq).*95.76);

    %eliminate thin layers as they are not susceptible to lateral spread.
    %Define a thin layer as less than 0.3 m thick
    i = []; j =[]; k = [];
    i = find(plinc>0.01);
    j = i-1;
```

```
itop = setdiff(j,i); %index to top of every simulated sublayer
k = i + 1;
ibot = setdiff(k,i); %index to bottom of every simulated sublayer

for m = 1:length(itop);
   i1 = find(i > itop(m));
   i2 = find(i < ibot(m));
   ilay = intersect(i1,i2);
   if length(ilay) < round(0.3/CINC(idx).increment);
      plinc(i(ilay)) = 0; %layer is too thin
   end
end

%solve for depth to maximum probability of liquefaction in a sounding.
%Set this depth as critical depth, and find its associated values of
%qc1, rf, c, sigma, sigma'
iz = []; izs = []; plmax = [];
[plmax,iz] = max(plinc);
izs = sub2ind([length(CINC(idx).z) n],iz,[1:n]); %convert index to matrix

CINC(idx).dcr = CINC(idx).z(iz)'; %in ft.
CINC(idx).qc1cr = qc1(izs); %in tsf
CINC(idx).rfcr = CINC(idx).rf(iz)'; %in (%)
CINC(idx).ccr = c(izs);
CINC(idx).escr = effstress(izs); %in tsf
CINC(idx).tscr = totalstress(izs); %in tsf
```

```
    %solve for N160 with depth using regression eqn.
    qtN60 = []; N60 = []; cn = []; N160 = []; muqtN60 = [];
    qtN60 = zeros(length(CINC(idx).z),n);
    N60 = zeros(length(CINC(idx).z),n);
    cn = zeros(length(CINC(idx).z),n);
    N160 = zeros(length(CINC(idx).z),n);
    muqtN60 = 10.^(1.26 - 0.295.*ic);
    qtN60 = muqtN60 + 10.^(0.156.*randn(length(CINC(idx).z),n));
    N60 = repmat(CINC(idx).qt,1,n)./qtN60;
    cn = 2.2./(1.2 + effstress);
    i = cn > 1.7;
    cn(i) = 1.7;
    N160 = cn.*N60;

    %Find average N160 value in the upper 100' per ASCE 7
    nb = N160;
    i = nb == 0;
    nb(i) = 1; %so that won't divide by zero.
    i = nb > 100;
    nb(i) = 100;
    CINC(idx).Nbar =
sum(repmat(CINC(idx).z,1,n))./sum((repmat(CINC(idx).z,1,n))./nb);
    CINC(idx).Nbarmed = median(CINC(idx).Nbar);
    CINC(idx).zmax = max(CINC(idx).z);
```

```
%solve for prob. of SI given IC with depth
p1 = []; p3 = []; p4 = []; p5 = []; p6 = [];
[p1, p3, p4, p5, p6] = pointest_16(ic);

%solve for T15 and x
%T15 is defined as the cumulative thickness of saturated, cohesionless
%soil with N160 <= 15 in the upper 15 meters of a site.
incs = []; xi1 = []; xi3 = []; xi4 = []; xi5 = []; t15i = [];
t15=zeros(1,n);
x = zeros(5,n);

i50 = find(repmat(CINC(idx).z,1,n) <= 50);
i15 = find(N160 <= 15);
i5015 = intersect(i50,i15);
it15 = intersect(i5015,isat);
incs = repmat(inc,1,n);
t15i = zeros(length(CINC(idx).z),n);
t15i(it15) = 1; %binary matrix indicating which zones are susceptible to l.s.
xi1 = sum(p1.*incs.*t15i); %total thickness of T15 for SI = 1 (in ft)
xi3 = sum(p3.*incs.*t15i);
xi4 = sum(p4.*incs.*t15i);
xi5 = sum(p5.*incs.*t15i);
t15 = 0.3048.*(xi1+xi3+xi4+xi5); %in meters
inan = isnan(t15) == 1;
t15(inan) = 0; %replace NaN's with zeros
```

```
    x(1,:) = 0.3048.*xi1./t15;
    x(3,:) = 0.3048.*xi3./t15;
    x(4,:) = 0.3048.*xi4./t15;
    x(5,:) = 0.3048.*xi5./t15;
    inan = isnan(x) == 1;
    x(inan) = 0; %replace NaN's with zeros

    %solve for T15cs
    CINC(idx).t15cs = t15e(t15,x); %in meters
end

save CPTINC CINC; %save results
```

5. BINC_CINC_COMBINER.m

```
%Script extracts information from BLOWINC, and CPTINC and puts it into a
%combined table format (exports ALLSITE.mat).

clear all
close all
load BLOWINC
load CPTINC
load BLOWINCSLC %load  BLOWINC table containing Salt Lake County data

n = 300;
```

```
%compile id numbers and insitu test types
siteidno = [BINC.siteidno]';
spts = ones(length(BINC),1); %set index to 1 for spt data

cptidno = [CINC.cptidno]';
cpts = 2.*ones(length(CINC),1); %set index to 2 for cpt data

ssiteidno = [SINC.siteidno]';
sspts = ones(length(SINC),1);

AS.idno = vertcat(siteidno,cptidno, ssiteidno);
AS.test = vertcat(spts,cpts,sspts);

%compile geologic units
sgeology = [BINC.geolunit]';
cgeology = [CINC.geolunit]';
slcgeology = [SINC.geolunit]';

AS.geolunit = vertcat(sgeology, cgeology, slcgeology);

%compile gwt depths
sgwt = [BINC.depthgw]';
cgwt = [CINC.depthgw]';
slcgwt = [SINC.depthgw]';
AS.depthgw = vertcat(sgwt,cgwt,slcgwt);
```

```
%compile coordinates
seasting = [BINC.easting]';
ceasting = [CINC.easting]';
slceasting = [SINC.easting]';
snorthing = [BINC.northing]';
cnorthing = [CINC.northing]';
slcnorthing = [SINC.northing]';

AS.easting = vertcat(seasting,ceasting,slceasting);
AS.northing = vertcat(snorthing,cnorthing,slcnorthing);

%compile median values of Nbar
%adjust those values where there was refusal (N = 100 for rock from zmax to
%100')
irefuse = [139 166 514 515 516 517 518]; %SITEIDNO's with reported refusal
for i = 1:length(irefuse);
   idx = find([BINC.siteidno]==irefuse(i));
   zmax = BINC(idx).zmax;
   nbar = BINC(idx).Nbarmed;
   nbarnew = zmax/100*nbar + (100-zmax)/100*100;
   BINC(idx).Nbarmed = nbarnew;
   BINC(idx).zmax = 100; %update max. depth to 100'
end

snbar = [BINC.Nbarmed]';
cnbar = [CINC.Nbarmed]';
```

```
slcnbar = nan(length(SINC),1);
AS.Nbar = vertcat(snbar,cnbar,slcnbar);

%compile maximum depths
smaxz = [BINC.zmax]';
cmaxz = [CINC.zmax]';
slcmaxz = nan(length(SINC),1);
AS.zmax = vertcat(smaxz,cmaxz,slcmaxz);

%compile critical depths
sdcr = fliplr(rot90(reshape([BINC.dcr],n,length(BINC)),-1));
cdcr = fliplr(rot90(reshape([CINC.dcr],n,length(CINC)),-1));
slcdcr = fliplr(rot90(reshape([SINC.dcr],n,length(SINC)),-1));

AS.dcr = vertcat(sdcr,cdcr,slcdcr);

%compile critical total stresses
stscr = fliplr(rot90(reshape([BINC.tscr],n,length(BINC)),-1));
ctscr = fliplr(rot90(reshape([CINC.tscr],n,length(CINC)),-1));
slctscr = fliplr(rot90(reshape([SINC.tscr],n,length(SINC)),-1));
AS.tscr = vertcat(stscr,ctscr,slctscr);

%compile critical effective stresses
sescr = fliplr(rot90(reshape([BINC.escr],n,length(BINC)),-1));
cescr = fliplr(rot90(reshape([CINC.escr],n,length(CINC)),-1));
slcescr = fliplr(rot90(reshape([SINC.escr],n,length(SINC)),-1));
```

```
AS.escr = vertcat(sescr,cescr,slcescr);

%compile t15cs
st15cs = fliplr(rot90(reshape([BINC.t15cs],n,length(BINC)),-1));
ct15cs = fliplr(rot90(reshape([CINC.t15cs],n,length(CINC)),-1));
slct15cs = fliplr(rot90(reshape([SINC.t15cs],n,length(SINC)),-1));
AS.t15cs = vertcat(st15cs,ct15cs,slct15cs);

%compile N160cr, N160cscr
sn160cr = fliplr(rot90(reshape([BINC.n160cr],n,length(BINC)),-1));
slcn160cr = fliplr(rot90(reshape([SINC.n160cr],n,length(SINC)),-1));

sn160cscr = fliplr(rot90(reshape([BINC.n160cscr],n,length(BINC)),-1));
slcn160cscr = fliplr(rot90(reshape([SINC.n160cscr],n,length(SINC)),-1));
cn160cscr = fliplr(rot90(reshape([CINC.n160cscr],n,length(CINC)),-1));

cnan = nan(length(CINC),n); %fill in nan's for cpt data
AS.n160cr = vertcat(sn160cr, cnan, slcn160cr);
AS.n160cscr = vertcat(sn160cscr, cn160cscr, slcn160cscr);

%compile qc1cr, rfcr, and ccr
snan = nan(length(BINC),n); %fill in nan's for spt data
qc1cr = fliplr(rot90(reshape([CINC.qc1cr],n,length(CINC)),-1));
ccr = fliplr(rot90(reshape([CINC.ccr],n,length(CINC)),-1));
rfcr = fliplr(rot90(reshape([CINC.rfcr],n,length(CINC)),-1));
slcnan = nan(length(SINC),n);
```

```
AS.qc1cr = vertcat(snan, qc1cr,slcnan);
AS.ccr = vertcat(snan, ccr,slcnan);
AS.rfcr = vertcat(snan, rfcr,slcnan);

%assign "deposit" indices according to geologic units
load DEPOSITS; %this file assigns each geologic unit an index corresponding to its
deposit class (11 in Weber County)
[Bg Ig Jg] = unique(AS.geolunit);
[Bd Id Jd] = unique(DEP.usites);
deposit_index = interp1([1:length(Bg)],Jd,Jg,'nearest');
AS.deposit = Bd(deposit_index);
AS.idxdeposit = deposit_index;

%compute median values of N160cscr, t15cs, and escr
AS.N160CSCR = median(AS.n160cscr,2);
AS.T15CS = median(AS.t15cs,2); %in meters
AS.ESCR = median(AS.escr,2); %in tsf
i = AS.T15CS == 0;
AS.N160CSCR(i) = NaN;
AS.ESCR(i) = NaN;
save ALLSITE AS; %save results to ALLSITE table
```

6. GRID_READER.m

```
%Script loads grid shapefile from Arcmap.  Use this file after running
%latticespot (in ArcGIS) and extracting the age, idxdeposit, siteclass, dem10m, and
%slope raster values at each grid point.  This file outputs a GRIDDATA.mat type
%file that can be solved in Matlab.

%Load the attribute table of the grid points.  This table should be filled with values
%extracted from raster images.
[S,A] = shaperead('D:\WEBER_COUNTY_GIS\Grids\sgridpts.shp','Attributes',{'age'
'idxdeposit' 'siteclass' 'dem10m' 'slope' });

GRID.easting = [S.X]';
GRID.northing = [S.Y]';
GRID.age = [A.age]';
GRID.idxdeposit = [A.idxdeposit]';
idxclass = [A.siteclass];
GRID.elev = [A.dem10m]';
GRID.slope = [A.slope]';

%remove nan data (empty data because grid points are outside of rasters)

inan = find(GRID.age == 0);
GRID.easting(inan) = [];
GRID.northing(inan) = [];
GRID.age(inan) = [];
GRID.idxdeposit(inan) = [];
```

```
idxclass(inan) = [];

GRID.elev(inan) = [];

GRID.slope(inan) = [];


%replace data such that slope is between 0.1 - 6 %.  Note: this represents less

%than 5% of the study area

j = find(GRID.slope < 0.1);

GRID.slope(j) = 0.1;

j = find(GRID.slope > 6);

GRID.slope(j) = 6;


%assign site class values, 1 = 'E', 2 = 'D'

i = idxclass == 1;

siteclass(i) = {'E'};


i = idxclass == 2;

siteclass(i) = {'D'};


GRID.siteclass = siteclass';


save GRIDDATA GRID; %save results
```

7. mr_finder.m

```
% Script spatially interpolates for seismic inputs from a grid.  It uses the
% spatial_interpvec.m function for 2-D bilinear interpolation

clear all
close all

%load desired seismic event
load 10P50; %gridded values for a 10% in 50 yr. seismic event in Weber County

%specify grid points for analysis
load GRIDDATA;

%grid points should be in NAD83, Zone 12 N
% Use utm2deg function written by Rafael Palacios, Matlab central
% Version: Apr/06, Jun/06, Aug/06
utmzone(1:length(GRID.northing),1) = {'12 T'};

%convert grid points into lats and longs
[lat,long] = utm2deg(GRID.easting, GRID.northing,char(utmzone));

%spatially interpolate for amax, Mw, and R (in km) based on gridded points'
%site class.
siteclass = char(GRID.siteclass);

i = siteclass == 'E';
```

```
amax(i) = spatial_interpvec(SEIS.LONG, SEIS.LAT, SEIS.PGA_E, long(i), lat(i));
Mw(i) = spatial_interpvec(SEIS.LONG, SEIS.LAT, SEIS.MW_E, long(i), lat(i));
R(i) = spatial_interpvec(SEIS.LONG, SEIS.LAT, SEIS.R_E, long(i), lat(i));

i = siteclass == 'D';
amax(i) = spatial_interpvec(SEIS.LONG, SEIS.LAT, SEIS.PGA_D, long(i), lat(i));
Mw(i) = spatial_interpvec(SEIS.LONG, SEIS.LAT, SEIS.MW_D, long(i), lat(i));
R(i) = spatial_interpvec(SEIS.LONG, SEIS.LAT, SEIS.R_D, long(i), lat(i));

i = siteclass == 'C';
amax(i) = spatial_interpvec(SEIS.LONG, SEIS.LAT, SEIS.PGA_C, long(i), lat(i));
Mw(i) = spatial_interpvec(SEIS.LONG, SEIS.LAT, SEIS.MW_C, long(i), lat(i));
R(i) = spatial_interpvec(SEIS.LONG, SEIS.LAT, SEIS.R_C, long(i), lat(i));

%output results
GRID.amax = amax'; %in units of gravity
GRID.Mw = Mw';
GRID.R = R'; %in km

save GRIDDATA GRID; %save results
```

8. spatial_interpvec.m

```
function [ siteVals ] = spatial_interpvec( gridLons, gridLats, gridVals, siteLons,
siteLats )

%This function executes 2-d bilinear interpolation given a table of seismic data.
table
%structured as columns of lat, long, and seismic value
% Input
% -----
% gridLons = ( # grid points x 1 ) vector of longitudes for gridded seismic
% values
% gridLats = ( # grid points x 1 ) vector of latitudes for gridded seismic
% values
% gridVals = ( # grid points x # values ) matrix of seismic values
% siteLons  = ( # sites x 1 ) vector of longitudes for new grid
% siteLats  = ( # sites x 1 ) vector of latitudes for new grid
%
% Ouput
% -----
% siteVals  = ( # sites x # values ) matrix of interpolated values
%

X = unique( gridLons )';
nLons = length( X );

XI = siteLons;
```

```
Y = flipud( unique( gridLats ) );
nLats = length( Y );

YI = siteLats;

nVals = size( gridVals, 2 );
for j = 1:nVals

   Z = reshape( gridVals(:,j), nLons, nLats )';
   tmp = interp2( X, Y, Z, XI, YI, 'linear', NaN )';
   siteVals(:,j) = tmp(:);

end
```

9. w_finder.m

```
%Script computes the free-face ratio (W) for a list of grid points.  It finds
%the elevation difference between the grid point and the bottom of the
%nearest free-face feature (H).  It divides this difference by the distance
%from the grid point to that free-face feature (L).

clear all
close all

%specify grid points for analysis
load GRIDDATA;
```

```
%load the polyline shapefile for the free-face features, A = bottom of channel
elevation
%Z_Mean from ArcMap "Add surface information" tool.  This tool assigns
%elevations from a raster DEM to each line segment.  The
%bottom of the channel was found at each short line segment using said tool and a
%10 m DEM in Arcmap.
[S,A] =
shaperead('D:\WEBER_COUNTY_GIS\Major_Rivers\MajorRivers\Final\webrivexp.shp',
'Attributes',{'Z_Mean'});

for i = 1:length(S);
   S(i).Z(1,1:length(S(i).X)) = A(i).Z_Mean; %set depth of channel equal to its
attribute in A array
end

%convert shapefile structure into a list of vectors of xy0, xy1, and z
X = [S.X]';
Y = [S.Y]';
Z = [S.Z];

inan = find(isnan(X) == 1);  %index to NaN's which are ends of a feature
inan2 = inan;
inan2(length(inan)) = [];

ibegin = ones(length(X),1);
```

```
ibegin(inan) = 0;

ibegin(inan - 1) = 0;

ib = ibegin == 1;


iend = ones(length(X),1);

iend(inan) = 0;

iend(inan2+1) = 0;

iend(1) = 0;

ie = iend == 1;


xy0 = [X(ib) Y(ib)];

xy1 = [X(ie) Y(ie)];

z = Z(ib)';


% %plot to verify channels were loaded properly

% line(X,Y); hold on;

% for i = 1:length(xy0);

%     east = [xy0(i,1) xy1(i,1)];

%     north = [xy0(i,2) xy1(i,2)];

%     plot(east,north,'r-','linewidth',2); hold on;

% end


xyP = zeros(length(xy0),2); %preallocate the points


W = zeros(length(GRID.northing),1);
```

```
%Find W using distptolineseg function
for i = 1:length(GRID.northing);
   coords = [GRID.easting(i) GRID.northing(i)];
   xyP = repmat(coords,length(xy0),1);
         % find distance to nearest channel segment, r = L
   [r,ir] = min(distptolineseg(xy0,xy1,xyP));
   w = (GRID.elev(i) - z(ir))./r.*100; %define H of free face as elevation at point
                              %minus elevation of the bottom of the
                              %nearest channel segment
   W(i) = w;
end

i = W > 20;%limit W to 20 % (less than 2% of data)
W(i) = 20;
i = W < 1;
W(i) = 0; %if W is less than 1%, it's not influential.  Use slope model instead.

GRID.W = W;

save GRIDDATA GRID; %save results
```

10. distptolineseg.m

```
function r = distptolineseg( xy0, xy1, xyP )
% function calculates the distance from an input point row vector (xyP) to
% a line segment with endpoint row vectors xy0 and xy1.
```

```
vx = xy0(:,1)-xyP(:,1);

vy = xy0(:,2)-xyP(:,2);

ux = xy1(:,1)-xy0(:,1);

uy = xy1(:,2)-xy0(:,2);

lenSqr= (ux.*ux+uy.*uy); %squared length of line segment

detP= -1.*vx.*ux + -1.*vy.*uy; %area of parallelogram created by the 3 vectors


r = abs(ux.*vy-uy.*vx)./sqrt(lenSqr); %perpendicular distance from point to line

i = detP < 0;

r(i) = sqrt((xy0(i,1) - xyP(i,1)).^2 + (xy0(i,2) - xyP(i,2)).^2); %distance from point
to end point 1 of line

i = detP > lenSqr;

r(i) = sqrt((xy1(i,1) - xyP(i,1)).^2 + (xy1(i,2) - xyP(i,2)).^2); %distance from point
to end point 2 of line


end
```

11. grid_solver.m

```
%Script solves for probability of liquefaction triggering and the
%probability of lateral spreads exceeding displacement thresholds for each grid
%point.  It uses the Monte Carlo random sampling method and several Matlab
%function files.  This is the "work-horse" script for solving the grid


clear all

close all

load GRIDDATA; %specify grid points for analysis
```

```
load VSTRUCT; %load variogram fitted to data (output of variogramfit.m), named
"S"
%refer to Matlab central for the variogramfit.m function written by Wolfgang
%Schwanghart, October, 2010.
load ALLSITE; %load table of all geotechnical data (output from
%BINC_CINC_COMBINER.m)

s = 1;
e = length(GRID.northing);

%simulate 3,000 rounds
n = 1000; %number of samples taken for analysis
m = 3; %number of columns taken from critical layer simulations (1 - 300)
test = repmat(AS.test,1,300); %300 is total number of columns in ALLSITE.mat

for idx = s:e;

   %Find weights according to the variogram.  If a sampled site is within
   %95 meters of the grid point, it will have a higher weight
   %Uses BLUE_weights.m to solve for weights

   dist = []; isamp = [];
   dist = ((GRID.easting(idx) - AS.easting).^2 + (GRID.northing(idx) -
AS.northing).^2).^0.5; %distance to every point in database (in meters)
   inear = find(dist<95);
   igeo = find(AS.idxdeposit == GRID.idxdeposit(idx));
```

```
    isamp = unique(vertcat(inear,igeo)); %index to all sites that are nearby or within
same depositional environment.

    if isempty(inear) == 1;
        weights = ones(length(isamp),1)./length(isamp); %set weights as equally
likely if none are within 95 meters.
    else
        weights =
BLUE_weights(S,AS.easting(isamp),AS.northing(isamp),GRID.easting(idx),GRID.nort
hing(idx));
        weights(length(isamp)+1) = []; %remove the lagrange multiplier
        j = find(weights < 0.001); %remove weights that are essentially zero
compared to nearby weights
        weights(j) = [];
        isamp(j) = [];
        weights = weights./sum(weights); %re-scale so that weights sum to one
    end

    %randomly sample the sites (or SPT/CPT investigations) according to the weights
(with replacement)
    if length(isamp) == 1;
        rrand = repmat(isamp,n,m); %indicates grid point is on top of a sample point
    else
        rrand = repmat(randsample(isamp,n,true,weights),1,m); %random index to
sites
    end
```

```
crand = randi(300,[n,m]);
ind = sub2ind(size(AS.dcr),rrand,crand); %index to all selected random samples
in ALLSITE.mat

%solve for the rigidity factor, rd.  Use rd.m function.
Rd = []; sigmard = []; sim_rd = [];
[Rd, sigmard] = rd(0.3048.*AS.dcr(ind),GRID.amax(idx),GRID.Mw(idx));
sim_rd = Rd + sigmard.*randn(n,m);
i = sim_rd > 1;
sim_rd(i) = 1;
i = sim_rd < 0.18;
sim_rd(i) = 0.18;  %cap rd between 0.18 and 1 (per Cetin et al. figure)

%solve for kdr, as a function of age.  From Hayati and Andrus (2009),
% kdr = 0.13 log10(age) + 0.83 with sigma = 0.24.
mukdr = []; kdr = [];
mukdr = 0.13.*log10(GRID.age(idx)) + 0.83;
kdr = mukdr + 0.24.*randn(n,m);
i = kdr > 3; %cap kdr from 0.7 to 3
kdr(i) = 3;
i = kdr < 0.7;
kdr(i) = 0.7;

%solve for csr
csr = [];
csr = 0.65 .* GRID.amax(idx) .* AS.tscr(ind)./AS.escr(ind).*sim_rd./kdr;
```

```
    inan = isnan(csr) == 1;
    csr(inan) = 0; %if the csr = NaN, indicates there is no critical layer.  Set to zero
so prob. of liq = 0

    %solve for prob. of liquefaction, PL.  Use probliq function for SPT-based data and
    %probliqcpt function for CPT-based data
    PL = [];
    inds = test(ind) == 1; %SPT data
    indc = test(ind) == 2; %CPT data
    PL(inds) = probliq(
AS.n160cscr(ind(inds)),0,csr(inds),GRID.Mw(idx),AS.escr(ind(inds))); %use SPT
data and Cetin's method
    PL(indc) =
probliqcpt(0.09576.*AS.qc1cr(ind(indc)),AS.rfcr(ind(indc)),AS.ccr(ind(indc)),csr(indc
),GRID.Mw(idx),95.76.*AS.escr(ind(indc))); %use CPT data and Moss's method
    PL = reshape(PL,n,m);

    %solve for probability of lateral spread exceeding specific thresholds
    %(in increments of 0.1 meters).  Use mlr_gillins function.
    DHw = []; DHs = []; DHbar = [];
    pd1 = []; pd2 = []; pd3 = []; pd4 =[]; pd5 = []; pd6 = []; pd7 = [];
    pd8 = []; pd9 = []; pd10 = [];
    if GRID.W(idx) == 0;
       DHw = zeros(n,m);
    else
```

```
        DHw =
mlr_gillins(1,GRID.Mw(idx),GRID.R(idx),GRID.W(idx),GRID.slope(idx),AS.t15cs(ind),
[0 0 1 0 0]);
    end
    DHs =
mlr_gillins(0,GRID.Mw(idx),GRID.R(idx),GRID.W(idx),GRID.slope(idx),AS.t15cs(ind),
[0 0 1 0 0]);
    DHbar = max(DHw,DHs); %controlling topographic condition between slope and
free-face conditions (in meters)

    %sigma_logDH = 0.2182
    %probability lateral spread exceeds 0.1 - 1.0 meters given seismic event
    pd1 = (1 - cdf('normal',log10(0.1),log10(DHbar),0.2182)).*PL;
    pd2 = (1 - cdf('normal',log10(0.2),log10(DHbar),0.2182)).*PL;
    pd3 = (1 - cdf('normal',log10(0.3),log10(DHbar),0.2182)).*PL;
    pd4 = (1 - cdf('normal',log10(0.4),log10(DHbar),0.2182)).*PL;
    pd5 = (1 - cdf('normal',log10(0.5),log10(DHbar),0.2182)).*PL;
    pd6 = (1 - cdf('normal',log10(0.6),log10(DHbar),0.2182)).*PL;
    pd7 = (1 - cdf('normal',log10(0.7),log10(DHbar),0.2182)).*PL;
    pd8 = (1 - cdf('normal',log10(0.8),log10(DHbar),0.2182)).*PL;
    pd9 = (1 - cdf('normal',log10(0.9),log10(DHbar),0.2182)).*PL;
    pd10 = (1 - cdf('normal',log10(1.0),log10(DHbar),0.2182)).*PL;

    %output resulting 16th, 50th, and 84th percentile values from each
    %distribution. Also output mean & st. dev. of each distribution
    GRID.PL(idx,1:3) = prctile(reshape(PL,numel(PL),1),[16 50 84]);
```

```
GRID.pd1(idx,1:3) = prctile(reshape(pd1,numel(PL),1),[16 50 84]);
GRID.pd2(idx,1:3) = prctile(reshape(pd2,numel(PL),1),[16 50 84]);
GRID.pd3(idx,1:3) = prctile(reshape(pd3,numel(PL),1),[16 50 84]);
GRID.pd4(idx,1:3) = prctile(reshape(pd4,numel(PL),1),[16 50 84]);
GRID.pd5(idx,1:3) = prctile(reshape(pd5,numel(PL),1),[16 50 84]);
GRID.pd6(idx,1:3) = prctile(reshape(pd6,numel(PL),1),[16 50 84]);
GRID.pd7(idx,1:3) = prctile(reshape(pd7,numel(PL),1),[16 50 84]);
GRID.pd8(idx,1:3) = prctile(reshape(pd8,numel(PL),1),[16 50 84]);
GRID.pd9(idx,1:3) = prctile(reshape(pd9,numel(PL),1),[16 50 84]);
GRID.pd10(idx,1:3) = prctile(reshape(pd10,numel(PL),1),[16 50 84]);

GRID.PL(idx,4) = mean(reshape(PL,numel(PL),1));
GRID.pd1(idx,4) = mean(reshape(pd1,numel(PL),1));
GRID.pd2(idx,4) = mean(reshape(pd2,numel(PL),1));
GRID.pd3(idx,4) = mean(reshape(pd3,numel(PL),1));
GRID.pd4(idx,4) = mean(reshape(pd4,numel(PL),1));
GRID.pd5(idx,4) = mean(reshape(pd5,numel(PL),1));
GRID.pd6(idx,4) = mean(reshape(pd6,numel(PL),1));
GRID.pd7(idx,4) = mean(reshape(pd7,numel(PL),1));
GRID.pd8(idx,4) = mean(reshape(pd8,numel(PL),1));
GRID.pd9(idx,4) = mean(reshape(pd9,numel(PL),1));
GRID.pd10(idx,4) = mean(reshape(pd10,numel(PL),1));

GRID.PL(idx,5) = std(reshape(PL,numel(PL),1));
GRID.pd1(idx,5) = std(reshape(pd1,numel(PL),1));
GRID.pd2(idx,5) = std(reshape(pd2,numel(PL),1));
```

```
    GRID.pd3(idx,5) = std(reshape(pd3,numel(PL),1));
    GRID.pd4(idx,5) = std(reshape(pd4,numel(PL),1));
    GRID.pd5(idx,5) = std(reshape(pd5,numel(PL),1));
    GRID.pd6(idx,5) = std(reshape(pd6,numel(PL),1));
    GRID.pd7(idx,5) = std(reshape(pd7,numel(PL),1));
    GRID.pd8(idx,5) = std(reshape(pd8,numel(PL),1));
    GRID.pd9(idx,5) = std(reshape(pd9,numel(PL),1));
    GRID.pd10(idx,5) = std(reshape(pd10,numel(PL),1));

end

save GRIDDATA GRID %save results
```

12. BLUE_weights.m

```
function [lambda] = BLUE_weights(vstruct,x,y,xi,yi,chunksize)

% function solves for the weights using ordinary kriging theory
% A significant portion of this code is from kriging.m function written by
% Wolfgang Schwanghart, Matlab central, dated October, 2010

% Input arguments:
%
%     vstruct   structure array with variogram information as returned
%               from variogramfit.m
% refer to Matlab central for the variogramfit.m function written by Wolfgang
% Schwanghart, October, 2010.
```

```
%     x,y       coordinates of observations (i.e., location of SPT/CPT's)
%     xi,yi     coordinates of locations for predictions (i.e., grid point)
%     chunksize nr of elements in zi that are processed at one time.
%               The default is 100, but this depends largely on your
%               available main memory and numel(x).
%
% Output arguments:
%
%     lambda  weights to each observation
%
% size of input arguments
sizest = size(xi);
numest = numel(xi);
numobs = numel(x);

% force column vectors
xi = xi(:);
yi = yi(:);
x  = x(:);
y  = y(:);

if nargin == 5;
   chunksize = 100;
elseif nargin == 6;
else
   error('wrong number of input arguments')
```

```
end

% check if the latest version of variogramfit is used
if ~isfield(vstruct, 'func')
    error('please download the latest version of variogramfit from the FEX')
end

% variogram function definitions
switch lower(vstruct.model)
    case {'whittle' 'matern'}
        error('whittle and matern are not supported yet');
    case 'stable'
        stablealpha = vstruct.stablealpha; %#ok<NASGU> % will be used in an
anonymous function
end

% distance matrix of locations with known values
Dx = hypot(bsxfun(@minus,x,x'),bsxfun(@minus,y,y'));

% if we have a bounded variogram model, it is convenient to set distances
% that are longer than the range to the range since from here on the
% variogram value remains the same and we do not need composite functions.
switch vstruct.type;
    case 'bounded'
        Dx = min(Dx,vstruct.range);
    otherwise
```

```
end

% now calculate the matrix with variogram values
A = vstruct.func([vstruct.range vstruct.sill],Dx);
% if ~isempty(vstruct.nugget)
%     A = A+vstruct.nugget;
% end

% the matrix must be expanded by one line and one row to account for
% condition, that all weights must sum to one (lagrange multiplier)
A = [[A ones(numobs,1)];ones(1,numobs) 0];

% A is often very badly conditioned. Hence we use the Pseudo-Inverse for
% solving the equations
A = pinv(A);

% parametrize engine
nrloops   = ceil(numest/chunksize);

% initialize the waitbar
h  = waitbar(0,'Kr...kr...kriging');

% now loop
for r = 1:nrloops;
   % waitbar
   waitbar(r / nrloops,h);
```

```
% built chunks
if r<nrloops
   IX = (r-1)*chunksize +1 : r*chunksize;
else
   IX = (r-1)*chunksize +1 : numest;
   chunksize = numel(IX);
end

% build b
b = hypot(bsxfun(@minus,x,xi(IX)'),bsxfun(@minus,y,yi(IX)'));
% again set maximum distances to the range
switch vstruct.type
   case 'bounded'
      b = min(vstruct.range,b);
end

% expand b with ones
b = [vstruct.func([vstruct.range vstruct.sill],b);ones(1,chunksize)];
if ~isempty(vstruct.nugget)
   b = b+vstruct.nugget;
end

% solve system
lambda = A*b; %solve for weights
```

```
end

% close waitbar
close(h)

end
```

13. rd.m

```
function [rdhat, sigmard] = rd(d, amax, Mw)

%function calculates the nonlinear shear mass participation factor, rd, based on
Cetin
%et al.,2004.  This function is simplified so to eliminate Vs40' as per Moss et al.,
%2006.

%Inputs: amax = pga from a seismic event in units of gravity
%       Mw = moment magnitude
%       d = depth in meters at the midpoint of the critical layer

%Outputs:  rdhat = mean stress reduction factor
%         sigmard = standard deviation of the stress reduction factor

if d < 20;
   rdtop = (1 + (-9.147 - 4.173 .* amax + 0.652.*Mw ) ./ (10.567 + 0.089 .*
exp(0.089 .* (-1.*d .* 3.28 - 7.760 .* amax + 78.576))));
```

```
   rdbot = (1 + (-9.147 - 4.173 .* amax + 0.652.*Mw ) ./ (10.567 + 0.089 .*
exp(0.089 .* (-7.760 .* amax + 78.576))));

   rdhat = rdtop ./ rdbot;
else
   rdtop = (1 + (-9.147 - 4.173 .* amax + 0.652.*Mw ) ./ (10.567 + 0.089 .*
exp(0.089 .* (-1.*d .* 3.28 - 7.760 .* amax + 78.576))));
   rdbot = (1 + (-9.147 - 4.173 .* amax + 0.652.*Mw ) ./ (10.567 + 0.089 .*
exp(0.089 .* (-7.760 .* amax + 78.576))));

   rdhat = rdtop ./ rdbot - 0.0014.*(d.*3.28-65);
end

sigmard = (d .* 3.28) .^ 0.864 .* 0.00814;
i = find(d >= 12.2);
sigmard(i) = 40 .^ 0.864 .* 0.00814;

end
```

14. probliq.m

```
function [PL, brack] = probliq( N160, FC, CSR, Mw, effstress)

%function calculates the probability of liquefaction using methods outlined
%by Cetin et al. 2004

%Inputs: N160 -- corrected SPT blowcounts for the liquefiable layer
```

```
%       FC -- fines content for liquefiable layer (%)
%       CSR -- equivalent uniform CSR =
%                   0.65*(amax/g)*(sigma/sigma')*rd/kdr
%       Mw -- earthquake's moment magnitude
%       effstress -- effective stress (in atm)

%Outputs: PL -- probability of liquefaction (in decimal)

brack = -1.*(N160 .* (1 + 0.004 .* FC) - 13.32.*log(CSR)-29.53.*log(Mw)-
3.70.*log(effstress)+0.05.*FC + 16.85)./2.70;

PL = cdf('norm',brack,0,1);

end
```

15. probliqcpt.m

```
function [PL] = probliqcpt( qc1, rf, c, CSR, Mw, effstress)

%function calculates the probability of liquefaction using methods outlined
%by Moss et al. 2006, for CPT

%Inputs: qc1 -- corrected tip resistance for the liquefiable layer (in MPa)
%       rf -- friction ratio (%)
%       c -- overburden stress normalization exponent
%       CSR -- equivalent uniform CSR =
%                   0.65*(amax/g)*(sigma/sigma')*rd/kdr
```

```
%       Mw -- earthquake's moment magnitude
%       effstress -- effective stress (in KPa)

%Outputs: PL -- probability of liquefaction (in decimal)

brack = -1.*(qc1.^1.045 + qc1.*(0.110.*rf)+(0.001.*rf) + c.*(1 + 0.850.*rf) -
7.177.*log(CSR) - 0.848.*log(Mw) - 0.002.*log(effstress) - 20.923)./1.632;

PL = cdf('norm',brack,0,1);

end
```

16. mlr_gillins

```
function [spread] = mlr_gillins(X_topo, M, R, W, S, T15, x)

%This function calculates the amount of lateral spread (in meters) using
%the modified MLR model (Gillins and Bartlett empirical model)

%INPUTS
%X_topo = controlling topographic condition (1 for free-face, 0 for slope)
% M = earthquake moment magnitude
% R = distance from point to fault (km)
% W = percentage of height of free face to distance from face to point (%)
% S = ground slope (%)
% T15 = thickness of spreadable layer (m)
% x = 1x6 vector that makes up the ratios of T15 (i.e., x(1) = ratio gravel,
```

```
%   x(2)=ratio very coarse sand and gravel, x(3)=ratio coarse and medium sand
such as SP,SP-SM,
%   x(4)=ratio fine sand such as SM, and x(5)=ratio silt ML

%OUTPUTS
% spread = expected lateral displacement (m)

Rstar = R + 10^(0.89*M - 5.64);

if X_topo==1; %free-facing conditions so S term = 0
   logDh = -8.453 - 0.342 + 1.348*M - 1.068*log10(Rstar) - 0.017*R +
0.453*log10(W) + 0.588*log10(T15) - 0.647*x(1) + 0.278*x(3)+0.032*x(4) -
0.571*x(5);
elseif X_topo==0; %sloping-ground conditions so W term = 0
   logDh = -8.453 + 1.348*M - 1.068*log10(Rstar) - 0.017*R + 0.334*log10(S) +
0.588*log10(T15) - 0.647*x(1) + 0.278*x(3)+0.032*x(4) - 0.571*x(5);
end

spread = 10.^logDh;

end
```